



Innovative x-ray diagnostic for impurity transport on ITER

Colette Damien

► To cite this version:

Colette Damien. Innovative x-ray diagnostic for impurity transport on ITER. Plasma Physics [physics.plasm-ph]. Aix-Marseille Université, 2021. English. NNT: . tel-03153486

HAL Id: tel-03153486

<https://hal.science/tel-03153486>

Submitted on 26 Feb 2021

HAL is a multi-disciplinary open access archive for the deposit and dissemination of scientific research documents, whether they are published or not. The documents may come from teaching and research institutions in France or abroad, or from public or private research centers.

L'archive ouverte pluridisciplinaire **HAL**, est destinée au dépôt et à la diffusion de documents scientifiques de niveau recherche, publiés ou non, émanant des établissements d'enseignement et de recherche français ou étrangers, des laboratoires publics ou privés.

PhD THESIS

Soutenue à Aix-Marseille Université
le 11 janvier 2021 par

Damien COLETTE

Titre de la thèse:
Étude du transport d'impuretés sur ITER et du choix de
diagnostics X innovants associé

Discipline

Physique et Sciences de la Matière

Spécialité

Énergie, rayonnement et plasma

École doctorale

École doctorale 352 : Physique et Sciences de la Matière

Laboratoire/Partenaires de recherche

Institut de Recherche sur la Fusion par confinement Magnétique, CEA Cadarache
ITER Organization

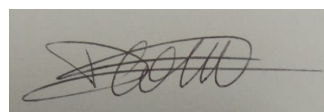
Composition du jury

Clemente ANGIONI IPP Garching	Rapporteur
Marek SCHOLZ IFJ-PAN	Rapporteur
Didier MAZON IRFM, CEA Cadarache	Directeur de thèse
Robin BARNESLEY ITER Organization	Examineur
Conrad BECKER Aix-Marseille Université	Examineur
Sehila GONZALEZ DE VI- CENTE IAEA	Examinatrice
Geert VERDOOLAEGE Ghent University	Examineur

Je soussigné, Damien Colette, déclare par la présente que le travail présenté dans ce manuscrit est mon propre travail, réalisé sous la direction scientifique de Didier Mazon, dans le respect des principes d'honnêteté, d'intégrité et de responsabilité inhérents à la mission de recherche. Les travaux de recherche et la rédaction de ce manuscrit ont été réalisées dans le respect à la fois de la charte nationale de déontologie des métiers de la recherche et de la charte d'Aix-Marseille Université relative à la lutte contre le plagiat.

Ce travail n'a pas été précédemment soumis en France ou à l'étranger dans une version identique ou similaire à un organisme examinateur.

Fait à Cadarache le 22/10/2020



Cette œuvre est mise à disposition selon les termes de la [Licence Creative Commons Attribution - Pas d'Utilisation Commerciale - Pas de Modification 4.0 International](https://creativecommons.org/licenses/by-nc-nd/4.0/).

Résumé

La grande majorité de l'énergie mondiale provient de la combustion de combustibles fossiles. Les réserves de ces combustibles ont atteint un niveau critique ces dernières années et leur combustion émet des gaz à effets de serre, qui sont les principaux responsables du dérèglement climatique. Il est donc impératif de trouver des sources d'énergies propres et durables pour remplacer ces combustibles fossiles. La fusion thermonucléaire contrôlée est un candidat de choix. Le tokamak ITER a pour objectif de démontrer la faisabilité d'un réacteur de fusion générant plus d'énergie qu'il n'en consomme ($Q > 10$). Les composants face au plasma d'ITER seront à l'origine d'une pollution de ce dernier par des impuretés lourdes telles que le tungstène. Ces impuretés sont à l'origine d'importantes pertes radiatives dans la gamme des rayons X dont la mesure est nécessaire pour étudier le transport de ces impuretés et, à terme, pouvoir identifier des actuateurs permettant de limiter leur propagation jusqu'au cœur du plasma. L'environnement radiatif d'ITER limite le choix de détecteurs X aux seuls détecteurs à gaz, dont le LVIC (Low Voltage Ionization Chamber) est le candidat principal. Cette thèse a pour but l'étude des capacités du LVIC pour la mesure de rayons X sur ITER. Un diagnostic synthétique est adapté à partir du GEM (Gas Electron Multiplier) afin de simuler la mesure par ce détecteur. L'inversion tomographique de l'émissivité X à l'aide de LVIC est étudiée et des lignes de visées additionnelles, compatibles avec les contraintes d'intégration sur ITER, sont proposées. La possibilité de discriminer le flux X en énergie est investiguée à travers une modification innovante du détecteur. Une méthode d'inversion basée sur la méthode des moindres carrés est spécifiquement développée pour la déconvolution du spectre X. Le profil de température électronique du plasma est extrait du spectre X avec succès. La capacité d'étude du transport d'impuretés du LVIC est démontrée à travers la reconstruction des coefficients de convection et de diffusion du tungstène d'un plasma ITER.

Abstract

The vast majority of the energy consumed in the world is coming from burning fossil fuels. The natural reserves of these fuels have reached a critical level in the last years and their combustion releases greenhouse effect gases, which are the main cause for global warming. It is therefore crucial to develop clean and sustainable energy sources in order to replace fossil fuels. Controlled thermonuclear fusion is one of the main candidates. The ITER tokamak aims at demonstrating the feasibility of a fusion reactor generating more energy than it consumes ($Q>10$). The ITER plasma facing components will be the source of pollution by heavy impurities such as tungsten in the plasma. Such impurities lead to great radiative losses in the X-ray range. X-ray measurement is mandatory for impurity transport studies in order to, with time, be able to identify actuators preventing impurity accumulation in the plasma core. The ITER radiative environment limits the choice of X-ray detectors to gas detectors, of which the LVIC (Low Voltage Ionization Chamber) is the most promising candidate. This thesis aims at studying the capabilities of the LVIC for X-ray measurement on ITER. A synthetic diagnostic tool has been adapted from the GEM (Gas Electron Multiplier) in order to simulate the measurement with an LVIC. Tomographic inversion of the X-ray emissivity using LVIC is studied and additional lines-of-sight, compliant with the ITER integration constraints, are proposed. The possibility of energy discrimination is investigated through an innovative modification of the detector. An inversion method based on the least squares method is specifically developed to deconvolute the X-ray spectrum. The electron temperature profile is successfully extracted from the X-ray spectrum. The capability of impurity transport study of the LVIC is demonstrated through the reconstruction of the tungsten convection and diffusion coefficients of an ITER plasma.

Remerciements

Je souhaiterais commencer par remercier Didier Mazon, Mike Walsh, Robin Barnsley et Antoine Sirinelli pour m'avoir donné l'opportunité de travailler sur ce projet.

La thèse est un travail d'équipe et je n'aurai pu rêver meilleur coéquipier que mon directeur de thèse, Didier Mazon. Merci pour ta supervision bienveillante, tes conseils, et nos conversations. Tu as toujours été là pour moi, à n'importe quelle heure de la semaine ou du weekend.

Je souhaiterais aussi remercier Robin Barnsley pour son aide. Thank you Robin for your guidance, for sharing your enthusiasm for science and diagnostics. I enjoyed every one of our chats which made me feel like a kid in a sandbox, thrilled at the thought of all the possibilities ahead of him.

Axel Jardin m'a énormément aidé lors de ces trois années et je ne saurai l'en remercier assez. La plupart de mon travail a été rendue possible grâce à tes conseils. Merci aussi pour ton amitié et pour ces déplacements à Garching.

J'adresse une mention spéciale à un petit poisson rouge sans mémoire, nommé Anastasia. You are by far my biggest inspiration and I feel blessed to have you in my life. This thesis is yours as well as mine, because I would not have made it without your incredible support (and cakes!).

Je souhaiterais remercier Matthieu Simeoni qui avant d'être un collaborateur est l'un de mes plus proches amis. J'apprécie énormément la confiance que tu as en moi et je suis très heureux que l'on ait pu travailler ensemble.

Je remercie l'ensemble des membres de l'IRFM que j'ai eu l'occasion de cotoyer pendant ma thèse : Philippe (merci pour ton accueil, et nos concerts ratés - on se rattrapera après le covid!), Didier (merci beaucoup pour tes conseils), Guillaume (homme sobre et sérieux), Camille (pour ta compagnie et tes jeux de mots de qualité), Adrien (le seul toujours là pour les séances de sport Pomonesques), Elizabetta et Alejandro (pour ces épiques Catan), Flavio (seul témoin des abus dont j'ai été victime par les dames de la cantine), Christian, Laurent, Éléonore, Robin, Mathieu, Arthur, Serafina, Samuele, Raffaele, Alberto, Matteo, Julien, Emily, Julio, Jorge.

Je suis également très reconnaissant envers l'équipe diagnostics d'ITER pour son accueil, en particulier Antoine, Mike, Julie, Silvia, Artur et Raphaël. Merci aussi à Martin O'Mullane et Christian Ingesson pour leur aide et conseils techniques.

D'un point de vue personnel je souhaite remercier :

- ma famille, notamment mes parents (et beaux-parents!), frères et soeurs (et riens!)
- mes géniaux colocs pomoniens Adrien, Camille, Clément, Davide, Lucie, Mylène et Jerry
- à mes amis Matthieu, Paolo et Sébastien
- Goji, le meilleur chaton du monde (même si sa contribution au manuscrit "hgfd-sollllll" n'a pas passé la première relecture)

Contents

Résumé	3
Abstract	4
Remerciements	6
Contents	7
List of Figures	11
List of Tables	24
1 Introduction	25
1.1 The challenge of energy	25
1.1.1 Historical approach	25
1.1.2 Fossil fuels: availability and consequences	26
1.1.3 Alternative energy sources	27
1.1.4 Energy generation from nuclear fusion	28
1.2 Nuclear fusion reactor	29
1.2.1 Fusion reactions	30
1.2.2 Ignition	31
1.2.3 Confinement	33
1.2.4 Tokamak	35
1.2.5 Existing tokamaks	40
1.3 Scope of this thesis	46
2 X-ray radiation	49
2.1 Introduction	49
2.2 X-ray emission	50
2.2.1 Bremsstrahlung emission	50
2.2.2 Radiative recombination	52
2.2.3 Spontaneous emission	53
2.3 Ionization equilibrium	54
2.3.1 Local Thermodynamical Equilibrium	55
2.3.2 Corona Equilibrium	57
2.3.3 Collisional Radiative models	58
2.3.4 Effect of impurity transport on the equilibrium	59

2.4	Total plasma emissivity	60
2.4.1	X-ray emissivity on ITER	62
2.4.2	Influence of impurity transport on the X-ray emissivity	63
2.5	Extraction of plasma parameters from X-ray measurement	64
2.5.1	Impurity density	65
2.5.2	Impurity transport coefficients	65
2.5.3	Electron temperature	66
3	X-ray measurement	69
3.1	Photodiodes	69
3.1.1	Semiconductor photodiodes	69
3.1.2	Vacuum photodiodes	72
3.2	Gas detectors	74
3.2.1	Ionization chambers	74
3.2.2	Multi-anodes Low Voltage Ionization Chamber	77
3.2.3	Gas Electron Multipliers	79
3.2.4	X-rays detectors for ITER nuclear phase	80
3.3	X-ray tomography	81
3.3.1	Overview	81
3.3.2	Minimum Fisher Information method	82
3.4	Accuracy of the X-ray emissivity calculation tool	83
4	Simulation of a Low Voltage Ionization Chamber on ITER	87
4.1	Line-integration of the emissivity	87
4.1.1	Simplified representation of a detector-aperture system	89
4.1.2	Pixelization of the plasma	91
4.2	Interaction between X-ray photons and matter	91
4.2.1	Absorption processes	92
4.2.2	Inelastic scattering: Compton effect	93
4.2.3	Elastic scattering processes	94
4.2.4	Pair production	95
4.2.5	Relative importance of the different processes	96
4.3	Synthetic diagnostic	97
4.3.1	Computation of the different physical processes	97
4.3.2	Monte Carlo-based synthetic diagnostic	99
4.3.3	Matrix-based synthetic diagnostic	101
4.3.4	Comparison of the two methods	103
5	X-ray tomography on ITER	107
5.1	ITER radial X-ray cameras	107
5.2	Tomographic capabilities	109
5.2.1	Figures of merit	109
5.2.2	Emissivity profiles	110
5.2.3	Tomographic reconstructions	112

5.3	Addition of lines-of-sight: proof of concept	116
5.4	Geometry proposal	119
5.4.1	60 vertical lines-of-sight configuration	120
5.4.2	44 vertical lines-of-sight configuration	123
6	Application of the synthetic diagnostic	127
6.1	X-ray measurement on ITER with Low Voltage Ionization Chambers . .	127
6.1.1	Influence of the filling gas	128
6.1.2	Influence of the filter	130
6.1.3	Influence of the length pressure product	130
6.2	Calibration of the LVIC measured current	131
6.2.1	Calibration methodology	132
6.2.2	Line-of-sight dependency of the calibration factor	134
6.2.3	Application to simulation results	134
6.3	Tomography using LVIC	136
6.3.1	Tomographic reconstruction of a SXR-restricted emissivity profile	136
6.3.2	Influence of the calibration method on the tomographic recon- struction	141
6.3.3	Tomographic reconstruction over a wide energy range	142
6.3.4	Influence of perturbative noise on the tomographic reconstruction	143
6.3.5	Alternative calibration method	145
7	Application to impurity transport study	149
7.1	Reconstruction of the tungsten transport coefficients on ITER	149
7.1.1	Scenarios	150
7.1.2	LVIC measurement	155
7.1.3	Negative V scenario reconstruction	156
7.1.4	Positive V scenario reconstruction	164
7.2	Poloidal asymmetries	171
7.2.1	Collisional regimes	172
7.2.2	Theory of parallel forces	172
7.2.3	Poloidal asymmetries on ITER	174
8	Energy discrimination using LVIC	183
8.1	Spectral deconvolution method	183
8.1.1	Hypothesis on the X-ray spectrum	185
8.1.2	Minimization algorithm	187
8.2	Application to ITER	189
8.2.1	Figures of merit	189
8.2.2	Spectral deconvolution using argon-filled MA-LVIC	189
8.2.3	Spectral deconvolution using xenon-filled MA-LVIC	195
8.2.4	Comparison between argon and xenon	199
8.2.5	Improving the reconstruction in the [2, 3] keV energy band . . .	199
8.2.6	Sensitivity analysis	201

8.3	Energy-resolved X-ray tomography	202
8.3.1	Figures of merit	203
8.3.2	Results	203
8.3.3	Sensitivity analysis	206
8.4	Reconstruction of the electron temperature	208
8.4.1	Figures of merit	208
8.4.2	Results	209
8.4.3	Sensitivity analysis	210
9	Conclusion and perspectives	211
	Bibliography	213

List of Figures

1.1	Global direct primary energy consumption as a function of time, distinguishing each energy source. [1, 2]	26
1.2	Aston curve: binding energy per nucleon as a function of the total amount of nucleons. Figure adapted from [7]	30
1.3	Cross sections of several fusion reactions. [8, 9]	31
1.4	Two stellarator configurations. Left: Stellarator with two sets of coils. Reproduced from [13] Right: Stellarator with a single set of coils. Reproduced from [14]	34
1.5	Principle of the Tokamak. [15]	35
1.6	Illustration of the poloidal cross-section of a tokamak.	36
1.7	Illustration of L and H confinement modes.	37
1.8	Schematic representation of the different heating sources of a tokamak. [16]	38
1.9	Left: ignition curves for different concentrations of W. Right: ignition curves for different concentrations of C. Figure adapted from [17]. . . .	39
1.10	Comparison of the Tore Supra (left) and WEST (right) poloidal cross sections. [19]	40
1.11	Top view of the WEST tokamak with details of its ex-vessel diagnostics. [21]	41
1.12	Poloidal cross-section view of WEST soft X-ray lines-of-sight.	42
1.13	Poloidal cross-section view of ASDEX Upgrade soft X-ray lines-of-sight.	43
1.14	Drawing of the ITER tokamak and integrated plant system.	44
1.15	Preliminary drawing of Korea's version of DEMO: K-DEMO.	46
2.1	Electronic radiation spectrum from microwaves to gamma-rays.	50
2.2	Atomic processes leading to X-ray emission in a plasma.	51
2.3	Left: Bremsstrahlung radiation spectrum of hydrogen for different electron temperatures. Right: Radiative recombination spectrum of hydrogen for different electron temperatures.	52
2.4	Influence of transport on the density of ions of charge z in ground state in the case of unidirectional transport along the x direction and no source term.	60
2.5	Cooling factors of hydrogen and tungsten as a function of T_e . The W and H coefficients are taken from the open ADAS database. [32]	61
2.6	Electron temperature (left) and density (right) profiles of the ITER 15MA baseline inductive scenario.	62

2.7	Radiated power profile as a function of photon energy and normalized radius for the standard high power D-T scenario.	63
2.8	Radiated power profile as a function of photon energy and normalized radius for the standard high power D-T scenario, in the case of a hydrogen plasma with $10^{-3}\%$ of tungsten. Left: Radiated profile with impurity transport. Right: Radiated profile without impurity transport.	64
3.1	Sketch of a semiconductor p-n junction, with bias voltage V_B . The upper part of the figure shows the energy of the valence and conduction bands and the lower part shows a schematic representation of the p-n junction.	70
3.2	Spectral response of the Si semiconducting diodes used on the tokamak WEST. The filter consists of a beryllium window of $50\mu m$	71
3.3	Schematic representation of a vacuum photodiode.	72
3.4	Schematic representation of an ionization chamber.	74
3.5	Pulse size (number of charges collected) as a function of the electric field in a chamber irradiated by α , β , and X-ray particles. The different regions of operations of the detector are as follows: recombination region (I), ionization chamber region (II), proportional region (III), limited proportionality region (IV), Geiger-Müller region (V) and continuous discharge region (VI). Figure reprinted from [59] with data from [60]	75
3.6	Schematic representation of two pixels of a LVIC.	76
3.7	Mean free path as a function of energy for photons in argon and xenon at $T = 300K$ and $P = 1bar$. Cross-sections data was extracted from the NIST XCOM database [63].	77
3.8	Schematic representation of a MA-LVIC with two anodes.	78
3.9	Spectral response for an argon-filled LVIC with five anodes. The length pressure products of the sub-chambers are respectively 5, 15, 50, 175, and $500\text{ mm} \cdot atm$ and the filter consists of $200\mu m$ of beryllium.	79
3.10	Schematic representation of a GEM detector with one GEM foil.	79
3.11	Possible solutions to a tomographic inversion in a 3×3 pixels space with 6 line-integrated measurements in the horizontal and vertical directions.	82
3.12	Transmission through the beryllium window (T_{Be}), absorption in the photodiode (A_{diode}) and spectral response (η) of AUG photodiodes with $75\mu m$ of beryllium window.	84
3.13	Left: electron density as a function of time and normalised radius for AUG shot #32773. Right: electron temperature as a function of time and normalised radius for AUG shot #32773.	85
3.14	Left: simulated SXR emissivity measured by the detector as a function of time and normalised radius for AUG shot #32773. Right: experimental SXR emissivity measured by the detector as a function of time and normalised radius for AUG shot #32773.	85

4.1	3D layout of a detector-aperture system in the case of rectangle detector and apertures.	88
4.2	2D layout of a detector-aperture system in a poloidal section of the plasma.	89
4.3	Sketch of a discretized poloidal cross-section of a tokamak.	91
4.4	Different stages of the photoionization process: (a) absorption of the incoming photon and ionization of the electron, (b) excited ion, (c) de-excitation through X-ray fluorescence, (d) de-excitation through Auger electron emission	92
4.5	Different stages of photon disintegration: (a) absorption of the photon by the nucleus, (b) emission of a nucleon, (c) de-excitation through γ -ray emission.	93
4.6	Different stages of Compton scattering: (a) collision between the incident photon and an electron, (b) the electron is ionized and the photon is deviated.	94
4.7	Different stages of Thomson scattering: (a) absorption of the photon by the electron, (b) forced oscillation of the electron, (c) emission of a photon of same energy and different direction.	94
4.8	Different stages of Rayleigh scattering: (a) absorption of the photon by the electron cloud, (b) in phase oscillations of the electrons, (c) emission of a photon of same energy and different direction.	95
4.9	Different stages of pair production: (a) conversion of the photon into an electron-positron pair, (b) annihilation of the positron with an electron.	95
4.10	Contribution of the different atomic processes to the total cross-section of argon (left) and xenon (right). The upper limit of the energy range (100 keV) considered on ITER in the scope of this thesis is indicated by a red vertical line.	96
4.11	Left: Total cross-sections of the different elements considered as filters. Right: Transmission ratio of different monoelement filters.	97
4.12	Photoelectric absorption ration for argon (left) and xenon (right) gas detectors with different design parameter.	98
4.13	Architecture of the Monte Carlo-based synthetic diagnostic. $T_{filter}(h\nu)$ denotes the transmission ratio through the filter for a photon of energy $h\nu$, $A_{gas}^{p-e}(h\nu)$ denotes the photo-electric effect absorption ratio in the gas for a photon of energy $h\nu$, $P(fluorescence)$ is the probability of X-ray fluorescence, $E_{fluorescence}$ is the energy of the emitted photon, W is the mean ionization energy of the gas, and F is the Fano factor of the gas.	100
4.14	Comparison of the monte carlo and matrix-based synthetic diagnostics. Left: Photon flux incoming on the detectors. Right: Flux transmitted through $200\mu m$ of beryllium.	103
4.15	Comparison of the monte carlo and matrix-based synthetic diagnostics. Left: Spectrum measured by the detector, taking X-ray fluorescence into account. Right: Distribution of the charge generated by each photon.	104

4.16	Simulation time as a function of the amount of particles simulated for the matrix and monte carlo-based synthetic diagnostic tools.	104
5.1	Left: ITER radial X-ray cameras in the EPP 12. Right: EPP 12 with the X-ray lines-of-sight.	107
5.2	ITER X-ray lines-of-sight.	108
5.3	Geometrical etendue for each line-of-sight of the radial X-ray cameras.	109
5.4	Plasma regions considered in the computation of the figures of merit. The pixels in the plasma core are displayed in red. The LCMS enclosed region contains both red and blue pixels.	110
5.5	Phantom emissivity profiles used for the assessment of the tomographic capabilities of a lines-of-sight geometry. Upper left: gaussian profile. Upper right: hollow profile. Lower left: LFS asymmetry. Lower right: HFS asymmetry.	111
5.6	Phantom emissivity profile (left), tomographic reconstruction (center) and line-integrated emissivity (right) of different emissivity configurations with the ITER radial X-ray cameras. First row: Gaussian emissivity profile. Second row: Hollow emissivity profile.	113
5.7	Phantom emissivity profile (left), tomographic reconstruction (center) and line-integrated emissivity (right) of different emissivity configurations with the ITER radial X-ray cameras. First row: LFS asymmetry. Second row: HFS asymmetry.	114
5.8	Left: Sinogram of a tomographic system made of three sets of lines-of-sight. Right: Geometry of the lines-of-sight.	115
5.9	Left: Sinogram of the radial X-ray cameras lines-of-sight. Right: Geometry of the associated lines-of-sight.	115
5.10	Left: Sinogram of the theoretical configuration. Right: Geometry of the associated lines-of-sight.	116
5.11	Phantom emissivity profile (left), tomographic reconstruction (center) and line-integrated emissivity (right) of different emissivity configurations with the theoretical lines-of-sight configuration. First row: Gaussian emissivity profile. Second row: Hollow emissivity profile.	117
5.12	Phantom emissivity profile (left), tomographic reconstruction (center) and line-integrated emissivity (right) of different emissivity configurations with the theoretical lines-of-sight configuration. First row: LFS asymmetry. Second row: HFS asymmetry.	118
5.13	Left: Sinogram of the 60 vertical lines-of-sight configuration. Right: Geometry of the associated lines-of-sight.	119
5.14	Phantom emissivity profile (left), tomographic reconstruction (center) and line-integrated emissivity (right) of different emissivity configurations with the 60 vertical lines-of-sight configuration. First row: Gaussian emissivity profile. Second row: Hollow emissivity profile.	120

5.15	Phantom emissivity profile (left), tomographic reconstruction (center) and line-integrated emissivity (right) of different emissivity configurations with 60 vertical lines-of-sight configuration. First row: LFS asymmetry. Second row: HFS asymmetry.	121
5.16	Left: Sinogram of the 44 vertical lines-of-sight configuration. Right: Geometry of the associated lines-of-sight.	122
5.17	Phantom emissivity profile (left), tomographic reconstruction (center) and line-integrated emissivity (right) of different emissivity configurations with the 44 vertical lines-of-sight configuration. First row: Gaussian emissivity profile. Second row: Hollow emissivity profile.	123
5.18	Phantom emissivity profile (left), tomographic reconstruction (center) and line-integrated emissivity (right) of different emissivity configurations with the 44 vertical lines-of-sight configuration. First row: LFS asymmetry. Second row: HFS asymmetry.	124
5.19	Geometrical etendue for each 60 vertical lines-of-sight configuration. .	125
6.1	Radiated power profile as a function of photon energy and normalized radius for the standard high power D-T scenario.	128
6.2	Current collected by a LVIC filled with argon (blue) or xenon (red) in the high power D-T emissivity scenario. The chamber has a pressure length product of $50\text{ mm} \cdot \text{atm}$ and a filter made of $200\mu\text{m}$ of beryllium.	129
6.3	Current collected by an argon-filled (left) and xenon-filled (right) LVIC with different filters. The chamber has a pressure length product of $50\text{ mm} \cdot \text{atm}$ and the emissivity comes from the high power D-T emissivity scenario.	130
6.4	Current collected by an argon-filled (left) and xenon-filled (right) LVIC with different length pressure products. The filter is made of $200\mu\text{m}$ and the emissivity comes from the high power D-T emissivity scenario. . .	131
6.5	$\langle \eta \rangle$ for each channel for various incoming flux, gas, and length (for a gas pressure of 1 bar). Top left: Xe LVIC with high power D-T scenario emissivity restricted to $[0, 20]$ keV. Top right: Xe LVIC with high power D-T scenario emissivity up to 100 keV. Bottom left: Ar LVIC with high power D-T scenario emissivity restricted to $[0, 20]$ keV. Bottom right: Ar LVIC with high power D-T scenario emissivity up to 100 keV.	133
6.6	Comparison of the reconstructed and original line-integrated plasma emission. Left: in the full spectral range $[0, 100]$ keV. Right: in the $[0, 31]$ keV range. Calibrated output are obtained from Xe LVICs ($50\text{ mm} \cdot \text{atm}$). The filter was made of $150\mu\text{m}$ of beryllium and $11\mu\text{m}$ of mylar.	135
6.7	Comparison of the reconstructed and original line-integrated plasma emission. Left: in the $[0, 49]$ keV range. Right: in the $[0, 23]$ keV range. Calibrated output are obtained from Xe (left) and Ar (right) LVICs ($150\text{ mm} \cdot \text{atm}$). The filter was made of $150\mu\text{m}$ of beryllium and $11\mu\text{m}$ of mylar.	136

6.8	Soft x-ray emissivity profile in the [0, 20] keV range of a high power D-T ITER scenario.	137
6.9	Reconstruction of a soft x-ray only emissivity profile using Ar and Xe. Top line: Tomographic reconstruction using 150 mm · atm Xe LVICs (right: reconstructed profile, left: reconstruction error). Bottom line: Tomographic reconstruction using 150 mm · atm Ar LVICs (right: reconstructed profile, left: reconstruction error).	139
6.10	Comparison of the tomographic reconstruction relative error and the relative calibration error through vertical (at R = 6.59m) and radial (at Z = 0.84m) cross-sections. The x-axis coordinate of each line-of-sight corresponds to its Z-coordinate (resp: R-coordinate) at the intersection with the cross-section straight line (green line in the upper figures) in the case of the vertical (resp: radial). The upper figures display the cross-section geometry and the lower ones show the relative errors for both tomographic reconstruction and calibration. The vertical (resp: radial) cross-section plots are located on the left (resp: right) side.	140
6.11	Reconstruction of a soft x-ray only emissivity profile using 150 mm · atm Ar LVICs with ideal calibration coefficients. Right: reconstructed profile. Left: reconstruction error.	141
6.12	X-ray (in the [0, 100] keV range) emissivity profile of a high power D-T ITER scenario.	143
6.13	Reconstruction of a wide emissivity profile using different detectors. Left: reconstructed profile ($W \cdot m^{-3}$). Center: reconstruction error (%). Right: line-integrated emissivity and backfitting ($W \cdot m^{-2}$). Top line: 150 mm · atm LVIC filled with Xe, reconstructing the emissivity in the [0, 49] keV range. Middle line: 50 mm · atm LVIC filled with Xe, reconstructing the emissivity in the [0, 31] keV range. Bottom line: 150 mm · atm LVIC filled with Ar, reconstructing the emissivity in the [0, 23] keV range. . .	144
6.14	Reconstruction of a wide emissivity profile with different levels of measurement noise. Reconstruction over the [0, 49] keV range using xenon-filled 150 mm · atm LVIC. Top line: Tomographic reconstruction ($W \cdot m^{-3}$). Bottom line: Reconstruction error (%). Left column: 1% of noise. Middle column: 2% of noise. Right column: 5% of noise.	145
6.15	Left: Spectral response as a function of photon energy. Right: Power impacting the detector convoluted by the spectral response and its reconstruction. The detector is an argon-filled LVIC with a length pressure product of 150mm · atm and a filter made of 150μm of beryllium and 11μm of mylar.	146
6.16	Left: Plasma emissivity convoluted by the spectral response of the detector. Center: Tomographic reconstruction. Right: Reconstruction error. The detector is an argon-filled LVIC with a length pressure product of 150mm · atm and a filter made of 150μm of beryllium and 11μm of mylar.	147

6.17	Left: Spectral response as a function of photon energy. Right: Power impacting the detector convoluted by the spectral response and its reconstruction. The detector is a xenon-filled LVIC with a length pressure product of $150\text{mm} \cdot \text{atm}$ and a filter made of $150\mu\text{m}$ of beryllium and $11\mu\text{m}$ of mylar.	148
6.18	Left: Plasma emissivity convoluted by the spectral response of the detector. Center: Tomographic reconstruction. Right: Reconstruction error. The detector is a xenon-filled LVIC with a length pressure product of $150\text{mm} \cdot \text{atm}$ and a filter made of $150\mu\text{m}$ of beryllium and $11\mu\text{m}$ of mylar.	148
7.1	Electron temperature (left) and density (right) profiles of the ITER high power D-T scenario.	150
7.2	Left: Radial profile of the diffusive and convective coefficients of tungsten in the <i>core negative V</i> scenario. Right: Radial profile of the diffusive and convective coefficients of tungsten in the <i>core positive V</i> scenario.	151
7.3	Tungsten density as a function of time for several radial positions for the <i>core negative V</i> (left) and the <i>core positive V</i> (right) scenarios.	151
7.4	Tungsten density as a function of time and normalised radius for the <i>core negative V</i> (top) and the <i>core positive V</i> (bottom) scenarios.	152
7.5	Tungsten density (with initial state subtracted) as a function of time and normalised radius for the <i>core negative V</i> (top) and the <i>core positive V</i> (bottom) scenarios.	153
7.6	Total X-ray emissivity as a function of time and normalised radius for the <i>core negative V</i> (top) and the <i>core positive V</i> (bottom) scenarios.	154
7.7	X-ray emissivity spectrum at $t = 1.5\text{s}$ at various radial positions for the <i>core negative V</i> (left) and the <i>core positive V</i> (right) scenarios.	155
7.8	Transmission ratio of a $200\mu\text{m}$ Be window, absorption ratio of a $100\text{mm} \cdot \text{atm}$ Xe-filled LVIC, and spectral response of the combination of the two.	156
7.9	Total (top) and background subtracted (bottom) X-ray emissivities convoluted by the spectral response of the detector as a function of time and normalised radius in the case of the <i>negative V coefficient</i> scenario.	157
7.10	Total (top) and background subtracted (bottom) line-integrated emissivities convoluted by the spectral response of the detector as a function of time and line-of-sight number in the case of the <i>negative V coefficient</i> scenario.	159
7.11	Total (top) and background subtracted (bottom) reconstructed line-integrated emissivities convoluted by the spectral response of the detector as a function of time and line-of-sight number in the case of the <i>negative V coefficient</i> scenario.	160

7.12	Total (top) and background subtracted (bottom) reconstructed X-ray emissivities convoluted by the spectral response of the detector as a function of time and normalised radius in the case of the <i>negative V coefficient</i> scenario.	161
7.13	Total (top) and background subtracted (bottom) reconstructed tungsten densities as a function of time and normalised radius in the case of the <i>negative V coefficient</i> scenario.	162
7.14	Γ_W/n_W as a function of $dn_W/dt/n_W$ for several radial positions in the case of the <i>negative V coefficient</i> scenario. The dash line represents the result which would be obtained with the D and V coefficients of the scenario.	163
7.15	D and V coefficients of the <i>negative V coefficient</i> scenario and their reconstruction.	163
7.16	Total (top) and background subtracted (bottom) X-ray emissivities convoluted by the spectral response of the detector as a function of time and normalised radius in the case of the <i>positive V coefficient</i> scenario.	164
7.17	Total (top) and background subtracted (bottom) line-integrated emissivities convoluted by the spectral response of the detector as a function of time and line-of-sight number in the case of the <i>positive V coefficient</i> scenario.	166
7.18	Total (top) and background subtracted (bottom) reconstructed line-integrated emissivities convoluted by the spectral response of the detector as a function of time and line-of-sight number in the case of the <i>positive V coefficient</i> scenario.	167
7.19	Total (top) and background subtracted (bottom) reconstructed X-ray emissivities convoluted by the spectral response of the detector as a function of time and normalised radius in the case of the <i>positive V coefficient</i> scenario.	168
7.20	Total (top) and background subtracted (bottom) reconstructed tungsten densities as a function of time and normalised radius in the case of the <i>positive V coefficient</i> scenario.	169
7.21	Γ_W/n_W as a function of $dn_W/dt/n_W$ for several radial positions in the case of the <i>positive V coefficient</i> scenario. The dash line represents the result which would be obtained with the D and V coefficients of the scenario.	170
7.22	D and V coefficients of the <i>positive V coefficient</i> scenario and their reconstruction.	170
7.23	Soft x-ray radiation profiles observed for two different heating strategies in the JET tokamak. Reprinted from [104]	171
7.24	Banana-shaped orbit of a trapped particle. Figure reprinted from [105].	172
7.25	2D tungsten density profile (left) and its reconstruction (right) in the case of a symmetrical tungsten density profile.	175

7.26 Tungsten density poloidal fluctuation (left) and its reconstruction (right) in the case of a symmetrical tungsten density profile.	175
7.27 Left: radial profile of the toroidal rotation frequency. Right: Radial profile of the minority temperature anisotropy ratio.	176
7.28 Radial profile of the ion and electron temperatures.	177
7.29 2D tungsten density profile (left) and its reconstruction (right) in the case of a tungsten density profile exhibiting an electric field-induced asymmetry.	177
7.30 Tungsten density poloidal fluctuation (left) and its reconstruction (right) in the case of a tungsten density profile exhibiting an electric field-induced asymmetry.	178
7.31 2D tungsten density profile (left) and its reconstruction (right) in the case of a tungsten density profile exhibiting a centrifugal force-induced asymmetry.	179
7.32 Tungsten density poloidal fluctuation (left) and its reconstruction (right) in the case of a tungsten density profile exhibiting a centrifugal force-induced asymmetry.	179
7.33 2D tungsten density profile (left) and its reconstruction (right) in the case of a tungsten density profile exhibiting an asymmetry induced by both an electric field and the centrifugal force.	180
7.34 Tungsten density poloidal fluctuation (left) and its reconstruction (right) in the case of a tungsten density profile exhibiting an asymmetry induced by both an electric field and the centrifugal force.	181
8.1 Schematics of a multi-anodes low voltage ionization chamber.	184
8.2 Contribution of each impurity to the incoming photon flux of line-of-sight number 96 which goes through the very core of the plasma.	185
8.3 Fitting of the line-of-sight number 96 incoming photon flux. In this figure, the parameters of the function are $X_1 = 1.40 \cdot 10^9$ ph/s, $X_2 = 2.26 \cdot 10^{-2} \text{ keV}^{-1}$, $X_3 = 5.0 \cdot 10^9$ ph/s, and $X_4 = 6.0 \cdot 10^8$ ph/s.	186
8.4 Architecture of the minimization algorithm.	188
8.5 Spectral response of each sub-chamber in a 5 anodes argon-filled MA-LVIC. The length pressure products of the sub-chamber are respectively 5, 15, 50, 175, and 500 $\text{mm} \cdot \text{atm}$, and the filter consists of $200\mu\text{m}$ of beryllium.	190
8.6 Left: Spectral deconvolution of the photon flux of line-of-sight 45 ($r/a \approx 0.5$). Right: Spectral deconvolution of the photon flux of line-of-sight 96 ($r/a \approx 0$). The MA-LVIC is filled with argon and the sub-chambers have respective length pressure products of 5, 15, 50, 175 and 500 $\text{mm} \cdot \text{atm}$. The beryllium window is $200\mu\text{m}$ wide.	190

8.7	Left: Spectral deconvolution of the photon flux of line-of-sight 5 ($r/a \approx 1$). Right: Measured and reconstructed currents for each sub-chamber for lines-of-sight 5, 45 and 96. The MA-LVIC is filled with argon and the sub-chambers have respective length pressure products of 5, 15, 50, 175 and 500 $mm \cdot atm$. The beryllium window is $200\mu m$ wide.	191
8.8	Left: Figures of merit of spectral deconvolution. Right: Spectral deconvolution of the photon flux of line-of-sight 4 ($r/a \approx 1$). The MA-LVIC is filled with argon and the sub-chambers have respective length pressure products of 5, 15, 50, 175 and 500 $mm \cdot atm$. The beryllium window is $200\mu m$ wide.	192
8.9	Left: Surface integrated power as a function of the photon energy and the line-of-sight number. Right: Reconstructed surface integrated power as a function of the photon energy and the line-of-sight number. The MA-LVIC is filled with argon and the sub-chambers have respective length pressure products of 5, 15, 50, 175 and 500 $mm \cdot atm$. The beryllium window is $200\mu m$ wide.	193
8.10	Left: Reconstruction of the line-integrated X-ray emissivity in the [2, 3] keV range for each line-of-sight. Right: Reconstruction of the line-integrated X-ray emissivity in the [6, 10] keV range for each line-of-sight. The MA-LVIC is filled with argon and the sub-chambers have respective length pressure products of 5, 15, 50, 175 and 500 $mm \cdot atm$. The beryllium window is $200\mu m$ wide.	193
8.11	Left: Reconstruction of the line-integrated X-ray emissivity in the [10, 100] keV range for each line-of-sight. Right: Reconstruction of the line-integrated X-ray emissivity in the [2, 100] keV range for each line-of-sight. The MA-LVIC is filled with argon and the sub-chambers have respective length pressure products of 5, 15, 50, 175 and 500 $mm \cdot atm$. The beryllium window is $200\mu m$ wide.	194
8.12	Spectral response of each sub-chamber in a 5 anodes xenon-filled MA-LVIC. The length pressure products of the sub-chamber are respectively 5, 30, 60, 100 and 150 $mm \cdot atm$, and the filter consists of $200\mu m$ of beryllium.	195
8.13	Left: Spectral deconvolution of the photon flux of line-of-sight 45 ($r/a \approx 0.5$). Right: Spectral deconvolution of the photon flux of line-of-sight 96 ($r/a \approx 0$). The MA-LVIC is filled with xenon and the sub-chambers have respective length pressure products of 5, 30, 60, 100 and 150 $mm \cdot atm$. The beryllium window is $200\mu m$ wide.	196
8.14	Left: Spectral deconvolution of the photon flux of line-of-sight 5 ($r/a \approx 1$). Right: Measured and reconstructed currents for each sub-chamber for lines-of-sight 5, 45 and 96. The MA-LVIC is filled with xenon and the sub-chambers have respective length pressure products of 5, 30, 60, 100 and 150 $mm \cdot atm$. The beryllium window is $200\mu m$ wide.	196

8.15	Left: Figures of merit of spectral deconvolution. Right: Spectral deconvolution of the photon flux of line-of-sight 4 ($r/a \approx 1$). The MA-LVIC is filled with xenon and the sub-chambers have respective length pressure products of 5, 30, 60, 100 and 150 $mm \cdot atm$. The beryllium window is 200 μm wide.	197
8.16	Left: Surface integrated power as a function of the photon energy and the line-of-sight number. Right: Reconstructed surface integrated power as a function of the photon energy and the line-of-sight number. The MA-LVIC is filled with xenon and the sub-chambers have respective length pressure products of 5, 30, 60, 100 and 150 $mm \cdot atm$. The beryllium window is 200 μm wide.	197
8.17	Left: Reconstruction of the line-integrated X-ray emissivity in the [2, 3] keV range for each line-of-sight. Right: Reconstruction of the line-integrated X-ray emissivity in the [6, 10] keV range for each line-of-sight. The MA-LVIC is filled with xenon and the sub-chambers have respective length pressure products of 5, 30, 60, 100 and 150 $mm \cdot atm$. The beryllium window is 200 μm wide.	198
8.18	Left: Reconstruction of the line-integrated X-ray emissivity in the [10, 100] keV range for each line-of-sight. Right: Reconstruction of the line-integrated X-ray emissivity in the [2, 100] keV range for each line-of-sight. The MA-LVIC is filled with xenon and the sub-chambers have respective length pressure products of 5, 30, 60, 100 and 150 $mm \cdot atm$. The beryllium window is 200 μm wide.	199
8.19	Reconstruction of the line-integrated X-ray emissivity in the [2, 3] keV range as a function of the line-of-sight number for different widths of the beryllium window. The MA-LVIC is filled with xenon and the sub-chambers have respective length pressure products of 5, 30, 60, 100 and 150 $mm \cdot atm$	200
8.20	Left: RMS_{dec} and its 1% noise envelope. Right: Reconstruction of the line-integrated X-ray emissivity in the [2, 3] keV energy range and its 1% envelope. The MA-LVIC is filled with xenon and the sub-chambers have respective length pressure products of 5, 30, 60, 100 and 150 $mm \cdot atm$. The beryllium window is 200 μm wide.	201
8.21	Left: Reconstruction of the line-integrated X-ray emissivity in the [6, 10] keV energy range and its 1% envelope. Right: Reconstruction of the line-integrated X-ray emissivity in the [10, 100] keV energy range and its 1% envelope. The MA-LVIC is filled with xenon and the sub-chambers have respective length pressure products of 5, 30, 60, 100 and 150 $mm \cdot atm$. The beryllium window is 200 μm wide.	202

8.22	Left: Radiated power profile on ITER as a function of photon energy and normalized radius. Right: Reconstructed radiated power profile as a function of photon energy and normalized radius. The MA-LVIC is filled with xenon and the sub-chambers have respective length pressure products of 5, 30, 60, 100 and 150 $mm \cdot atm$. The beryllium window is 200 μm wide.	204
8.23	Left: Figures of merit of energy resolved tomography: RMS_{line} , RMS_{lcms}^{lcms} , and RMS_{tomo}^{core} . Right: Reconstruction of the local plasma emissivity in the plasma core (at $R = 6.27m$ and $Z = 0.57m$). For this pixel, $RMS_{pix} = 3.7 \cdot 10^{-3}$. The MA-LVIC is filled with xenon and the sub-chambers have respective length pressure products of 5, 30, 60, 100 and 150 $mm \cdot atm$. The beryllium window is 200 μm wide.	204
8.24	Figure of merit RMS_{pix} of energy resolved tomography. The MA-LVIC is filled with xenon and the sub-chambers have respective length pressure products of 5, 30, 60, 100 and 150 $mm \cdot atm$. The beryllium window is 200 μm wide.	205
8.25	Left: Reconstruction of the local emissivity spectrum in the plasma core (at $R = 6.27m$ and $Z = 0.57m$) with 1% of perturbative noise added to the measurement. Right: Figures of merit of energy resolved tomography: RMS_{line} , RMS_{tomo}^{LCMS} and RMS_{tomo}^{core} (respectively labelled as FOM_{LoS} , FOM_{lcms} , and FOM_{core}), with 1% of gaussian perturbative noise on the LVIC measurement. The MA-LVIC is filled with xenon and the sub-chambers have respective length pressure products of 5, 30, 60, 100 and 150 $mm \cdot atm$. The beryllium window is 200 μm wide.	206
8.26	Left: Figure of merit RMS_{pix} of energy resolved tomography with 1% of gaussian perturbative noise on the LVIC measurement computed in the [4, 10] keV range. Right: Figure of merit RMS_{pix} of energy resolved tomography with 1% of gaussian perturbative noise on the LVIC measurement computed in the [10, 100] keV range. The MA-LVIC is filled with xenon and the sub-chambers have respective length pressure products of 5, 30, 60, 100 and 150 $mm \cdot atm$. The beryllium window is 200 μm wide.	207
8.27	Left: 2D profile of the electron temperature in the ITER high power D-T scenario. Right: Reconstructed 2D profile of the electron temperature. The MA-LVIC is filled with xenon and the sub-chambers have respective length pressure products of 5, 30, 60, 100 and 150 $mm \cdot atm$. The beryllium window is 200 μm wide.	208
8.28	Relative error of the electron temperature reconstruction. The MA-LVIC is filled with xenon and the sub-chambers have respective length pressure products of 5, 30, 60, 100 and 150 $mm \cdot atm$. The beryllium window is 200 μm wide.	209

8.29	Left: Reconstructed electron temperature profile obtained after energy resolved tomography with 1% of gaussian perturbative noise on the LVIC measurement. Right: Relative error of the electron temperature reconstruction with 1% of gaussian perturbative noise on the LVIC measurement. The MA-LVIC is filled with xenon and the sub-chambers have respective length pressure products of 5, 30, 60, 100 and 150 $mm \cdot atm$. The beryllium window is $200\mu m$ wide.	210
------	--	-----

List of Tables

1.1	Parameters of the WEST tokamak.	41
1.2	Parameters of the ASDEX Upgrade tokamak.	43
1.3	Parameters of the ITER tokamak.	45
1.4	Parameters of the European version of the DEMO tokamak.	45
5.1	Figures of merit for tomographic reconstruction of phantom emissivity profiles with the radial X-ray cameras.	112
5.2	Figures of merit for tomographic reconstruction of phantom emissivity profiles with the theoretical lines-of-sight configuration.	117
5.3	Figures of merit for tomographic reconstruction of phantom emissivity profiles with the 60 vertical lines-of-sight configuration.	122
5.4	Figures of merit for tomographic reconstruction of phantom emissivity profiles with the 44 vertical lines-of-sight configuration.	123
6.1	Figures of merit for tomographic reconstruction over [0, 20] keV.	137
6.2	Figures of merit for tomographic reconstruction over [0, 100] keV.	143
6.3	Figures of merit for the noise study.	145
6.4	Figures of merit for tomographic reconstruction of the emissivity convoluted with the spectral response of the detector.	146

1 Introduction

Sommaire

1.1	The challenge of energy	25
1.1.1	Historical approach	25
1.1.2	Fossil fuels: availability and consequences	26
1.1.3	Alternative energy sources	27
1.1.4	Energy generation from nuclear fusion	28
1.2	Nuclear fusion reactor	29
1.2.1	Fusion reactions	30
1.2.2	Ignition	31
1.2.3	Confinement	33
1.2.3.1	Gravitational confinement	33
1.2.3.2	Inertial confinement	33
1.2.3.3	Magnetic confinement	33
1.2.4	Tokamak	35
1.2.4.1	Geometry	35
1.2.4.2	Confinement modes	36
1.2.4.3	Heating	37
1.2.4.4	Key challenges	38
1.2.5	Existing tokamaks	40
1.2.5.1	WEST	40
1.2.5.2	ASDEX Upgrade	42
1.2.5.3	ITER	44
1.2.5.4	DEMO	45
1.3	Scope of this thesis	46

1.1 The challenge of energy

1.1.1 Historical approach

Energy is a physical quantity which characterises the ability of a system to produce work, which describes the change of state (e.g. position, speed, heat, pressure) of said system. In other words, energy reflects the ability of mankind to master (or transform) its environment: energy is what allows us to eat, heat our homes, travel or charge our computers.

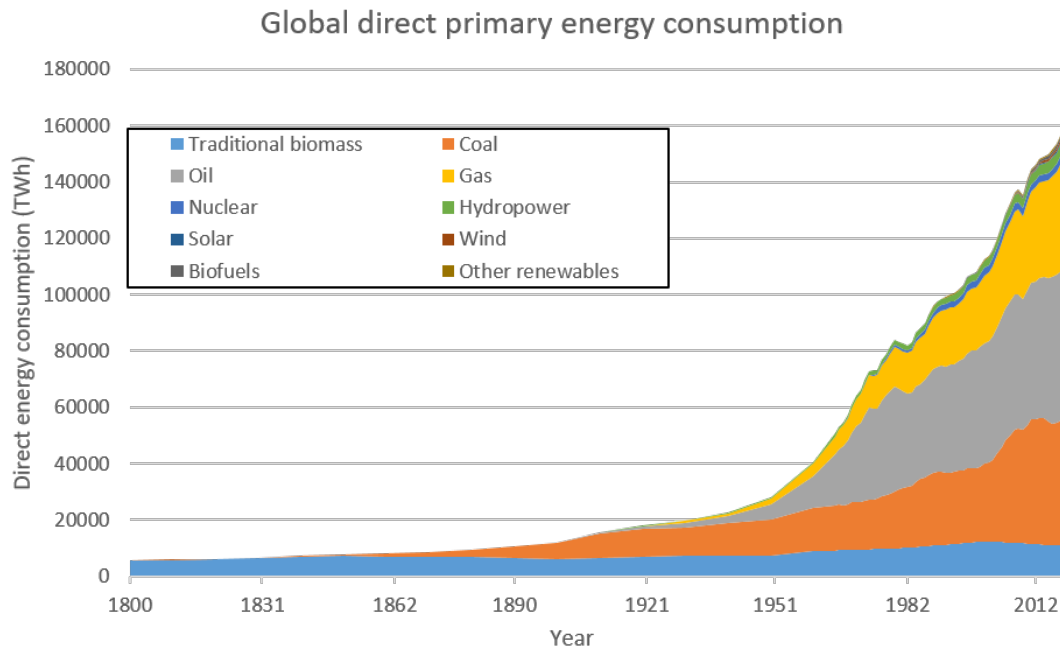


Figure 1.1 – Global direct primary energy consumption as a function of time, distinguishing each energy source. [1, 2]

Throughout most of mankind history, the amount of energy available was mostly limited to wood (for heating) and animals (mainly for transportation or field labour). These two sources are the so-called *traditional biomass* displayed on figure 1.1. The invention of the steam engine by James Watt at the end of the eighteenth century allowed mankind to extend its energy consumption through the use of machines. The first energy source used to power engines is coal, followed by oil which made its appearance in the nineteenth century. Other energy sources such as gas, nuclear, hydro or solar have been domesticated in the twentieth century. This abundance of energy has permitted mankind to shape the world as we know it. It can be noted on figure 1.1 that the world energy consumption has been rising constantly for the last 200 years, and this rise is expected to keep on. [3] In this section, the energy challenge is addressed through energy generation but it should be kept in mind that an increase in energy efficiency and a more efficient use of energy (e.g. limiting waste, public transportation, better house thermal isolation, consumption of local products) are also key to solving the energy challenge.

1.1.2 Fossil fuels: availability and consequences

Fossil fuels are the remains of the decomposition of organic matter such as dead organisms. Their creation occurred on the scale of millions of years, and therefore it can be considered that the world reserves of fossil fuel are constant. Three different fossil fuels (coal, oil, gas) are currently used to generate more than 80% of the world energy.

Energy is generated by oxidation of the fuel, which is achieved through combustion. The current reserves of coal are estimated to last around 130 years at the current rate. In the case of oil, the proven reserves should allow 50 to 60 years of energy at the current rate. Gas offers 90 years of energy if there is not increase of energy consumption. It can be seen on figure 1.1 that energy demand has been increasing fairly linearly in the 1950-2019 interval and this is likely to keep on. New fossil fuel discoveries are therefore necessary in order to keep on using fossil fuel for up to 130 years. In the scale of human history, such duration is however very limited and fossil fuels cannot be considered as a long-term energy source.

Availability is not however the only limitation to the use of fossil fuels, their impact on the environment and on health should also be considered. [4] Extraction of fossil fuels (whether it is underground or at the surface) leads to extensive land degradation, water pollution and gas emissions (benzene and formaldehyde). These can lead to health hazards, both on minors and the population. The combustion of these fuels in order to create energy releases harmful particles in the atmosphere which lead to an increase in acid rains and respiratory illnesses. The main issue regarding fossil fuels is the release of greenhouse effect gases which participate in the human-induced global warming of the world. The consequences of global warming include an increase in the frequency and intensity of extreme meteorological events (e.g. floods, droughts, hurricanes), rising of the sea level (jeopardizing most coastline cities), ice melting in the poles and biodiversity extinction.

In conclusion on fossil fuels, current reserves would only allow the current energy production for up to around a hundred years. However if climate change is to be mitigated to bearable limits both for the environment and our society, most of the remaining fossil fuel should remain underground.

1.1.3 Alternative energy sources

We are now facing a challenge requiring a shift in the energy mix if we are to limit global warming. Several energy sources can be considered as potential alternatives to fossil fuel. So-called renewable sources of energy have the main advantage that their availability is not limited in time as they are constantly renewed.

Wind and solar power are the first examples of renewable energy which come to mind. Electricity can be generated by adding a generator to a windmill or by using photovoltaic panels which convert light into electrons. These processes are not very energy efficient, but do not release greenhouse effect gases during operation. However their production and maintenance is quite costly in terms of energy and the greenhouse effects gases released in the process should be taken into account. Both sources depend on the weather and are therefore intermittent and not controllable. Their production peaks do not necessarily coincide with the demand peaks. As a result, a controllable source is required in order to provide energy when wind and/or solar are not producing.

Hydro power is the conversion of the potential energy of water in a dam into kinetic en-

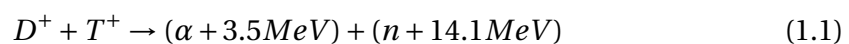
ergy (the rotation of a turbine) and then into electricity through the use of a generator. It is a controllable source of energy which does not release green house effect gases during operation. Its construction is quite costly but its lifetime makes the overall green house effect production very low. A dam can be used as an energy storage facility by pumping water uphill. However, the installation of a dam creates considerable changes in the environment due to the drowning of a large zone and its failure could prove deadly. The hydro power can hardly be increased in developed countries because most of the areas available for dams are already exploited.

Biofuels are a promising source of energy which consists of burning oil or ethanol obtained from plants (e.g. rape, wheat). The combustion of biofuels leads to greenhouse effect gases emission. However, the crops where such plants are cultivated absorb carbon dioxide and therefore reduce the net greenhouse effect gases production of biofuels. These crops are in competition with food crops and the quantities of biofuel which can be produced are constrained by land availability.

Nuclear fission is another alternative to fossil fuels. It is not a renewable source of energy as the energy is extracted from a metal (uranium or plutonium) through fission reactions. Nuclear fission has the advantage that it is a controllable source of energy which is not intermittent. Approximately 100 years of reserves of ^{235}U are available, but the development of fast neutrons reactors could allow the use of ^{238}U for which 10,000 years of fuel are available. The main drawbacks of nuclear energy are safety and waste management. Accidents in nuclear power plants are extremely rare but can release a high amount of radioactive material in the atmosphere and have very serious health consequences. The fission reaction leads to the generation of hazardous waste with a very long radioactive decay time compared to human time scale. At the moment, the only solution foreseen to dispose of such waste is deep burial underground. It can be seen that each alternative to fossil fuels comes with its own advantages and drawbacks. Renewable energies do not allow a massive energy production adapted to the demand, either because of fluctuating production or land occupation. They should be used in coordination with an energy source which can deliver such production. Promising candidates are fourth generation fast neutrons fission reactors, carbon-trapping thermal reactors fuelled with coal or nuclear fusion reactors.

1.1.4 Energy generation from nuclear fusion

Due to the topic of this thesis, a special focus is given on generation of energy through nuclear fusion. Fusion reactions of light elements release energy in the form of kinetic energy of the fusion products. The so-called D-T fusion reaction is the most accessible in reactor conditions. D stands for deuterium, which is the ^2H isotope of hydrogen, and T stands for tritium, which is the ^3H isotope of hydrogen. Nuclei of deuterium and tritium fuse together at high temperature in the following reaction:



where α is a He^{2+} nucleus and n is a neutron. The total energy generated by a D-T reaction is $\Delta E = 17.6 MeV$, which is around 8 times higher than a ^{235}U fission reaction but with reactants around 50 times lighter.

In terms of availability, nuclear fusion exhibits the advantage that deuterium is a very common isotope of hydrogen which can be extracted from seawater at a low cost. At the present energy consumption, enough deuterium can be extracted for several billions of years of electricity production. Tritium is a radioactive isotope of hydrogen with a very short decay period. The naturally generated tritium has decayed long ago and the world tritium inventory has been produced by nuclear reactions of neutrons with heavy water in nuclear reactors or with lithium. Tritium generation can be achieved in nuclear fusion power plants by surrounding the reactor with lithium blankets. This technique is called *tritium breeding* and requires neutron multiplication in order for the reactor to be self-sufficient tritium-wise. The availability of nuclear fusion therefore depends on lithium, for which the reserves are expected to last for a thousand years. [5] This value is subject to a high uncertainty as lithium use is massive (electronics, batteries, ...).

The environmental impact of nuclear fusion is very low compared to the energy sources listed previously. Indeed, the fusion product are neutrons and helium. Helium is an inert gas which is not radioactive. Neutrons however irradiate the fusion reactor which becomes radioactive. The decay period of a fusion reactor at the end of its lifetime is around 100 years, which is a ridiculously low duration in comparison with fission products.

Fusion reactors are inherently safe. Indeed they operate in very specific conditions, and in the case of a disruption fusion reactions just end prematurely. No reaction avalanche leading to the release of the reactor energy content in a short amount of time can therefore be observed. Due to constant fuelling of the reactor, only a small quantity of fuel is present at any given time (a couple of minutes in a fusion reactor compared to several months in a fission reactor). Moreover, the fuelling can be stopped if necessary. Even if the magnetic energy damaging the reactor, it has been demonstrated that no tritium leaking nor confinement failure is expected. [6] And in the case where the reactor is damaged by an outside event, the maximal amount of tritium released is around 1kg which should have limited consequences on health, and only in a small region and period of time.

1.2 Nuclear fusion reactor

This section describes the different aspects of nuclear fusion and how they led to the design of the tokamak.

1.2.1 Fusion reactions

The binding energy per nucleon for the different elements of the periodic table is shown on figure 1.2. It reflects the stability of an atom: the higher the binding energy per nucleon the more stable the atom. One can notice that iron (^{56}Fe) is the most stable element in the table. Heavier elements can become more stable by splitting into lighter elements and lighter elements can become more stable by merging into heavier elements. These two processes are respectively nuclear fission and nuclear fusion. When the products of a nuclear reaction are more stable than the reactants, energy is released (usually in the shape of kinetic energy or radiation).

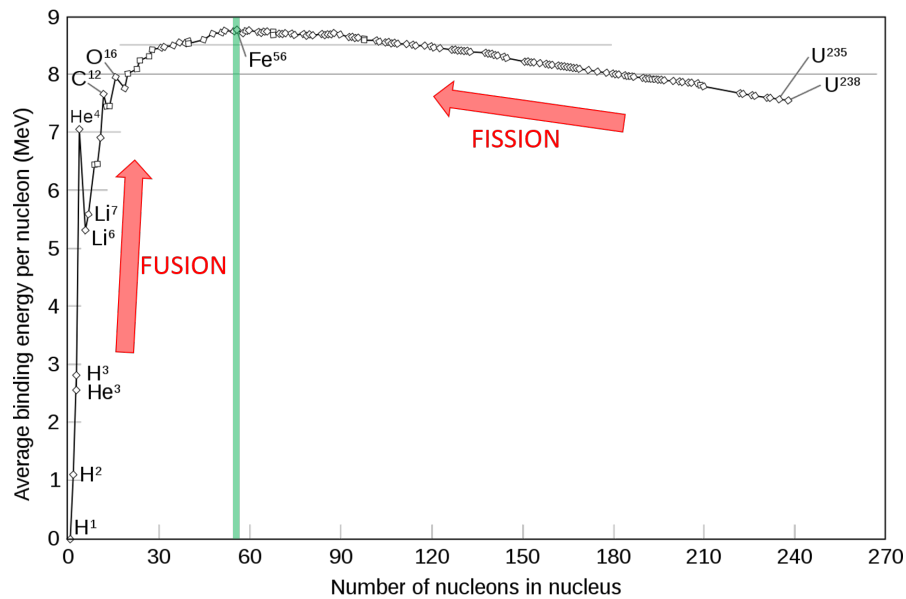


Figure 1.2 – Aston curve: binding energy per nucleon as a function of the total amount of nucleons. Figure adapted from [7]

The slope of the Aston curve denotes the gain of energy per nucleon. It is clear that fusion reactions of hydrogen isotopes into helium are the most energy-efficient reactions. Nuclear reactions are defined by their cross-sections, which describes the probability of occurrence of such reactions and are usually expressed in barns: $1b = 10^{-28}m^2$. The cross-sections of the main candidates for power generation from nuclear fusion are displayed on figure 1.3. It can be clearly seen that the D-T fusion reaction (see equation 1.1) is the most likely to take place in a fusion reactor below several hundreds keV. The D-T reaction reaches its peak cross-section at $E \approx 100keV$, which corresponds to $T \approx 10^9K$ with $E = k_B \cdot T$ ($1eV \rightarrow 11594K$). In plasma physics, it is common for temperatures to be expressed in electron-volts and to refer to $k_B \cdot T$. It is the case in this thesis.

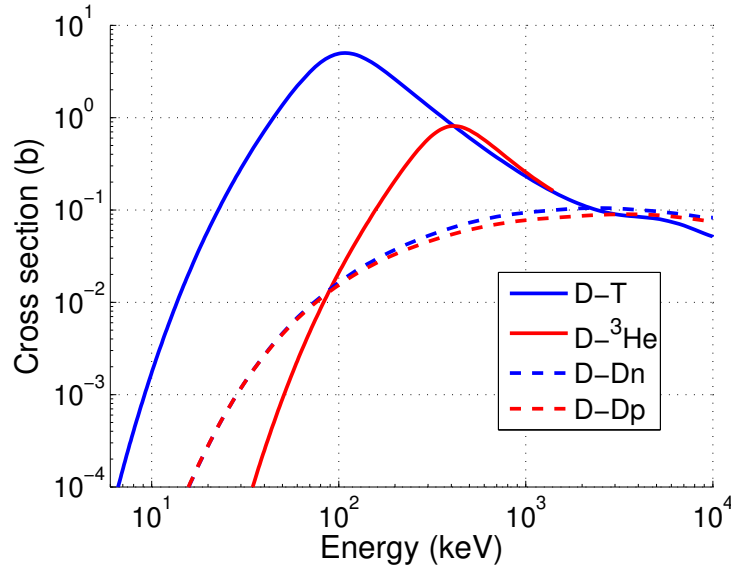


Figure 1.3 – Cross sections of several fusion reactions. [8, 9]

In nuclear fusion reactors, the temperatures reached are of the order of 10keV only but it is sufficient to generate a significant amount of D-T reactions. High temperatures are required in order to overcome the Coulomb repulsion of D^+ and T^+ , which is achieved by tunnel effect. In such conditions, the matter only exists in plasma state.

1.2.2 Ignition

The power generated by D-T reactions is given by:

$$P_{D-T} = R_{D-T} \cdot \Delta E = n_D n_T \langle \sigma v \rangle \Delta E \quad (1.2)$$

where R_{D-T} is the D-T reaction rate in s^{-1} , $\Delta E = 17.6\text{MeV}$ is the energy generated by a D-T fusion reaction, n_D and n_T are respectively the deuterium and tritium densities in m^{-3} , $\langle . \rangle$ is the average over the Maxwellian velocity distribution. This power is maximised for $n_D = n_T = \frac{n}{2}$:

$$P_{D-T} = \frac{n^2}{4} \langle \sigma v \rangle \Delta E \quad (1.3)$$

Each fusion product has a different destiny in the plasma, and so does their energy. Indeed, the α particle deposits its energy in the plasma through collisions while the neutron exits the plasma volume without interacting (in most cases). The energy of the neutron is therefore lost to the plasma, but can be used for electricity generation. During operation the power lost (through radiation and conduction [10]) P_L must be offset by the power incoming in the plasma $P_H + P_\alpha$ (P_H is the heating power): $P_L = P_H + P_\alpha$. Ignition is achieved when α heating is enough to compensate for

radiation losses: $P_\alpha \geq P_L$.

The α heating P_α is given by:

$$P_\alpha = \frac{n^2}{4} \langle \sigma v \rangle E_\alpha \quad (1.4)$$

where $E_\alpha = 3.5 \text{ MeV}$ is the energy of the alpha particle.

The energy confinement time of the plasma τ_E is defined as the time it would take the plasma to lose all its energy if the energy sources were stopped: $\tau_E = W/P_L$. The power losses can therefore be written as:

$$P_L = \frac{W}{\tau_E} \quad (1.5)$$

The local energy content of the plasma w is given by:

$$w = \frac{3}{2} (n_e T_e + n_i T_i) \quad (1.6)$$

where n_e and n_i are respectively the electron and ion densities. In the case of a hydrogen plasma ($n_e = n_i = n$) in which electrons and nuclei have the same temperature ($T_e = T_i = T$), equation 1.6 becomes:

$$w = 3nT \quad (1.7)$$

In an homogeneous plasma, the power losses become:

$$P_L = \frac{3nT}{\tau_E} \quad (1.8)$$

During the operation of a fusion reactor the power balance is given by:

$$P_H + P_\alpha = P_L \iff P_H + \frac{n^2}{4} \langle \sigma v \rangle E_\alpha = \frac{3nT}{\tau_E} \quad (1.9)$$

The ignition is reached for $P_\alpha \geq P_L$, which gives:

$$\frac{n^2}{4} \langle \sigma v \rangle E_\alpha \geq \frac{3nT}{\tau_E} \iff nT\tau_E \geq \frac{12T^2}{\langle \sigma v \rangle E_\alpha} \quad (1.10)$$

The triple product $nT\tau_E$ is an adequate indicator of the efficiency of plasma confinement. The ratio $\frac{T^2}{\langle \sigma v \rangle}$ has a minimal value for $T = 14 \text{ keV}$, leading to the following ignition criterion [10]:

$$nT\tau_E \geq 3 \cdot 10^{21} \text{ m}^{-3} \cdot \text{s} \cdot \text{keV} \quad (1.11)$$

The previous expression considers flat temperature profiles but in tokamaks the temperature profiles usually are peaked, in which case:

$$nT\tau_E \geq 5 \cdot 10^{21} m^{-3} \cdot s \cdot keV \quad (1.12)$$

The fusion amplification factor can be defined as:

$$Q = \frac{P_{D-T}}{P_H} = \frac{5 \cdot P_\alpha}{P_H} \quad (1.13)$$

Ignition corresponds to $Q \rightarrow \infty$ and $Q = 1$ means that P_α corresponds to 20% of the total heating power. One of the major ITER goals is to achieve $Q \geq 10$ which means that alpha particles provide more than two thirds of the total heating power.

1.2.3 Confinement

As seen in section 1.2.2, confinement of the plasma is key to achieve ignition. Moreover, an efficient confinement of the plasma protects the plasma facing components (PFC) from the very hot plasma and avoids cooling of the plasma on the walls of the vacuum vessel. This section describes the main confinement strategies linked to nuclear fusion.

1.2.3.1 Gravitational confinement

Gravitational confinement occurs naturally in stars. Due to their huge mass, gravitational forces are high enough to create conditions such that $nT\tau_E$ is high enough to achieve ignition. For obvious reasons it is not possible to replicate such confinement strategy on Earth and other solutions have been developed.

1.2.3.2 Inertial confinement

Inertial confinement consists of a very high compression of deuterium and tritium for a very short time. In such conditions, temperature and density must be high enough to compensate for the short confinement time in order to reach ignition. This approach is used in H bombs where the compression is obtained by detonating a fission bomb. Another solution for such compression is the use of numerous high power lasers on a small D-T target. It is the approach used at the Laser Megajoule in France [11] and the National Ignition Facility in the USA [12]. The possibility to use such approach for energy production has not been demonstrated yet.

1.2.3.3 Magnetic confinement

Another approach for confinement is based on the fact that, at the temperatures required for ignition, the matter is in a plasma state. In a plasma electrons and ions, which are charged particles, are separated. A magnetic field can therefore be used to

confine them. Indeed, charged particles follow the helical trajectories centered on magnetic field lines due to the Lorentz force. Magnetic field lines are lines over which the magnetic field is constant (they are tangential to the magnetic field). For a particle of charge $Z \cdot |e|$, mass m , velocity (orthogonal to the magnetic field) and in a magnetic field of amplitude B , the helical movement is defined by its radius and pulsation:

$$\begin{aligned}\rho &= \frac{mV}{ZeB} \\ \omega_C &= \frac{ZeB}{m}\end{aligned}\tag{1.14}$$

The radius of the oscillation is the so-called Larmor radius and its pulsation is the cyclotron pulsation.

A reactor with linear magnetic field lines with magnetic mirrors at both ends could be an easy solution for plasma confinement. However localised instabilities (called flute instabilities due to their shape) appear at the edges of such device, leading to significant edge losses and possibly to the loss of confinement of the plasma. Another solution would be to use a torus shaped reactor with circular magnetic field lines. In such configuration, the particles would be subject to a vertical drift due to the gradient and curvature of the magnetic field. The direction of the drift depends on the charge, thus leading to the creation of an unwanted electric field in the plasma that would eject the particle out of it.

This effect can be compensated by the use of helical field lines, created by the superposition of a poloidal and toroidal magnetic field. The toroidal direction is defined as the direction following the torus and the poloidal plane is defined as the plane which is orthogonal to it. Helical magnetic field lines are achieved in two different magnetic configurations.

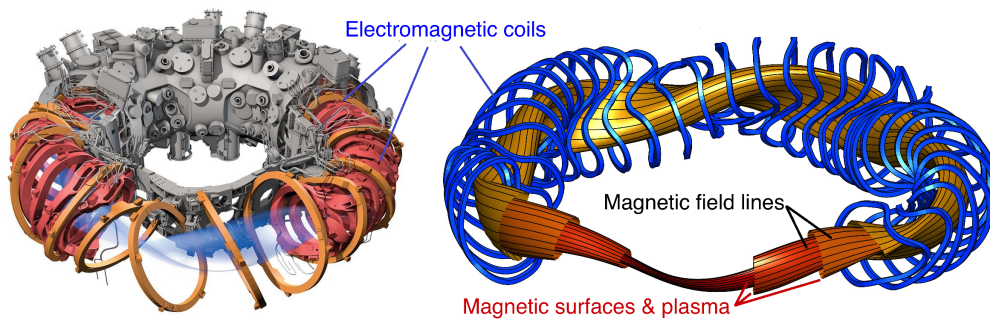


Figure 1.4 – Two stellarator configurations. Left: Stellarator with two sets of coils. Reproduced from [13] Right: Stellarator with a single set of coils. Reproduced from [14]

A first configuration consists of shaping the coils specifically in order to obtain a helical magnetic field. Such machines are called stellarators and are very complex to build. Two options are available when shaping the magnetic field: a single set of

complex non-planar coils or two different sets of simpler coils can be used. In the two sets approach, one set of coils shapes the toroidal magnetic field and the other one shapes the poloidal magnetic field.

The second approach, which is the most widely spread, is used on devices called Tokamaks (see figure 1.5). In such machines, planar toroidal coils shape the toroidal magnetic field. The poloidal magnetic field results from the generation of a toroidal current in the plasma. This current is generated by the addition of a central solenoid which plays the role of the primary circuit of a transformer, the secondary circuit being the plasma. Current flowing in the primary circuit leads to the generation of a current in the secondary circuit by induction. Additional coils can be added to the tokamak to control the shape and position of the plasma.

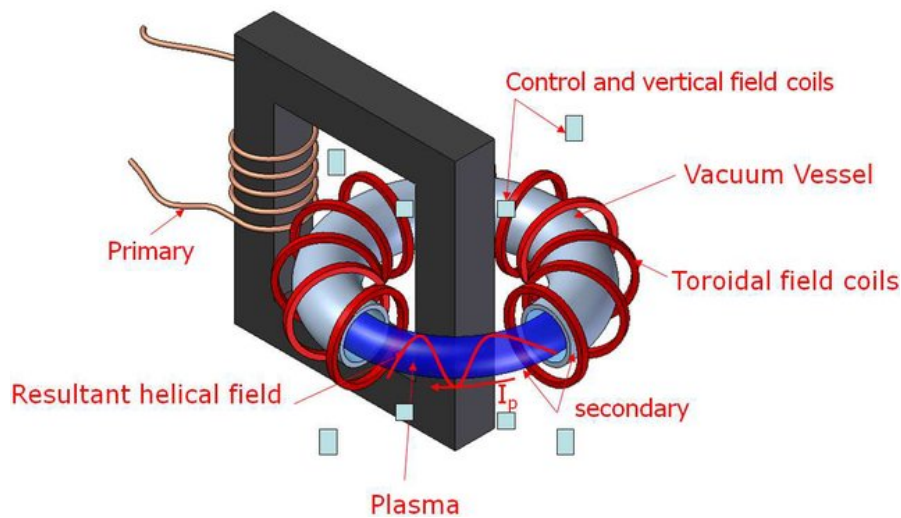


Figure 1.5 – Principle of the Tokamak. [15]

1.2.4 Tokamak

1.2.4.1 Geometry

In order to understand the geometry of a tokamak, a poloidal cross-section of a tokamak is displayed on figure 1.6. The tokamak is made of a vacuum vessel containing a plasma, the aforementioned coils, and additional systems (e.g. heating, diagnostics, pumping). The plasma is constrained in size by either a limiter or a divertor.

The limiter is simply a plasma facing component coming in tangential contact with the plasma. This leads to the opening of the magnetic surfaces located behind the limiter and therefore a restriction of the plasma to the region before the contact with the limiter. The limiter configuration leads to a significant pollution of the plasma by impurities ejected from the limiter, which affects the tokamak performance.

On the other hand, the divertor affects the magnetic topology of the Last Closed Magnetic Surface (LCMS) in order to create a so-called x-point. The x-point divides the

plasma into a confined and a non-confined region. As a result, the interface between the divertor and the plasma takes place outside of the LCMS and pollution from the divertor does not reach the plasma core. The divertor configuration is nowadays used in most tokamaks.

The plasma boundary is the so-called separatrix (also referred to as LCMS). The LCMS is separated from vacuum by the Scrape-Off Layer (SOL) which goes up to the divertor leg. In high confinement (H-mode introduced in section 1.2.4.2) the plasma core is separated from the LCMS by the pedestal, which is a region where high density and temperature gradients are observed (see section 1.2.4.2).

The magnetic axis is located at (R_0, Z_0) , R_0 is also referred to as the major radius of the tokamak. The minor radius of the device, a , denotes the radial distance between the magnetic axis and the separatrix. b denotes the vertical distance between the magnetic axis and the separatrix.

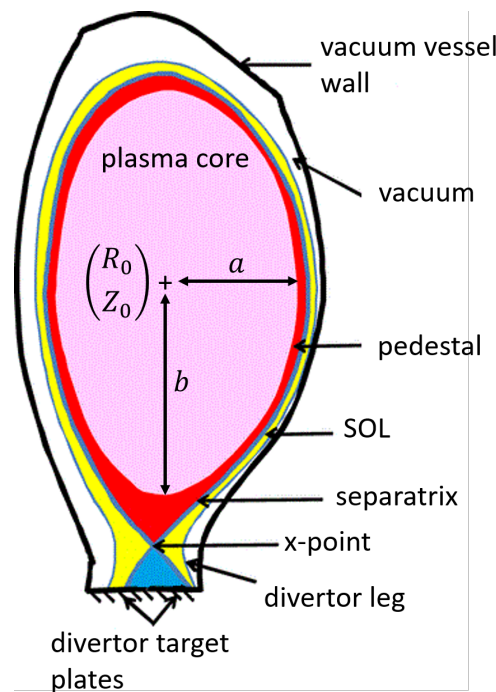


Figure 1.6 – Illustration of the poloidal cross-section of a tokamak.

1.2.4.2 Confinement modes

The confinement mode of a plasma describes how well the energy is confined. The L-mode stands for Low confinement mode which exhibits high particle and energy transport. The confinement time in L-mode is short.

An improved mode of confinement was observed in the ASDEX tokamak: the H-mode, or high confinement mode. It is characterized by a sudden rise of the core density and temperature, and by steep gradients at the plasma edge. This high gradient region is

called the pedestal (it is only present in H-mode) and exhibits much lower transport coefficients and therefore a better confinement.

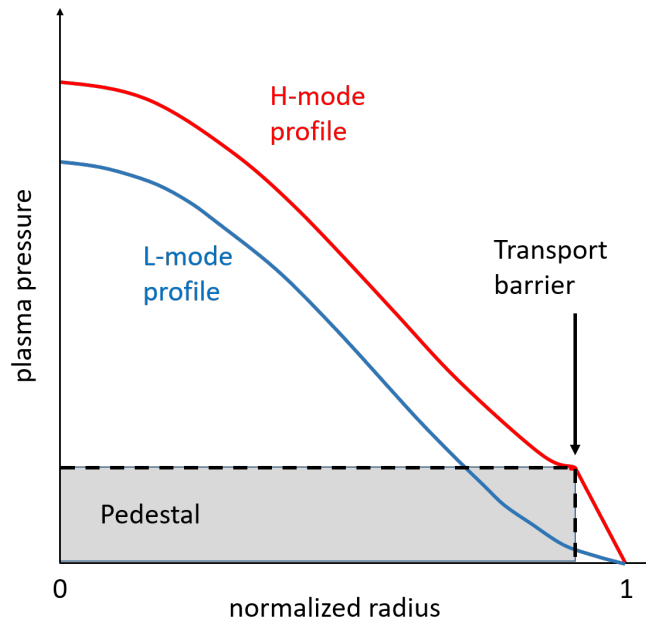


Figure 1.7 – Illustration of L and H confinement modes.

1.2.4.3 Heating

Heating of the plasma can be achieved through several techniques (see figure 1.8) in order to compensate for radiation losses.

Induction is the first way to heat the plasma. It is necessary to generate plasma current which leads to Ohmic heating to do the plasma resistivity.

α -particles heating takes place once D-T fusion reactions occur in the plasma.

RadioFrequency (RF) heating can be achieved by injecting electromagnetic waves at specific frequencies. The waves are absorbed by different particles depending on their frequency. RF heating is divided into Electron Cyclotron Resonance Heating (ECRH), Ion Cyclotron Resonance Heating (ICRH), and Lower Hybrid Current Drive (LHCD).

Fast neutral particles can be injected in the plasma core using a Neutral Beam Injector. Once ionized, they transfer their energy to the plasma by Coulomb collisions.

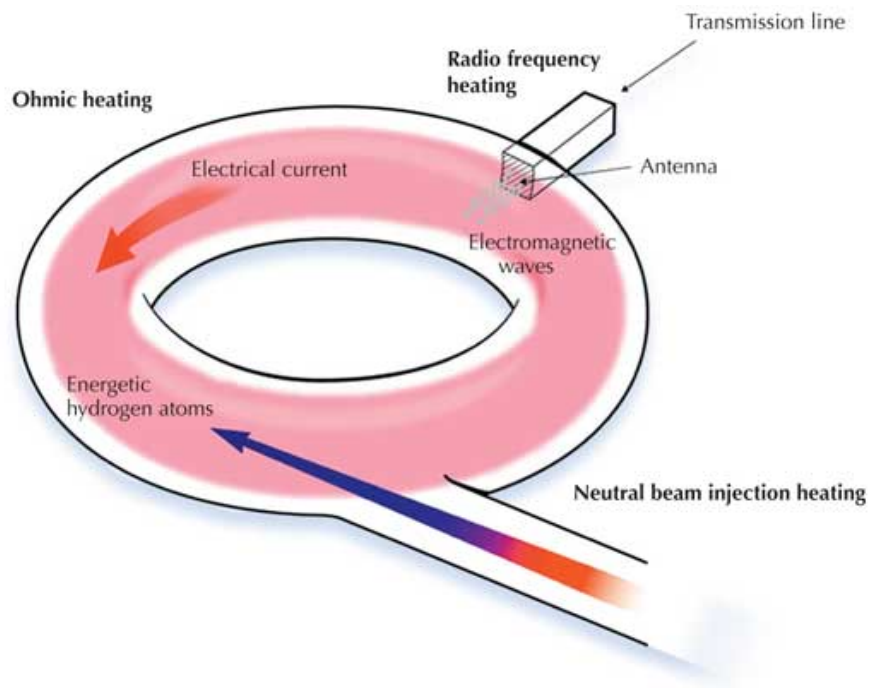


Figure 1.8 – Schematic representation of the different heating sources of a tokamak. [16]

1.2.4.4 Key challenges

In this section, the main challenges faced by magnetic confinement fusion are described. Tritium and nuclear waste management have been discussed in section 1.1.4, this section focuses on tokamak operation issues.

MagnetoHydroDynamics (MHD) instabilities in tokamak plasmas tend to increase radial transport and are therefore detrimental to energy confinement. The main MHD instabilities observed in tokamak plasmas are the so-called sawtooth oscillations, Edge Localised Modes (ELMs), and tearing modes.

Sawtooth crashes are a periodic instability which ejects energy and particles out of the plasma core. The name comes from the shape of the temperature and density profiles during such instabilities. They are characterised by a build-up phase during which the density and temperature profiles get more and more peaked followed by a sudden redistribution which flattens the profiles. This instability strongly affects particle and energy confinement, and can lead to plasma ending. However, evidence suggests that controlled sawtooth oscillations could be used to avoid impurity accumulation and limit fuel dilution by expelling He ashes.

Edge Localised Modes are a MHD instability which is observed in the plasma edge in H-mode plasmas. Tearing modes are a localised instability which changes the magnetic configuration of a plasma region, leading to the creation of magnetic islands. These islands increase radial transport and therefore deteriorate the confinement.

Another challenge is the choice of materials for PFC. Historically, carbon has been the first choice for PFC in tokamaks. It is a cheap material with a high thermal conductivity, a good resilience to heat fluxes and a relatively low atomic number. However, its tritium retention would lead to biological hazard during D-T operation and the high sputtering rate of carbon is concerning for tokamaks such as ITER or DEMO. As a results, tungsten (W) and beryllium (Be) have been chosen for ITER PFC. The ITER main chamber will be made of Be due to its low atomic number and low tritium retention. The divertor as well as other PFC will be made of W due to its good thermal conductivity, very low tritium retention and sputtering capabilities. The study of the W source in the plasma due to sputtering is crucial to ITER as it limits the lifetime of the PFCs and can generate accumulation of impurities in the core.

Most of the eroded PFC particles and filaments are exhausted towards the divertor without reaching the plasma, but a small fraction can enter the SOL and migrate towards the plasma core. In such environment the impurity is ionized and radiates a significant amount of energy which decreases the plasma performance and can even lead to a radiative collapse of the plasma. The radiated losses are in the range of X-rays and the processes leading to their emission are described in section 2.2. The radiated power increases with the atomic number of the impurity. Heavy impurities such as tungsten are therefore more detrimental to the plasma performance than light impurities such as carbon. This is illustrated by figure 1.9 which displays ignition curves for different concentrations of tungsten and carbon. It can be observed that there are three orders of magnitude of difference between the acceptable tungsten and carbon concentrations for a similar ignition curve. On ITER, the reactor performance is affected by impurities for $C_W \geq 10^{-4}$ in the plasma core. The divertor configuration is expected to keep c_W low enough but tungsten-induced radiative losses remain a major concern for ITER nonetheless.

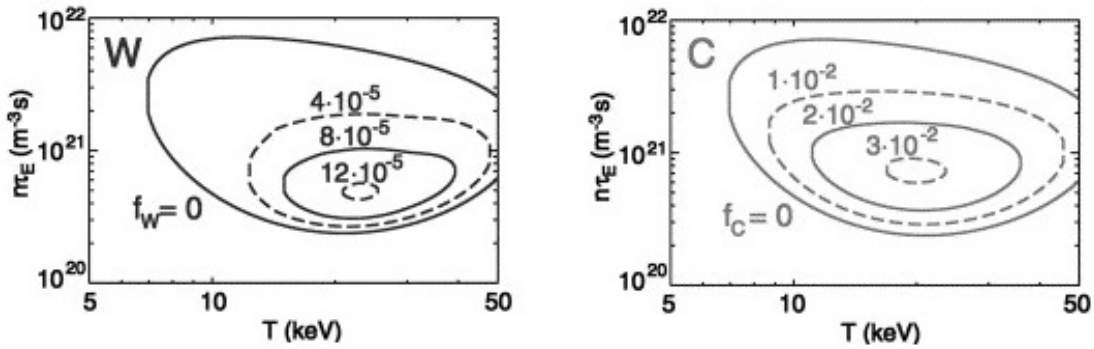


Figure 1.9 – Left: ignition curves for different concentrations of W. Right: ignition curves for different concentrations of C. Figure adapted from [17].

One of the products of a D-T fusion reaction is a highly energetic neutron ($E = 14.1\text{MeV}$). This neutron is most likely to escape the plasma volume without interacting and can then activate the materials of the vacuum vessel or deteriorate PFCs.

Radiation sensitive diagnostics such as mirrors or semiconductor photodiodes can be damaged if located too close to the plasma. Silicon photodiodes indeed exhibit diminished sensitivity and I-V curve (the plot of the collected current as a function of the voltage) after neutron irradiation. [18]

1.2.5 Existing tokamaks

In the scope of this thesis, X-ray measurements are performed or simulated in three tokamaks: WEST, ASDEX-Upgrade, and ITER. These tokamaks are presented in this section, as well as the tokamak DEMO which is the step after ITER on the nuclear fusion roadmap.

1.2.5.1 WEST

The W (tungsten) Environment Steady-state Tokamak (WEST) is a French tokamak operated by the IRFM (Institut de Recherche pour la Fusion par confinement Magnétique) in CEA (Commissariat à l'Énergie Atomique et aux Énergies Alternatives) Cadarache. CEA is a French government-funded research organization which covers a wide range of subjects: energy, defense and security, information technologies and health technologies. It was created in 1945 with the initial assignment to pursue research towards the use of atomic energy for science, industry and defense purposes.

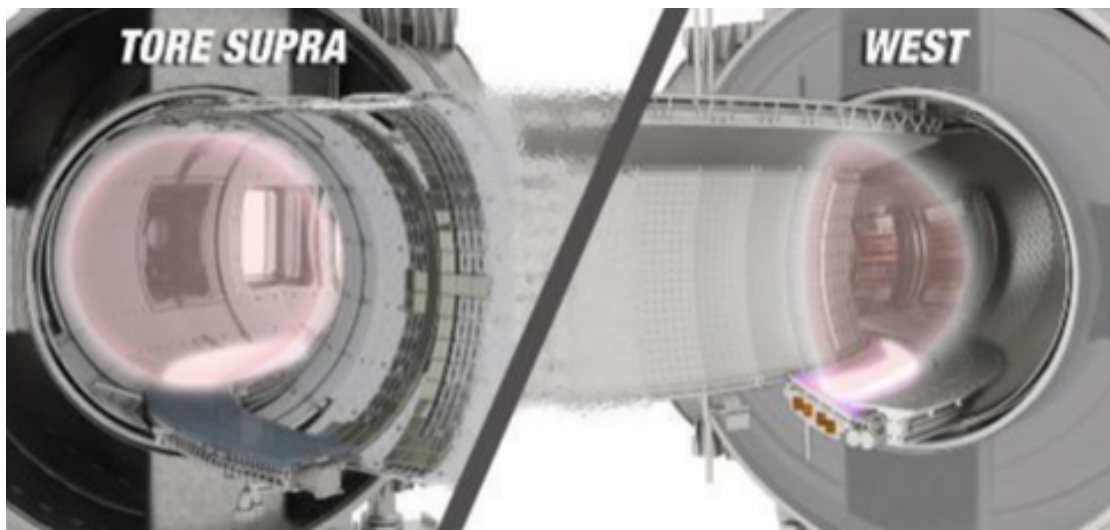


Figure 1.10 – Comparison of the Tore Supra (left) and WEST (right) poloidal cross sections. [19]

WEST is the upgrade of the Tore Supra (which stands for Superconducting Torus in French) tokamak, it aims at installing and testing an actively cooled ITER-like divertor as well as developing integrated plasma scenarios for long-pulse operation in a metallic environment. Tore Supra operation took place from 1988 to 2010, leading notably

plasma current I_p	1 MA
toroidal field B	3.65 T
major radius R	2.5 m
minor radius a	0.5 m
Plasma volume V_p	15 m^3
ICRH max. power	9 MW
LHCD max. power	7 MW
Flat top duration	1000 s

Table 1.1 – Parameters of the WEST tokamak.

to a record 6.5 minutes plasma in 2003. [20] The upgrade to WEST was completed in 2016. The Tore Supra superconducting magnets, heating and active water cooling systems are installed on WEST. This allow WEST to be the only metallic machine capable of long-pulse operation.

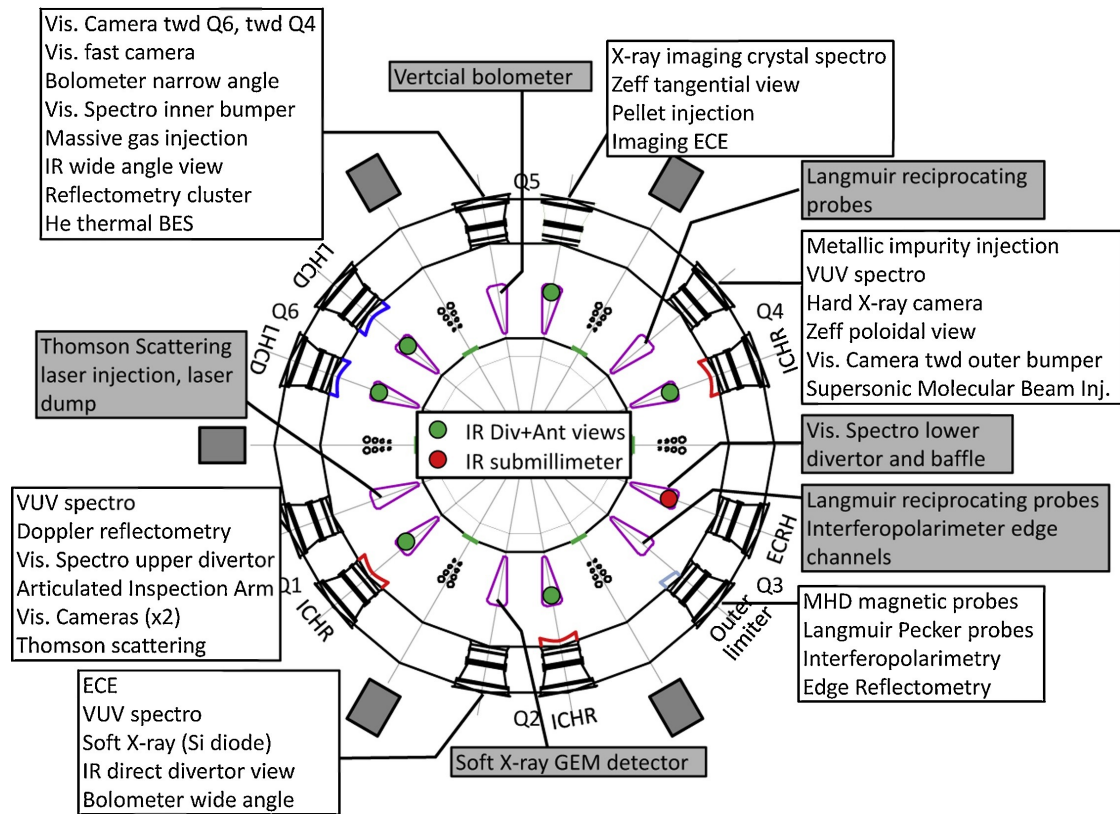


Figure 1.11 – Top view of the WEST tokamak with details of its ex-vessel diagnostics. [21]

The diagnostics installed on WEST are displayed on figure 1.11. In the scope of this thesis, focus is put on WEST soft X-ray diagnostics. The silicon photodiodes installed

on Tore Supra have been replaced by two Gas Electron Multiplier detectors (presented in section 3.2.3), one covering the plasma radially and the other one vertically. The corresponding lines-of-sight are displayed on figure 1.12.

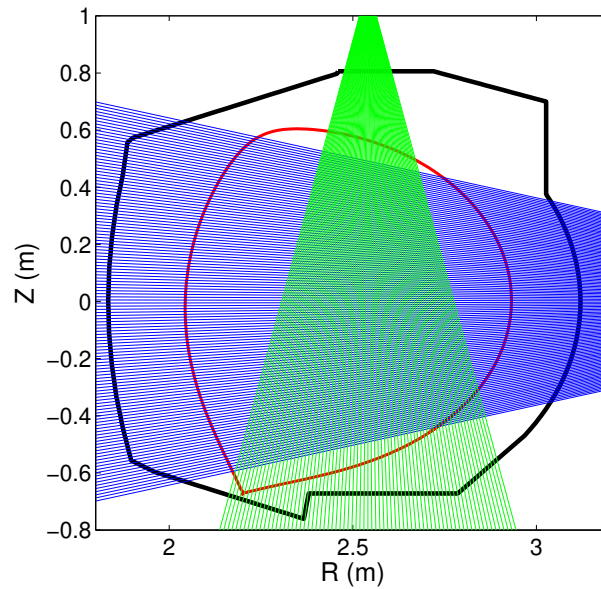


Figure 1.12 – Poloidal cross-section view of WEST soft X-ray lines-of-sight.

1.2.5.2 ASDEX Upgrade

ASDEX (Axially Symmetric Divertor EXperiment) Upgrade is a tokamak located at the Max-Planck-Institut für Plasmaphysik in Garching, Germany. It is considered as a midsize tokamak, in comparison with bigger machines such as JET. The ASDEX tokamak has been in operation from 1980 to 1990 and ASDEX Upgrade started operation in 1991 and still operates to this day. It has the specificity that it features an all-tungsten first wall and divertor, leading to significant soft X-ray emissions.

Soft x-ray measurement is performed by semiconductor photodiodes which cover the plasma cross section from various angles: 15 cameras are installed for a total of 208 lines-of-sight. The corresponding lines-of-sight geometry is shown on figure 1.13.

plasma current I_p	2 MA
toroidal field B	3.1 T
major radius R	1.65 m
minor radius a	0.5 - 0.8 m
Plasma volume V_p	14 m^3
Ohmic max. power	1 MW
NBI max. power	20 MW
ICRH max. power	6 MW
ECRH max. power	2x2 MW
Flat top duration	<10 s

Table 1.2 – Parameters of the ASDEX Upgrade tokamak.

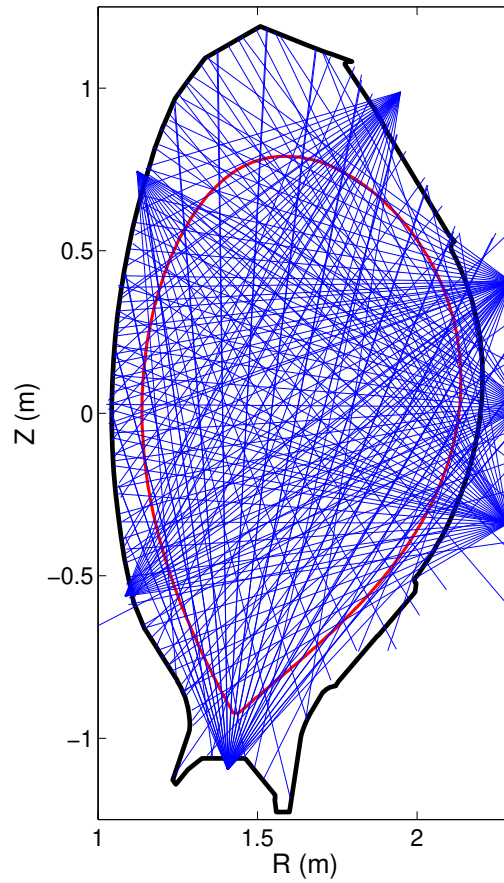


Figure 1.13 – Poloidal cross-section view of ASDEX Upgrade soft X-ray lines-of-sight.

1.2.5.3 ITER

The International Thermonuclear Experimental Reactor (ITER) is an international experimental fusion reactor currently under construction in Saint-Paul-lès-Durance, France. ITER is a joint effort, funded and run by 7 seven member entities: the European Union (plus Switzerland), China, India, Japan, Russia, South Korea and the United States of America. The project was initiated in 1985 with the aim to demonstrate the scientific and technical feasibility of a fusion reactor. The first plasma on ITER is expected to take place at the end of 2025, for a D-T nuclear phase which should start in 2035. Its current goals are the following [22]:

- Produce 500 MW of fusion power for pulses of 400 s
- Demonstrate the integrated operation of technologies for a fusion power plant
- Achieve a deuterium-tritium plasma in which the reaction is sustained through internal heating (alpha power)
- Test tritium breeding
- Demonstrate the safety characteristics of a fusion device

ITER will be the largest tokamak in the world, a comparison between the tables 1.1, 1.2, and 1.3 shows the extent of ITER's magnitude. The ITER X-ray diagnostics geometry is described in section 5.1.

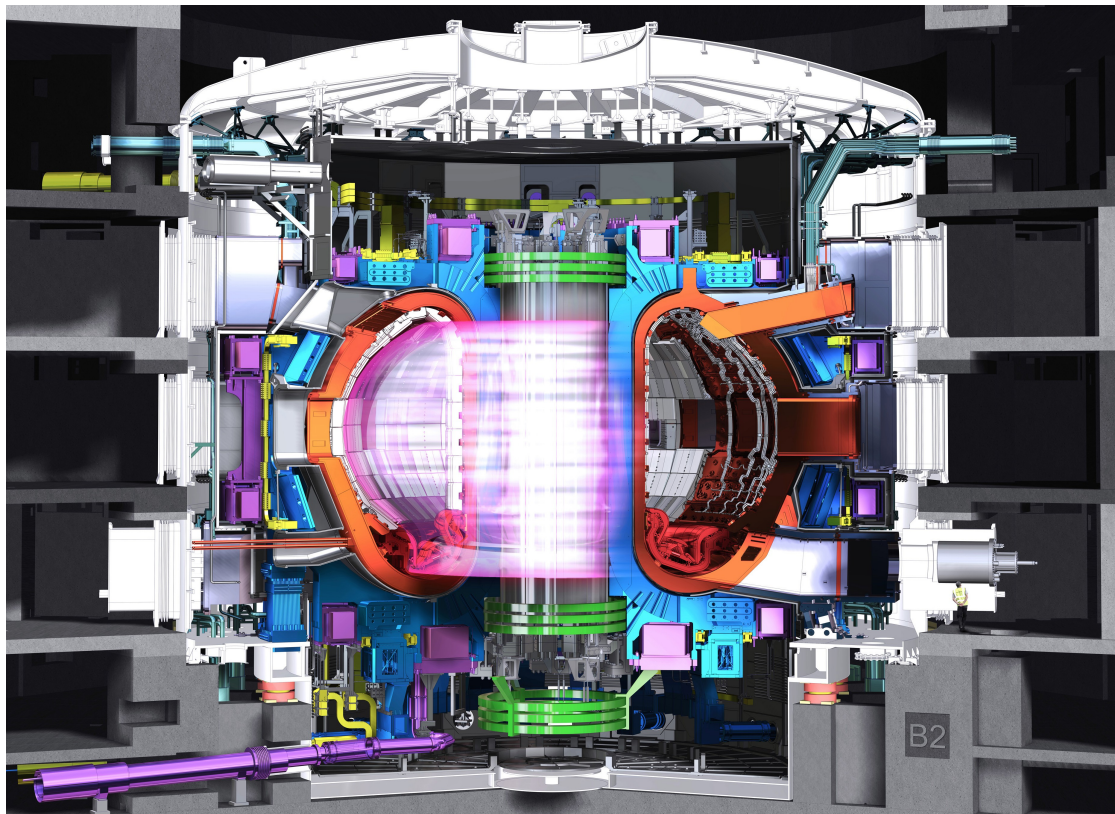


Figure 1.14 – Drawing of the ITER tokamak and integrated plant system.

plasma current I_p	15 MA
toroidal field B	5.3 T
major radius R	6.2 m
minor radius a	2.0 m
Plasma volume V_p	837 m^3
NBI max. power	33 MW
ICRH max. power	20 MW
ECRH max. power	20 MW
Flat top duration	>400 s

Table 1.3 – Parameters of the ITER tokamak.

plasma current I_p	18 MA
toroidal field B	6.9 T
major radius R	8.6 m
minor radius a	2.9 m
Total heating power	270 MW

Table 1.4 – Parameters of the European version of the DEMO tokamak.

1.2.5.4 DEMO

DEMONstration Power Station (DEMO) is an industrial reactor prototype (as opposed to ITER which is a research reactor prototype). DEMO is the first step after ITER, with goals oriented towards energy production. DEMO is not an international collaboration such as ITER, and each country or entity is preparing their own reactor prototype. Its design is expected to be based on the ITER design but at a larger scale. Therefore tungsten plasma facing components are to be expected and, as a result, so is a high X-ray emissivity. The parameters of the European version of the DEMO reactor are displayed in table 1.4. China and Korea also have started working on their version of DEMO, respectively named China Fusion Engineering Test Reactor (CFETR) and K-DEMO.

A preliminary sketch of K-DEMO (Korea's DEMO reactor) is shown on figure 1.15. It can be noticed that an additional system, based on water heating and an alternator, is present in order to convert fusion energy into electrical power. Moreover, the absence of diagnostics in the sketch is revealing of the fact that DEMO is an industrial prototype in which measurement systems are limited to those necessary for operation only.

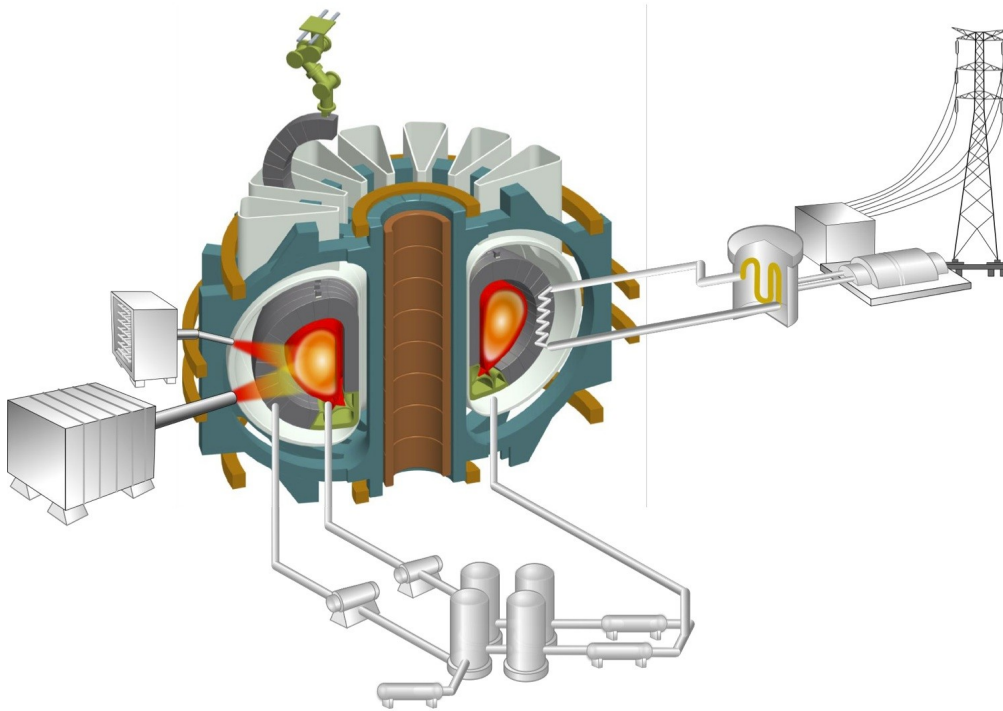


Figure 1.15 – Preliminary drawing of Korea’s version of DEMO: K-DEMO.

1.3 Scope of this thesis

We have seen that impurity accumulation, especially for tungsten, in the plasma core is a major concern for ITER. X-ray tomography is a key tomography for impurity transport studies, and a reliable X-ray diagnostic system is of the utmost importance for ITER success. Due to the high neutron fluence which will be generated during the D-D and D-T nuclear phases, classic silicon photodiodes cannot be used for X-ray measurement. Advanced detectors exhibiting a renewable detection volume such as gas detectors are foreseen for the ITER nuclear phase. Due to its simplicity of design and low voltage operation, the Low Voltage Ionization Chamber (LVIC) is the most promising candidate for X-ray measurement. [23, 24]

In comparison with existing tokamaks, very high temperatures are expected in ITER, leading to significant X-ray emission over the whole plasma volume. As a result, X-ray tomography must be performed over a set of lines-of-sight which covers the whole poloidal section of the tokamak. X-ray emissivity will take place up to high energy ($\approx 100\text{keV}$) which allows the extraction of the electron temperature from an energy-resolved X-ray measurement.

The aim of this PhD thesis is to contribute to the development of advanced X-ray detectors for ITER by providing tools allowing a reliable and precise measurement of the plasma emissivity. The manuscript is organised as follows:

- Chapter 2 gives a general description of X-ray emission and the effect of transport
- In chapter 3 the different technologies which can be used for X-ray measurement are presented and compared in the scope of measurement on ITER. Tomography is introduced.
- Chapter 4 describes a synthetic diagnostic tool which allows the simulation of the detection process using LVIC
- In chapter 5 the fitness of the ITER X-ray lines-of-sight for tomography is studied through the reconstruction of phantom emissivity profiles
- In chapter 6 a full tomographic chain using LVIC is simulated on ITER in order to demonstrate the tomographic capabilities of the detector
- Chapter 7 covers the influence of impurity transport, its study through X-ray tomography and the reconstruction of radial transport parameters in different ITER scenarios
- In chapter 8 an innovative modification of the LVIC, allowing spectral deconvolution of the X-ray emissivity, and the associated spectral reconstruction method are proposed and applied to ITER. The capability of the system to reconstruct the electron temperature in the core is demonstrated.
- Chapter 9 concludes this manuscript and gives perspectives for the future of X-ray measurement for nuclear tokamaks

2 X-ray radiation

Sommaire

2.1	Introduction	49
2.2	X-ray emission	50
2.2.1	Bremsstrahlung emission	50
2.2.2	Radiative recombination	52
2.2.3	Spontaneous emission	53
2.3	Ionization equilibrium	54
2.3.1	Local Thermodynamical Equilibrium	55
2.3.2	Corona Equilibrium	57
2.3.3	Collisional Radiative models	58
2.3.4	Effect of impurity transport on the equilibrium	59
2.4	Total plasma emissivity	60
2.4.1	X-ray emissivity on ITER	62
2.4.2	Influence of impurity transport on the X-ray emissivity	63
2.5	Extraction of plasma parameters from X-ray measurement	64
2.5.1	Impurity density	65
2.5.2	Impurity transport coefficients	65
2.5.3	Electron temperature	66

2.1 Introduction

X-ray is a form of electromagnetic radiation with an energy ranging from 100 eV to several MeV. They have been experimentally discovered in 1895 by Wilhelm Röntgen while experimenting with electric discharge tubes. [25] X-rays are photons, and therefore have no mass nor electric charge. The energy, frequency and wavelength of a photon are linked by the Planck-Einstein relation:

$$E = h\nu = h\frac{c}{\lambda} \quad (2.1)$$

where E is the photon energy in eV, $h \approx 4.1 \cdot 10^{-15} \text{ eV} \cdot \text{s}$ is the Planck constant, $c \approx 3 \cdot 10^8 \text{ m} \cdot \text{s}^{-1}$ is the speed of light in vacuum and λ is the wavelength in m .

As it can be seen in fig. 2.1, the X-ray range is divided into the soft X-ray (SXR) and hard X-ray (HXR) ranges. SXR are usually defined as X-ray photons with energy lower than 15 keV, however in the framework of tokamak plasma physics this range is extended

to 20 keV. This is explained by the fact that SXR measurement devices (usually semi-conducting diodes) have a decreasing spectral response which is non-negligible up to 20 keV (see Chapter 3). In the scope of this thesis, the boundary between SXR and HXR will be taken as 20 keV.

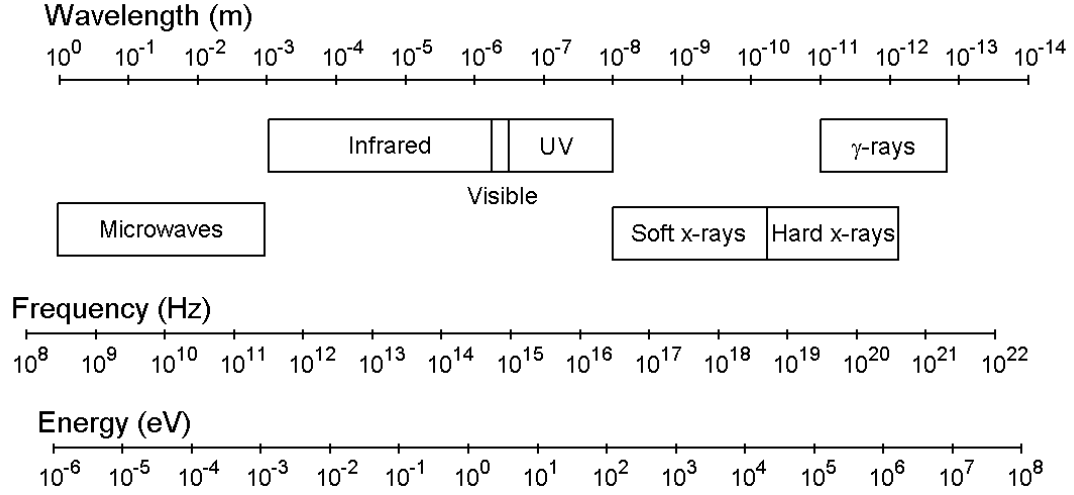


Figure 2.1 – Electronic radiation spectrum from microwaves to gamma-rays.

X-ray radiation is observed in tokamak plasmas with a temperature $T > 1$ keV. SXR emission results from the interaction of an electron with an ion (Bremsstrahlung and radiative recombination) or from the de-excitation of a nucleus (line emission). Bremsstrahlung and radiative recombination are continuous spectrally speaking and extend to the HXR range. HXR and γ -rays can be generated by fast particles such as fast α -particles or suprathermal electrons. Lower energy electromagnetic radiation is observed in tokamak plasmas: the plasma edge radiates in the visible-ultraviolet (VUV) ranges and the plasma facing components (PFC) radiate in the infrared and visible ranges when heated by the plasma. Thus, a very wide part of the electromagnetic spectrum is used in tokamaks for diagnostic purposes.

2.2 X-ray emission

X-ray emission results from the interaction between electrons and ions. In tokamak plasmas, three different types of atomic processes lead to X-ray emission (see fig. 2.2): Bremsstrahlung, radiative recombination, and spontaneous emission (also referred to as line radiation).

2.2.1 Bremsstrahlung emission

Bremsstrahlung emission occurs when the interaction between charged particles does not affect the internal energetic level of each particle and results in photon

emission through charged particle acceleration. It is labelled as *free-free* interaction as both particles are free (unbounded) before and after the collision. The process is the following, with A the species of the charged particle (it can be an electron), z its charge number, $h\nu$ the emitted photon, and e, e' electrons of different energy:



The inverse process to Bremsstrahlung emission is called reverse Bremsstrahlung and mainly occurs in laser-generated plasmas [26, 27]. In tokamak plasmas, ion-electron free-free interaction is the main contributor to Bremsstrahlung SXR radiation and fast electron-electron free-free interaction mainly lead to HXR radiation. The spectrum associated with Bremsstrahlung radiation is continuous in the case of a Maxwellian electron velocity distribution (see fig. 2.3 and eq. 2.2).

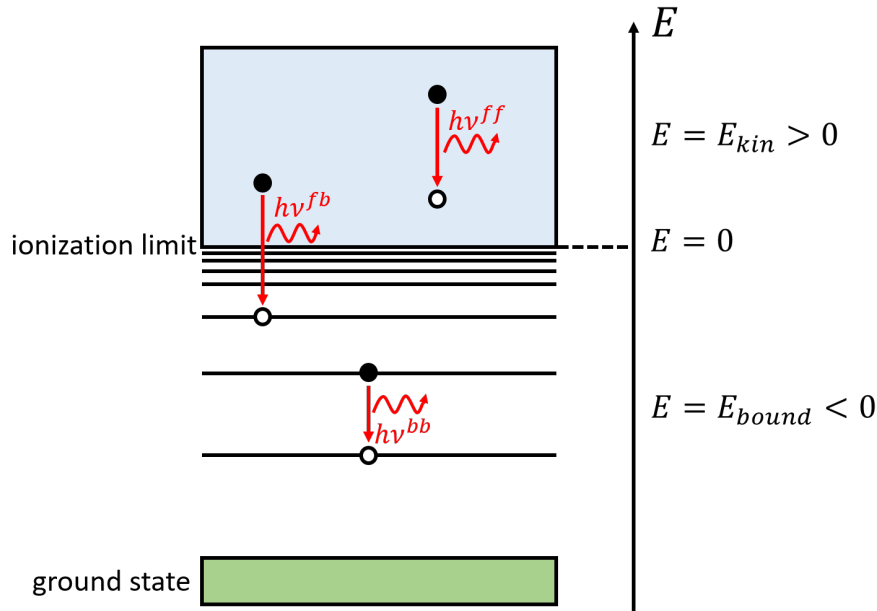


Figure 2.2 – Atomic processes leading to X-ray emission in a plasma.

In the case of a plasma where the electron distribution is Maxwellian, the contribution to the spectral emissivity of the fully ionized species S of charge z is given by [28]:

$$\epsilon_{S,z}^{ff}(h\nu) = n_e n_Z Z^2 \frac{32\sqrt{\pi}(\alpha a_0)^3}{3^{\frac{3}{2}} hc} \left(\frac{E_R^3}{T_e} \right)^{\frac{1}{2}} \exp\left(-\frac{h\nu}{T_e}\right) G^{ff} = n_e n_Z k_{S,z}^{ff} \quad (2.3)$$

where α is the fine structure constant, a_0 is the first Bohr radius, E_R is the Rydberg energy, G^{ff} is the Bremsstrahlung Gaunt factor (close to unity in the [0.1, 100] keV domain for a plasma with an electron temperature of several tens of keV, and $k_{S,z}^{ff}$ is the free-free emission coefficient of the species S of ionization state z . In the case of

non-fully ionized ions, it is necessary to include a correction factor in order to take into account the ion internal structure which affects the *free-free* interaction cross-section.

2.2.2 Radiative recombination

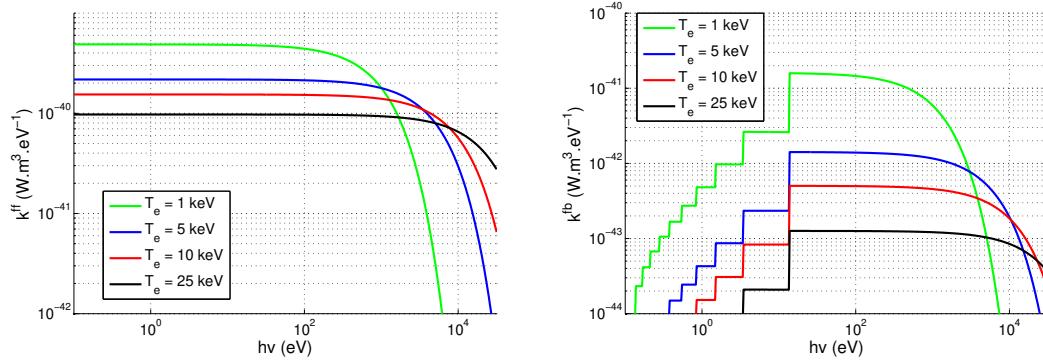


Figure 2.3 – Left: Bremsstrahlung radiation spectrum of hydrogen for different electron temperatures. Right: Radiative recombination spectrum of hydrogen for different electron temperatures.

Radiative recombination is the process of capture of an electron by an ion, which results in the ion (with a degree of ionisation lowered by one) and the emission of a photon:



where A is the species of the charged particle (it can be an electron), z its charge number, $h\nu$ is the emitted photon, and e the captured electron. This process is labelled as *free-bound* as the incident particles are free (unbounded) and bound in the recombination process. Its inverse reaction is photo-ionization, which is described in sec. 4.2.1.1.

In tokamak plasmas, ionised impurities contribute to most of the emitted radiative recombination-induced radiation as such interaction with hydrogen isotopes is negligible. The spectrum associated with *free-bound* interaction is a semi-continuum. Indeed, the incident electron must have a kinetic energy higher than the ionization energy of the recombined orbit of the nucleus:

$$h\nu^{fb} = E_{kin} + \Delta E_{\infty j}^{(z)} \quad (2.5)$$

where E_{kin} is the kinetic energy of the electron and $\Delta E_{\infty j}^{(z)}$ is the difference between the ion ionization energy and the energy level j of the recombined electron. As the electron's kinetic energy increases, higher orbits become accessible which leads to discontinuities in the spectrum called recombination edges (see fig. 2.3).

In the case of fully-stripped ions of electric charge Z , turning into their hydrogenic ions

of charge $Z - 1$, a simplified expression of the contribution to the spectral emissivity is given by [28]:

$$\epsilon^{fb}(h\nu) = n_e n_Z Z^4 \frac{64\sqrt{\pi}(\alpha a_0)^3 E_R}{3^{\frac{3}{2}} h c} \left(\frac{E_R}{k_B T_e} \right)^{\frac{3}{2}} \exp\left(-\frac{h\nu}{k_B T_e}\right) \sum_{n > n_{min}} \frac{1}{n^3} \exp\left(\frac{Z^2 E_R}{n^2 T_e}\right) G^{fb} \\ = n_e n_Z k_{S,z}^{fb} \quad (2.6)$$

where α is the fine structure constant, a_0 is the first Bohr radius, E_R is the Rydberg energy, n is the atomic orbit (limited by a lower value n_{min} which depends on the energy of the electron), G^{fb} is the radiative recombination Gaunt factor (also close to unity in the [0.1, 100] keV domain for a plasma with an electron temperature of several tens of keV, and $k_{S,z}^{fb}$ is the free-bound emission coefficient of species S in ionization stage z . It can be seen in eq. 2.6 that the contribution of the atomic orbits decreases rapidly with n , thus a summation over a limited number of orbits (less than 10) gives an accurate estimation for most of the contributions.

2.2.3 Spontaneous emission

Spontaneous emission occurs during the relaxation of an excited ion via radiative decay. The process is the following:

$$(A^{(z)})^* \rightleftharpoons A^{(z)} + h\nu \quad (2.7)$$

In tokamak plasmas, excitation of an ion mostly result from electron collision excitation ($A^{(z)} + e \rightleftharpoons (A^{(z)})^* + e'$), which only affects non-fully stripped ions. Spontaneous emission is labelled as *bound-bound* because the electron responsible for the photon emission is bound to the nucleus before and after the relaxation. The energy of the emitted photon is exactly equal to the difference between the energy of the excited level j and the energy of the de-excited level i :

$$h\nu_{j \rightarrow i}^{bb} = \Delta E_{ij} = E(j) - E(i) > 0 \quad (2.8)$$

As a result the spectrum associated with spontaneous emission is composed of numerous discrete lines, which explains why spontaneous emission is also referred to as *line emission* or *line radiation*.

The emissivity associated with the $i \rightarrow j$ line is given by:

$$\epsilon_{j \rightarrow i}^{bb,(z)} = n_j^{(z)} A_{j \rightarrow i}^{(z)} \frac{h\nu_{j \rightarrow i}^{bb}}{e} \quad (2.9)$$

where $\epsilon_{j \rightarrow i}^{(z)}$ is the emissivity in $W \cdot m^{-3}$, $n_j^{(z)}$ is the population of the energy level j in m^{-3} , $A_{j \rightarrow i}^{(z)}$ is the Einstein coefficient of spontaneous emission from level j to level i in s^{-1} , and e is the conversion coefficient from eV to J.

Ions can reach the energy level j by electron collision excitation (first term in equation 2.10) and line radiation from a higher energy level (second term in equation 2.10), and can leave it by electron collision excitation (third term in equation 2.10) and line radiation to a lower energy level (fourth term in equation 2.10). Thus the evolution of the population $n_j^{(z)}$ is given by:

$$\frac{dn_j^{(z)}}{dt} = n_e \sum_{k \neq j} n_k^{(z)} X_{kj}^{(z)} + \sum_{k > j} n_k^{(z)} A_{kj}^{(z)} - n_e \sum_{k \neq j} n_j^{(z)} X_{jk}^{(z)} - \sum_{k < j} n_j^{(z)} A_{jk}^{(z)} \quad (2.10)$$

where n_e is the electron density and $X_{ij}^{(z)}$ is the electron excitation coefficient from energy level i to energy level j . If the equilibrium between internal energy levels of any ionization state is reached, then $\frac{dn_j^{(z)}}{dt} = 0$ and equation 2.10 can be rewritten as:

$$n_j^{(z)} A_{ji}^{(z)} = n_e n_z \left(\sum_{k \neq j} f_k^{(z)} X_{jk}^{(z)} - \sum_{k \neq j} f_j^{(z)} X_{kj}^{(z)} - \frac{1}{n_e} \sum_{k > j} f_k^{(z)} A_{kj}^{(z)} \right) B_{ji}^{(z)} \quad (2.11)$$

where $f_k^{(z)} = \frac{n_k^{(z)}}{n_z}$ is the fractional abundance of energy level k in ionization stage z and $B_{ji}^{(z)} = \frac{A_{ji}^{(z)}}{\sum_{k < j} A_{jk}^{(z)}}$ is the so-called branching ratio of transition $j \rightarrow i$. The fractional abundances as well as the Einstein and electron excitation coefficients only depend on n_e and T_e , and therefore equation 2.9 can be reformulated as:

$$\epsilon_{j \rightarrow i}^{bb,(z)} = n_e n_z PEC_{ji}^{(z)} \quad (2.12)$$

where $PEC_{ji}^{(z)}$ is the Photon Emissivity Coefficient (PEC) in $W \cdot m^3$. The total emissivity resulting from spontaneous emission of species S in ionization state z is therefore given by:

$$\epsilon_{S,z}^{bb}(h\nu) = n_e n_{S,z} \sum_{i < j} PEC_{ji}^{(z)} = n_e n_{S,z} k_{S,z}^{bb} \quad (2.13)$$

In plasma regions where $T_e > 1 \text{ keV}$, light impurities, hydrogen and helium are fully ionized and thus do not radiate through line emission. In such conditions, spontaneous emission is only significant for medium and heavy impurities.

2.3 Ionization equilibrium

Section 2.2 covers the calculation of the X-ray emissivity induced by a species S at ionization level z . In order to compute the spectral emissivity of the plasma it is therefore necessary to solve the ionization equilibrium of all the species it contains. The population of each energy level inside an ionization state must be solved as well. The atomic state in an ion can be modified through collisional and radiative

transitions. In tokamak plasmas photo-absorption can be neglected as the plasma can be considered optically thin (i.e. photons do not interact with it) and therefore radiative excitation can be neglected as well. The density of atomic state j of ions of charge z $n_j^{(z)}$ is described by the following equation:

$$\frac{dn_j^{(z)}}{dt} = n_e C_{\rightarrow j}^{(z)} + R_{\rightarrow j}^{(z)} - n_e C_{j \rightarrow}^{(z)} - R_{j \rightarrow}^{(z)} \quad (2.14)$$

where $n_e C_{\rightarrow j}^{(z)}$ (resp: $R_{\rightarrow j}^{(z)}$) is the rate of collisional (resp: radiative) transitions affecting atomic level j . These coefficients include all the processes leading to transitions to and from atomic level j , which covers a significant amount of transitions. Solving equation 2.14 without simplifying assumptions practically impossible due to the large number of possible transitions and the fact that not all the transition rates and probabilities are known accurately.

Simplified models have been developed in order to solve the ionization equilibrium through the choice of assumptions fitting specific plasma conditions. These assumptions concern the time scales of all the different processes involved in the ionization equilibrium: the time scales of the non-dominant mechanisms in given plasma conditions are neglected. Two simplified methods are presented in this section: the local thermodynamical equilibrium (LTE) and the Corona Equilibrium (CE). More global approaches, referred to as collisional-radiative models, which solve the ionization equilibrium through the comparison of characteristic time scales are described.

2.3.1 Local Thermodynamical Equilibrium

The Local Thermodynamical Equilibrium is based on the assumption that at high plasma densities electron collisions are sufficient to reach the equilibrium between energy levels and that it follows a Boltzmann distribution:

$$\frac{n_j^{(z)}}{n_i^{(z)}} = \frac{g_j^{(z)}}{g_i^{(z)}} \exp\left(-\frac{E_j^{(z)} - E_i^{(z)}}{T}\right) \quad (2.15)$$

where $g_k^{(z)}$ is the degeneracy level of atomic state k , $E_k^{(z)}$ is the energy of the atomic state k and T is the temperature. The sum of equation 2.15 over all the atomic states i leads to the fraction of the atomic state j $n_j^{(z)} / n^{(z)}$:

$$\frac{n_j^{(z)}}{n^{(z)}} = \frac{g_j^{(z)}}{U^{(z)}(T)} \exp\left(-\frac{E_j^{(z)} - E_g^{(z)}}{T}\right) \quad (2.16)$$

where subscript g denotes the ground state of the ion and $U^{(z)}(T)$ the partition function of the ionization stage:

$$U^{(z)}(T) = \sum_{i=g}^{\infty} g_i^{(z)} \exp\left(-\frac{E_i^{(z)} - E_g^{(z)}}{T}\right) \quad (2.17)$$

In a plasma each ion is affected by the Coulomb field of all the other charged particles, which results in a lowering of the ionization energy of the ion. As a result, a finite number of bound states are available which lead to the truncature of equation 2.17. The upper limit of the ionization is n_{max} given by:

$$n_{max} = Z \sqrt{-\frac{E_R}{\Delta E_{\infty}^{(z)}}} \quad (2.18)$$

where E_R is the Rydberg energy and $\Delta E_{\infty}^{(z)} < 0$ is the lowered ionization energy. Equation 2.15 can be expanded to free electrons:

$$\frac{dn_e}{dg_e} = \frac{n_j^{(z)}}{g_j^{(z)}} \exp\left(-\frac{E_e - E_i^{(z)}}{k_B T}\right) \quad (2.19)$$

with dn_e the density of electrons with kinetic energies in the $[E_e, E_e + dE_e]$ range and dg_e the associated statistical weight:

$$dg_e = 2 \frac{g_j^{(z+1)}}{n_j^{(z+1)}} \left(\frac{m_e}{2\pi\hbar^2}\right)^{\frac{3}{2}} \sqrt{\frac{E_e}{\pi}} dE_e \quad (2.20)$$

with m_e the electron mass and \hbar the reduced Planck constant. By substituting dg_e in equation 2.19 and integrating over all electron energies, we obtain the Saha equation:

$$\frac{n^{(z+1)} n_e}{n^{(z)}} = 2 \frac{U^{(z+1)}(T)}{U^{(z)}(T)} \frac{1}{\lambda_B^3} \exp\left(-\frac{E_{\infty}^{(z)} - E_g^{(z)}}{k_B T}\right) \quad (2.21)$$

where $\lambda_B = \sqrt{\frac{h^3}{m_e k_B T}}$ is the thermal de Broglie wavelength of the electron.

Plasmas in LTE are often labelled *collision dominated* as it is the high frequency of collisions which maintain steady-state populations densities satisfying the Boltzmann relation and the Saha equation. The condition on the electron density is given by [29]:

$$n_e > 1.8 \cdot 10^{20} \cdot \sqrt{k_B T_e} \cdot (E_j - E_i)^3 \quad (2.22)$$

with E_j , E_i and $k_B T_e$ in eV and n_e in m^{-3} . In the case of an hydrogen plasma with $k_B T_e = 10 \text{ keV}$, we have $n_e \geq 1.8 \cdot 10^{20} \cdot \sqrt{10} \cdot 10.20^3$ which lead to $n_e \geq 6 \cdot 10^{23}$. This condition is not fulfilled in tokamak plasmas, where the electron density is of the

order of magnitude of $10^{20} m^{-3}$. However, the LTE model can be used in the scope of collisional-radiative models to group together energy levels for which $E_j - E_i$ is close enough.

2.3.2 Corona Equilibrium

The Corona Equilibrium (CE) is based on the assumption that at low electron densities, collisional processes become weak compared to radiative processes. The name of the model comes from the fact that this assumption applies well to the solar corona. In CE an energy level is only populated by electron collision (radiative processes are neglected as the plasma is considered optically thin) and depopulated by radiative decay:

$$\frac{dn_j^{(z)}}{dt} = n_e \sum_{i < j} n_i^{(z)} X_{i \rightarrow j}^{(z)} - n_j^{(z)} A_{j \rightarrow}^{(z)} \quad (2.23)$$

where $A_{j \rightarrow}^{(z)}$ is the Einstein coefficient of spontaneous emission from energy level j and $X_{i \rightarrow j}^{(z)}$ is the electron excitation coefficient from energy level i to j . The radiative processes are dominant with regards to collisional processes: $A_{i \rightarrow j}^{(z)} \gg n_e X_{i \rightarrow j}^{(z)}$. As a result, the ground state g is the dominant energy level ($n_g^{(z)} \approx n^{(z)}$) and the population in higher energy levels only originates from electron collision from the ground state. The population density of energy level j at steady state is thus given by:

$$\frac{n_j^{(z)}}{n_g^{(z)}} = \frac{n_e X_{g \rightarrow j}^{(z)}}{A_{j \rightarrow}^{(z)}} \ll 1 \quad (2.24)$$

In corona equilibrium plasmas, the ionization of an electron is dominated by electron impact ionization and the recombination of a free electron is governed by radiative recombination. The evolution of the population of ions at ionization level $z + 1$ is therefore given by:

$$\frac{dn^{(z+1)}}{dt} = n_e n^{(z)} S_z - n_e n^{(z+1)} \alpha_{z+1} \quad (2.25)$$

where S_z is the electron impact ionization coefficient and α_{z+1} is the radiative recombination coefficient. In steady state the population is given by:

$$\frac{n^{(z+1)}}{n^{(z)}} = \frac{S_z}{\alpha_{z+1}} \quad (2.26)$$

In the frame of the corona equilibrium, the ratio of ions densities only depends on T_e (through the S and α coefficients) and is thus independent of n_e .

In order to be considered at coronal equilibrium, a plasma must verify the following

condition on electron density [30]:

$$n_e < 1.9 \cdot 10^{18} \cdot Z^6 \cdot \sqrt{T_e} \cdot \exp\left(\frac{1 \cdot 10^{-4} \cdot Z^2}{T_e}\right) \quad (2.27)$$

with T_e in keV , n_e in m^{-3} and Z the effective charge of the ion. For a fully-ionized hydrogen plasma at $T_e = 10keV$, the condition is $n_e < 6 \cdot 10^{18}m^{-3}$. Similarly as Local Thermodynamic Equilibrium, Corona Equilibrium is not reached in tokamak plasmas.

2.3.3 Collisional Radiative models

Collisional Radiative (CR) models aim at computing the population densities of an ion in the scope of plasmas with electron densities between the LTE and CE limits, by taking into account the following processes: electron collisional transitions and ionizations, radiative decay, and radiative recombination. This leads to the following dynamics for the population of ions in ionization stage z in energy level j :

$$\begin{aligned} \frac{dn_j^{(z)}}{dt} = & -n_j^{(z)} \sum_{i \neq j} n_e X_{j \rightarrow i} + \sum_{q \neq p} n_i^{(z)} n_e X_{i \rightarrow j}^{(z)} \\ & - n_j^{(z)} \sum_{i < j} A_{j \rightarrow i}^{(z)} + \sum_{i > j} n_i^{(z)} A_{i \rightarrow j}^{(z)} \\ & - n_j^{(z)} n_e S_{j \rightarrow g} + n_g^{(z+1)} n_e \alpha_{g \rightarrow j}^{(z+1)} \end{aligned} \quad (2.28)$$

The evolution of the population vector $N^{(z)} = \{n_g^{(z+1)}, \dots, n_j^{(z)}, \dots, n_g^{(z)}\}$ can be described by the following matrix system:

$$\frac{d}{dt} N^{(z)} = M \cdot N^{(z)} \quad (2.29)$$

where the matrix M is defined by:

$$M_{i,j} = \begin{cases} \sum_{i > j} (A_{i \rightarrow j}^{(z)} + n_e X_{i \rightarrow j}^{(z)}) & \text{if } i > j \\ \sum_{i < j} n_e X_{i \rightarrow j}^{(z)} & \text{if } i < j \\ -\sum_{i \neq j} n_e X_{j \rightarrow i}^{(z)} - \sum_{i < j} A_{j \rightarrow i}^{(z)} - n_e S_{j \rightarrow g}^{(z)} & \text{if } i = j \\ 0 & \text{if } i = j = 1 \\ n_e S_{j \rightarrow g}^{(z)} & \text{if } i = 1 \\ n_e \alpha_{g \rightarrow j}^{(z)} & \text{if } j = 1 \end{cases} \quad (2.30)$$

Simplification is achieved by comparing the different time scales involved in the equilibrium:

- The time constant t_{ex} describes the evolution of the population of excited level j for a given ionization state. The slowest way to reach steady-state population is

through radiative decay only, therefore $\tau = 1/A_{j \rightarrow}^{(z)} > t_{ex}$.

- The ionization equilibrium time constant t_{ion} illustrates the time period required to reach equilibrium between all the ionization state. Usually, $t_{ion} \gg t_{ex}$.
- The plasma macroscopic time scale t_p characterizes the evolution of plasma parameters such as temperature and density. Similarly to t_{ion} , generally $t_p \gg t_{ex}$.

As $t_{ex} \ll t_{ion}$ and $t_{ex} \ll t_p$, the energy levels in each ionization stage can be considered in quasi-equilibrium with their ground state: $dn_j^{(z)}/dt = 0$ for $j > g$. The matrix equation 2.29 can therefore be rewritten as:

$$\frac{dn_g^{(z)}}{dt} = n_e n^{(z-1)} S_{z-1}^{eff} + n_e n^{(z+1)} \alpha_{z+1}^{eff} - n_e n^{(z)} S_z^{eff} - n_e n^{(z)} \alpha_z^{eff} \quad (2.31)$$

with S_z^{eff} and α_z^{eff} the collisional-radiative ionization and recombination coefficients, which mainly depend on T_e (and weakly on n_e) in tokamak plasmas. These coefficients take into account all the processes of equations 2.28 and 2.30 and equation 2.31 fits the description of LTE (resp: CE) for high (resp: low) electron densities. The fractional abundance of the ionization state q of species S at steady state can be obtained through iterative summation of equation 2.31:

$$f_{S,q} = \frac{n_{S,q}}{n_S} = \frac{\prod_{k=1}^{q-1} \frac{S_k}{\alpha_{k-1}}}{1 + \sum_{j=0}^{Z_S-1} \prod_{k=0}^j \frac{S_k}{\alpha_{k-1}}} \quad (2.32)$$

Equation 2.32 will be referred to as the local ionization balance, or LIB. In the framework of this thesis, the fractional abundances are obtained through a script developed in [31] using the atomic coefficients freely provided by the Atomic Database and Analysis Structure (ADAS) [32].

2.3.4 Effect of impurity transport on the equilibrium

In the section 2.3.3, the ionization equilibrium has been derived under the assumption that it is achieved in a much shorter time scale than the transport time constant. This assumption is not always valid in the case of non-fully ionized species. The population of their ground state can be affected by transport and equation 2.31 should take it into account. In order to do so, equation 2.31 should be generalized to four dimensions (time and space):

$$\frac{\partial n_g^{(z)}}{\partial t}(\vec{r}, t) = S_g^{(z)}(\vec{r}, t) + T_g^{(z)}(\vec{r}, t) \quad (2.33)$$

where $S_g^{(z)}$ is the source term of ions of charge z in ground state and contains the different coefficients of equation 2.31 as well as an external source term at the plasma edge (covering impurity injection from the plasma facing components), and $T_g^{(z)}$ is the transport term of ions of charge z in ground state.

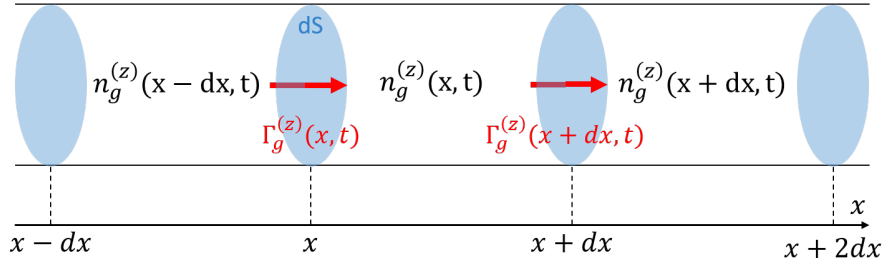


Figure 2.4 – Influence of transport on the density of ions of charge z in ground state in the case of unidirectional transport along the x direction and no source term.

In a system with unidirectional transport and a source term $S_g^{(z)} = 0$, the inventory of particles in an infinitesimal volume $dV = dS \cdot dx$ at time $t + dt$ is:

$$n_g^{(z)}(x, t + dt) \cdot dV = n_g^{(z)}(x, t) \cdot dV + \Gamma_g^{(z)}(x, t) \cdot dS \cdot dt - \Gamma_g^{(z)}(x + dx, t) \cdot dS \cdot dt \quad (2.34)$$

where $\Gamma_g^{(z)}$ is the particle flux per unit surface in $m^{-2} \cdot s^{-1}$ and is considered positive for particles moving to ascending x : $\Gamma_g^{(z)}(x, t)$ represents the transport from $x - dx$ to x . Dividing equation 2.34 by $dV \cdot dt$ and taking the limits $dV \rightarrow 0$ and $dt \rightarrow 0$ gives:

$$\frac{\partial n_g^{(z)}}{\partial t}(x, t) = \frac{\partial \Gamma_g^{(z)}}{\partial x}(x, t) \quad (2.35)$$

By generalising equation 2.35 to four dimensions, we obtain the contribution of transport to the evolution of the density:

$$\left(\frac{\partial n_g^{(z)}}{\partial t}(\vec{r}, t) \right)_{transport} = -\vec{\nabla} \cdot \vec{\Gamma}_g^{(z)}(\vec{r}, t) \quad (2.36)$$

Replacing the contribution of transport in equation 2.33 leads to the conservation equation:

$$\frac{\partial n_g^{(z)}}{\partial t}(\vec{r}, t) = S_g^{(z)}(\vec{r}, t) - \vec{\nabla} \cdot \vec{\Gamma}_g^{(z)}(\vec{r}, t) \quad (2.37)$$

2.4 Total plasma emissivity

In sections 2.2 and 2.3, the emissivity and fractional abundance of species S in ionization level z were derived. In this section, these results are combined in order to compute the total X-ray radiation emitted from the plasma.

The total emissivity from species S is obtained through summation over all its ioniza-

tion levels:

$$\varepsilon_S(h\nu) = \sum_{z=0}^Z f_{S,z} \cdot \varepsilon_{S,z}^{tot}(h\nu) = \sum_{z=0}^Z f_{S,z} (\varepsilon_{S,z}^{ff}(h\nu) + \varepsilon_{S,z}^{fb}(h\nu) + \varepsilon_{S,z}^{bb}(h\nu)) \quad (2.38)$$

with $\varepsilon(h\nu)$ the emissivity in $W \cdot m^{-3} \cdot eV^{-1}$, Z is the atomic number of species S . Substitution of the expression of ε^{ff} , ε^{fb} , and ε^{bb} from equations 2.3, 2.6 and 2.13 gives:

$$\varepsilon_S(h\nu) = n_S n_e \sum_{q=0}^Z f_{S,z} (k_{S,z}^{ff}(h\nu) + k_{S,z}^{fb}(h\nu) + k_{S,z}^{bb}(h\nu)) \quad (2.39)$$

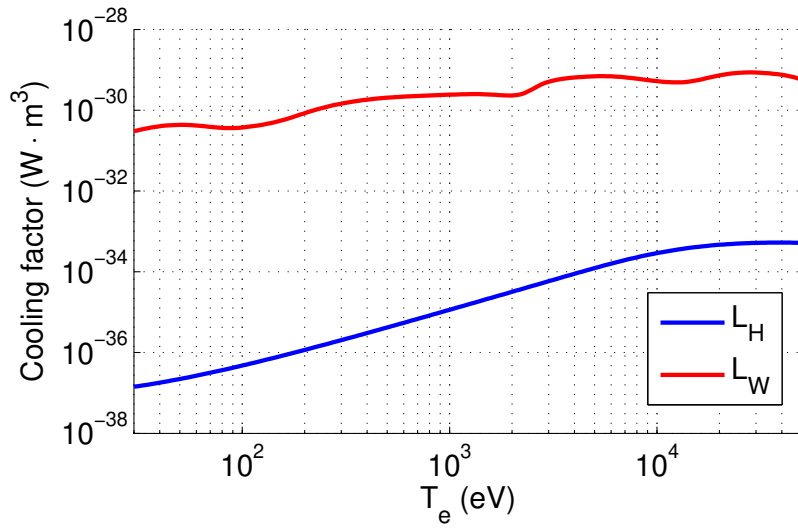


Figure 2.5 – Cooling factors of hydrogen and tungsten as a function of T_e . The W and H coefficients are taken from the open ADAS database. [32]

A radiating function $L_S(h\nu)$, in $W \cdot m^3 \cdot eV^{-1}$ can be defined such that $\varepsilon_S^{tot}(h\nu) = n_S n_e L_S(h\nu)$. Its expression is given by:

$$L_S(h\nu) = \sum_{q=0}^Z f_{S,z} (k_{S,z}^{ff}(h\nu) + k_{S,z}^{fb}(h\nu) + k_{S,z}^{bb}(h\nu)) \quad (2.40)$$

Integration over the emissivity spectrum gives:

$$\varepsilon_S = n_S n_e \int_0^\infty L_S(h\nu) d h\nu = n_S n_e L_S \quad (2.41)$$

with $L_S = \int_0^\infty L_S(h\nu) d h\nu$ the cooling factor of species S in $W \cdot m^3$.

2.4.1 X-ray emissivity on ITER

Simulation of the plasma X-ray emissivity, taking impurity transport into account, in the $[10^{-3}, 10^2]$ keV energy range has been performed in order to assess bolometer performance.[33] The parameters of the plasma are those of the ITER 15MA baseline inductive scenario ($T_e(r/a=0) \approx 25\text{keV}$ and $n_e(r/a=0) \approx 10^{20}\text{m}^{-3}$).[34] The electron temperature and density are displayed on figure 2.6.

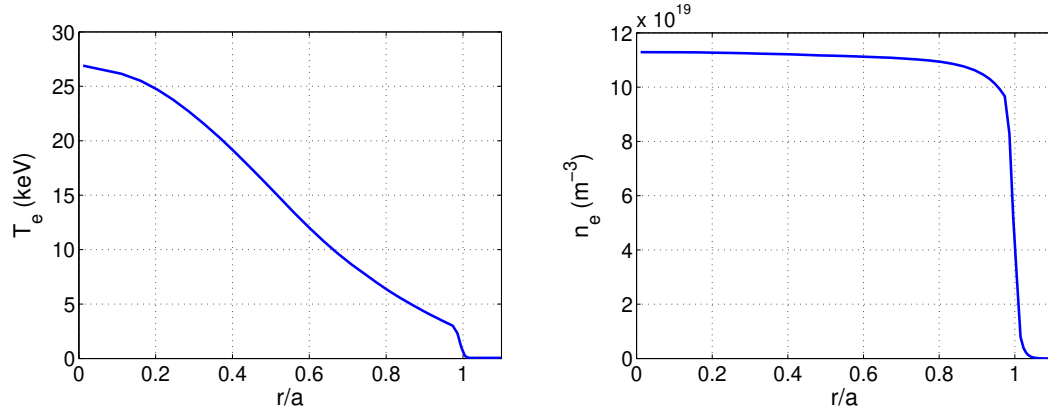


Figure 2.6 – Electron temperature (left) and density (right) profiles of the ITER 15MA baseline inductive scenario.

The mix of elements used to obtain the X-ray emissivity profile is the following:

- H: 94.626%
- Be: 1%
- Fe: 0.05%
- W: 0.001%

The impurity concentrations are chosen in order to obtain an effective atomic number $Z_{eff} \approx 1.5$ and a total radiated power in the core $P_{rad} \approx 50\text{MW}$. In the simulated scenario, the obtained values for these parameters are $Z_{eff} = 1.4990$ and $P_{rad} = 54.46\text{MW}$.

The X-ray emissivity is computed over the $[10^{-3}, 10^2]$ keV energy range, which is divided into 236 logarithmically equal energy bins, increasing in width with energy. This binning creates so-called 5% bandpass energy bins defined by: for i in $\{1, \dots, n\}$, $E_{edge} = E_{low} \cdot 1.05^i$ with $E_{low} = 1\text{eV}$ [33]. Put into words, the higher boundary of the energy bin increase by 5% from a bin to the next.

For the simulation of the emissivity, line emission was calculated using the *adas810* database[35] and predicted ITER plasma conditions were input into the SANCO impurity transport code to obtain a steady state equilibrium in the plasma core (inside the LCMS). The emissivity in the scrape-off layer is computed by using the SOLPS plasma edge simulating code.[36] The obtained emissivity profile is shown on figure 2.7.

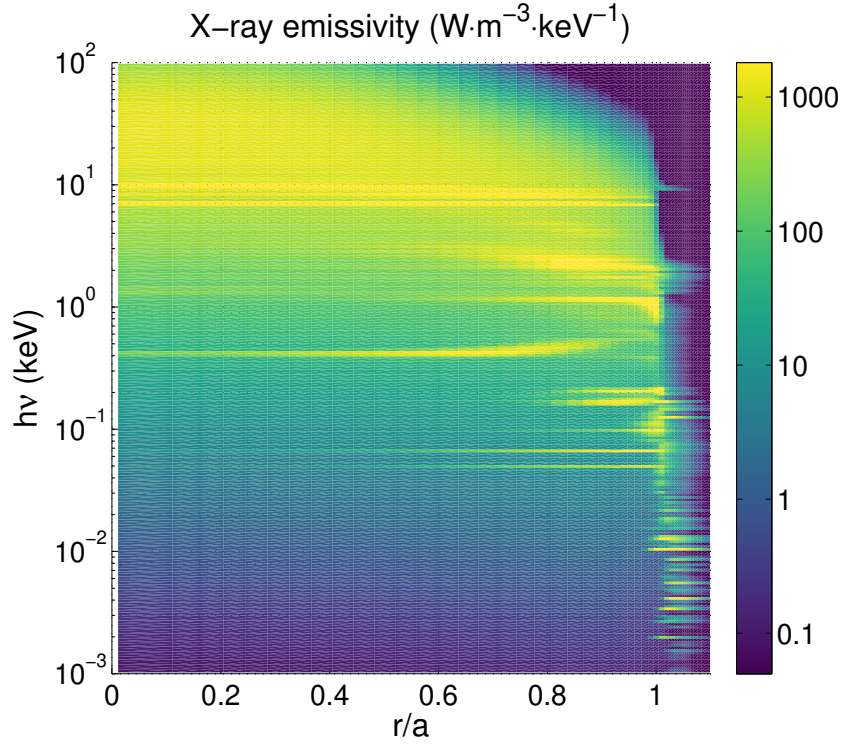


Figure 2.7 – Radiated power profile as a function of photon energy and normalized radius for the standard high power D-T scenario.

The lines observed over the whole plasma around 7 keV are due to iron and the 10 keV line results from tungsten line emission. Tungsten is also dominant in the plasma edge between 0.5 and 2 keV. The low energy ($h\nu < 500\text{eV}$) lines located in the SOL correspond to hydrogen line emission. Line radiation is added on top of the smooth continuum emission to obtain the total radiated power. The continuum is dominant at high energy ($h\nu > 10\text{keV}$).

2.4.2 Influence of impurity transport on the X-ray emissivity

A comparison between the radiated power profiles with and without taking impurity transport into account is performed. The plasma parameters used for the simulation of the emissivity are those of the ITER 15MA baseline inductive scenario. Electron temperature and density profiles are shown on figure 2.6. The results of the simulation described in section 2.4.1 (discriminated for each impurity species) are used to create the power radiated by a hydrogen plasma with $c_W = 10^{-3}\%$ of tungsten, which takes impurity transport into account.

The solving of the local ionization balance without taking impurity transport into account is performed through the use of a collisional-radiative model. The atomic data provided by the Open-ADAS database[32] is used to compute the X-ray emissivity profile. The obtained radiated power profiles are shown on figure 2.8

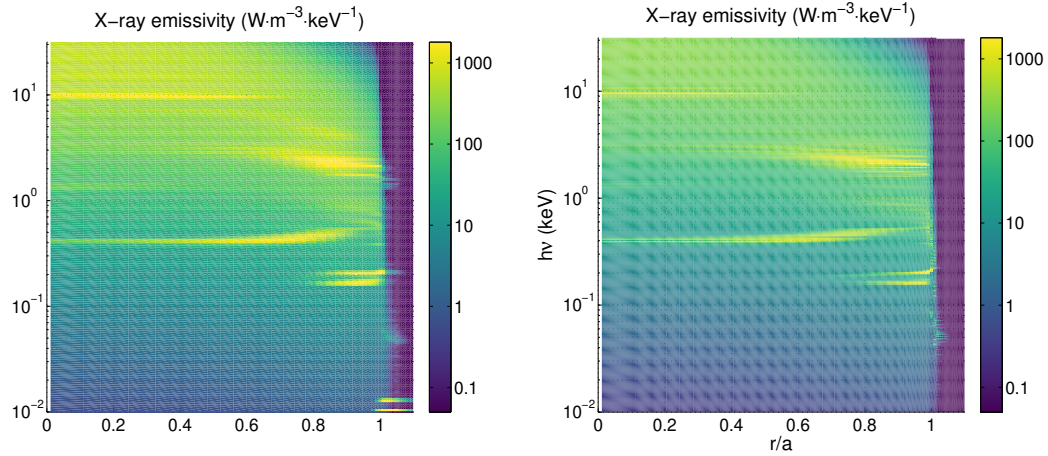


Figure 2.8 – Radiated power profile as a function of photon energy and normalized radius for the standard high power D-T scenario, in the case of a hydrogen plasma with $10^{-3}\%$ of tungsten. Left: Radiated profile with impurity transport. Right: Radiated profile without impurity transport.

The energy binning is different in both profiles: the binning for the simulation without impurity transport is finer. This explains why some lines seem wider in the left part of figure 2.8.

At the plasma edge ($0.8 < r/a < 1.1$), the radiated power profiles are similar with and without transport. The fact that the influence of impurity transport is low in this region makes sense as the plasma edge is the zone where impurities are generated in the plasma. Differences in the radiated power profile can be spotted closer to the plasma core. The simulation taking impurity transport into account yields a higher emissivity at high energy ($h\nu > 10\text{keV}$) in the whole plasma region where $r/a < 0.6$. Impurity transport leads to a widening of the region where line emission at 1.5 keV (resp: 9.5 keV) occurs: from $r/a < 0.4$ (resp: $r/a < 0.6$) to $r/a < 0.5$ (resp: $r/a < 0.8$). Outside of these differences, both radiated power profiles are very similar. As a result, simulations of the emissivity which do not include impurity transport are considered a good enough approximation of the X-ray emissivity for detection modelling in the scope of this thesis.

2.5 Extraction of plasma parameters from X-ray measurement

The plasma is transparent to X-rays, i.e. does not absorb nor deviates them, which makes X-ray radiation a very interesting quantity measurement-wise. Resonance and cut-off frequencies induced by ICRH and ECRH heating (respectively several tens of MHz and several hundreds of GHz) are located far from the X-ray range (around 10^6 THz) and do not affect X-ray propagation. This means that the X-ray measurement in

a line-of-sight does not require processing (e.g. the consideration of re-absorption in the plasma) and is simply the integration of the emissivity in the plasma volume seen by the detector convoluted by the solid angle of the detector as seen by the plasma. As seen in equations 2.3, 2.6 and 2.13, X-ray emissivity conveys information about various plasma parameters such as the electron temperature and density, the impurity densities (and therefore the impurity transport).

2.5.1 Impurity density

In the scope of X-ray measurement, the emissivity obtained in section 2.4 must be filtered by the spectral response of the detector η :

$$\varepsilon_S^\eta = n_S n_e \int_0^\infty \eta(h\nu) L_S(h\nu) d h\nu = n_S n_e L_S^\eta \quad (2.42)$$

with $L_S^\eta = \int_0^\infty \eta(h\nu) L_S(h\nu) d h\nu$ the radiating function of species S , in $W \cdot m^3$, convoluted by the spectral response of the detector. L_S (and therefore L_S^η) mainly depend on T_e and the transport of species S .

In the case of a single element plasma of species S , the X-ray measurement allows the computation of the density n_S from equation 2.42:

$$n_S = \frac{\varepsilon^\eta}{n_e L_S^\eta} \quad (2.43)$$

In the case of a plasma with several species, the measured X-ray emissivity becomes:

$$\varepsilon^\eta = n_e \sum_S n_S L_S^\eta \quad (2.44)$$

In a hydrogen and tungsten plasma with $n_H \gg n_W$, the quasi-neutrality gives $n_H = n_e$. Therefore the application of equation 2.44 to such a plasma gives:

$$\varepsilon^\eta = n_e n_W L_W^\eta + n_e^2 L_H^\eta \quad (2.45)$$

Which leads to:

$$n_W = \frac{\varepsilon^\eta - n_e^2 L_H^\eta}{n_e L_W^\eta} \quad (2.46)$$

The result of equation 2.46 is of great importance for X-ray diagnosticians as it allows the estimation of impurity density from emissivity measurement.

2.5.2 Impurity transport coefficients

Diffusion and convection are the main sources of transport in a plasma. In the case of a tokamak plasma, the transport around the magnetic field lines is dominant in comparison with radial transport. In the absence of radial asymmetries, the impurity

density can be considered constant over the magnetic field lines. Therefore, only radial transport is of interest, and the radial flux of impurities for species S is given by:

$$\vec{\Gamma}_S(r, t) = -D(r)\vec{\nabla}_r n_S(r, t) + n_S(r, t)V(r) \quad (2.47)$$

where $D(r)$ is the diffusive coefficient in $m^2 \cdot s^{-1}$, $V(r)$ is the convection coefficient in $m \cdot s^{-1}$ and $\vec{\nabla}_r$ denotes the radial gradient: $\vec{\nabla}_r f = \partial f / \partial r \cdot \vec{r} / \|r\|$. The characteristic variation time of the D and V transport coefficients is larger than the characteristic variation time of the density, these coefficients are therefore considered constant in equation 2.47.

The radial flux of impurities is defined by:

$$\vec{\Gamma}_S(r, t) = \frac{1}{r} \int_0^r \frac{\partial n_S}{\partial t}(r', t) r' dr' \quad (2.48)$$

Equation 2.48 allows the estimation of the flux of impurities from the computation of the impurity density only, which is obtained in equation 2.46. Equation 2.47 divided by $n_S(r, t)$ gives:

$$\frac{\vec{\Gamma}_S(r, t)}{n_S(r, t)} = -D(r) \frac{\vec{\nabla}_r n_S(r, t)}{n_S(r, t)} + V(r) \quad (2.49)$$

A linear fit of $\vec{\Gamma}_S(r, t)/n_S(r, t)$ with respect to $\vec{\nabla}_r n_S(r, t)/n_S(r, t)$ gives the transport coefficients: $D(r)$ is the slope of the straight line and $V(r)$ its intercept.

2.5.3 Electron temperature

Line radiation in a plasma leads to photon emission up to around 10 keV. At higher energies, the plasma X-ray emissivity only originates from Bremsstrahlung or radiative recombination emission. The total emissivity can be written as:

$$\varepsilon^{tot} = \varepsilon^{fb} + \varepsilon^{ff} = C^{fb} G^{fb} \exp\left(-\frac{h\nu}{T_e}\right) + C^{ff} G^{ff} \exp\left(-\frac{h\nu}{T_e}\right) \quad (2.50)$$

where C^{ff} and C^{fb} are constant with energy, and G^{ff} and G^{fb} denote the Gaunt factors. The Gaunt factors are close to unity in the X-ray range, and their variation with energy can be neglected. The total emissivity can therefore be rewritten as: $\varepsilon^{tot} = C^{tot} \cdot \exp\left(-\frac{h\nu}{T_e}\right)$. Its derivative with respect to the photon energy gives:

$$\frac{d\varepsilon^{tot}}{dh\nu} = -\frac{C^{tot}}{T_e} \exp\left(-\frac{h\nu}{T_e}\right) = -\frac{\varepsilon^{tot}}{T_e} \quad (2.51)$$

The electron temperature is therefore given as:

$$T_e = -\varepsilon^{tot} \frac{dh\nu}{d\varepsilon^{tot}} \quad (2.52)$$

The estimation of the electron temperature from X-ray measurement requires the knowledge of the emissivity spectrum in the continuous spectrum region. Therefore, a spectrally resolved X-ray detector is mandatory for such application.

3 X-ray measurement

Sommaire

3.1	Photodiodes	69
3.1.1	Semiconductor photodiodes	69
3.1.2	Vacuum photodiodes	72
3.2	Gas detectors	74
3.2.1	Ionization chambers	74
3.2.2	Multi-anodes Low Voltage Ionization Chamber	77
3.2.3	Gas Electron Multipliers	79
3.2.4	X-rays detectors for ITER nuclear phase	80
3.3	X-ray tomography	81
3.3.1	Overview	81
3.3.2	Minimum Fisher Information method	82
3.4	Accuracy of the X-ray emissivity calculation tool	83

3.1 Photodiodes

A photodiode is a device which converts incoming light into an electrical current. In the scope of X-ray measurements, two technologies of photodiodes are of interest: semi-conductor photodiodes and vacuum photodiodes.

3.1.1 Semiconductor photodiodes

Semiconductor photodiodes detect photons in the soft X-ray range through photo-electric effect. Si-based semiconductors are the most commonly used in SXR detectors. Semiconductor atoms exhibit an outermost layer composed of four electrons. When assembled together, they form a crystal in which these four electrons are shared with neighbouring atoms through covalent bonding. The outermost layer is then populated by eight electrons, which form the conduction band. The electrons of the lower layers (which are fully occupied) compose the so-called valence band. Charge migration occurs in the conduction band through the movement of electrons and holes (absence of electron) and generate an electrical current. The flows of electrons and holes have opposite directions.

The difference in energy potential between the conduction and valence bands defines the conducting properties of the crystal: a large gap gives insulating properties (e.g.

diamond crystal with more than 5 eV of gap) and smaller gaps lead to semiconductors (e.g. silicon exhibits a gap around 1.2 eV). Pure semiconductors typically display an electrical conductivity which is lower than conductors and higher than insulators. The value of the gap diminishes with temperature, which increases the amount of electrons that can be excited into the conduction band. Temperature can therefore significantly increase the conducting properties of the semiconductor.

The energy level of the electron population at equilibrium is called the Fermi level. In pure semiconductors, widely referred to as intrinsic semiconductors, the Fermi level is close to the average of the energy levels of the conduction and valence bands. Substituting silicon atoms by elements which do not possess four electrons on their outermost layer can modify the Fermi level. This process is called doping. If the added impurity has more electrons in its outermost layer, the Fermi level is moved closer to the conduction band. The Si crystal is called n-doped, where n stands for negatively. The Si crystal can be p-doped (p stands for positively) if the added impurity has less electrons in its outermost layer, and the Fermi level is moved closer to the valence band.

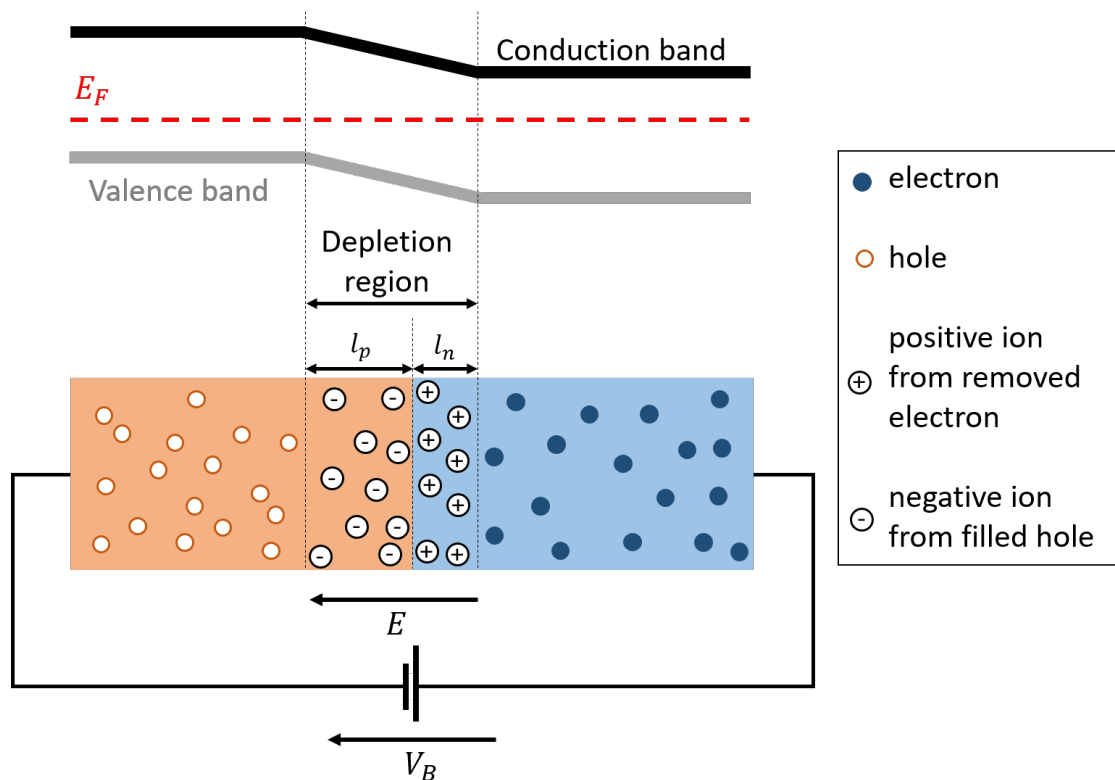


Figure 3.1 – Sketch of a semiconductor p-n junction, with bias voltage V_B . The upper part of the figure shows the energy of the valence and conduction bands and the lower part shows a schematic representation of the p-n junction.

P-doped crystals and n-doped crystals can be joined together in order to form a p-n junction. Upon connection, the system is not at equilibrium as there is a dis-

continuity in the Fermi levels of both semiconductors. The concentration gradient in charge carriers leads to a diffusion of electrons (resp: holes) from the n-doped (resp: p-doped) semiconductor towards the p-doped (resp: n-doped) semiconductor. The region of the n-doped (resp: p-doped) semiconductor close to the junction gets therefore charged positively (resp: negatively) and an electric potential arises from charge migration. The electric field compensates the movement of ions and electrons: an equilibrium state is reached. The region where charge migration occurred is called the depletion region as it is the region with the lowest density of charge carriers. In the scope of soft x-ray measurement, p-n and p-i-n (i stands for intrinsic) junctions of silicon are the most commonly used semiconductors. Photons are absorbed in the depletion region and excite electrons in the process, leading to the production of a photocurrent.

A bias voltage can be applied to the junction, as shown on figure 3.1. In SXR measurement a negative bias $V_B < 0$ is used in order to increase the electric potential of the depletion region. This additional potential affects the size of the depletion region which expands with the square root of the bias voltage [37, 38]. This property is of great importance as the depletion region is the sensitive region of the diode, and therefore its sensitivity is directly linked to its width.

In the absence of photon flux, a biased p-n junction produces a current called the dark current. This current comes from electrons of the p-doped region getting through the junction. Prior to their crossing, these electrons have been excited through thermal effects. The dark current is mostly dependent on the diode temperature, but also on the bias voltage.

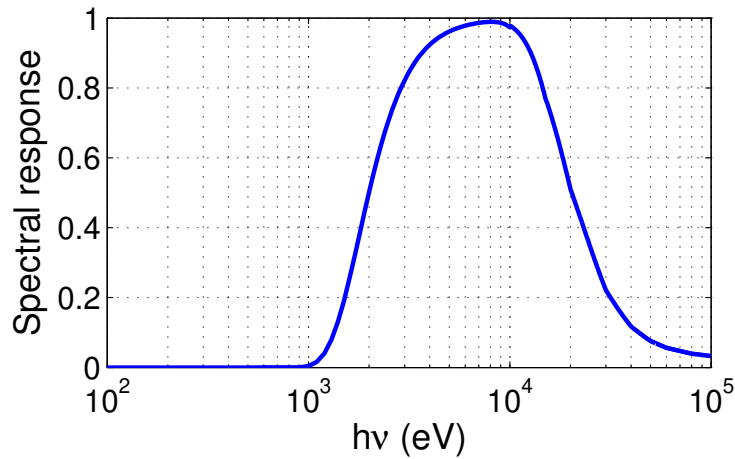


Figure 3.2 – Spectral response of the Si semiconducting diodes used on the tokamak WEST. The filter consists of a beryllium window of $50\mu m$.

Semiconducting diodes are used on most tokamaks for SXR measurement [39–43]. They absorb photons up to around 20 keV (see figure 3.2). Their lower limit of their detection range depends on the filter placed in front of the detector. The

advantages of Si diodes are their relatively low cost, their ease of use and the fact that their spectral response is quite sharp and localised. However semiconducting diodes are not very resilient to radiation as n-doped Si turns into p-doped under neutron irradiation [44–46], and p-n junctions operate in current mode and cannot count photons nor determine the incoming X-ray spectrum.

The addition of an intrinsic semiconductor layer at the junction, creating a p-i-n junction, allows a significant improvement in the response time. The electric field of the junction extends to the intrinsic layer, increasing the velocity of the charge carriers. In such a configuration Si diodes can perform photon counting, provided that the acquisition system is fast enough (e.g. Multi-channel analysers). [47]

Energy discriminated have been achieved in Multi-Energy X-ray cameras through the use of different filters and therefore different cut-off energy thresholds. Locating the filters in several pinholes leading to overlapping tangential lines-of-sights has been performed successfully in the tokamaks NSTX [48] and EAST. [49] With the progress of technology, complex 2D arrays of photodiode pixels have been developed with each pixel having a tunable energy threshold. The small size of the pixels allows the assumption that the incoming flux is similar on all the pixels in a given direction, lines for example. Each line therefore measures a different photon spectrum which can be deconvolved through the use of different energy thresholds. Such detectors are called Multi-Energy X-ray Cameras (ME-X) and have been tested on the Madison Symmetric Torus. [50] Due to the very high amount of pixels (up to several million pixels), these ME-X cameras have very good spectral and spatial resolutions.

3.1.2 Vacuum photodiodes

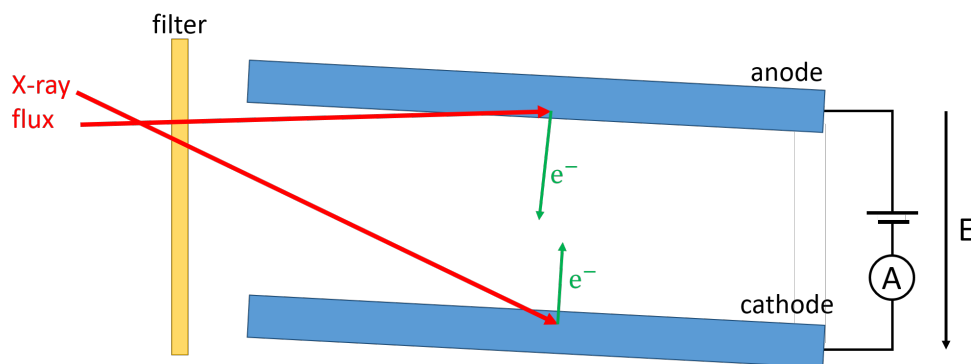


Figure 3.3 – Schematic representation of a vacuum photodiode.

Vacuum Photoelectric Detectors (VPD) have been investigated in the scope of X-ray measurement as a radiation-tolerant alternative to semiconducting photodiodes. They are also based on the generation of electrons through photoelectric effect. A vacuum photodiode is made of facing electrodes (cathode and anode). Under X-ray irradiation, two electron fluxes are created: from the anode to the cathode and from

the cathode to the anode, as depicted in figure 3.3. If these two electron flows are different, an electric current starts to flow between the electrodes and can be measured. High Z materials such as tungsten ($Z = 74$) or tantalum ($Z = 73$) have a high photon to electron conversion efficiency. However, the mean free path of electrons in such materials is much smaller than the X-ray penetration depth. In order for the electron to escape the electrode and participate to the electron flux, it must be generated close to the limit of the electrode. This is achieved if photon flux must have a grazing incidence angle ($2 - 5^\circ$). [51] Under such incidence angle, the photon can penetrate in the electrode while remaining close enough to vacuum so that the generated electrons can escape the electrode.

The VPD measures a current which is the difference between the two opposite electron flows (from the anode to the cathode and vice versa). With similar electrodes (same material) it is necessary to apply an electric field between the electrodes in order to ensure that the electron flows are different. When the electrodes are at different potentials, the electric field creates a force pushing electrons towards the anode. Electrons leaving the cathode are accelerated towards the anode, and those leaving the anode are pushed back towards it. If these electrons have a high enough velocity they can overcome the electric field and reach the cathode, but the flux of electrons from anode to cathode is overall greatly reduced.

The other way to force the electron flows to be different is the use of different materials for the electrodes. Each electrode would therefore have a different photon to electron conversion efficiency. As a result, the electrode with the highest efficiency would generate a higher electron flux. Such VPD are referred to as bimetallic vacuum photodiodes.

Bimetallic vacuum photodiodes can be designed to be resilient to gamma radiation. X-rays generate slow photoelectrons ($E_{ink} < 50\text{eV}$) whereas gamma radiation generates a flux of fast electrons ($E_{kin} > 50\text{eV}$). A thin layer (several tens of nm) of tantalum (Ta) is enough to absorb all the slow flux of photoelectrons. By coating a beryllium electrode with such layer, one can ensure that the flow of electrons generated by X-rays is fully absorbed and does not leave the electrode. The coated electrode therefore generates a flow of electrons only originating from gamma radiation, while the non-coated electrode generates a flux of electrons coming from both X-ray and gamma-rays. The current measured by the VPD being the difference of the electron fluxes, the gamma-generated electron flows compensate each other and the collected current only contains information on the X-ray flux.

Vacuum photodiodes are an interesting alternative to semiconducting diodes through their ability to separate gamma background from X-ray induced current. The fact that they are made of metal makes them more resilient to neutron and gamma radiation than Si detectors. Even though the X-ray sensitivity of VPD is limited both in terms of energy range (VPD are transparent to photons of $h\nu > 10\text{keV}$) and amplitude, VPD could be of interest for ITER. However, they still exhibit aging effects under high irradiation fluxes and their internal efficiency is expected to decrease during the ITER nuclear phase. [52] In this regard, detectors which allow easy replacement of the

detection volume are better candidates for tokamaks such as ITER and DEMO.

3.2 Gas detectors

Gas-filled detectors are based on the photoionization of a gas by incident radiation and are widely used in various devices such as particle accelerators, nuclear reactors, tokamaks and in radiobiology research centers. Due to their large amounts of applications, a variety of different technologies have been developed: proportional counters [53], Geiger-Muller counters [54], multi-wire proportional chambers [55], microstrip gas chambers [56], micro-mesh gaseous structure (MICROMEGAS) [57] or gas electron multiplier (GEM).[58] All these detectors are based on the concept of the ionization chamber. In this section, the principle of the ionization chamber is described as well as two detectors derived from it which are of interest in the scope of X-ray measurement on ITER: the multi-anodes low voltage ionization chamber (MA-LVIC) and the gas electron multiplier (GEM).

3.2.1 Ionization chambers

The ionization chamber is the most elementary technology of gas detectors. It is simply made of a gas chamber and two electrodes, in addition to eventual filters which can be added in order to set an energy threshold to the detector. The transport of a flux of particles through the gas leads to the ionization of atoms of gas. In the presence of an electric field between the electrodes, the charges created are transported to the electrodes: towards the anode for electrons and the cathode for ions.

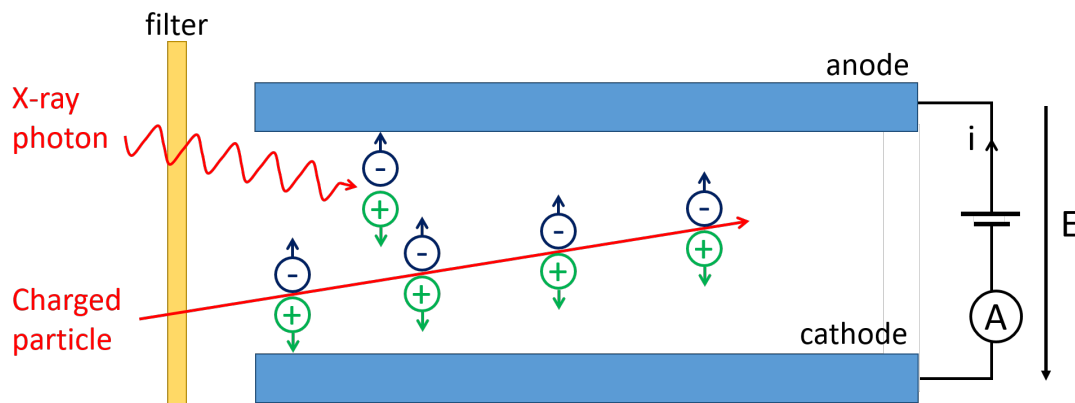


Figure 3.4 – Schematic representation of an ionization chamber.

Heavy charged particles continuously lose momentum in the gas by ionizing atoms in the gas in a straight line. Due to their electric charge the straight line is slowly shifted towards an electrode (the anode for negatively charged ions and the cathode for positively charged ions). Light charged particles are transported towards the

electrode corresponding to their electric charge and ionize the gas in the process. The use of ionization chambers in the scope of this thesis is focused on X-ray photons, charged particles detection is therefore not studied. X-ray photons mostly interact with the gas through photoionization (see section 4.2), generating an electron and an ion in the process. Photons are neutral particles and their trajectory is therefore not affected by the electric field in the chamber.

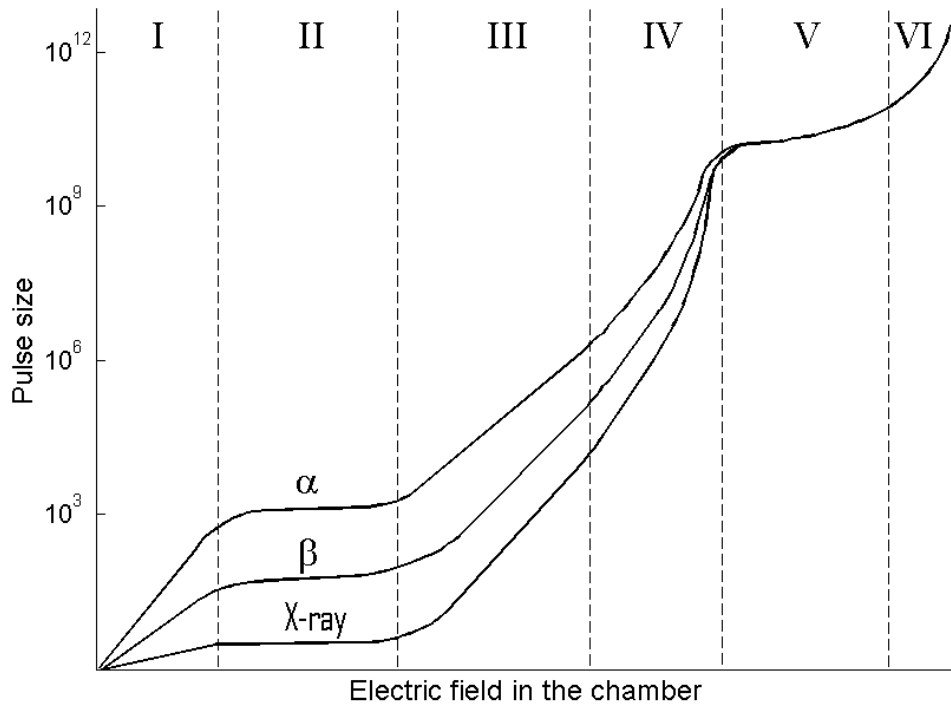


Figure 3.5 – Pulse size (number of charges collected) as a function of the electric field in a chamber irradiated by α , β , and X-ray particles. The different regions of operations of the detector are as follows: recombination region (I), ionization chamber region (II), proportional region (III), limited proportionality region (IV), Geiger-Müller region (V) and continuous discharge region (VI). Figure reprinted from [59] with data from [60]

The electric field in the gas chamber affects the amount of charges collected. Under a given threshold, the transit time is high enough for recombination to take place and therefore the measured current does not contain all the primary generated charge. This is the recombination region of figure 3.5. If the electric field allows collection of all the primary charges but is too weak for electron and ion avalanches, the detector is in the Ionization chamber regime. In ionization chambers, the amount of charge collected due to the detection of a particle is directly linked to the energy of said particle. Stronger electric fields lead to charge multiplication during transit. Primary and

secondary charges are collected, and the amount of current generated is proportional to both the electric field and the particle energy. This regime is observed in GEM foils and corresponds to the proportional region of figure 3.5. For a high enough voltage the secondary ion cloud becomes so massive that it is locally shielding the electric field and non linear effects appear and the proportionality between energy and current becomes limited, hence the name of the regime: the limited proportionality region. With further increase of the voltage, the positive ion cloud increases until it reduces the electric field below the point at which charge multiplication takes place. As a result the amount of collected charges is constant for all particle energies. This is the regime used in Geiger-Müller counters. If the electric field is increased further, continuous discharges are observed in the gas independently of the impact of particles. This is the continuous discharge region.

In the scope of X-ray measurement in radiative environment, ionization chambers have the advantage that the detection volume can be replaced easily and that the detection does not occur in a solid material with a lattice which can be damaged by irradiation. The simplicity of the ionization chamber design therefore grants it a fairly high resilience to radiation. That resilience can be improved by decrease the inter-electrodes distance, thus diminishing the required voltage to reach the ionization chamber regime. This allows the detection volume to be divided into many pixels as depicted in figure 3.6, improving the spatial resolution of the system. Such detectors are called Low Voltage Ionization Chambers and have been investigated for X-ray measurement on ITER. [23, 24, 61] The downsides of the LVIC reside on the low amount of charge collected which limits the operation of the detector to current mode. As a result it is not possible to extract information on the energy of the measurement photon and energy discrimination can therefore not be performed with LVIC.

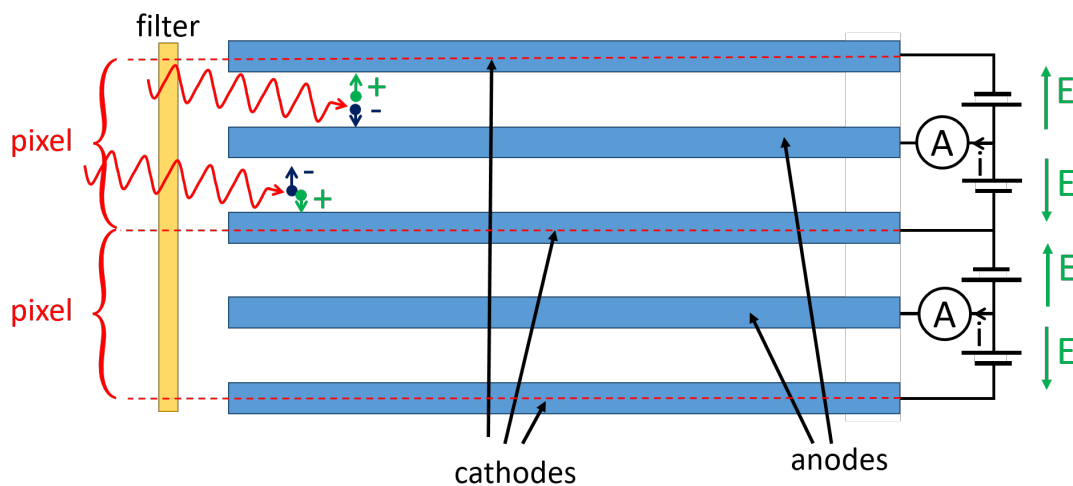


Figure 3.6 – Schematic representation of two pixels of a LVIC.

3.2.2 Multi-anodes Low Voltage Ionization Chamber

In the scope of this thesis, the possibility of spectral deconvolution using LVIC has been studied. However the LVIC as presented in the previous section does not allow such feature. A modification of the detector design is therefore mandatory in order to extract information on the energy distribution of the incident X-ray flux. [62] proposes a modulation of gas detectors in order to allow energy discrimination. The principle is based on the fact that the penetration of photons in gas increases with their energy, i.e. high energy photons go further in the detector. This can be observed for argon and xenon on figure 3.7.

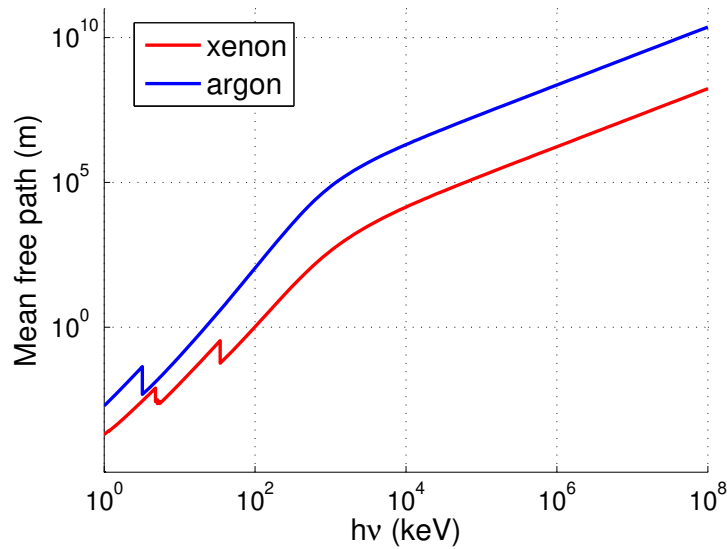


Figure 3.7 – Mean free path as a function of energy for photons in argon and xenon at $T = 300K$ and $P = 1\text{ bar}$. Cross-sections data was extracted from the NIST XCOM database [63].

This approach can be used for the LVIC by splitting the anode into several smaller anodes, thus dividing the detection volume into sub-chambers. Such detectors will be referred to as Multi-Anodes Low Voltage Ionization Chambers (MA-LVIC). The sub-chambers consist of the volume between the corresponding anode and the cathode, as depicted on figure 3.8. In order to simplify visualization and modelling the MA-LVIC is represented as a classic ionization chamber (as opposed to the representation of the LVIC from figure 3.6) with an additional anode in the scope of this work. In this thesis, the sub-chambers are numbered as they are encountered by the photons while progressing inside the detection volume: the first sub-chamber will be the first volume of gas penetrated by the X-ray flux, and so on. The spectral response of the

i-th sub-chamber is therefore expressed as:

$$\eta_i(h\nu) = T(h\nu) \cdot A_i(h\nu) \cdot \prod_{k=1}^{i-1} (1 - A_k(h\nu)) \quad (3.1)$$

where $h\nu$ is the photon energy, T is the coefficient of transmission through the filter, and A_i is the coefficient of absorption in the i-th subchamber.

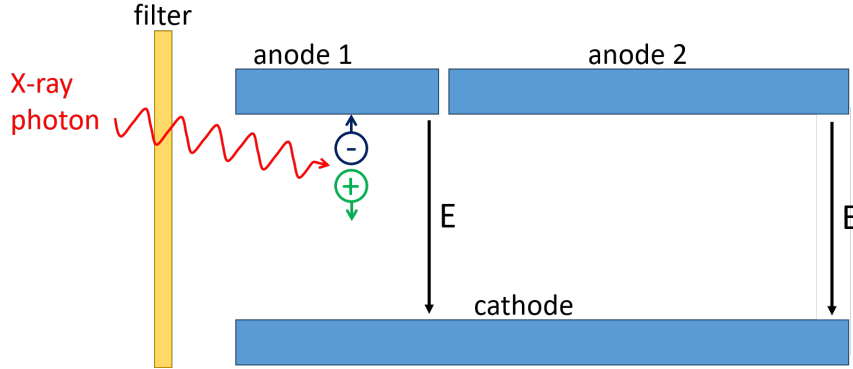


Figure 3.8 – Schematic representation of a MA-LVIC with two anodes.

The idea underlying behind this detector is the fact that as low energy photons are absorbed in the first sub-chamber, the photon flux entering the second sub-chamber is shifted towards higher energies. Therefore the spectral response of the sub-chambers are shifted towards higher energies as well. The current measured by each sub-chamber can be deconvoluted in order to give spectral information on the incoming X-ray flux.

If all the sub-chambers have the same depth (i.e. the anodes have the same length), then $\eta_{i+1}(h\nu) < \eta_i(h\nu)$ as $(1 - A_i(h\nu)) < 1$. The lower limit of the range of detection is indeed shifted towards higher energies but the spectral response of the sub-chambers decreases, leading to a smaller amount of collected charges. Increasing sub-chambers lengths can lead to an improvement of the high energy spectral response from a sub-chamber to the next. Using properly scaled anode sizes can therefore combine the shift of the lower energy threshold to an increase of the detection probability at high energy, as shown in figure 3.9.

Thanks to the different spectral response of each sub-chamber, the currents collected by each anode can be used to deconvolute the photon spectrum. In these conditions, spectral deconvolution is an ill-posed inversion problem as it aims at reconstructing a continuous spectrum from a finite amount of measurements. A method for its resolution is presented in section 8.1.

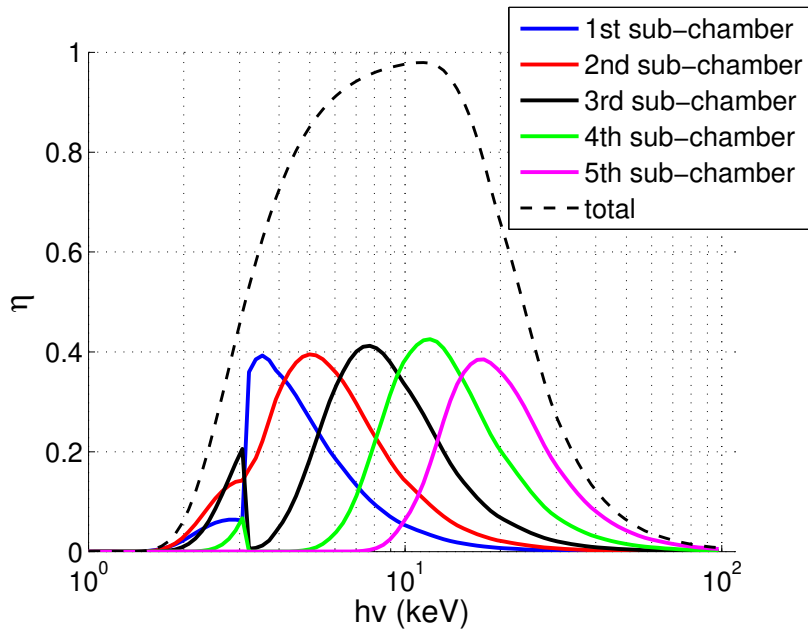


Figure 3.9 – Spectral response for an argon-filled LVIC with five anodes. The length pressure products of the sub-chambers are respectively 5, 15, 50, 175, and 500 $mm \cdot atm$ and the filter consists of 200 μm of beryllium.

3.2.3 Gas Electron Multipliers

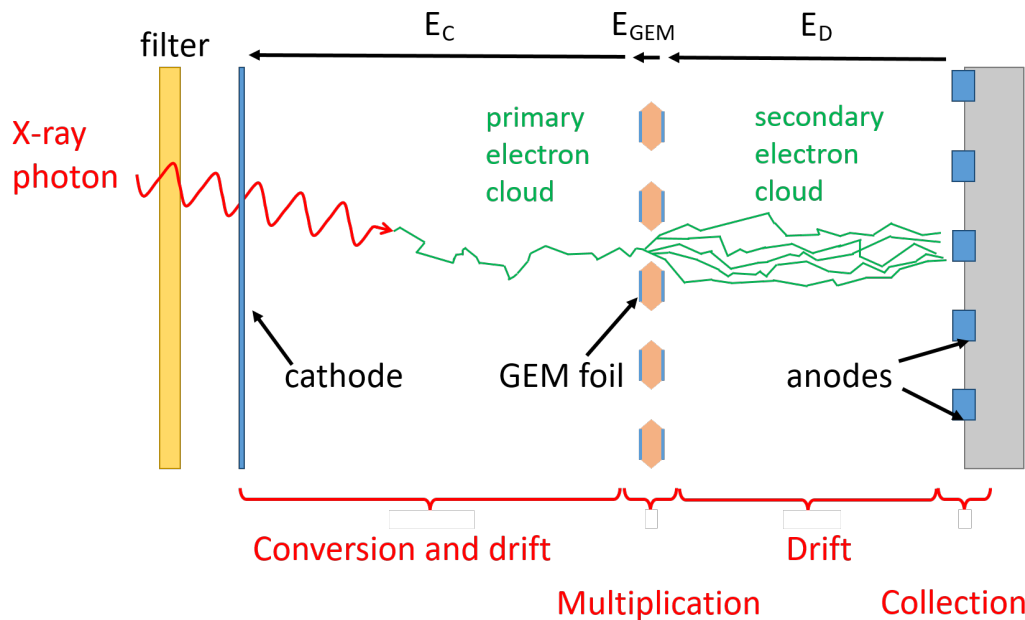


Figure 3.10 – Schematic representation of a GEM detector with one GEM foil.

Gas Electron Multipliers (GEM) have been developed in the late nineteen nineties at CERN [58]. It combines the regions II and III of figure 3.5: primary charges are generated in a first part of the detector (the drift chamber) and transported through one or more multiplication stages, referred to as GEM foils, before being collected on an anode. The amount of charge collected is proportional to the energy of the incident photon. Spatial discrimination can be achieved through pixelization the anode plan into an array or a 2D matrix, as displayed on figure 3.10.

The GEM foil is a copper-clad micro-perforated kapton foil which is several tens of microns wide. Conical micro-holes, of dimensions close to the foil width, allow the passage of electrons through the foil. A high voltage applied between the copper layers of the foil creates a strong electric field in the holes, leading to electrons avalanching as they pass through.

The most widespread version of the GEM is the triple GEM which contains three GEM foils. The cloud of electrons is therefore multiplied successively, allowing the collection of a large amount of charges. The electric field in the GEM holes is of the order of $E_{GEM} \approx 50 - 100 \text{ kV} \cdot \text{cm}^{-1}$. A voltage of several hundreds volts is required for such an electric field. In the regions of drift and/or conversion, the electric field should only be high enough to transport the electrons to the anodes without recombination (region II of figure 3.5) and a couple $\text{kV} \cdot \text{cm}^{-1}$ is enough.

Noble gases such as argon offer a good spectral response in the SXR region but are limited when it comes to electron avalanching. The addition of a quenching gas such as CO_2 is necessary for the noble gas-filled GEM in order to obtain sufficient charge multiplication. In such conditions and with proper electronics, the triple GEM the amount of collected charge and the acquisition speed of the detector are high enough to work in photon-counting mode with a discrimination on the photon energy. More detailed descriptions of the triple GEM can be found in [58, 64–66].

3.2.4 X-rays detectors for ITER nuclear phase

This section sums up the overview of the different detectors available for X-ray measurement by comparing them in the scope of using them on ITER during its nuclear phase.

The most widespread X-ray detectors on tokamaks are semiconductor diodes. They benefit from a simple design and are easy to operate, without requiring high voltage. However semiconductor photodiodes have a slow time response which limits them to current mode, thus energy discrimination cannot be performed with semiconductor photodiodes. Their sensitivity to X-ray photons is fairly low and limited to the SXR range. In highly radiative environments, the aging of p-n and p-i-n junctions is problematic and their detection properties (sensitivity, response time, dark current, ...) change with time under irradiation.

Vacuum photodiodes can be considered as a more radiation-resilient version of semiconductor diodes. However, they also exhibit a low sensitivity and slow time response and therefore do not give any information on the energy distribution of the incoming

flux. Their size limits the spatial resolution of the detection system.

Gas detectors are a promising alternative to photodiodes radiation-wise. Their renewable detection volume means that only the solid components of the detector (chamber, electrodes, GEM foils) will be subject to aging. The sensitivity, gain and time response of the detector will not be affected by their radiative environment. In this regard, LVIC and MA-LVIC are more interesting in the fact that several tens of volts are enough for photon detection [23] and therefore the amplifiers can be located several tens of meters away from the detector. On the other side, GEM detectors require several hundreds of volts which means that the amplifiers have to be located less than ten meters away from the GEM. Polycapillary optics could be considered in order to carry the X-ray flux to the detector, allowing the detector itself to be removed from the vicinity of the plasma. [67, 68] This option is only stated for informative purposes and has not been studied in the context of this thesis. In comparison with photodiodes, gas detectors exhibit a high sensitivity to X-ray photons. That sensitivity can be tuned through the pressure and dimensions of the detector. However, the handling of the gas adds a complexity which is not present with semiconductors. The LVIC is the most simple gas detector considered for ITER X-ray measurement but does not allow photon counting mode (due to the low amount of collected charges) nor energy discrimination. However the MA-LVIC, although it does not allow photon counting, can deconvolute the incident X-ray spectrum when coupled to the adequate inversion method. [69] Both the GEM, the LVIC and the MA-LVIC have demonstrated their tomographic capabilities through experiments and/or simulation. [24, 66] Considering these elements, this thesis will focus on the capabilities of the LVIC on ITER for spectrally-integrated X-ray measurement and will investigate the possibility to use the MA-LVIC for spectrally-resolved X-ray measurement on ITER.

3.3 X-ray tomography

Tomography is a technique used for imaging planar fields from a finite amount of measurements. It allows the reconstruction of the section of objects which cannot be accessed easily such as body parts, fragile fossils or the local X-ray emissivity in a tokamak plasma. Tomographic methods are widely used in medicine (e.g. magnetic resonance imaging [70], X-ray computed tomography [71]), archaeology (synchrotron X-ray tomographic microscopy [72]), and in tokamaks (e.g. X-rays [39], neutrons). In this section, a brief overview of tomography is given followed by a description of the method used for tomography in the scope of this thesis.

3.3.1 Overview

In X-ray tomography, the measurements are line-integrated through a poloidal cross-section of the tokamak and are given by the Radon transform [73, 74] of the 2D plasma X-ray emissivity. Tomography aims at inverting this process in order to retrieve

the local emissivity profile from line-integrated measurements. Due to the limited amount of detectors, this problem does not have a unique solution (as illustrated on figure 3.11) and inversion of the Radon transform cannot be performed. In the presence of experimental noise on the measurement, tomographic inversion is an ill-posed problem with regards to Hadamard's definition of a well-posed problem [75].

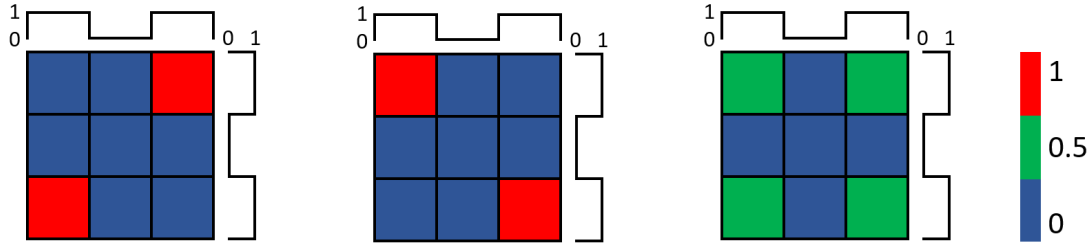


Figure 3.11 – Possible solutions to a tomographic inversion in a 3x3 pixels space with 6 line-integrated measurements in the horizontal and vertical directions.

In order to compute the plasma X-ray emissivity profile from line-integrated measurements, inversion methods limit the solution space through *a priori* information and constraints based on physical knowledge of the X-ray emissivity in tokamaks. Various methods can be considered for such inversions. The most simple is the Abel inversion [76], which assumes that the plasma emissivity is poloidally symmetric. This method is not applicable to X-ray tomography on tokamaks as poloidal asymmetries can occur. More advanced methods such as the Fourier-Bessel [77], the Tikhonov regularization [78], the Minimum Fisher Information (MFI) [79], Bayesian techniques [80–82] or the Total Variation method [83–86] can be applied to tokamaks. None of these methods were developed in the scope of this thesis, they are cited for informative purposes.

3.3.2 Minimum Fisher Information method

The X-ray tomographic inversions presented in this thesis are obtained using the tomographic algorithm implemented for SXR measurement on the WEST tokamak which is based on the Minimum Fisher Information method [65, 66]. Tomographic algorithms aim at finding the emissivity ε which balances best the fitting of the measurement m and of the added constraints which ensure that the solution has a physical meaning. The fitting of the measurement is described by χ^2 :

$$\chi^2(\varepsilon) = {}^t(m - f(\varepsilon)) \cdot (m - f(\varepsilon)) \quad (3.2)$$

where ${}^t A$ is the transpose of matrix A and f is the mathematical function converting the 2D X-ray emissivity into line-integrated measurement. The additional constraints are added through the so-called regularization of the system [87], the regularization

term is called $R(\varepsilon)$. The solution is given by:

$$\varepsilon_0 = \arg \min_{\varepsilon} (\chi^2(\varepsilon) + \lambda R(\varepsilon)) \quad (3.3)$$

where λ is the regularization parameter which is determined by the user. Different methods for λ determination can be found in [31, 88, 89]. The MFI method regularizes the system by minimising the Fisher information, which describes the amount of information carried by the emissivity and is given by:

$$I_F(\varepsilon) = \int \frac{1}{\varepsilon(r)} \left(\frac{d\varepsilon(r)}{dr} \right)^2 dr \quad (3.4)$$

With such regularization, the solution of equation 3.3 is given by:

$$\varepsilon_0 = \left({}^t F F + \lambda \cdot \varepsilon_0 \cdot {}^t \nabla \cdot W \cdot \nabla \cdot \varepsilon_0 \right)^{-1} \cdot {}^t F \cdot m \quad (3.5)$$

where F is the matrix corresponding to the f function of equation 3.2, ∇ is a discrete approximation of the gradient, $W = \text{diag}(1/\min(\varepsilon_0, \varepsilon_{\min}))$ is the ponderation matrix. The ponderation imposes a gradient smoothness which decreases with the emissivity: the smoothing constraint is high in the regions where the emissivity is low (the plasma edge in our case) but decreases in high emissivity regions (e.g the plasma core). It can be noticed in equation 3.5 that the solution computation of ε_0 requires its prior knowledge. Iterative algorithms are used to get around that problem: the $W^{(k)}$ matrix used to compute the emissivity in the k -th iteration $\varepsilon_0^{(k)}$ is calculated from the emissivity obtained in the previous iteration $\varepsilon_0^{(k-1)}$. Iterations stop when convergence of $\varepsilon_0^{(k)}$ is reached.

Additional regularization is added by considering that the plasma emissivity gradients is higher in the radial direction than in the poloidal direction. It is achieved by separating the regularization term:

$${}^t \nabla \cdot W \cdot \nabla = \sigma \cdot {}^t \nabla_r \cdot W \cdot \nabla_r + (1 - \sigma) \cdot {}^t \nabla_\theta \cdot W \cdot \nabla_\theta \quad (3.6)$$

where $0 \leq \sigma \leq 1$ is the anisotropic parameter. With a low σ the gradients in the poloidal direction are more constrained than the gradients in the radial direction, leading to poloidally-symmetrical emissivities being favoured by the algorithm. The solution of the inversion problem is therefore given by:

$$\varepsilon_0 = \left({}^t F F + \lambda \cdot \varepsilon_0 \cdot (\sigma \cdot {}^t \nabla_r \cdot W \cdot \nabla_r + (1 - \sigma) \cdot {}^t \nabla_\theta \cdot W \cdot \nabla_\theta) \cdot \varepsilon_0 \right)^{-1} \cdot {}^t F \cdot m \quad (3.7)$$

3.4 Accuracy of the X-ray emissivity calculation tool

In this section, the experimental data from the Asdex Upgrade shot #32773 is used in order to estimate the accuracy of the X-ray emissivity calculation without transport

presented in section 2.4.2. In order to do so, the experimental radial profiles of n_e and T_e are used to compute the X-ray emissivity. n_W is considered homothetic to the electron density with a concentration chosen as $c_W = 10^{-4}$ which is the expected tungsten concentration. The obtained X-ray emissivity is convoluted by the spectral response of the soft X-ray detectors on Asdex Upgrade and integrated over the detection range in order to compute the simulated measurement. The simulated and experimental measurements are then compared in order to assess the quality of the X-ray emissivity calculation.

Asdex Upgrade uses silicon photodiodes with a beryllium window of $75\mu m$. Their spectral response is displayed on figure 3.12. The detection range of the detector is approximately soft x-ray range: photons with $h\nu < 1keV$ are absorbed in the beryllium window and those with $h\nu > 20keV$ have a low probability of being detected.

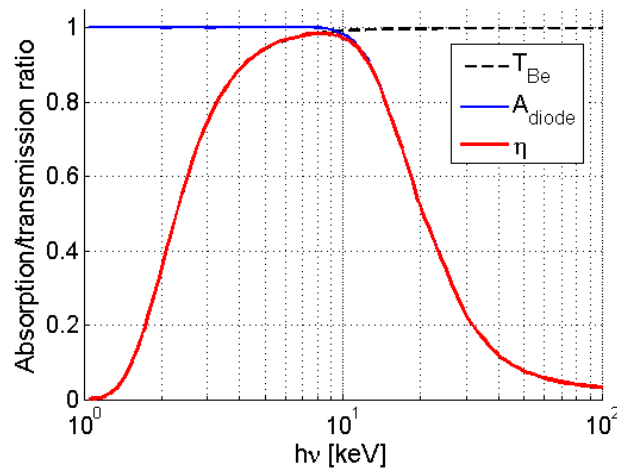


Figure 3.12 – Transmission through the beryllium window (T_{Be}), absorption in the photodiode (A_{diode}) and spectral response (η) of AUG photodiodes with $75\mu m$ of beryllium window.

The electron density and temperature radial profiles are shown on figure 3.13. The SXR emissivity measured by the detector, both simulated and experimental, are displayed on figure 3.14. A clear agreement between both plots is observed. The different structures of the emissivity are well reproduced in the simulation, especially for $r/a < 0.4$. The only exception is the core emissivity for $2.8s < t < 3s$, which is heavily underestimated in the simulation. A possible reason for this underestimation is a tungsten accumulation in the core, which cannot be seen with the hypothesis that n_W is homothetic to n_e . However, the simulation gives an very precise emissivity overall and the simulation tool can therefore be considered accurate. Furthermore, it has been shown in [31] that the estimation of the emissivity without considering transport yields more accurate results with increasing temperature. As a result this simulation tool is expected to be more precise on ITER.

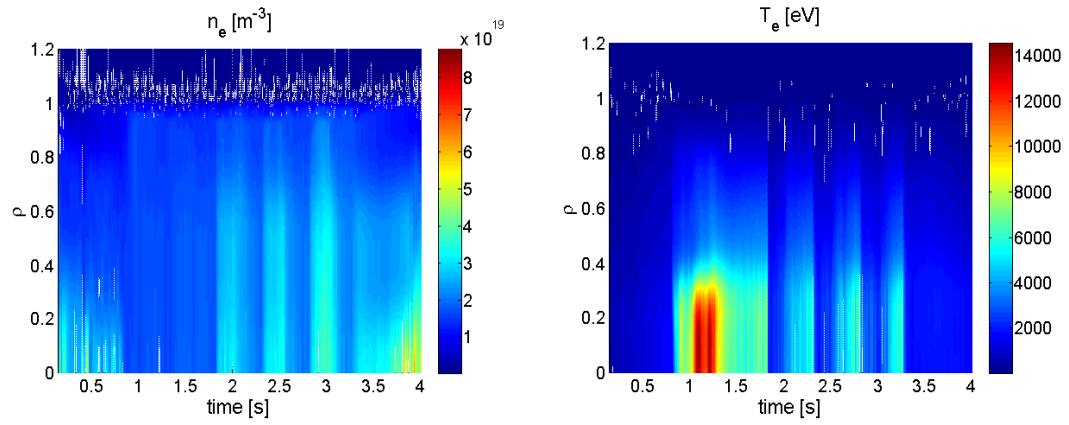


Figure 3.13 – Left: electron density as a function of time and normalised radius for AUG shot #32773. Right: electron temperature as a function of time and normalised radius for AUG shot #32773.

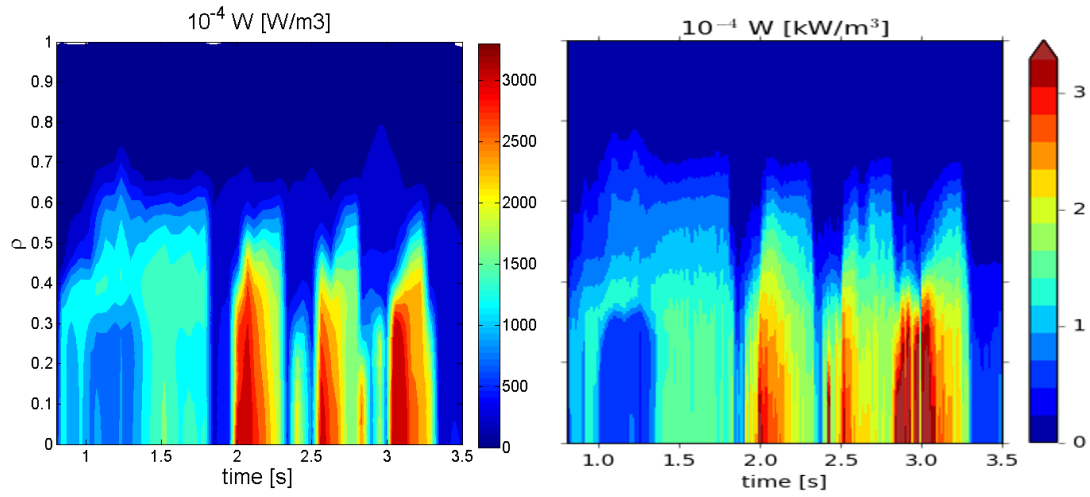


Figure 3.14 – Left: simulated SXR emissivity measured by the detector as a function of time and normalised radius for AUG shot #32773. Right: experimental SXR emissivity measured by the detector as a function of time and normalised radius for AUG shot #32773.

4 Simulation of a Low Voltage Ionization Chamber on ITER

Sommaire

4.1	Line-integration of the emissivity	87
4.1.1	Simplified representation of a detector-aperture system	89
4.1.2	Pixelization of the plasma	91
4.2	Interaction between X-ray photons and matter	91
4.2.1	Absorption processes	92
4.2.1.1	Photoelectric effect	92
4.2.1.2	Photonuclear reaction	93
4.2.2	Inelastic scattering: Compton effect	93
4.2.3	Elastic scattering processes	94
4.2.4	Pair production	95
4.2.5	Relative importance of the different processes	96
4.3	Synthetic diagnostic	97
4.3.1	Computation of the different physical processes	97
4.3.1.1	Transmission through the filter	97
4.3.1.2	Ionization of the gas	98
4.3.1.3	Charge generation and collection	99
4.3.2	Monte Carlo-based synthetic diagnostic	99
4.3.3	Matrix-based synthetic diagnostic	101
4.3.4	Comparison of the two methods	103

This chapter presents a synthetic diagnostic tool used to simulate X-ray detection with a Low Voltage Ionization Chamber which has been developed in the scope of this thesis. The integration of the emissivity over the detector lines-of-sight in order to compute the incoming photon flux is presented. The interaction between X-ray photons and matter as well as its application to the detector are described. Two different computational approaches are discussed and compared: a Monte Carlo and Markov chain.

4.1 Line-integration of the emissivity

The volume of plasma seen by a detector depends on the geometry of the detector itself and of the pinhole, which limits the dimension of the volume of detection.

Computing an exact estimation of the photon flux impacting the chamber in such a configuration can lead to quite complex calculations. Without any geometrical assumption, the solid angle of the detector as seen from the plasma through the pinhole must be convoluted by the emissivity and integrated over the whole volume of detection for each X-ray camera. Such calculations can be quite complex and require a significant amount of computing power. In this section, a simplified method based on standard assumptions for tomography in tokamak plasmas is presented. It has not been developed in the scope of this thesis and is presented as a tool. The interested reader can find more exhaustive calculations in [90].

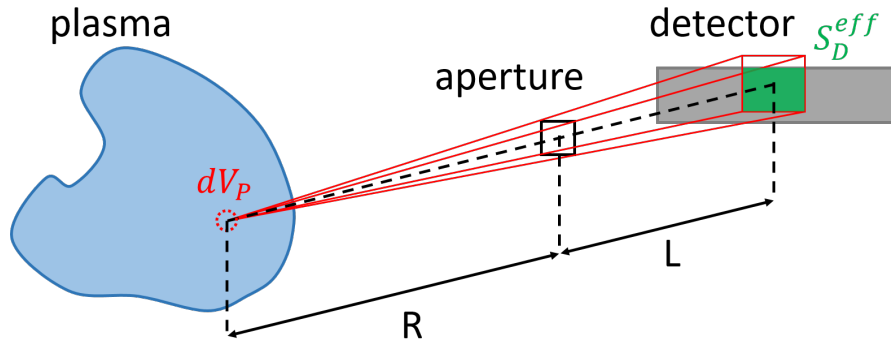


Figure 4.1 – 3D layout of a detector-aperture system in the case of rectangle detector and apertures.

In the system depicted in figure 4.1, R denotes the distance between the elementary plasma volume and the aperture, L is the aperture-detector distance and S_D^{eff} is the effective surface of the detector as seen by the plasma volume through the aperture. In this configuration, the photon flux emitted from the elementary volume dV_P that will reach the detector is given by:

$$d\phi = \varepsilon \cdot dV_P \cdot \frac{\Omega}{4\pi} = \varepsilon \cdot dV_P \cdot \frac{S_D^{eff}}{4\pi(R+L)^2} \quad (4.1)$$

where ε is the volumic emissivity in elementary volume dV_P , Ω is the solid angle of the detector as seen by dV_P through the aperture and S_D^{eff} is the effective (orthogonal to the flux direction) surface of the detector as seen by dV_P through the aperture. Integration of equation 4.1 over the whole plasma volume gives:

$$\phi = \int_{V_P} d\phi = \int_{V_P} \varepsilon \cdot \frac{S_D^{eff}}{4\pi R^2} \cdot dV_P \quad (4.2)$$

4.1.1 Simplified representation of a detector-aperture system

The first simplification consists of considering that the variation in the plasma emissivity occurs over a distance which is greater than the dimensions of the cross-section of the detection volume. This means that the emissivity can be considered constant over said cross-section and only depends on the distance between the aperture and the plasma volume. This simplification is similar to considering that the measurement is only integrated over a line-of-sight, and is commonly referred to as the *line-of-sight approximation*. [91]. As a result, the integral of equation 4.2 can be split:

$$\phi = \int_r \int_{S_P} \varepsilon \cdot \frac{S_D^{eff}}{4\pi R^2} \cdot dS_P \cdot dr = \int_r \varepsilon \int_{S_P} \frac{S_D^{eff}}{4\pi R^2} \cdot dS_P \cdot dr = \int_r \varepsilon \cdot E dr \quad (4.3)$$

where $E = \int_{S_P} \frac{S_D^{eff}}{4\pi R^2} \cdot dS_P$ is the geometrical etendue of the system which takes into account the solid angle Ω . In the case of detectors with a low toroidal expansion e_T the computation of ϕ becomes a two-dimensional problem as depicted in figure 4.2.

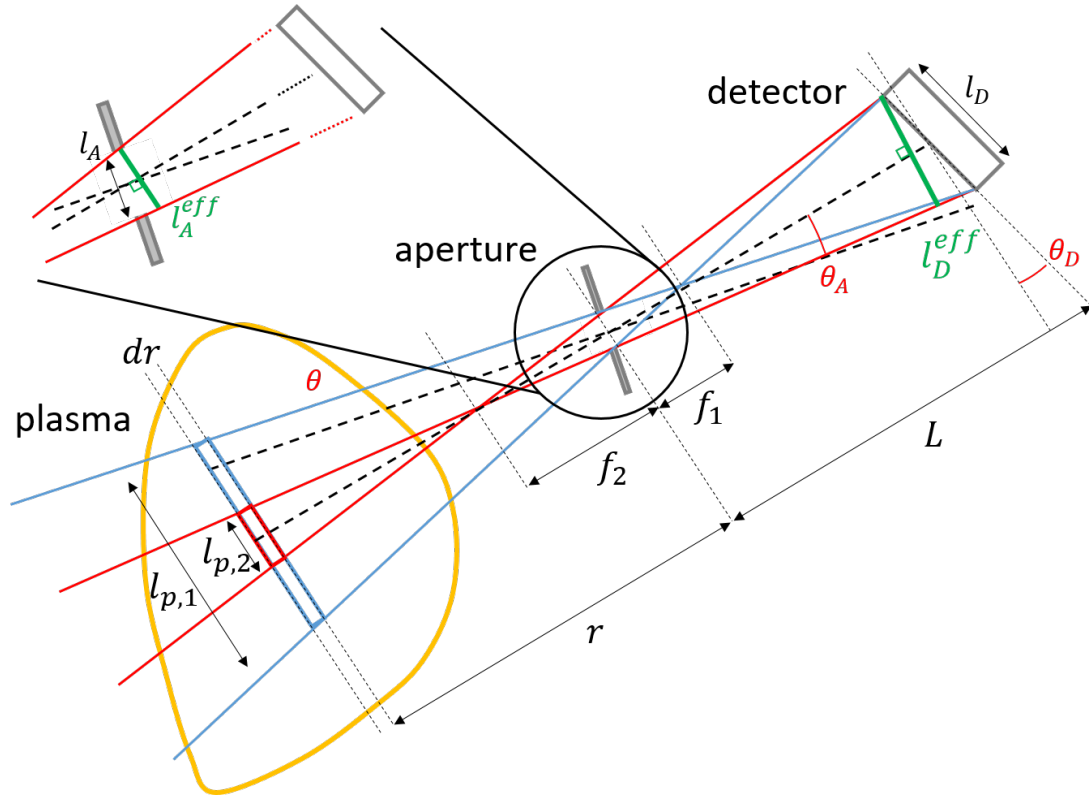


Figure 4.2 – 2D layout of a detector-aperture system in a poloidal section of the plasma.

The quantities represented in figure 4.2 are the following:

- r is the distance between the elementary plasma volume and the aperture

- dr is the width of the elementary plasma volume in the radial direction
- L is the detector-aperture distance
- l_A and l_D are respectively the width of the aperture and of the detector
- l_A^{eff} and l_D^{eff} are respectively the effective width of the aperture and of the detector
- f_1 and f_2 are the focal lengths of the detector-aperture system
- $l_{p,1}$ and $l_{p,2}$ are the effective widths of the plasma region contributing to the flux impacting the detector for a given r
- θ , θ_A and θ_D are respectively the angle of the cone of detection, the aperture, and the detector with the detector-aperture axis

The application of the Thales theorem to the red and blue lines of figure 4.2 lead to a four equations linear system:

$$\begin{cases} \frac{l_{p,1}}{r-f_2} = \frac{l_D^{eff}}{L+f_2} = \frac{l_D \cos(\theta_D)}{L+f_2} \\ \frac{l_{p,1}}{r-f_2} = \frac{l_A^{eff}}{f_2} = \frac{l_A \cos(\theta_A)}{f_2} \\ \frac{l_{p,2}}{r+f_1} = \frac{l_D^{eff}}{L-f_1} = \frac{l_D \cos(\theta_D)}{L-f_1} \\ \frac{l_{p,2}}{r+f_1} = \frac{l_A^{eff}}{f_1} = \frac{l_A \cos(\theta_A)}{f_1} \end{cases} \quad (4.4)$$

In the case where the plasma is further away from the aperture than the second focal point of the detector-aperture system ($r > f_2$), the system of equations 4.4 can be solved for $l_{p,1}$ and $l_{p,2}$:

$$\begin{cases} l_{p,1} = \frac{r}{L} \cdot (l_D \cos(\theta_D) + l_A \cos(\theta_A)) + l_A \cos(\theta_A) \\ l_{p,2} = \frac{r}{L} \cdot (l_D \cos(\theta_D) - l_A \cos(\theta_A)) - l_A \cos(\theta_A) \end{cases} \quad (4.5)$$

Most tomographic detection systems are scaled in such a way that the aperture can be approximated by a point, this is the *point-like pinhole approximation*. In such a configuration $l_A \ll l_D$ and therefore equation 4.5 becomes $l_{p,1} \approx l_{p,2} \approx l_D \cos(\theta_D) \cdot r/L$. The scaling of the detection system usually implies that θ is small enough to assume that the solid angle Ω is constant over the cross-section $S_p(r) = l_D \cos(\theta_D) \cdot l_T \cdot (r/L)^2$, where l_T is the toroidal extension of the system. Substituting in equation 4.1 gives:

$$d\phi = \varepsilon \cdot dr \cdot l_D \cos(\theta_D) \cdot l_T \cdot \frac{r^2}{L^2} \cdot \frac{l_A \cdot \cos(\theta_A) \cdot l_T}{4\pi r^2} = \varepsilon \cdot \frac{l_D \cos(\theta_D) l_A \cos(\theta_A) l_T^2}{4\pi L^2} \cdot dr \quad (4.6)$$

In equation 4.6, ε is the only variable depending on r . The etendue is therefore conserved. [92] This is explained by the facts that the increase of the section $S_p(r)$ contributing to the flux is compensated by the decrease in the solid angle of the detector as seen by the plasma through the aperture $\Omega(r)$. The geometrical etendue of the system is given by:

$$E = \frac{l_D \cos(\theta_D) \cdot l_A \cos(\theta_A) \cdot l_T^2}{4\pi \cdot L^2} \quad (4.7)$$

The total photon flux impacting the detector is:

$$\phi = E \int_r \varepsilon(r) dr \quad (4.8)$$

Equation 4.8 highlights the validity of the line-integration term is the scope of X-ray tomography.

4.1.2 Pixelization of the plasma

The Minimum Fisher regularization tomographic method presented in 3.3.2 works in a discrete space. The ITER emissivity scenario data (see section 2.4.1) is also spatially discrete. The poloidal cross-section of the plasma is therefore divided into $N_x \cdot N_y$ square pixels, as depicted on figure 4.3. The flux seen by the detector is given by:

$$\phi = E \sum_{i=1}^{N_x} \sum_{j=1}^{N_y} \varepsilon(i, j) \cdot L_{ij} \quad (4.9)$$

where E is the geometrical etendue of the aperture-detector system, $\varepsilon(i, j)$ is the emissivity in the pixel with coordinates (i, j) , and L_{ij} is the length of the line-of-sight in the pixel with coordinates (i, j) as shown on figure 4.3.

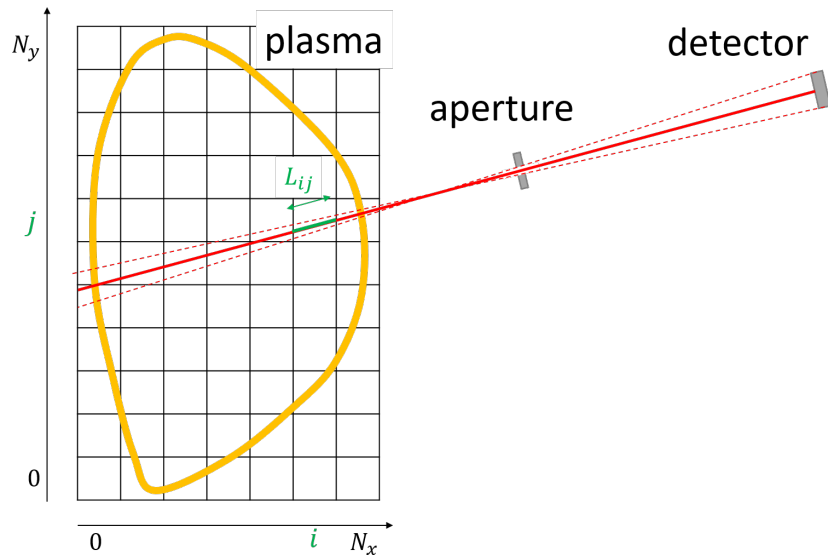


Figure 4.3 – Sketch of a discretized poloidal cross-section of a tokamak.

4.2 Interaction between X-ray photons and matter

Photons are electromagnetic radiation travelling at the speed of light. They do not possess mass nor electric charge. For this reason, they are not subject to Coulomb

interactions in matter and have therefore a much higher penetration potential than charged particles. In this section, the different interactions between photons and atoms are presented and the interest of modelling them in the synthetic diagnostic tool is discussed.

4.2.1 Absorption processes

4.2.1.1 Photoelectric effect

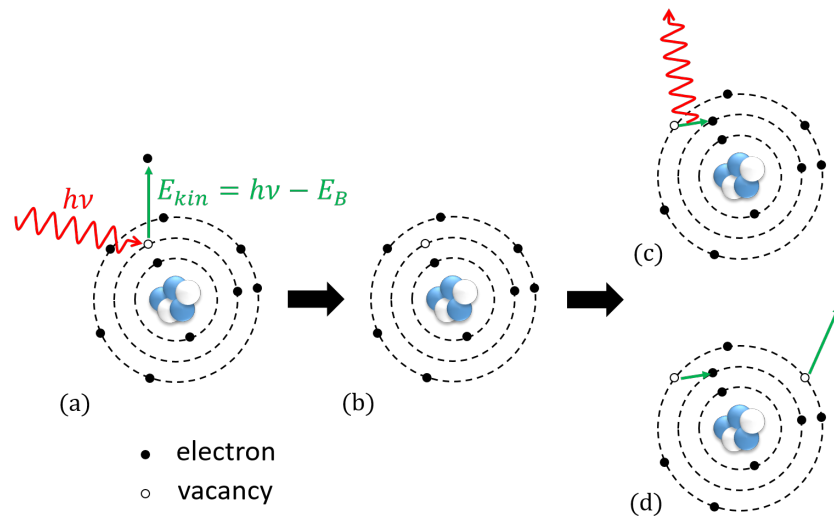


Figure 4.4 – Different stages of the photoionization process: (a) absorption of the incoming photon and ionization of the electron, (b) excited ion, (c) de-excitation through X-ray fluorescence, (d) de-excitation through Auger electron emission

When a photon of energy $h\nu$ impacts an atom, it can transfer all its energy to an electron. The photon is absorbed by the electron which is ionized in the process. The kinetic energy of the ionized electron is $E_{kin} = h\nu - E_B$ where E_B is the binding energy of the electron to the nucleus. Photo-ionization therefore has an energy threshold: $h\nu \geq E_B$. The nucleus is therefore in an excited state, and de-excitation occurs through one of two following processes: Auger electron emission and X-ray fluorescence. The Auger electron consists of the emission of an electron with the residual energy of the ion coupled to an electron of a higher level filling the vacancy left by the photoionized electron. X-ray fluorescence occurs when an electron of an atom of an inner orbit is emitted. The X-ray photon must therefore have an energy higher than the bounding energy of the inner layer. De-excitation then occurs by spontaneous emission: an electron from a higher orbit fills the vacancy and a X-ray photon is emitted in the process. The emitted photon has the energy of the transition between the two orbits. Atoms have low cross-sections at their transition energies and therefore the emitted

photon is likely to exit the detection volume without interaction. A part of the energy of the incident photon is not seen by the detector, and as a result photon counting detectors observe a so-called escape peak at $h\nu - E_B$ in the measured spectrum.

In argon, X-ray fluorescence takes place for $h\nu > 3.2\text{keV}$ with a probability of 14%. The energy of the emitted photon is 2.9 keV. [93] Xenon X-ray fluorescence takes place for $h\nu > 34.5\text{keV}$ with a probability of 88.9%. [94] The energy of the emitted photon is 29.46 keV.

4.2.1.2 Photonuclear reaction

At very high energy ($h\nu > 10\text{MeV}$), photons can be absorbed by the nucleus of the atom. Such interaction is often labelled photodisintegration. Several nucleons are emitted in the process through atomic reactions (e.g. (γ, n) , (γ, p)). The nucleus is then in an excited state, and usually radioactive, and de-excitation occurs by γ -ray emission.

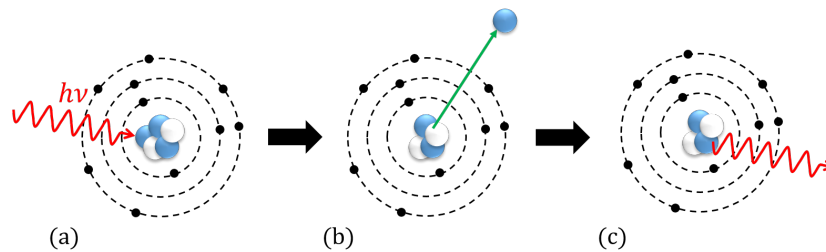


Figure 4.5 – Different stages of photon disintegration: (a) absorption of the photon by the nucleus, (b) emission of a nucleon, (c) de-excitation through γ -ray emission.

4.2.2 Inelastic scattering: Compton effect

Compton scattering is the interaction between a photon and an electron from an outer layer. The photon of energy $h\nu$ transfers a part of its energy to the electron and ionises it. The photon is deviated and its energy has decreased to $h\nu' < h\nu$. The energy transferred to the electron is $E_{kin} = h\nu - h\nu' - E_B$ where E_B is the binding energy of the electron. The energy transferred to the electron depends on the photon energy and the angle at which the electron is ejected. Compton effect becomes significant from around 50 keV, but at these energies a very small fraction of the photon energy is transferred to the electron.

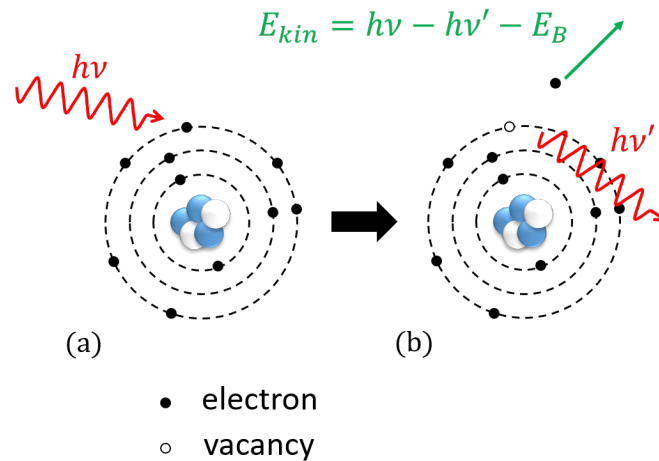


Figure 4.6 – Different stages of Compton scattering: (a) collision between the incident photon and an electron, (b) the electron is ionized and the photon is deviated.

4.2.3 Elastic scattering processes

Elastic scattering is an interaction between photons and electrons without any energy lost by the photon. Two different processes are differentiated: the Thomson scattering and the Rayleigh scattering (or coherent scattering). The Thomson scattering consists of the absorption of a photon of energy $h\nu$ by an electron. Due to the extra energy, the electron enters a forced oscillation regime until a photon of energy $h\nu$ is emitted. The energy of the photon is conserved but not its direction.

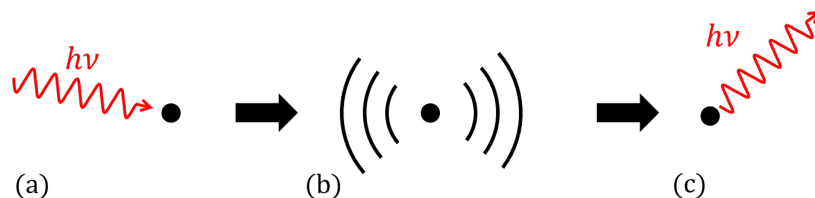


Figure 4.7 – Different stages of Thomson scattering: (a) absorption of the photon by the electron, (b) forced oscillation of the electron, (c) emission of a photon of same energy and different direction.

Rayleigh scattering is similar to Thomson scattering with the exception that the photon interacts with the whole electron cloud of the atom. All the electrons are subject to in phase oscillation before the emission of the second photon, which also has the same energy than the incident photon but a different direction.

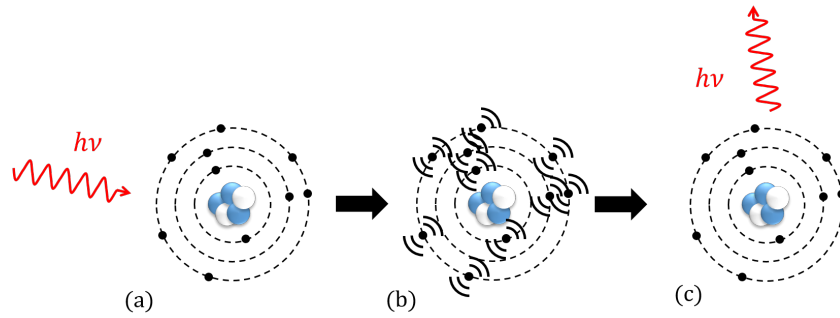


Figure 4.8 – Different stages of Rayleigh scattering: (a) absorption of the photon by the electron cloud, (b) in phase oscillations of the electrons, (c) emission of a photon of same energy and different direction.

4.2.4 Pair production

If a high energy photon is near an atomic nucleus, its energy can be converted into an electron-positron pair: $h\nu \rightarrow e^- + e^+$. This reaction needs to happen in the vicinity of a nucleus in order to conserve both the energy and momentum. In the case of photon with very high energies, it is possible to use an electron for energy and momentum conservation. The created positron quickly loses energy and eventually annihilates itself with an electron, leading to the emission of 2 photons of 511 keV in opposite directions.

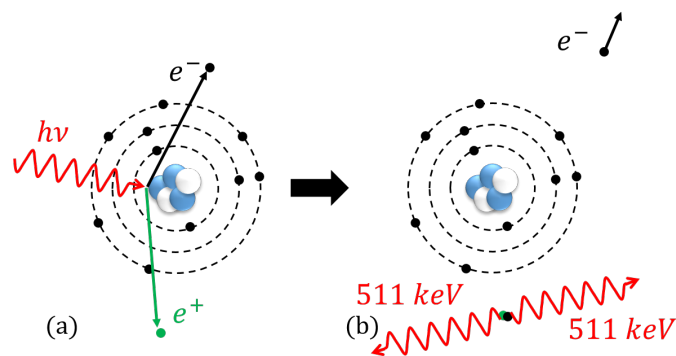


Figure 4.9 – Different stages of pair production: (a) conversion of the photon into an electron-positron pair, (b) annihilation of the positron with an electron.

4.2.5 Relative importance of the different processes

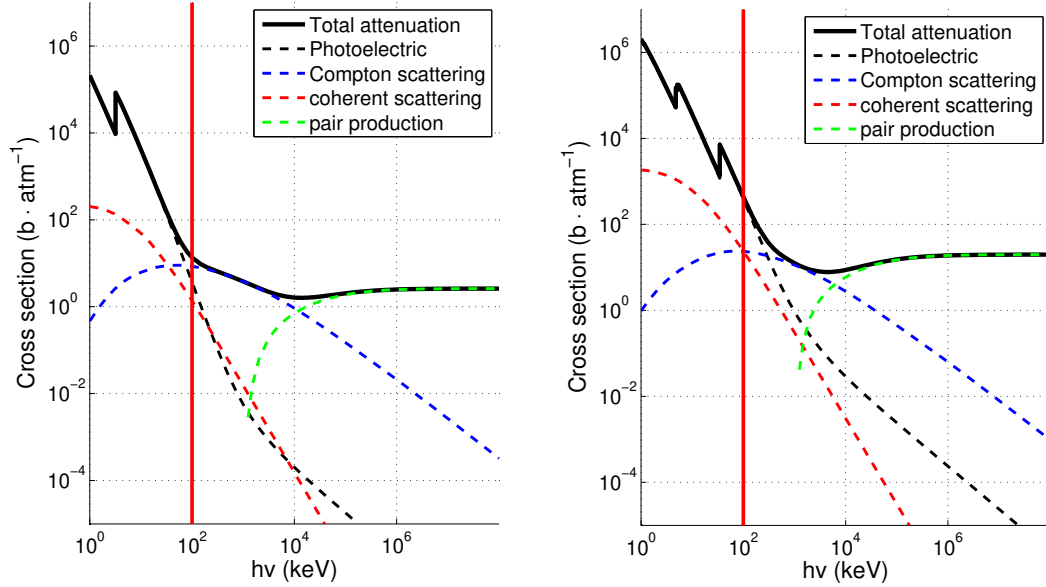


Figure 4.10 – Contribution of the different atomic processes to the total cross-section of argon (left) and xenon (right). The upper limit of the energy range (100 keV) considered on ITER in the scope of this thesis is indicated by a red vertical line.

The contribution of each atomic interaction to the cross-section is displayed in figure 4.10 for argon and xenon. In the energy range of interest for X-ray measurement on ITER ([1, 100] keV), the photoelectric effect is the dominant interaction between photons and atoms. At low energy, coherent scattering is the second interaction in terms of contribution. However, coherent scattering doesn't lead to charge creation nor photon energy loss and therefore does not affect the measurement. The Compton effect has a contribution which increases up to 100 keV, and becomes comparable to photoelectric effect in the case of argon. In the case of xenon, Compton scattering is more than ten times weaker than photoelectric effect. The fact that there is creation of charge through ionization of an electron makes this effect interesting modelling-wise. However, the amount of charge generated per Compton reaction is low and therefore the effect of this interaction on measurement should be limited, especially in the case of xenon. Pair productions have an energy threshold which is higher than 1 MeV and there is therefore no need to incorporate such interaction in the synthetic diagnostic model. As a result the synthetic diagnostic tool presented in section 4.3 computes the charges generated by photoelectric effect only. In the case of argon, Compton effect might lead to a non-negligible generation of charges in the gas and it would be interesting to model it in future work.

4.3 Synthetic diagnostic

In this section the architecture of the synthetic diagnostic tool is presented and two methods of simulation, one based on a Monte Carlo approach and one based on matrix calculations, are compared.

4.3.1 Computation of the different physical processes

The detection of photons in a LVIC can be divided into three main stages: transmission through the filter, ionization of the gas, and charge generation and collection.

4.3.1.1 Transmission through the filter

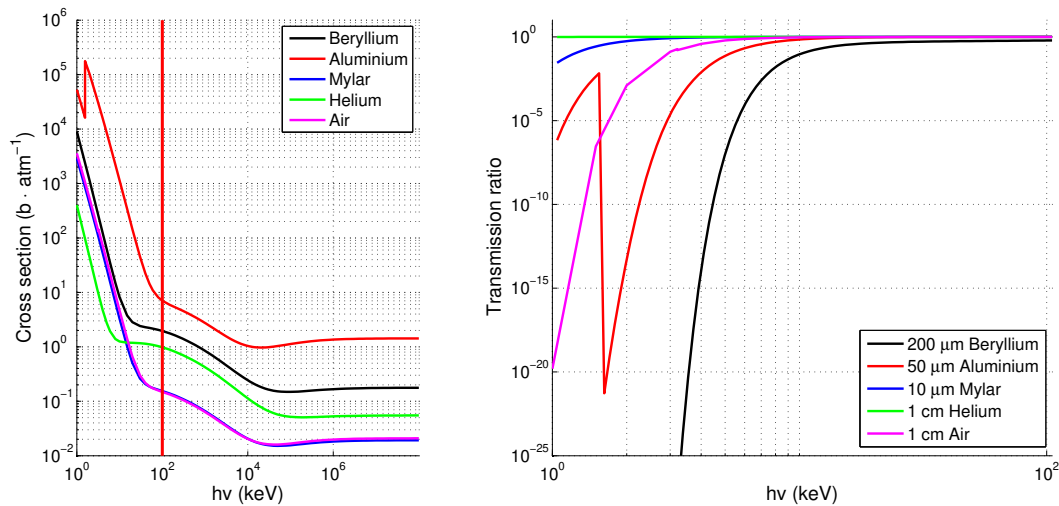


Figure 4.11 – Left: Total cross-sections of the different elements considered as filters. Right: Transmission ratio of different monoelement filters.

In the filter, the photon is subject to all the interactions described in section 4.2. However, the transmission coefficient does not account for the relative importance of each interaction but simply conveys information of the probability to go through the filter without interaction. Therefore, its computation only requires the total cross-section of each element in the filter. The most common filter for X-ray detectors is beryllium, but additional elements such as Mylar, aluminium, air or helium can be found in between a X-ray source and the detector. During tests in laboratory, the X-ray flux often goes through air and aluminium plates before detection. Mylar is a common material for the cathode which can be placed in the front end of the detector (e.g. GEM detectors) and therefore acts as a filter for the X-ray flux.

The probability of transmission of a photon of energy $h\nu$ through a mono-element filter is given by:

$$T(h\nu) = \exp(-d_m \cdot \sigma_{tot}(h\nu) \cdot l \cdot 10^{-28}) \quad (4.10)$$

where d_m is the density of the material in $atm \cdot m^{-3}$, $\sigma_{tot}(h\nu)$ the total cross section at energy $h\nu$ in $b \cdot atm^{-1}$ and l the width of the filter in m . For solid filters the probability of transmission depends only on the width of the filter and in the case of gases, the pressure as well as the width affect the transmission coefficient.

4.3.1.2 Ionization of the gas

As seen in section 4.2.5, the photoelectric effect is the main contributor to photon-gas interactions and therefore to charge generation. As a result, other interactions are neglected and the photoelectric effect cross-sections are used to calculate the detection probability.

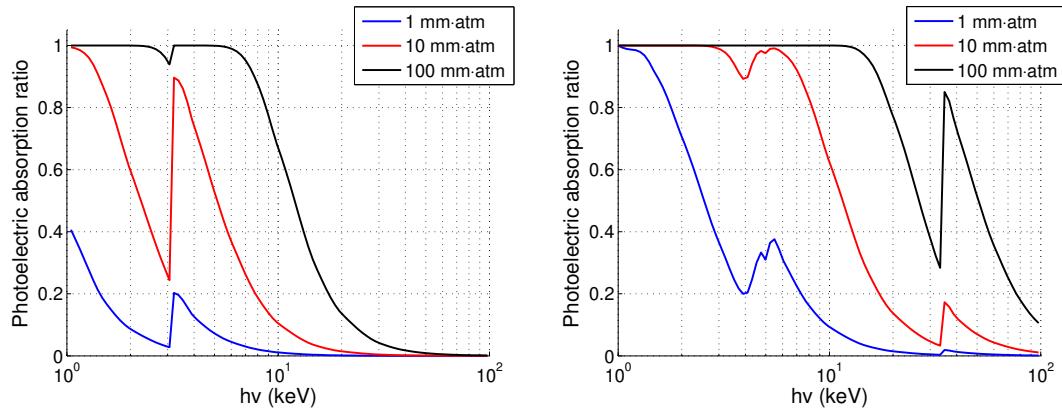


Figure 4.12 – Photoelectric absorption ratio for argon (left) and xenon (right) gas detectors with different design parameter.

The probability of photoelectric effect of a photon of energy $h\nu$ is given by:

$$A(h\nu) = 1 - \exp(-d_g \cdot \sigma_{ph}(h\nu) \cdot l \cdot 10^{-28}) \quad (4.11)$$

where d_g is the density of the gas in $atm \cdot m^{-3}$, $\sigma_{pe}(h\nu)$ the photoelectric effect cross section at energy $h\nu$ in $b \cdot atm^{-1}$ and l the length of the detector in m .

This probability depends both on the length and the pressure of the gas detector, such that the design parameter which defines the sensitivity of the detector is the product of the length and the pressure. For example, a LVIC with a depth of 10 mm filled with argon at 1 bar will have the same spectral response as an argon-filled LVIC with a depth of 5 mm and 2 bar of gas pressure.

The photoelectric absorption ratio in argon and xenon for different values of the length pressure product is displayed in figure 4.12. It can be noticed that as the length pressure product of the detector increases, so does its sensitivity to photons and

therefore its detection range. Xenon exhibits a significantly higher photon sensitivity than argon and its detection range is much wider as well.

4.3.1.3 Charge generation and collection

When a X-ray photon of energy $h\nu$ is absorbed by photoelectric effect, it leads to the creation of a primary electron cloud of size N given by:

$$N = \frac{h\nu - E_B}{W} \quad (4.12)$$

where E_B is the binding energy of the electron to the nucleus and W is the mean ionization energy of the gas. The mean ionization energy is 26 eV for argon [95] and 21 eV for xenon [96]. If the de-excitation of the ion occurs by Auger electron emission, the electron cloud becomes $N = h\nu/W$. In the case of X-ray fluorescence, absorption of the emitted photon is neglected and no additional charges are collected.

The size of the primary electron cloud is subject to a statistical fluctuation σ_N with:

$$\frac{\sigma_N^2}{\langle N \rangle^2} = \frac{F}{\langle N \rangle} \quad (4.13)$$

where $\langle N \rangle$ is the average size of the primary electron cloud and F is the so-called Fano factor [97]. The Fano factor is 0.23 for argon [98] and 0.29 for xenon [99].

Charge collection covers the transport of electrons and ions from the gas to the electrodes. In the scope of modelling the detection in a LVIC, it is assumed that the electric field applied to the chamber is high enough so that:

- electron absorption and ion neutralization in the gas can be neglected, i.e. all the charge is collected on the electrodes [100]
- the effect of the charge of the transiting ions and electrons on the electric field is negligible [100]

The effect of electric arcs and electron avalanches can be neglected thanks to the inherently low voltage of LVIC.

4.3.2 Monte Carlo-based synthetic diagnostic

A Monte Carlo approach can be used to simulate the detection process of a LVIC. [101] It relies on the individual simulation of each incident photon. Provided that enough statistics are provided (enough photons are simulated), Monte Carlo methods are very reliable and allow the simulation of complex problems in fields such as physics, systems engineering or finance.

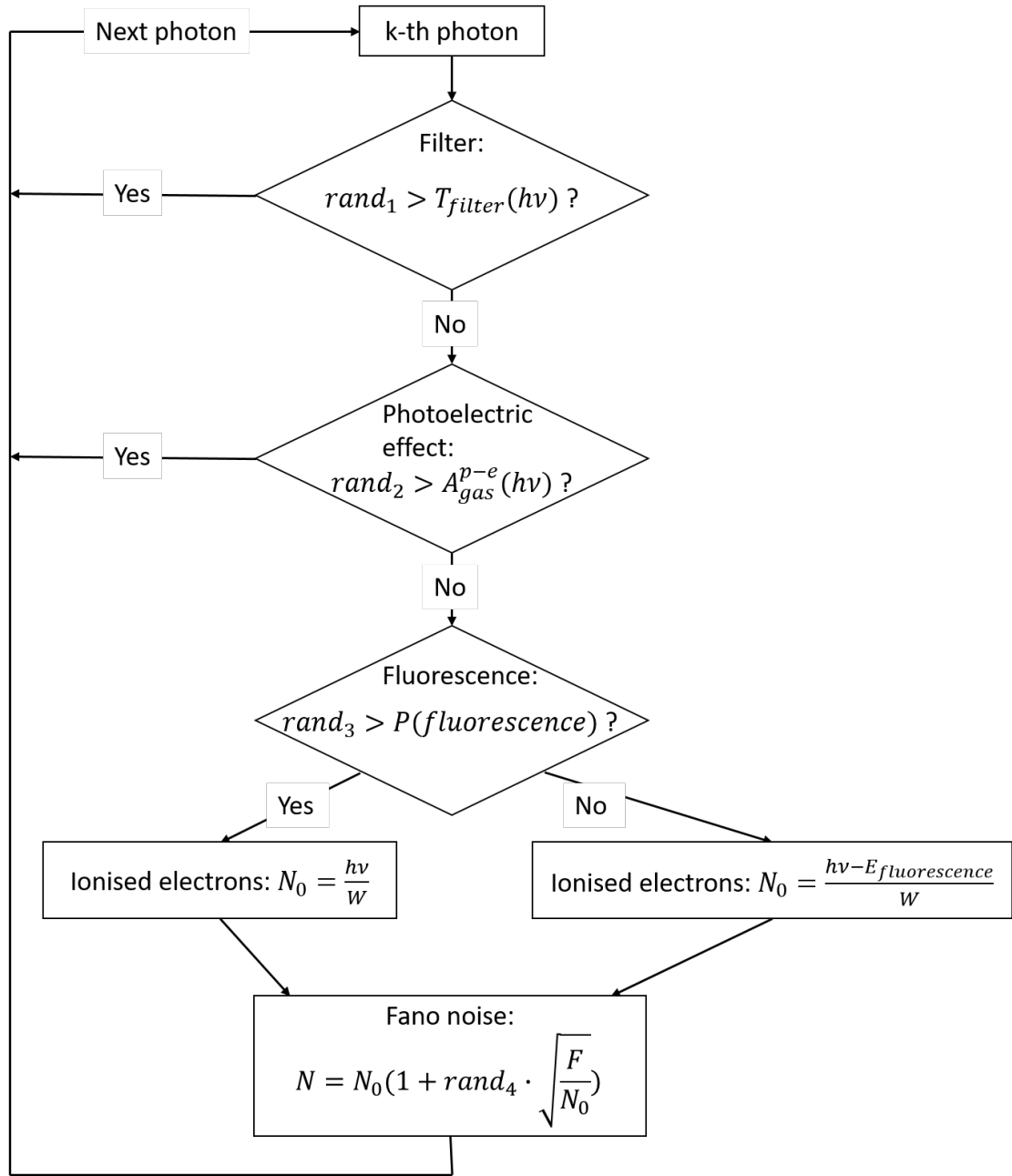


Figure 4.13 – Architecture of the Monte Carlo-based synthetic diagnostic. $T_{filter}(hv)$ denotes the transmission ratio through the filter for a photon of energy hv , $A_{gas}^{p-e}(hv)$ denotes the photo-electric effect absorption ratio in the gas for a photon of energy hv , $P(fluorescence)$ is the probability of X-ray fluorescence, $E_{fluorescence}$ is the energy of the emitted photon, W is the mean ionization energy of the gas, and F is the Fano factor of the gas.

The simulation of a photon is divided in four modules which are based on the

generation of a random number. The Filter, Photoelectric effect and Fluorescence modules use a random number between 0 and 1 generated from a flat probability distribution. If the random number is higher than the probability of an event then this event does not occur. The Fano noise module takes into account the gaussian statistical fluctuation of the amount of electrons ionized, and the associated random number is generated with a standard normal distribution.

4.3.3 Matrix-based synthetic diagnostic

In the case when the amount of incident particles is very high, matrix-based approaches are interesting as their computation time doesn't depend on the amount of incident particles. Their implementation is usually more complicated. Similarly as for the Monte Carlo approach, the synthetic diagnostic is divided into four modules: filter transmission, gas photo-electric effect, X-ray fluorescence, and charge collection (which takes the Fano noise into account).

The transmission through the filter is computed through the product of the vector of the incident flux by the diagonal matrix of the filter transmission ratio:

$$\phi_f = \begin{pmatrix} \phi_f(h\nu_1) \\ \vdots \\ \phi_f(h\nu_n) \end{pmatrix} = \begin{pmatrix} T_f(h\nu_1) & 0 & 0 \\ 0 & \ddots & \\ 0 & 0 & T_f(h\nu_n) \end{pmatrix} \begin{pmatrix} \phi(h\nu_1) \\ \vdots \\ \phi(h\nu_n) \end{pmatrix} = M_f \cdot \phi \quad (4.14)$$

where ϕ_f is the vector of the photon flux transmitted through the filter, T_f is the transmission ratio through the filter, $M_f = \text{diag}(T_f)$ is the matrix associated to filter transmission, and ϕ is the incident photon flux.

Photo-electric effect in the gas is simulated in a similar way as filter transmission:

$$\phi_a = \begin{pmatrix} A_{pe}(h\nu_1) & 0 & 0 \\ 0 & \ddots & \\ 0 & 0 & A_{pe}(h\nu_n) \end{pmatrix} \begin{pmatrix} \phi_f(h\nu_1) \\ \vdots \\ \phi_f(h\nu_n) \end{pmatrix} = M_A \cdot \phi_f \quad (4.15)$$

where ϕ_a is the vector of the photon flux absorbed in the chamber by photo-electric effect, A_{pe} is the photo-electric absorption ratio in the gas, $M_a = \text{diag}(A_{pe})$ is the matrix associated to photo-electric absorption in the gas, and ϕ_f is the filtered photon flux. X-ray fluorescence is computed by the following matrix multiplication:

$$\phi_X = \begin{pmatrix} 1 & 0 & 0 \\ 0 & \ddots & \\ P(X) & 0 & 1 - P(X) \\ 0 & \ddots & P(X) & 0 & 1 - P(X) \end{pmatrix} \begin{pmatrix} \phi_a(h\nu_1) \\ \vdots \\ \phi_a(h\nu_n) \end{pmatrix} = M_X \cdot \phi_a \quad (4.16)$$

where ϕ_X is the measured photon flux taking X-ray fluorescence into account, $P(X)$ is the probability of de-excitation through X-ray fluorescence and M_X is the matrix describing the effect of X-ray fluorescence on the photon flux. The upper left part of the matrix corresponds to the energy range where $h\nu < h\nu_{threshold}$, where the energy of the photon is not high enough for X-ray fluorescence to take place. The $1 - P(X)$ factor corresponds to the part of the photon population which does not lead to X-ray fluorescence: all the photon energy is measured by the detector. The $P(X)$ factor corresponds to the photon population which leads to X-ray fluorescence in the gas: the measured energy is $h\nu - h\nu_{threshold}$. The energy bin in which this photon population is added corresponds to the bin which is closest to $h\nu - h\nu_{fluorescence}$. Due to the discretization of the energy space, the difference between the energy bins is not exactly equal to $h\nu_{fluorescence}$ and the matrix approach introduces uncertainties when considering the X-ray fluorescence.

The charge collection module takes the Fano noise into account. A monoenergetic flux ϕ of photons of energy $h\nu$ leads to the following distribution in the amount of collected electrons:

$$N(k) = \int_{k-1}^k \frac{1}{\sqrt{2\pi \cdot N_0 \cdot F}} \exp\left(-\frac{1}{2} \left(\frac{x - N_0}{\sqrt{N_0 \cdot F}}\right)^2\right) dx \quad (4.17)$$

with $N(k)$ is the amount of photons leading to the collection of k electrons, $N_0 = h\nu/W$ is the average number of ionized electrons, and F is the Fano factor of the gas. This can be described using the M_C matrix given by:

$$M_C(i, j) = \int_{j-1}^j \frac{1}{\sqrt{2\pi \cdot \frac{h\nu_i}{W} \cdot F}} \exp\left(-\frac{1}{2} \left(\frac{x - \frac{h\nu_i}{W}}{\sqrt{\frac{h\nu_i}{W} \cdot F}}\right)^2\right) dx \quad (4.18)$$

where i is the number of the energy bin, $h\nu_i$ the associated energy, j is the number of ionized electrons, W is the mean ionization energy of the gas and F is the Fano factor of the gas. The computation of the M_C matrix is time consuming. As it only depends on the gas, the matrix can be stored in a separate file and loaded during each simulation. The total collected charge can then be computed:

$$C_{tot} = e \cdot \begin{pmatrix} 1 & \dots & n \end{pmatrix} \begin{pmatrix} N(1) \\ \vdots \\ N(n) \end{pmatrix} = M_C \cdot \phi_X \quad (4.19)$$

where e is the elementary charge of an electron. The calculation performed with the matrix approach is therefore:

$$C_{tot} = e \cdot M_C \cdot M_X \cdot M_A \cdot M_f \cdot \phi \quad (4.20)$$

where C_{tot} is the total amount of charge collected. The measured current is given by:

$$I = \frac{C_{tot}}{t} \quad (4.21)$$

where t is the duration over which the flux ϕ has impacted the detector.

4.3.4 Comparison of the two methods

The detection of a monoenergetic photon flux of 10^6 photons of energy $h\nu = 5\text{keV}$ is simulated with both methods. The detector used in this study is an argon-filled LVIC of $50\text{mm} \cdot \text{amt}^{-1}$ with a beryllium filter of $200\mu\text{m}$. The input flux and the flux transmitted through the filter are shown on figure 4.14. The equivalence of both methods for filter transmission can be clearly observed on the right part of the figure.

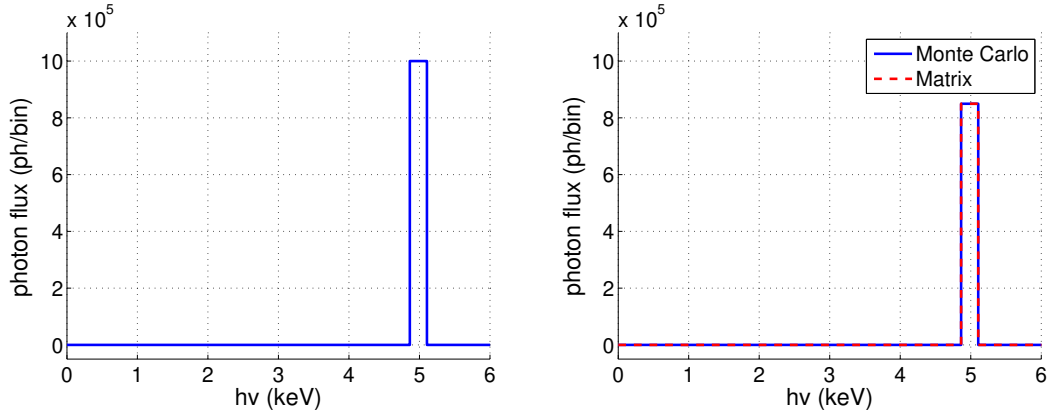


Figure 4.14 – Comparison of the monte carlo and matrix-based synthetic diagnostics. Left: Photon flux incoming on the detectors. Right: Flux transmitted through $200\mu\text{m}$ of beryllium.

The photons measured by the detector are plotted on the left part of figure 4.15. It includes the energy lost by X-ray fluorescence: if an atom de-excites through X-ray fluorescence then the measured energy of the corresponding photon is $h\nu - h\nu_X$ where $h\nu$ is the photon energy and $h\nu_X$ is the energy of the fluorescence photon. Both method yield the same result in terms of measured photons and X-ray fluorescence. When it comes to the collected charge, the two methods give slightly different results. We can indeed observe the main peak and the escape peak slightly shifted between the two simulations. The amplitude and width of each peak is not affected by the simulation method. In the case of a LVIC, which works in current mode, it is the total collected charge which is measured. In this regard the monte carlo approach leads to the collection of $7.64 \cdot 10^6$ electrons, compared to the $7.67 \cdot 10^6$ electrons collected through the matrix method. The difference between these results is lower than 0.5%.

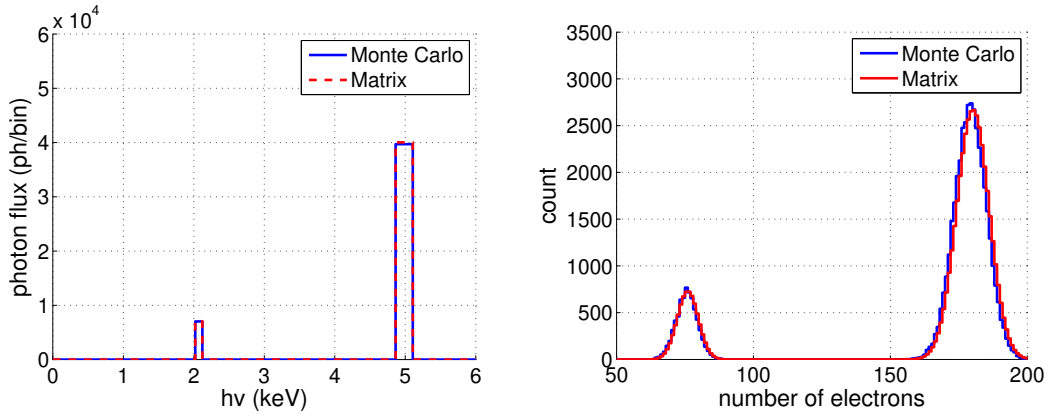


Figure 4.15 – Comparison of the monte carlo and matrix-based synthetic diagnostics. Left: Spectrum measured by the detector, taking X-ray fluorescence into account. Right: Distribution of the charge generated by each photon.

A study of the simulation time as a function of the number of incident particles is performed and the results are displayed on figure 4.16. For low amounts of incident particles ($N_{particles} < 10^4$), the simulation time of both methods is constant. In this region, the monte carlo method is around ten times faster than the matrix approach. From $N_{particles} \approx 10^4$, the simulation time of the monte carlo method increases linearly with $N_{particles}$. The time of simulation for both methods is equal for $N_{particles} \approx 10^5$, and for very high amounts of particles the matrix approach can be several orders of magnitude faster than the monte carlo approach.

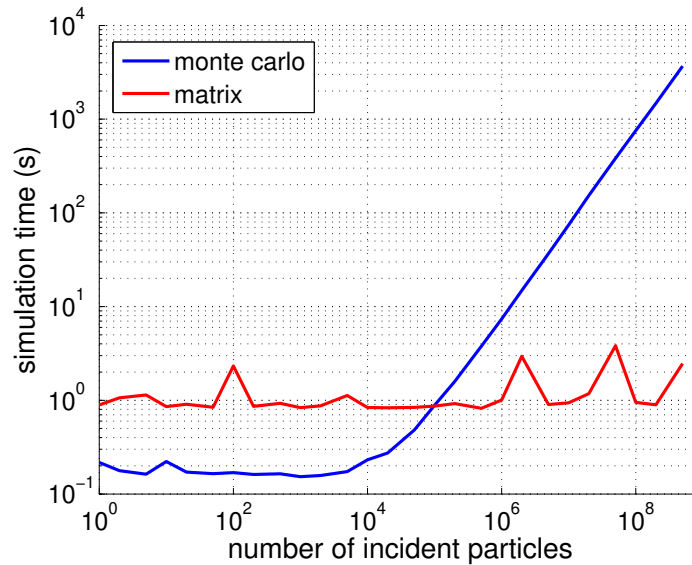


Figure 4.16 – Simulation time as a function of the amount of particles simulated for the matrix and monte carlo-based synthetic diagnostic tools.

In the ITER high power D-T scenario presented in section [2.4.1](#), the order of magnitude of the photon flux impinging the detectors looking at the plasma is $10^{11} \text{ ph} \cdot \text{s}^{-1}$. Therefore the use of the monte carlo approach cannot be considered for ITER detection modelling and the matrix-based synthetic diagnostic is used in the scope of this thesis.

5 X-ray tomography on ITER

Sommaire

5.1	ITER radial X-ray cameras	107
5.2	Tomographic capabilities	109
5.2.1	Figures of merit	109
5.2.2	Emissivity profiles	110
5.2.3	Tomographic reconstructions	112
5.3	Addition of lines-of-sight: proof of concept	116
5.4	Geometry proposal	119
5.4.1	60 vertical lines-of-sight configuration	120
5.4.2	44 vertical lines-of-sight configuration	123

5.1 ITER radial X-ray cameras

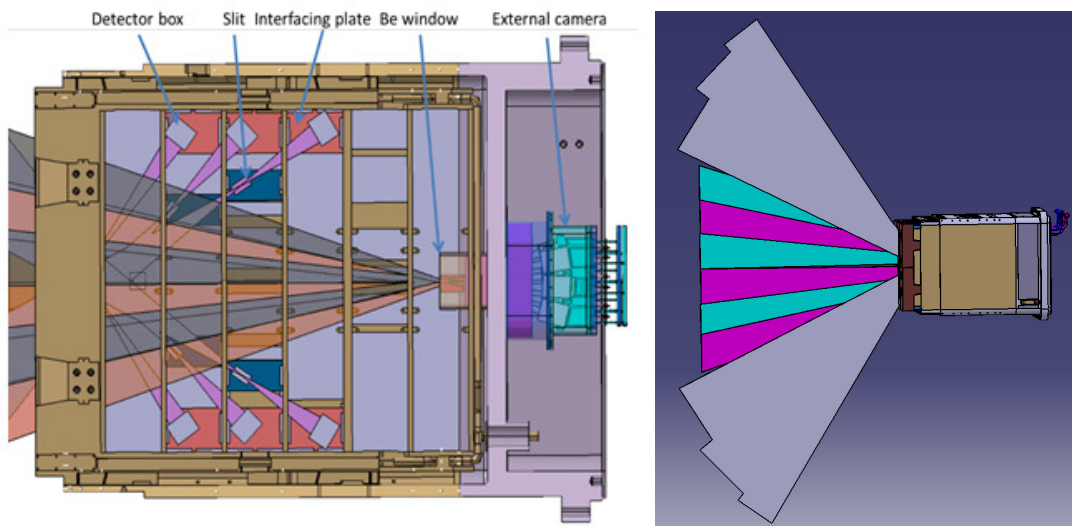


Figure 5.1 – Left: ITER radial X-ray cameras in the EPP 12. Right: EPP 12 with the X-ray lines-of-sight.

The ITER X-ray measurement system is made of twelve radial cameras, located in the Equatorial Port Plug (EPP) 12. Six of these cameras are placed before the closure plate

and are therefore in the vacuum vessel. They are referred to as the *internal cameras*. The other six cameras are positioned behind the closure plate and are referred to as the *external cameras*.

Each camera is divided into 16 lines-of-sight (LoS) for a total of 192 lines-of-sight. These lines-of-sight cover the entirety of the plasma, as shown on figure 5.2. The cameras are divided into three sets, displayed with a different color in figure 5.2. The upper internal cameras (lines-of-sight 1 to 48) which aim at the lower part of the plasma (in black in figure 5.2), the external cameras (lines-of-sight 49 to 144) which cover the plasma core (in green in figure 5.2) and the lower internal cameras (lines-of-sight 145 to 192) which aim at the upper part of the plasma (in blue in figure 5.2).

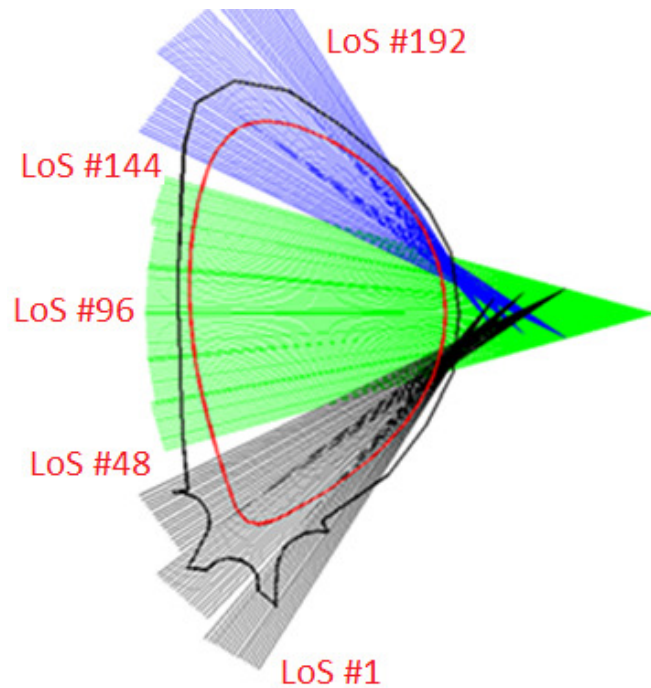


Figure 5.2 – ITER X-ray lines-of-sight.

The geometrical etendues associated with each line-of-sight are displayed on figure 5.3. Each camera has been designed with the same detector and aperture surface. As a result, the differences observed in the geometrical etendue solely come from the variation of the detector-aperture distance L and from the angle between the line-of-sight and the aperture. Variations in L explains the difference of etendue from one camera to another. One can notice that the external cameras (LoS 49-144) as well as the first upper and the last lower internal cameras (LoS 1-16 and 177-192) have the longest detector aperture distance, hence their lower geometrical etendues. The angle between the line-of-sight and the aperture is responsible for the mild semi-circle shape of the etendue inside a given camera, the central lines-of-sight having the highest etendue.

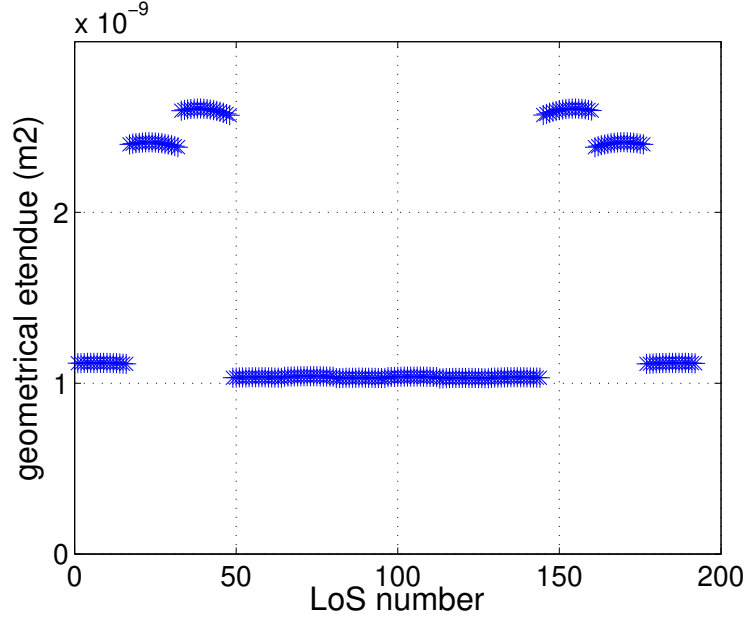


Figure 5.3 – Geometrical etendue for each line-of-sight of the radial X-ray cameras.

5.2 Tomographic capabilities

In this section the tomographic capabilities of the lines-of-sight geometry are studied. In order to do so, tomographic reconstructions of phantom emissivity profiles with various shapes are performed without considering the detection process: the line-integral of the emissivity profile is used as input. The Minimum Fisher Information tomographic method presented in section 3.3.2 is used for tomographic inversion.

5.2.1 Figures of merit

The quality of reconstruction is assessed through visual inspection as well as two figures of merit which are the root mean square of the tomographic reconstruction relative error and the root mean square of the line-integrals reconstruction relative error:

$$\begin{aligned} RMS_{tomo} &= \sqrt{\frac{1}{N_{pixels}} \sum_{i=1}^{N_{pixels}} \frac{(\epsilon(i) - \epsilon^{rec}(i))^2}{\epsilon(i)^2}} \\ RMS_{line} &= \sqrt{\frac{1}{N_{LoS}} \sum_{i=1}^{N_{LoS}} \frac{(f(i) - f^{rec}(i))^2}{f(i)^2}} \end{aligned} \quad (5.1)$$

where N_{pixels} is the amount of geometrical pixels used for reconstruction, ϵ is the input emissivity profile, ϵ^{rec} is the reconstructed emissivity profile, N_{LoS} is the amount of lines-of-sight, f is the line-integral of the input emissivity profile, and f^{rec} is the line-integral of the reconstructed emissivity profile.

RMS_{tomo} expresses the quality of reconstruction of the emissivity profile. In the scope

of this thesis, RMS_{tom} is computed over two plasma regions: the plasma core and the plasma inside the Last Closed Magnetic Surface (LCMS). The plasma core is defined as the region where $T_e > 10keV$ in the emissivity scenario presented in section 2.4.1. The pixels of both regions are displayed on figure 5.4.

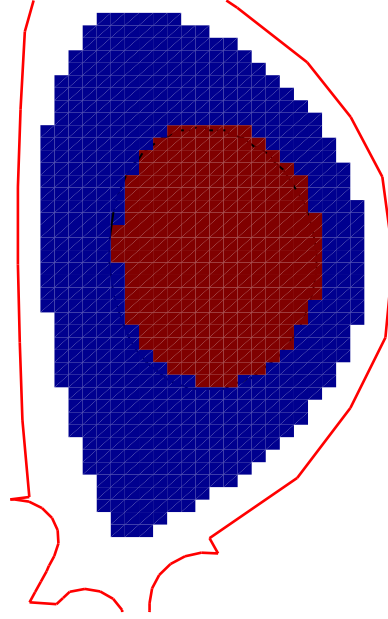


Figure 5.4 – Plasma regions considered in the computation of the figures of merit. The pixels in the plasma core are displayed in red. The LCMS enclosed region contains both red and blue pixels.

RMS_{line} expresses the quality of reconstruction of the line-integrals and therefore how much the tomographic reconstruction is in agreement with the measured data. During plasma experiments it is the only figure of merit available. A good agreement in the line-integrals (low RMS_{line}) coupled to a bad agreement in the emissivities (high RMS_{tom}) denotes a lack of information which does not allow the tomographic algorithm to find a better fitting emissivity profile.

5.2.2 Emissivity profiles

Four emissivity profiles are defined in order to assess the tomographic capabilities of the lines-of-sight configuration presented in section 5.1.

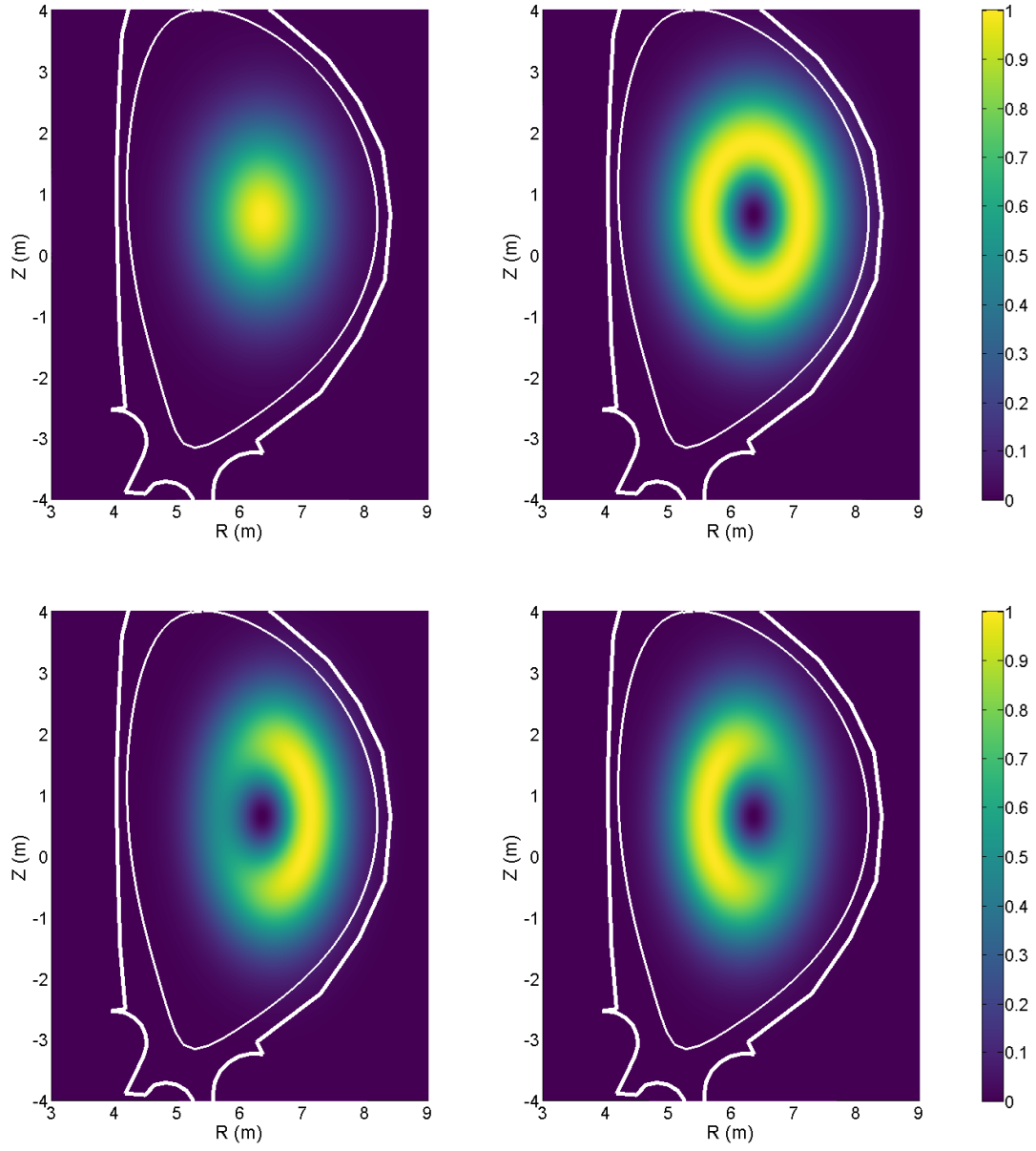


Figure 5.5 – Phantom emissivity profiles used for the assessment of the tomographic capabilities of a lines-of-sight geometry. Upper left: gaussian profile. Upper right: hollow profile. Lower left: LFS asymmetry. Lower right: HFS asymmetry.

The simplest profile has a gaussian shape and exhibits symmetry in all directions. It is defined as:

$$\varepsilon_{\text{gaussian}}(r, z) = \exp\left(-\frac{(r - r_p)^2}{2(\frac{\rho}{1.5})^2} - \frac{(z - z_p)^2}{2\rho^2}\right) \quad (5.2)$$

where $r_p = 6.353m$ and $z_p = 0.6447m$ are respectively the radial and vertical coordinates of the ITER magnetic axis, and ρ is a parameter defining the width of the gaussian shape. The parameter ρ was chosen as $1m$.

A hollow emissivity profile adds more complexity to the reconstruction while retaining the symmetry in all directions. It is defined as:

$$\varepsilon_{hollow}(r, z) = \frac{\varepsilon_{gaussian}(r, z)}{\max(\varepsilon_{hollow})} \exp\left(-\frac{(r - r_p)^2}{(\frac{\rho}{1.5})^2} - \frac{(z - z_p)^2}{\rho^2}\right) \quad (5.3)$$

ε_{hollow} is normalized to $[0, 1]$ by dividing it by its maximal value. The gaussian and hollow emissivity profiles are displayed on the upper part of figure 5.5.

Radial asymmetries are introduced in two emissivity profiles in order to test the ability of the lines-of-sight configuration to reconstruct such asymmetries. An emissivity profile exhibiting an asymmetry in the low field side of the plasma is defined as:

$$\varepsilon_{LFS}(r, z) = \frac{\varepsilon_{hollow}(r, z)}{\max(\varepsilon_{LFS})} \exp\left(-\frac{(r - r_p - \frac{\rho}{1.5})^2}{6(\frac{\rho}{1.5})^2}\right) \quad (5.4)$$

An emissivity profile exhibiting an asymmetry in the high field side of the plasma is defined as:

$$\varepsilon_{HFS}(r, z) = \frac{\varepsilon_{hollow}(r, z)}{\max(\varepsilon_{HFS})} \exp\left(-\frac{(r - r_p + \frac{\rho}{1.5})^2}{6(\frac{\rho}{1.5})^2}\right) \quad (5.5)$$

Similarly as for the hollow emissivity profile, both asymmetric profiles are normally to $[0, 1]$ and are displayed on the lower part of figure 5.5. These profiles are respectively referred to as LFS asymmetry and HFS asymmetry.

5.2.3 Tomographic reconstructions

Tomographic reconstruction is performed on the phantom emissivity profiles. The results are shown in table 5.1, figure 5.6, and figure 5.7.

	Gaussian	Hollow	LFS asymmetry	HFS asymmetry
RMS_{tomo}^{core}	$2.9 \cdot 10^{-2}$	$4.0 \cdot 10^{-2}$	$4.25 \cdot 10^{-1}$	$2.90 \cdot 10^{-1}$
RMS_{tomo}^{LCMS}	$3.7 \cdot 10^{-1}$	$3.7 \cdot 10^{-1}$	5.42	$9.1 \cdot 10^{-1}$
RMS_{line}	$4.3 \cdot 10^{-4}$	$4.9 \cdot 10^{-4}$	$6.9 \cdot 10^{-4}$	$2.44 \cdot 10^{-3}$

Table 5.1 – Figures of merit for tomographic reconstruction of phantom emissivity profiles with the radial X-ray cameras.

Visual inspection of the reconstruction of the gaussian emissivity profile shows that the shape and amplitude of the emissivity is accurately reconstructed (see figure 5.6). The line-integral seem to be perfectly fitted. Table 5.1 gives a more quantified assessment of the quality of tomographic reconstruction. The different figures of merit seem

quite low, but their use is limited in the absence of a point of comparison. These values will therefore serve as a benchmark for an accurate tomographic reconstruction.

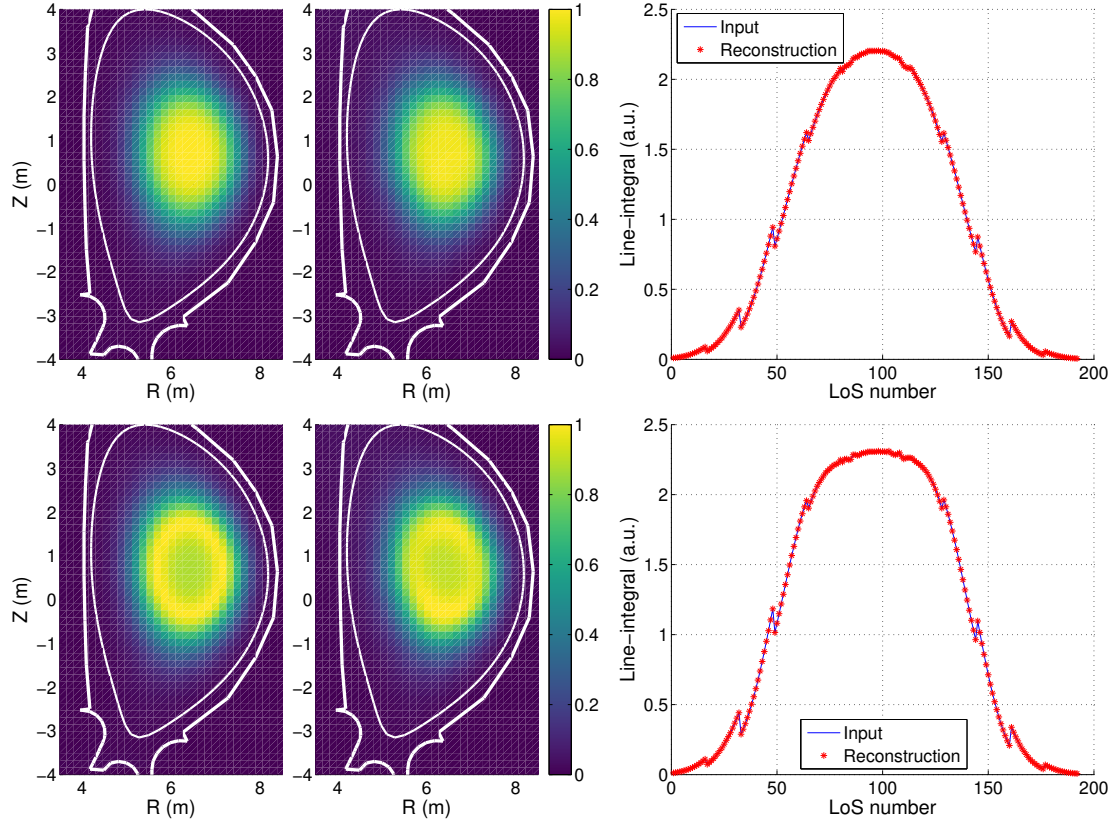


Figure 5.6 – Phantom emissivity profile (left), tomographic reconstruction (center) and line-integrated emissivity (right) of different emissivity configurations with the ITER radial X-ray cameras. First row: Gaussian emissivity profile. Second row: Hollow emissivity profile.

It can be noticed that the reconstruction accuracy in the core is much higher than over the LCMS-enclosed region: $RMS_{tomo}^{LCMS} > 10 \cdot RMS_{tomo}^{core}$. This is explained by the fact that tomographic algorithms tend to be more precise at the center of the reconstruction region. [102]

Similarly as the gaussian profile, the hollow profile exhibits a good visual agreement between the input and reconstructed emissivity and line-integral profiles. RMS_{tomo}^{core} shows that the accuracy of reconstruction is lower than for the gaussian profile in the plasma core, but of the same order of magnitude which is satisfactory. The RMS_{tomo}^{LCMS} are sensibly equal for both emissivity profiles, and the agreement between the line-integrated profiles has slightly decreased.

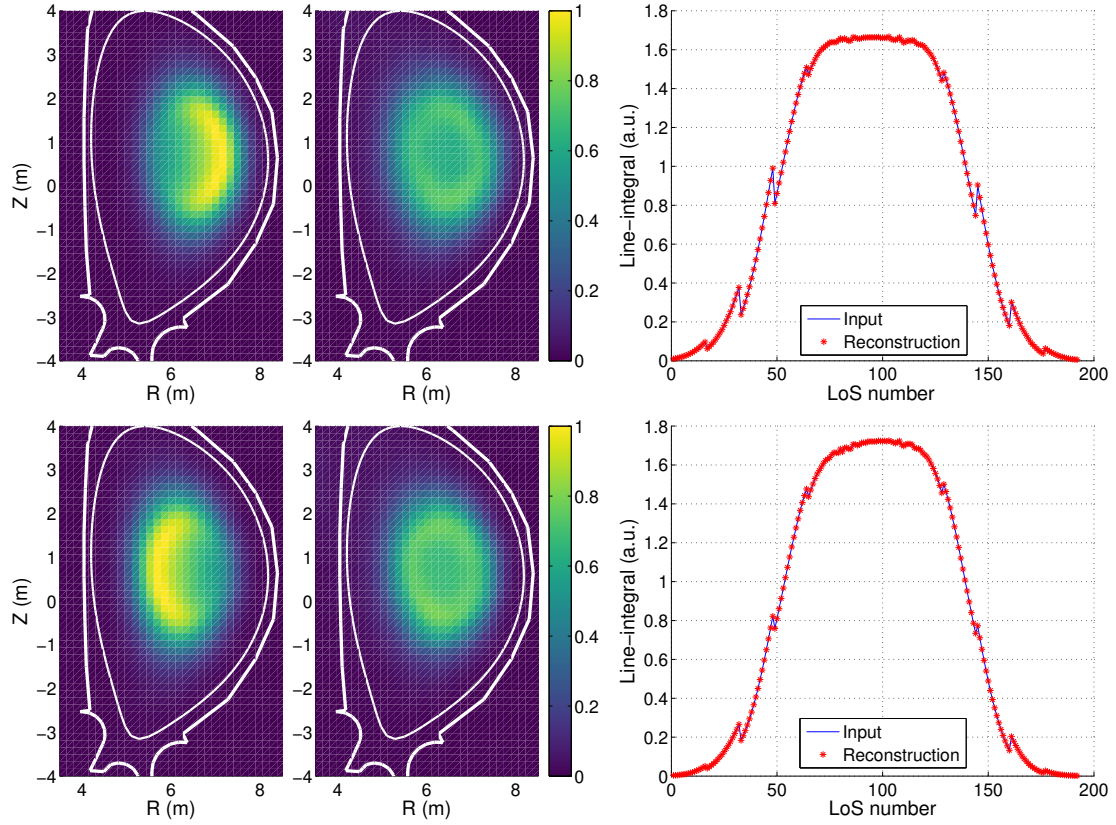


Figure 5.7 – Phantom emissivity profile (left), tomographic reconstruction (center) and line-integrated emissivity (right) of different emissivity configurations with the ITER radial X-ray cameras. First row: LFS asymmetry. Second row: HFS asymmetry.

It can be seen on figure 5.7 that the reconstruction of the LFS asymmetry profile is not accurate. Indeed, the shape of the reconstructed emissivity is hollow. However, there is a good agreement between the input and reconstructed line-integrals of the emissivity. These observations are corroborated by table 5.1: RMS_{tomo} is more than 10 times higher than for the gaussian emissivity profile, both in the core and the LCMS-enclosed region, while RMS_{line} is of the same order of magnitude for both emissivity profiles (although higher for the LFS profile).

A similar observation can be made for the HFS asymmetry profile. The reconstructed emissivity profile exhibits a hollow shape, by the agreement between the input and reconstructed line-integrals of the emissivity is very good. RMS_{tomo}^{core} is ten times higher than for the gaussian emissivity profile and RMS_{tomo}^{LCMS} has increased by a factor 3. Quantitative agreement between the line-integrals has decreased however, but with $RMS_{line} < 10^{-2}$ it seems to be within a reasonable margin.

It can be noticed that the shape of the line-integrals of the emissivity for the asymmetric profiles is very close to the one obtained with the hollow emissivity profile. This means that the information gathered by the radial X-ray cameras does not allow the

discrimination of these profiles. Such issues usually arise from a lack of lines-of-sight. In order to solve this problem we now investigate where extra lines-of-sight can be added.

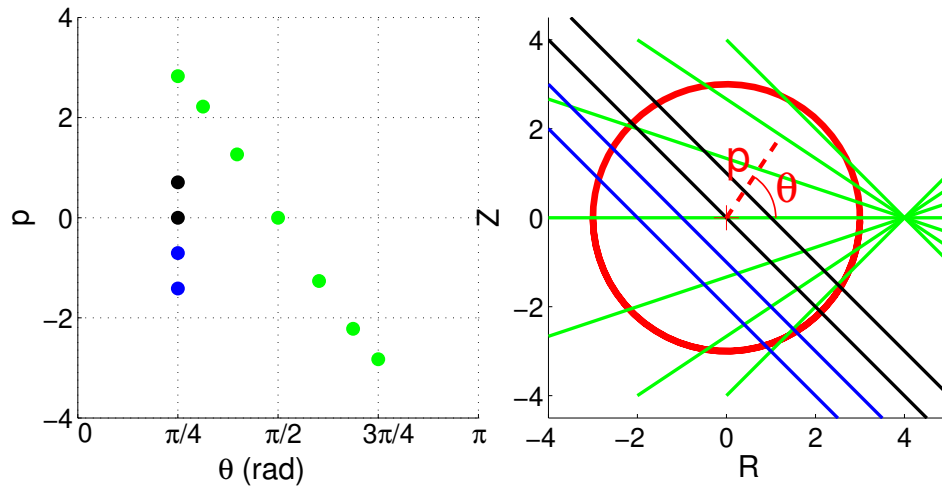


Figure 5.8 – Left: Sinogram of a tomographic system made of three sets of lines-of-sight. Right: Geometry of the lines-of-sight.

In order to study the fitness of a set of lines-of-sight for tomography, one can use a sinogram. In the context of the *line-of-sight approximation* described in section 4.1, a straight line can be used to characterize the volume of detection. This line can be parametrised easily in the (p, θ) space of the poloidal cross-section, as shown on figure 5.8.

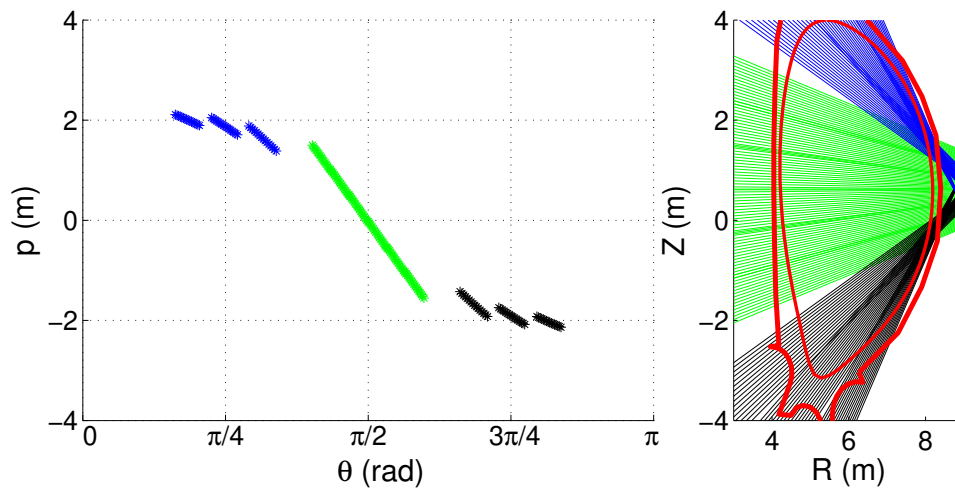


Figure 5.9 – Left: Sinogram of the radial X-ray cameras lines-of-sight. Right: Geometry of the associated lines-of-sight.

Such parametrisation can be plotted on a so-called sinogram, which is the representation of the lines-of-sight in the (p, θ) projection space. Sinograms are powerful tools to estimate the fitness of a set of lines-of-sight for tomographic reconstruction: the more coverage of the (p, θ) projection space, the more accurate the tomographic inversion.

The sinogram of the radial X-ray cameras is displayed in figure 5.9. The lines-of-sight cover the region of the diagonal from $(p = 2, \theta = \pi/4)$ to $(p = -2, \theta = 3\pi/4)$, but the rest of the (p, θ) projection space is not covered. The addition of lines-of-sight with θ centered on 0 ($[0, \pi/4] \cup [3\pi/4, \pi]$) could increase the tomographic capabilities of the system. These lines-of-sight would have a direction close to vertical.

5.3 Addition of lines-of-sight: proof of concept

The effect of adding lines-of-sight in terms of tomographic reconstruction is studied. A set of geometry displaying maximal lines-of-sight overlapping is used to demonstrate the feasibility of X-ray tomographic reconstruction with adequate lines-of-sight layout.

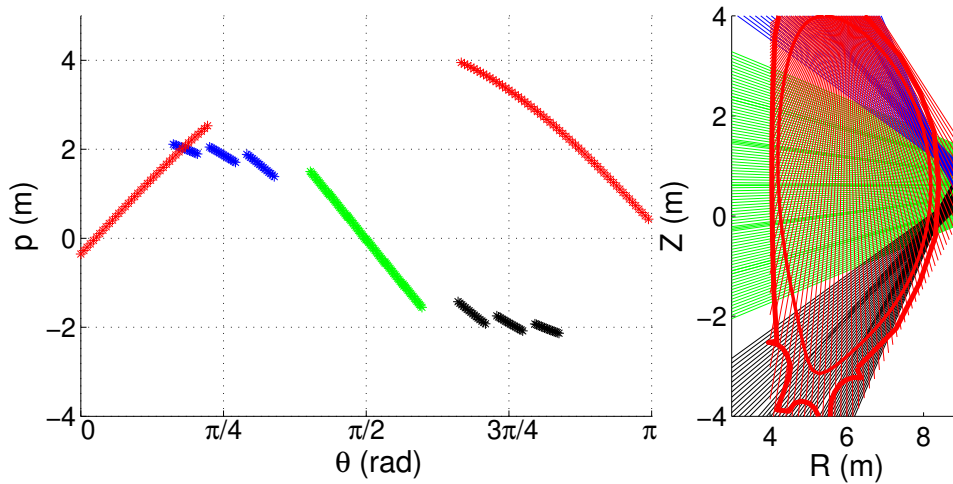


Figure 5.10 – Left: Sinogram of the theoretical configuration. Right: Geometry of the associated lines-of-sight.

The geometry contains the radial lines-of-sight presented in section 5.1 as well as a set of 101 so-called *vertical lines-of-sight*. These vertical lines-of-sight cannot be considered for ITER operation as they do not originate for a diagnostic purpose, and are therefore purely theoretical. This configuration is referred to as the *theoretical configuration* and its sinogram and geometry are displayed in figure 5.10. It can be noticed that the coverage of the (p, θ) projection space has been greatly improved.

	Gaussian	Hollow	LFS asymmetry	HFS asymmetry
RMS_{tomo}^{core}	$1.9 \cdot 10^{-2}$	$1.7 \cdot 10^{-2}$	$5.0 \cdot 10^{-2}$	$4.0 \cdot 10^{-2}$
RMS_{tomo}^{LCMS}	$6.8 \cdot 10^{-2}$	$6.1 \cdot 10^{-2}$	$7.9 \cdot 10^{-1}$	$3.0 \cdot 10^{-1}$
RMS_{line}	$1.8 \cdot 10^{-3}$	$1.4 \cdot 10^{-3}$	$1.6 \cdot 10^{-1}$	$2.8 \cdot 10^{-2}$

Table 5.2 – Figures of merit for tomographic reconstruction of phantom emissivity profiles with the theoretical lines-of-sight configuration.

Tomographic reconstructions of the phantom emissivity profiles have been performed in this lines-of-sight configuration. The resulting figures of merit are reported in table 5.2. Gaussian and hollow profile reconstructions are displayed in figure 5.11, and the LFS and HFS asymmetry profile reconstruction are shown on 5.12.

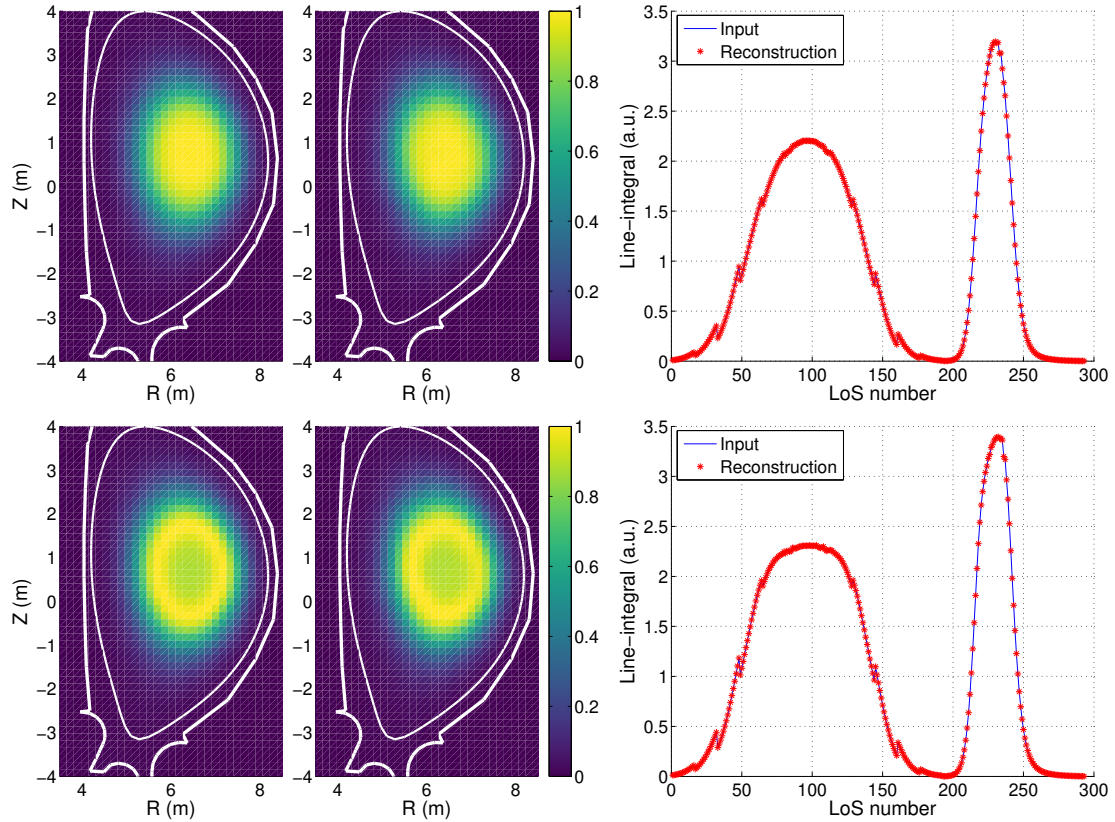


Figure 5.11 – Phantom emissivity profile (left), tomographic reconstruction (center) and line-integrated emissivity (right) of different emissivity configurations with the theoretical lines-of-sight configuration. First row: Gaussian emissivity profile. Second row: Hollow emissivity profile.

Visual inspection of the reconstruction of the gaussian profile does not show any difference with the radial X-ray cameras only: the reconstruction as well as the fitting of the line-integrals seem accurate. Thanks to the introduction of the additional lines-

of-sight, RMS_{tomo}^{core} has decreased by around 30% and RMS_{tomo}^{LCMS} has been divided by 5. There has therefore been a significant improvement in the quality of reconstruction on the gaussian profile, even though it was already well reconstructed with the radial lines-of-sight only. The increase in the amount of line-integrals to fit lead to an increase in RMS_{line} , which still remains reasonably low.

Similar observations can be made on the tomographic reconstruction of the hollow profile. Indeed, the shape and amplitude of the emissivity seem well reproduced, as well as the line-integrals. There is an improvement of more than a factor 2 on RMS_{tomo}^{core} and of around a factor 5 on RMS_{tomo}^{LCMS} . The fitting of the line-integrals also suffers from the presence of the additional lines-of-sight but RMS_{line} is still quite low.

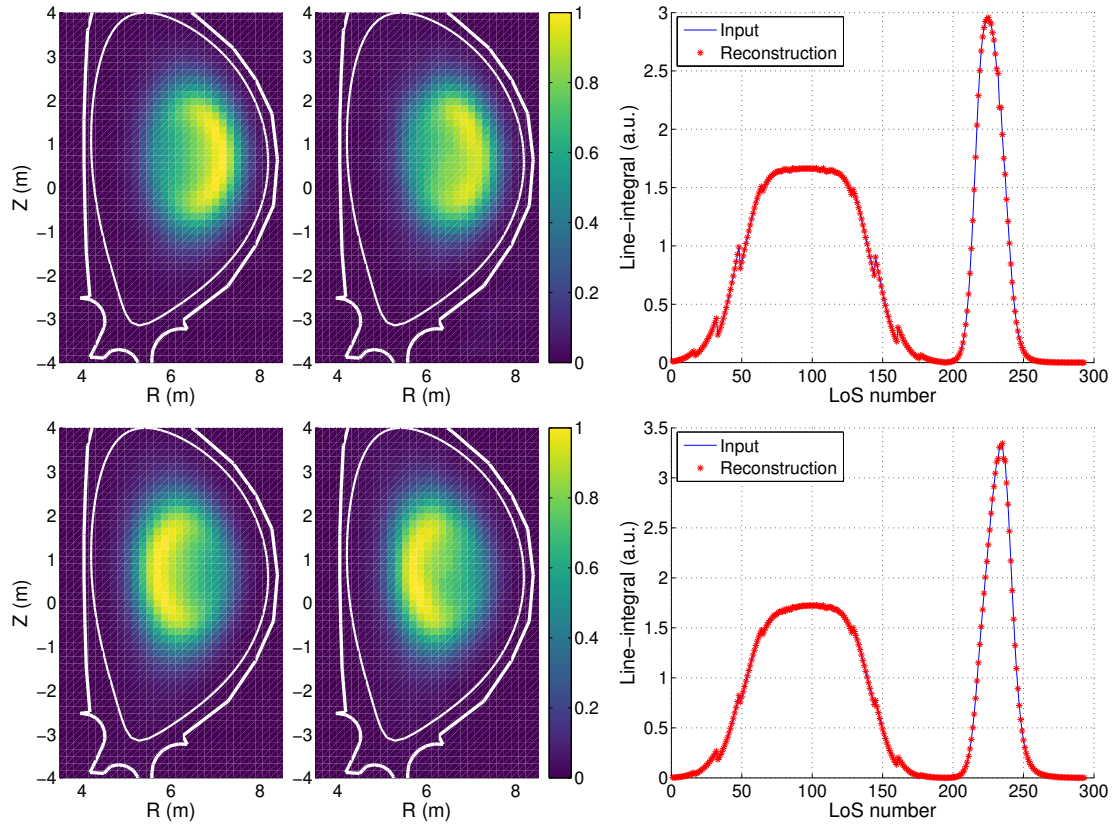


Figure 5.12 – Phantom emissivity profile (left), tomographic reconstruction (center) and line-integrated emissivity (right) of different emissivity configurations with the theoretical lines-of-sight configuration. First row: LFS asymmetry. Second row: HFS asymmetry.

The LFS asymmetry profile exhibits a very high improvement from the addition of the vertical lines-of-sight. The line-integrals, and the shape and amplitude of the emissivity seem well reconstructed. The inspection of the figures of merit confirms the previous observation: RMS_{tomo}^{core} has improved by around a factor 10, and RMS_{tomo}^{LCMS} has decreased by a factor 7. The fitting of the line-integrals has decreased by 3 orders

of magnitude. However, the visual agreement between the input and reconstructed line-integrals is good and therefore such a value of RMS_{line} is still considered acceptable.

The reconstruction of the HFS asymmetry profile also is significantly improved in the theoretical lines-of-sight configuration. Visual inspection of the input and emissivity profiles shows a good agreement between them, and the lines-integral of the emissivity are as well accurately reconstructed. Quantitative comparison of the figures of merit confirms this observation: RMS_{tomo}^{core} has decreased by factor of around 7, RMS_{tomo}^{LCMS} has been divided by 3. RMS_{line} has increased by a factor 10, but is still below 0.1.

Overall, the addition of vertical lines-of-sight proves to be very beneficial to the accuracy of the tomographic reconstruction. The vertical lines-of-sight provide information on the radial distribution of the emissivity, which is mandatory for X-ray tomography. Radially asymmetric profiles which could not be identified as such in a radial configuration are not properly reconstructed. Even radially symmetric profiles benefit from the additional lines-of-sight and are reconstructed more precisely.

5.4 Geometry proposal

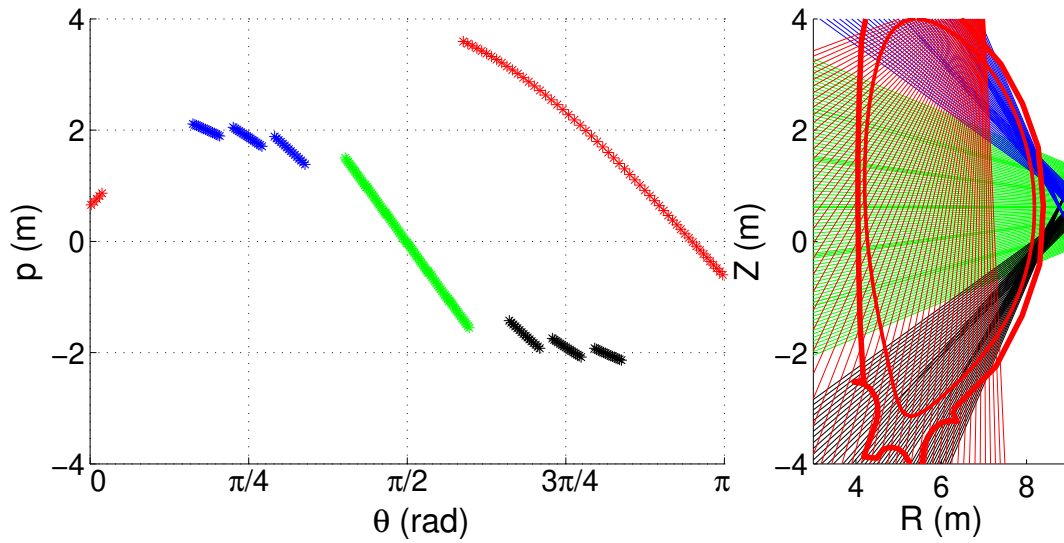


Figure 5.13 – Left: Sinogram of the 60 vertical lines-of-sight configuration. Right: Geometry of the associated lines-of-sight.

The necessity to use both radial and vertical lines-of-sight for accurate tomographic reconstruction of radially asymmetric emissivity profiles has been demonstrated in section 5.3. However, the vertical lines-of-sight used in the scope of that demonstration cannot be implemented on ITER as they would require drilling holes in the

vacuum vessel. In this section, two sets of vertical lines-of-sight which are compliant with the ITER geometry are investigated for tomography. The additional lines-of-sight are located in an upper port plug, and have an orientation close to the one of the theoretical configuration vertical lines-of-sight. The main difference is that the coverage of the plasma is mainly limited to the high field side. A first set of lines-of-sight is made of 60 vertical lines-of-sight scanning the plasma from the high field side to $r/a \approx 0.5$. It is referred to as the *60 vertical lines-of-sight configuration*. The second set covers the plasma from the high field side to the magnetic axis through 44 lines-of-sight and is referred to as *44 vertical lines-of-sight configuration*.

5.4.1 60 vertical lines-of-sight configuration

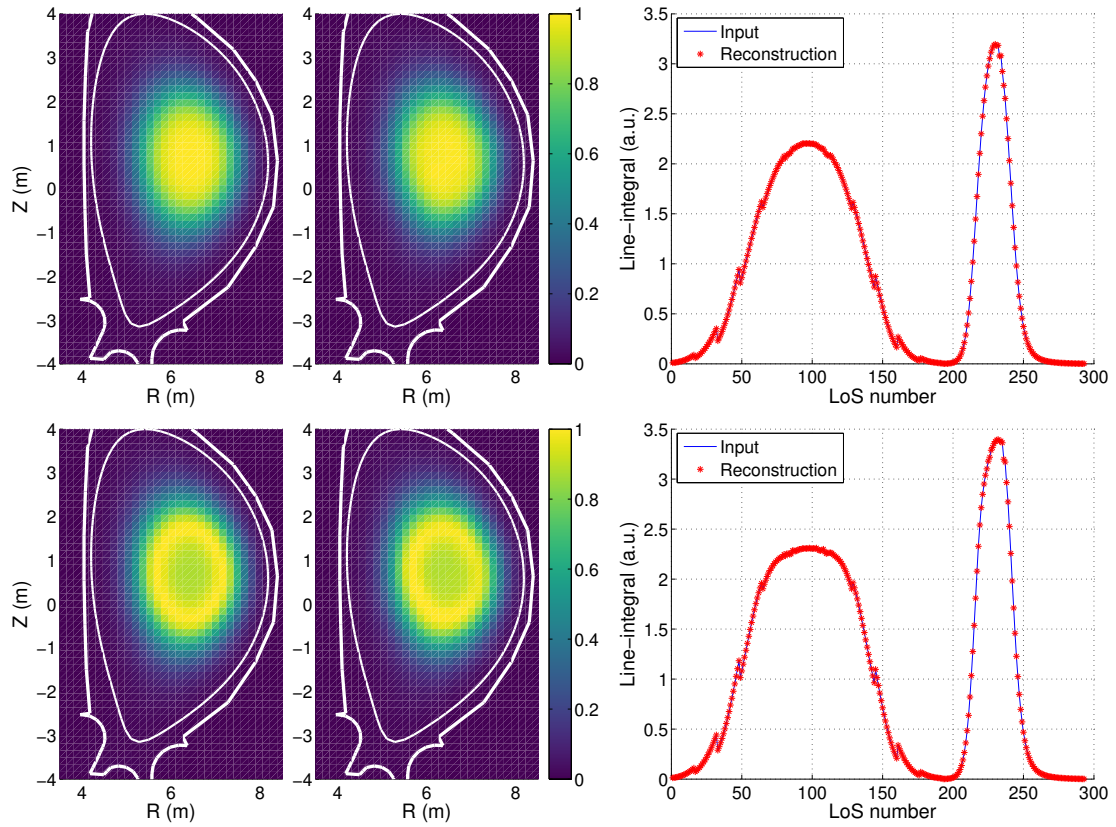


Figure 5.14 – Phantom emissivity profile (left), tomographic reconstruction (center) and line-integrated emissivity (right) of different emissivity configurations with the 60 vertical lines-of-sight configuration. First row: Gaussian emissivity profile. Second row: Hollow emissivity profile.

The sinogram of the 60 vertical lines-of-sight configuration is shown on figure 5.13. The coverage of the (p, θ) space is close to the one of the theoretical configuration,

with a loss of information in the $\theta = [0, \pi/4]$ range. The results of tomographic reconstruction using the 60 vertical lines-of-sight configuration are shown on table 5.3, figure 5.14 and figure 5.15.

Visually, the gaussian emissivity profile seems very well reconstructed and the same goes for the lines-integral. Comparing the figures of merit shows that the accuracy of the reconstruction in the plasma core is slightly better than for the theoretical configuration, but the difference is not significant compared to the other improvements observed in this study. In the LCMS-enclosed region, the theoretical configuration is more accurate with around 20% of improvement in RMS_{tomo}^{LCMS} .

The hollow emissivity profile exhibits a similar reconstruction: its shape, amplitude and line-integrals seem very well reconstructed and the associated figures of merit are slightly lower than those of the theoretical configuration in the plasma core and slightly higher in the LCMS-enclosed region.

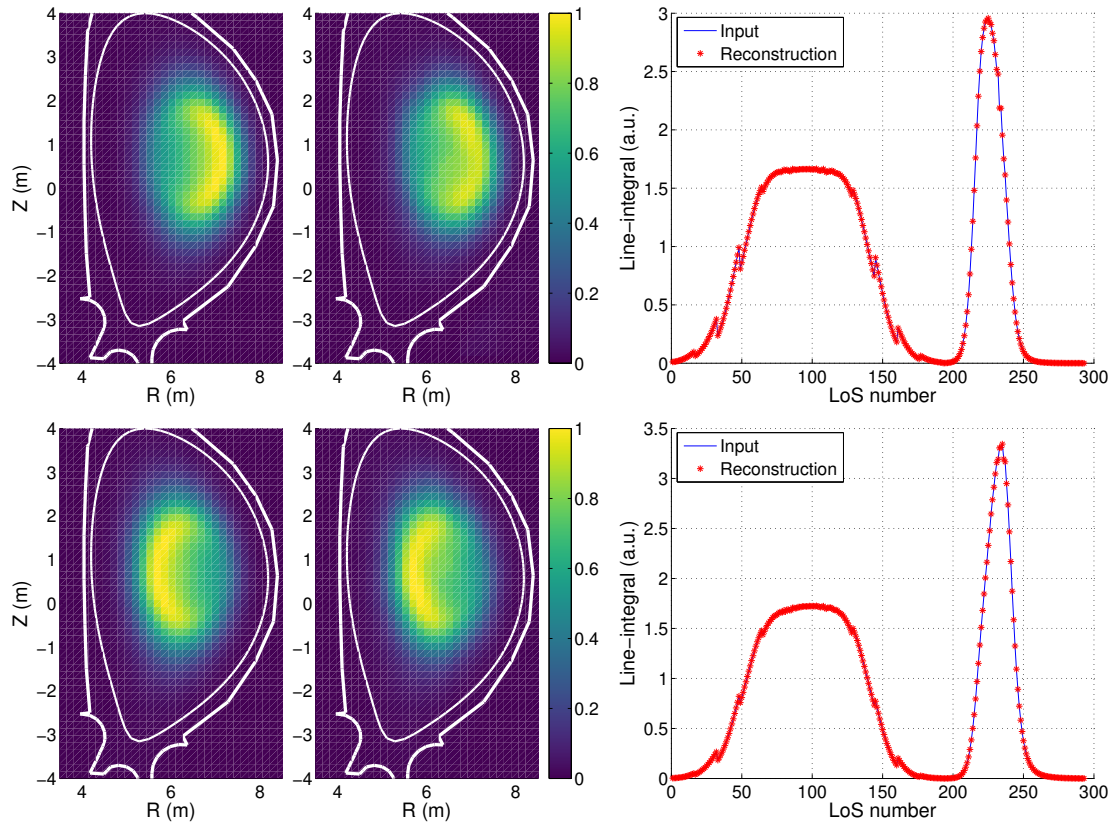


Figure 5.15 – Phantom emissivity profile (left), tomographic reconstruction (center) and line-integrated emissivity (right) of different emissivity configurations with 60 vertical lines-of-sight configuration. First row: LFS asymmetry. Second row: HFS asymmetry.

The LFS asymmetry profile exhibits a good visual agreement between the emissivity and its reconstruction. There has however been a decrease in the reconstruction

accuracy of around 30% in the plasma core and 15% in the LCMS-enclosed region, but the associated figures of merit still have a low value.

Similarly to the LFS profile, the HFS asymmetry profile is well reconstructed both in terms of shape, amplitude, and line-integrals. The value of RMS_{tomo}^{core} is very close to the one obtained in the theoretical configuration while RMS_{tomo}^{LCMS} has increased of around 30%.

Overall, the 60 vertical lines-of-sight allows an accurate reconstruction of the phantom profiles. The difference in the reconstruction of radially symmetric profiles is almost negligible in comparison with the theoretical configuration. Radially asymmetric profiles exhibit a higher drop of quality in the tomographic reconstruction but the associated reconstructed profiles are still quite accurate. The LFS asymmetry emissivity profile suffers from the lack of lines-of-sight in the LFS region where most of the emissivity is located, but the shape is well reconstructed whatsoever.

	Gaussian	Hollow	LFS asymmetry	HFS asymmetry
RMS_{tomo}^{core}	$1.8 \cdot 10^{-2}$	$1.6 \cdot 10^{-2}$	$6.4 \cdot 10^{-2}$	$4.3 \cdot 10^{-2}$
RMS_{tomo}^{LCMS}	$8.2 \cdot 10^{-2}$	$7.4 \cdot 10^{-2}$	$9.1 \cdot 10^{-1}$	$4.4 \cdot 10^{-1}$
RMS_{line}	$1.6 \cdot 10^{-3}$	$1.4 \cdot 10^{-3}$	$9.8 \cdot 10^{-2}$	$1.7 \cdot 10^{-2}$

Table 5.3 – Figures of merit for tomographic reconstruction of phantom emissivity profiles with the 60 vertical lines-of-sight configuration.

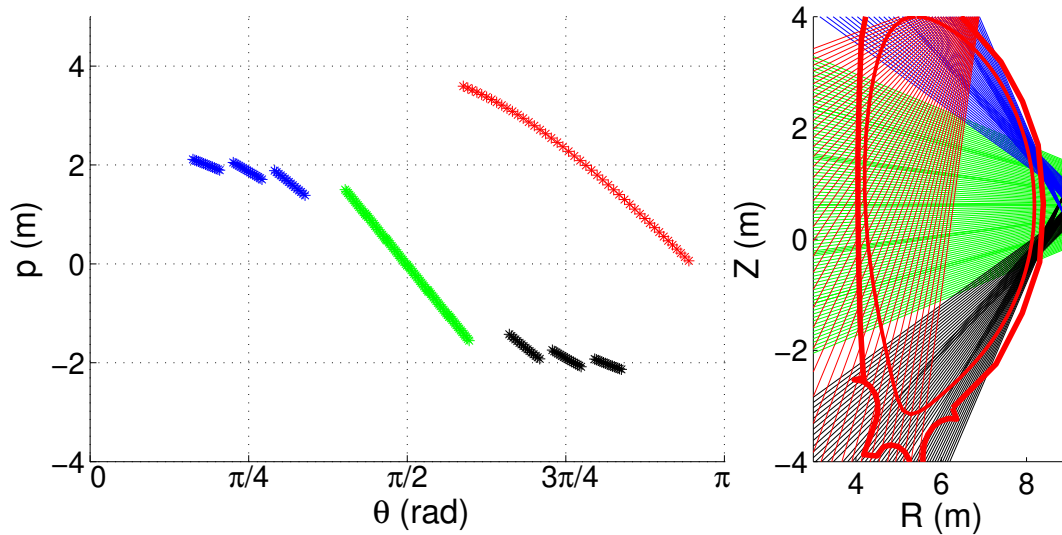


Figure 5.16 – Left: Sinogram of the 44 vertical lines-of-sight configuration. Right: Geometry of the associated lines-of-sight.

5.4.2 44 vertical lines-of-sight configuration

	Gaussian	Hollow	LFS asymmetry	HFS asymmetry
RMS_{tomo}^{core}	$1.8 \cdot 10^{-2}$	$2.2 \cdot 10^{-2}$	$1.1 \cdot 10^{-1}$	$5.1 \cdot 10^{-2}$
RMS_{tomo}^{LCMS}	$8.5 \cdot 10^{-2}$	$8.1 \cdot 10^{-2}$	$8.4 \cdot 10^{-1}$	$4.3 \cdot 10^{-1}$
RMS_{line}	$1.5 \cdot 10^{-3}$	$1.4 \cdot 10^{-3}$	$3.7 \cdot 10^{-2}$	$2.0 \cdot 10^{-2}$

Table 5.4 – Figures of merit for tomographic reconstruction of phantom emissivity profiles with the 44 vertical lines-of-sight configuration.

The sinogram associated with the 44 vertical lines-of-sight configuration is displayed on figure 5.16. The loss of vertical lines-of-sight can be seen around $\theta = 0$ and $\theta = \pi$. The results of tomographic reconstruction of the phantom emissivity profiles is shown on table 5.4, figure 5.17, and figure 5.18.

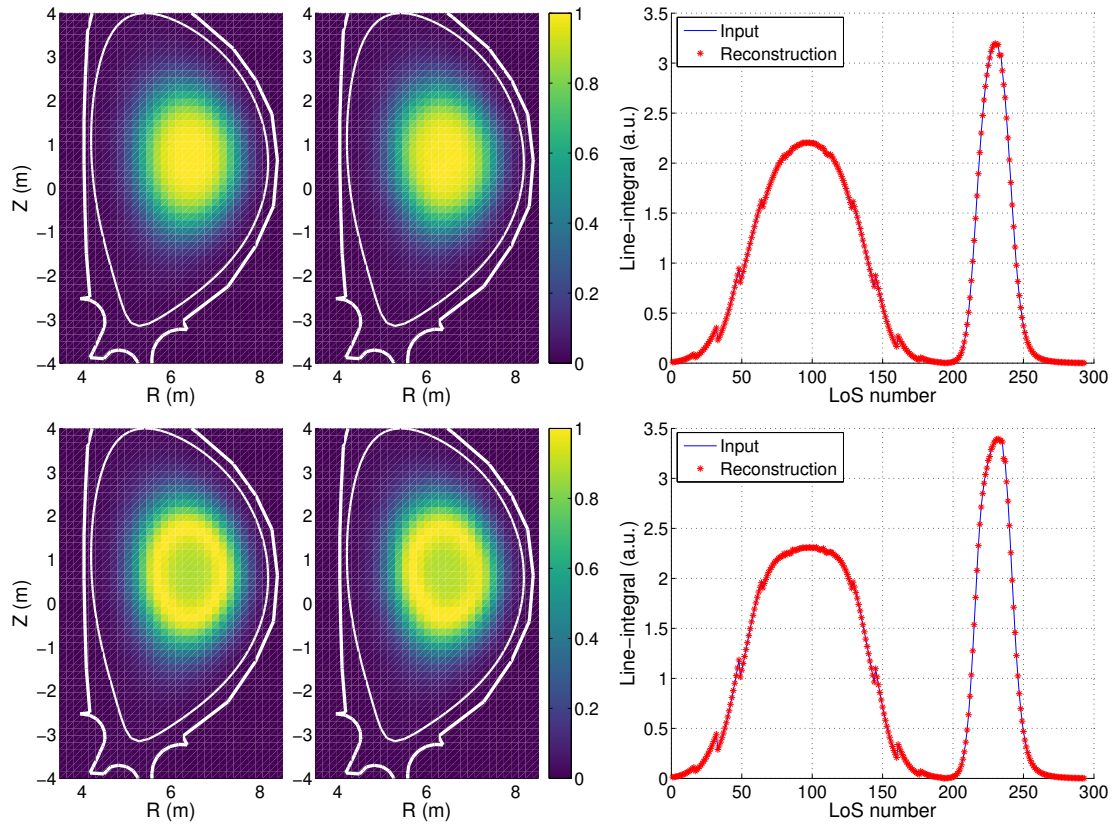


Figure 5.17 – Phantom emissivity profile (left), tomographic reconstruction (center) and line-integrated emissivity (right) of different emissivity configurations with the 44 vertical lines-of-sight configuration. First row: Gaussian emissivity profile. Second row: Hollow emissivity profile.

The reconstruction of the gaussian profile is very accurate, and so is the fitting of

the line-integrals. The associated figures of merit are very close to those of the 60 vertical lines-of-sight configuration, although slightly higher. A bit more difference can be noticed when comparing the hollow emissivity profile, with an increase of RMS_{tomo}^{core} of around 40%. However, the RMS_{tomo} figures of merit remain of the order of magnitude of 10^{-2} and are therefore considered very low.

Visual inspection of the reconstruction of the LFS asymmetric profile indicates that the overall amplitude, shape and line-integrals of the profile are pretty well reconstructed. The definition of the asymmetry in the core seems to have decreased, the profile seems slightly blurry in this area. The RMS_{tomo}^{core} has increased by around 70% between the 60 and 44 vertical lines-of-sight configurations, and is more than twice the RMS_{tomo}^{core} of the theoretical configuration. In the LCMS-enclosed region, the figure of merit has not changed significantly, a slight improvement can even be noticed when comparing with the 60 vertical lines-of-sight configuration.

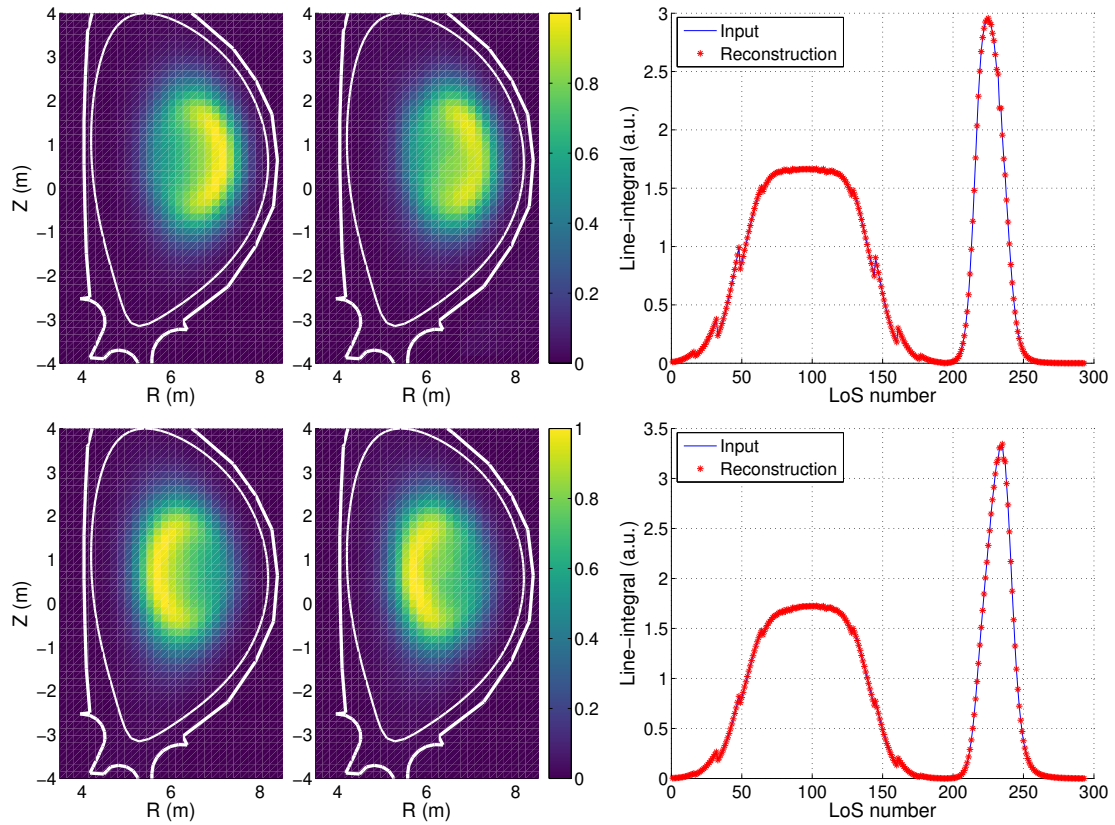


Figure 5.18 – Phantom emissivity profile (left), tomographic reconstruction (center) and line-integrated emissivity (right) of different emissivity configurations with the 44 vertical lines-of-sight configuration. First row: LFS asymmetry. Second row: HFS asymmetry.

Tomographic reconstruction of the HFS asymmetric profile seems accurate. The investigation of the figures of merit shows that there is a small loss of precision compared

to the 60 vertical lines-of-sight configuration: RMS_{tomo}^{core} has increased by around 20%. RMS_{tomo}^{LCMS} exhibits a small improvement, which is not significant. The comparison of both lines-of-sight configurations allows the investigation of the impact of radial coverage of the plasma on the reconstruction. For radially symmetric profiles, a lack of radial coverage decreases the accuracy of the reconstructed profile but this loss of accuracy is very limited and both configurations can be considered equivalent. When it comes to radially asymmetric profiles, the loss of accuracy is more pronounced and mostly depends on whether the main emissivity region is covered by lines-of-sight. In the case of the HFS profile, both configuration have the same coverage of the asymmetry and the consequence of the lower amount of lines-of-sight is small. In the case of the LFS profile, the 60 vertical lines-of-sight configuration exhibits a better coverage of the asymmetry and the improvement of the quality of reconstruction is significant. As a result, the 60 vertical lines-of-sight configuration will be used for tomographic reconstructions in the scope of this thesis. The geometrical etendues corresponding to this geometry are displayed on figure 5.19.

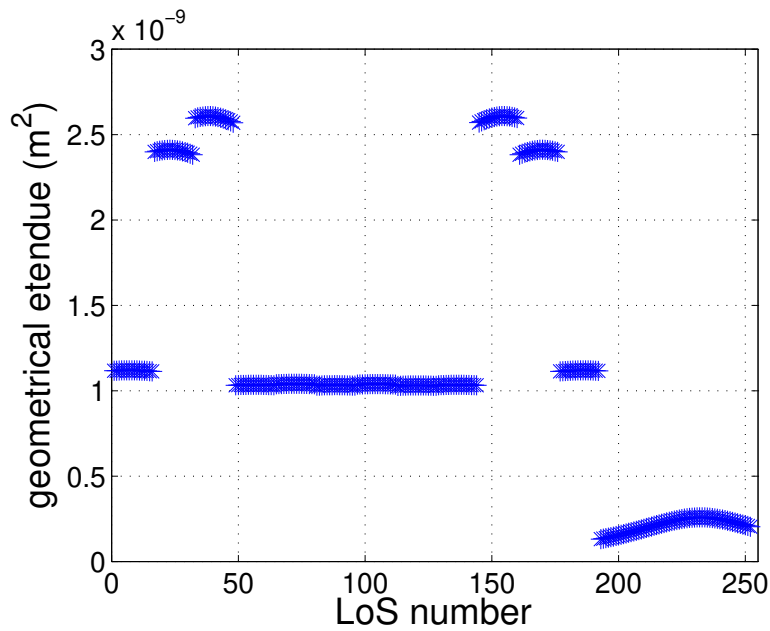


Figure 5.19 – Geometrical etendue for each 60 vertical lines-of-sight configuration.

6 Application of the synthetic diagnostic

Sommaire

6.1	X-ray measurement on ITER with Low Voltage Ionization Chambers . .	127
6.1.1	Influence of the filling gas	128
6.1.2	Influence of the filter	130
6.1.3	Influence of the length pressure product	130
6.2	Calibration of the LVIC measured current	131
6.2.1	Calibration methodology	132
6.2.2	Line-of-sight dependency of the calibration factor	134
6.2.3	Application to simulation results	134
6.3	Tomography using LVIC	136
6.3.1	Tomographic reconstruction of a SXR-restricted emissivity profile	136
6.3.2	Influence of the calibration method on the tomographic recon- struction	141
6.3.3	Tomographic reconstruction over a wide energy range	142
6.3.4	Influence of perturbative noise on the tomographic reconstruction	143
6.3.5	Alternative calibration method	145

6.1 X-ray measurement on ITER with Low Voltage Ionization Chambers

The synthetic diagnostic tool presented in section 4 is used to simulate the LVIC on the high power D-T emissivity scenario presented in section 2.4.1 in the *60 vertical lines-of-sight configuration* introduced in section 5.4.1. The simulation of the detector allows the investigation of the influence of its design parameters (e.g. gas filler, filter, chamber length or gas pressure).

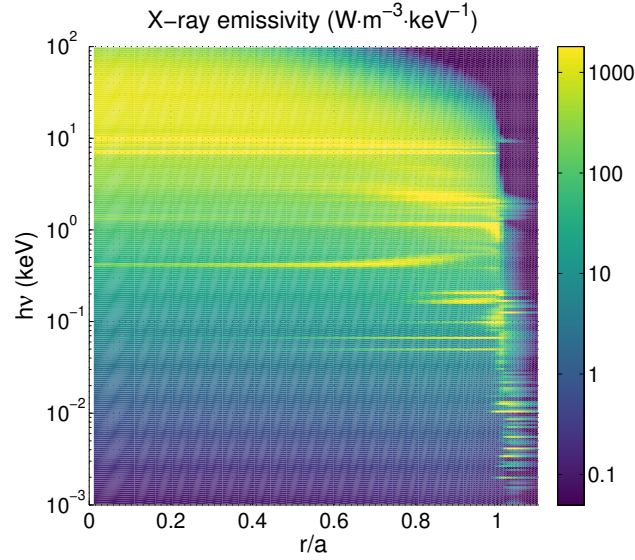


Figure 6.1 – Radiated power profile as a function of photon energy and normalized radius for the standard high power D-T scenario.

In the plasma core, displayed on figure 6.1 for $r/a < 0.5$, it can be noted that the emissivity profile is flat at low energy ($h\nu < 10\text{keV}$). Most of the core emissivity is located at high energies (and in the iron and tungsten line emissions which are spread over the whole plasma). Therefore, when measuring the plasma core (LoS 49-144 and 200-220), the shape of the current profile can give information on the detected energy range. A flat current profile (as seen for $1\text{mm} \cdot \text{atm}$ of xenon) indicates that the detector does not measure photons over 10 keV, and a higher amplitude of the bell shape indicates that the detector measures higher energy photons.

6.1.1 Influence of the filling gas

As seen in section 4.3.1.2, the sensitivity and upper limit of the energy detection range of the detector depend directly on the gas filling the LVIC. The collected currents for two LVIC filled with argon and xenon are displayed on figure 6.2. The product of gas pressure and chamber length is $50\text{mm} \cdot \text{atm}$ and the photon flux is filtered by $200\mu\text{m}$ of beryllium.

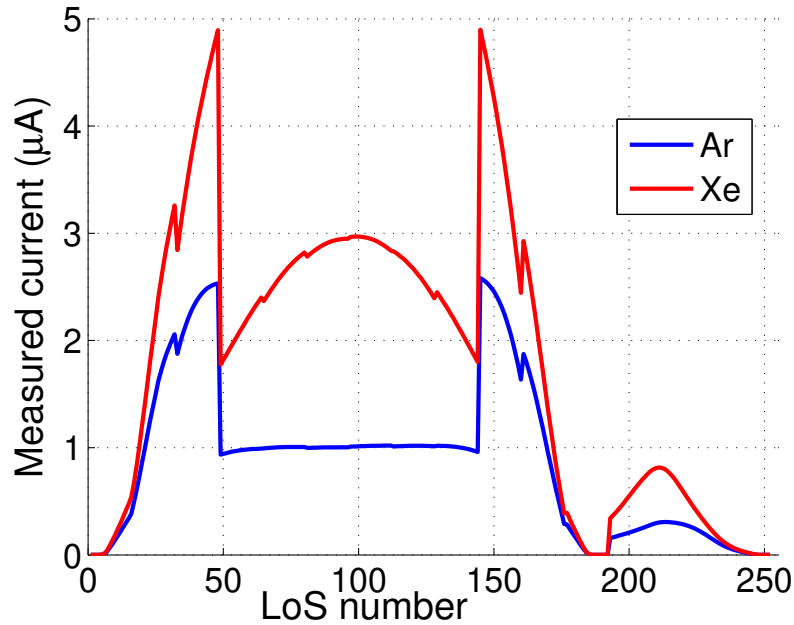


Figure 6.2 – Current collected by a LVIC filled with argon (blue) or xenon (red) in the high power D-T emissivity scenario. The chamber has a pressure length product of $50\text{mm} \cdot \text{atm}$ and a filter made of $200\mu\text{m}$ of beryllium.

The overall shape of the current profiles is consistent with the geometrical etendues presented in figure 5.19. The steps which can be observed at channels #32, #48, #144 and #160 are explained by the fact that different cameras are used and show the transition from a camera to another. The transition from radial X-ray cameras to the vertical lines-of-sight does not lead to a discontinuity in the measured current as the last radial line-of-sight and the first vertical line-of-sight are both aimed at the very edge of the plasma and therefore both collect an electrical current close to 0.

It can be noted on figure 6.2 that a xenon-filled LVIC collects a higher current than an argon-filled LVIC. Several factors explain this trend. Firstly, the detection probability is higher for xenon than argon. Therefore, more photons are detected in the xenon chamber. Secondly, the mean ionization energy is lower for xenon which means that more electrons are ionized in xenon for a photon at the same energy. Thirdly, x-ray fluorescence affects a wider energy range for argon than xenon due to its lower energy threshold and therefore argon chambers experience a higher loss of charge due to x-ray fluorescence.

The measured current in the detectors looking at the plasma core is constant for argon and bell-shaped for xenon, which indicates that the detection range is wider for xenon than it is for argon.

6.1.2 Influence of the filter

The filters are used to define the lower limit of the detection range. Indeed, figure 4.11 shows that there is no transmission through filters below a certain threshold and that the transmission ratio quickly increases to 1 after the threshold. The main characteristic of a filter is therefore the energy threshold under which the photons are absorbed in the filter.

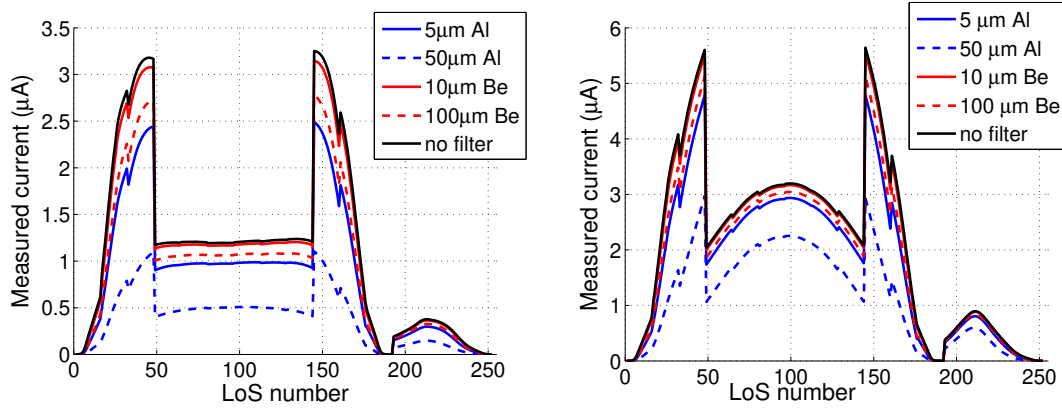


Figure 6.3 – Current collected by an argon-filled (left) and xenon-filled (right) LVIC with different filters. The chamber has a pressure length product of $50\text{mm} \cdot \text{atm}$ and the emissivity comes from the high power D-T emissivity scenario.

Inspection of figure 6.3 shows that aluminium absorbs photons up to a higher energy than beryllium. The effect of the beryllium window on the measured current is quite low. The fact that a beryllium window is transparent to photons of energy higher than a couple keV (depending on the width of the filter) is the reason why beryllium windows are used for X-ray filtering. With increasing filter width, the threshold energy of the filter increases and therefore the measured current decreases.

As argon-filled chambers have a more narrow detection range than xenon, the low energy part of the spectrum generates a more significant part of the measured current and therefore the current measured by an argon-filled LVIC is more affected by the filter than xenon. Similarly, the detectors looking at the plasma core are less affected by the filter because most of the flux detected in the chamber are not absorbed in the filter. One can notice that with increasing filter length the bell shape of the current measured by LoS 49 to 144 is mildly enhanced.

6.1.3 Influence of the length pressure product

For a given gas, the sensitivity and therefore the upper limit of the detection range of the LVIC are defined by the length pressure product of the chamber. It can indeed be observed on figure 6.4 that the measured current increases with the chamber length

and/or gas pressure.

For detectors looking towards the plasma edge (LoS 1-20, 172-192, and 230-252), the measured current seem to "saturate" once a certain length pressure product is reached ($50\text{ mm}\cdot\text{atm}$ for argon and $10\text{ mm}\cdot\text{atm}$ for xenon). After a certain limit, all the photon flux impinging these detectors is measured due to the high sensitivity.

For the detectors looking at the core (LoS 49-144 and 200-220) the bell-shape of the current is enhanced with chamber length and and/or pressure as a result of the increase in the upper limit of the detection range.

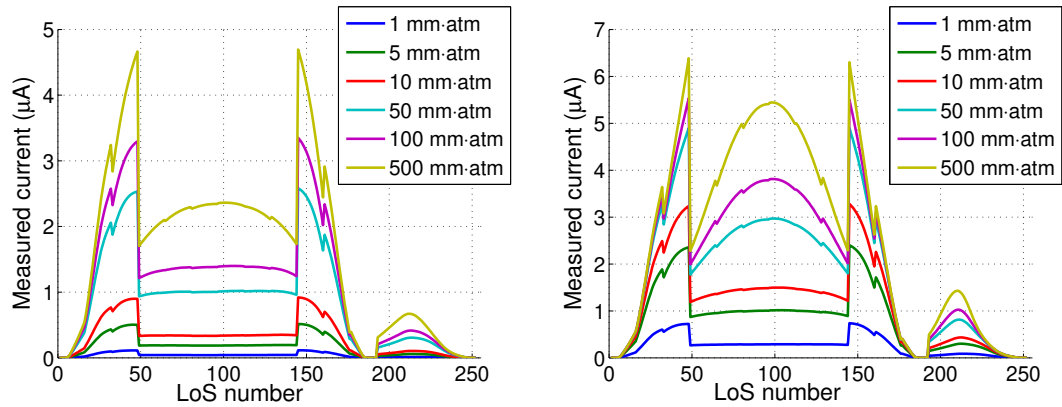


Figure 6.4 – Current collected by an argon-filled (left) and xenon-filled (right) LVIC with different length pressure products. The filter is made of $200\mu\text{m}$ and the emissivity comes from the high power D-T emissivity scenario.

6.2 Calibration of the LVIC measured current

In order to extract physically meaningful information on the plasma from the current measured by a LVIC, it is necessary to convert the detector output into a physical quantity. We thus aim at converting current into the integrated X-ray emissivity over the detector's line-of-sight (in $\text{W}\cdot\text{m}^{-2}$), which can be used as input for tomography. In the context of the approximations described in section 4.1, the line integrated X-ray emissivity is equal to the total x-ray power impacting the detector divided by its etendue.

This calibration depends on the parameters of the chamber (e.g gas, length, pressure) and the incoming photon flux (dependency which we aim at eliminating). This section describes the method used to calculate a calibration coefficient for the LVIC currents before applying it to synthetic diagnostic simulations results.

6.2.1 Calibration methodology

The tomographic inversion problem can be defined as:

$$f^\eta = \frac{P_X^\eta}{E} = \int_{LoS} \int_0^\infty \varepsilon(h\nu, \vec{r}) \cdot \eta(h\nu) \cdot d h\nu \cdot d r_{LoS} = \int_{LoS} \varepsilon_X^\eta(\vec{r}) \cdot d r_{LoS} \quad (6.1)$$

With f^η the line-integrated brightness in $W \cdot m^{-2}$ used as an input for the tomographic inversion, P_X^η the total power effectively detected by the LVIC in W , E the geometrical etendue in m^2 , $h\nu$ the photon energy in eV , $\varepsilon(h\nu, \vec{r})$ the plasma spectral emissivity in $W \cdot eV^{-1} \cdot m^{-3}$, η the spectral response of the detector (including transmission through the filters), and $\varepsilon_X^\eta(\vec{r})$ the LVIC-filtered emissivity field to be reconstructed in $W \cdot m^{-3}$. Here we can notice the relation:

$$\varphi(h\nu) = E \int_{LoS} \frac{\varepsilon(h\nu, \vec{r})}{h\nu \cdot e} \cdot d r_{LoS} \quad (6.2)$$

Where $\varphi(h\nu)$ is the surface integrated photon flux impacting the detector surface in $ph \cdot s^{-1} \cdot eV^{-1}$ and e is the elementary charge ($1.6 \cdot 10^{-19} C$) used to convert J into eV. $\varphi(h\nu)$ is per eV in order to take into account the energy binning. The total incoming photon flux of the i -th energy bin is given by: $\varphi^{tot}(i) = \varphi(h\nu(i)) \cdot d h\nu(i)$ where $d h\nu(i)$ is the width of the i -th energy bin in eV. Therefore:

$$\int_{LoS} \varepsilon(h\nu, \vec{r}) \cdot d r_{LoS} = \frac{h\nu \cdot e}{E} \cdot \varphi(h\nu) \quad (6.3)$$

The tomographic problem can then be re-written as:

$$f^\eta = \frac{P_X^\eta}{E} = \frac{e}{E} \int_0^\infty h\nu \cdot \eta(h\nu) \cdot \varphi(h\nu) \cdot d h\nu \quad (6.4)$$

If we neglect the influence of the escape peaks on the collected charge, the raw current output obtained from a LVIC can be expressed as:

$$I_\eta = e \int_0^\infty \frac{h\nu}{W} \cdot \eta(h\nu) \cdot \varphi(h\nu) \cdot d h\nu \quad (6.5)$$

where W the mean ionization energy of the gas in eV, and η the spectral response of the detector (including transmission through the filters) in ph^{-1} .

Therefore, we obtain:

$$f^\eta = \frac{P_X^\eta}{E} = \frac{W}{E} \cdot I_{LVIC} \quad (6.6)$$

However, the ultimate goal is to reconstruct the total (i.e. non-filtered) 2D emissivity field $\varepsilon(\vec{r})$:

$$f_{tot} = \frac{P_{tot}}{E} = \int_{LoS} \int_0^\infty \varepsilon(h\nu, \vec{r}) \cdot d h\nu \cdot d r_{LoS} = \int_{LoS} \varepsilon_{tot}(\vec{r}) \cdot d r_{LoS} \quad (6.7)$$

This can be performed using the fact that:

$$f_{tot} = \frac{P_{tot}}{E} \cdot \frac{P_X^\eta}{P_X^\eta} = \frac{I_{LVIC} \cdot W}{E} \cdot \frac{P_{tot}}{P_X^\eta} = C_{cal} \cdot I_{LVIC} \quad (6.8)$$

Where C_{cal} is a calibration coefficient used to determine the total line-integrated brightness (in $W \cdot m^{-2}$) from the electric current collected I_{LVIC} . The expression of the calibration coefficient is thus:

$$C_{cal} = \frac{W}{E} \cdot \frac{\int_0^\infty h\nu \cdot \varphi(h\nu) \cdot dh\nu}{\int_0^\infty h\nu \cdot \eta(h\nu) \cdot \varphi(h\nu) \cdot dh\nu} = \frac{W}{E \cdot \langle \eta \rangle} \quad (6.9)$$

Where $\langle \eta \rangle = \frac{\int_0^\infty h\nu \cdot \eta(h\nu) \cdot \varphi(h\nu) \cdot dh\nu}{\int_0^\infty h\nu \cdot \varphi(h\nu) \cdot dh\nu}$ is the average of the spectral response weighted by the incoming energy flux.

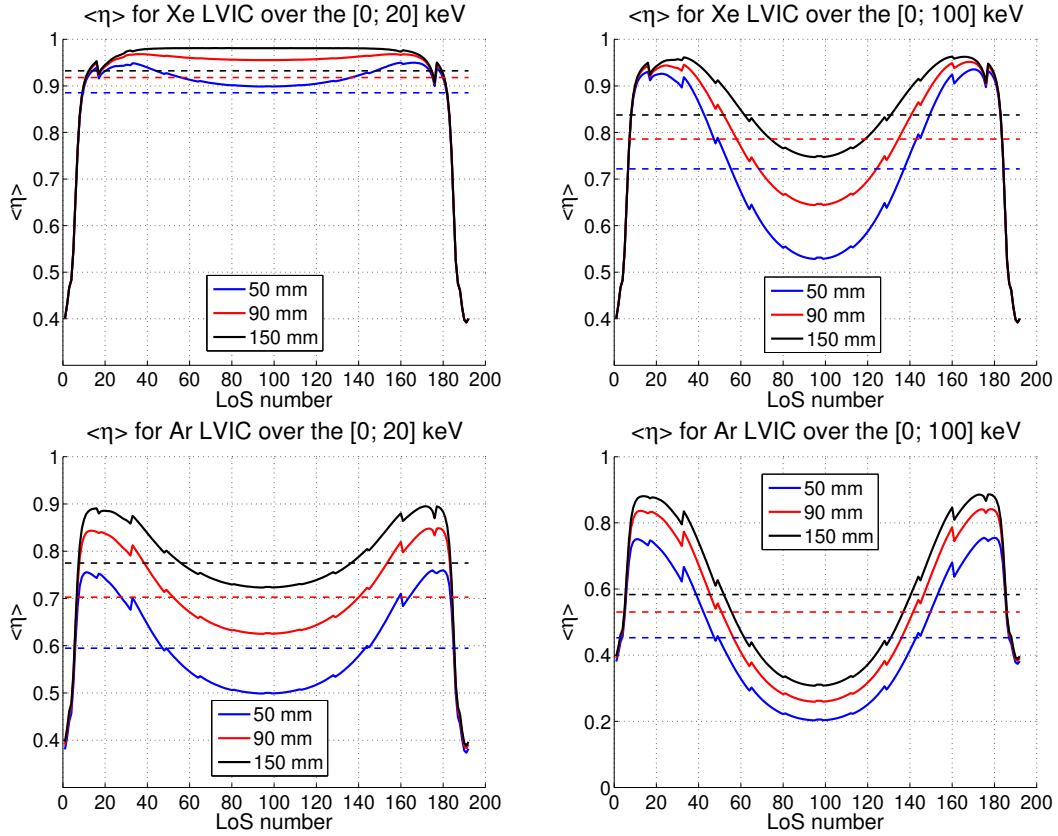


Figure 6.5 – $\langle \eta \rangle$ for each channel for various incoming flux, gas, and length (for a gas pressure of 1 bar). Top left: Xe LVIC with high power D-T scenario emissivity restricted to [0, 20] keV. Top right: Xe LVIC with high power D-T scenario emissivity up to 100 keV. Bottom left: Ar LVIC with high power D-T scenario emissivity restricted to [0, 20] keV. Bottom right: Ar LVIC with high power D-T scenario emissivity up to 100 keV.

The calibration coefficient previously calculated in equation 6.9 is different for each line-of-sight as it depends on the incoming photon flux.

6.2.2 Line-of-sight dependency of the calibration factor

For measurements performed during plasma experiments, it is not possible to calculate the calibration coefficient of equation 6.9 as it requires precise knowledge of the incoming photon flux. Through studies of different experimental plasma scenarios, a set of calibration coefficients can be established for various plasma parameters and used for real-time measurements. Another solution to eliminate the line-of-sight dependency of the calibration factors is to perform x-ray energy discrimination which would give an estimation of the incoming spectrum. Energy discrimination using LVICs is developed in section 8. However, in this section, none of these approaches are considered. In order to simulate a measurement without *a priori* information on the incoming flux, a constant calibration coefficient will be used for all the x-ray cameras. The parameters which affect the accuracy of this calibration approach are discussed in this section.

The variable part of the calibration coefficient ($\langle \eta \rangle$) is displayed in figure 6.5. One can notice that $\langle \eta \rangle$ exhibits a hollow shape. This hollowness limits the accuracy of calibration with a constant coefficient and decreases with the spectral response of the detector. It can indeed be observed in figure 6.5 that the hollowness decreases with the length pressure product. The use of xenon instead of argon (comparison between the top and bottom lines of figure 6.5) as well as a reduction of the considered energy range (comparison between the left and right columns of figure 6.5) lead to an increase in the spectral response of the chamber and therefore tend to flatten the $\langle \eta \rangle$ curve. In the case of a $150\text{mm} \cdot \text{atm}$ chamber filled with xenon reconstructing an incoming flux restricted to $[1, 20]$ keV (in the upper left corner of figure 6.5), the $\langle \eta \rangle$ has a plateau shape which offers a constant coefficient calibration for most of the lines-of-sight.

In this section, calibration has been conducted by averaging the coefficients over all the different lines-of-sight. The resulting coefficient is displayed by a dashed line on figure 6.5. This method leads to significant discrepancy between the line-integrated emissivity and the calibrated current because of the difference between $\langle \eta \rangle$ and its average. This limitation can be reduced by increasing the spectral response, using the parameters listed previously. The consequence of averaging $\langle \eta \rangle$ is an incorrect tomography input leading to tomographic reconstruction artefacts. These will be covered in sections 6.3.1 and 6.3.2.

6.2.3 Application to simulation results

The calibration method has been applied to different configurations (gas, length and/or pressure) of LVICs for validation purposes. The calibrated output of $50\text{mm} \cdot \text{atm}$ LVICs filled with xenon is shown on figure 6.6. The LVIC currents obtained in

this simulation are displayed on the right part of figure 6.4. When the simulated and reconstructed line-integrated X-ray powers are compared in the wide energy range $[0, 100]$ keV (left part of figure 6.6), a significant discrepancy can be noticed in the plasma core: the plasma emission is underestimated by more than 30%. This is explained by the spectral response of the detectors that decreases significantly for photons of energy higher than ~ 30 keV which do not have a high enough detection probability to be reconstructed. The reconstruction of the line integrated emissivity over a shortened energy range $[0, 31]$ keV is shown on the right part of figure 6.6. An increased accuracy over the whole plasma can be observed. The measured energy range of a LVIC is defined as the energy range for which the reconstruction is the most accurate ($[0, 31]$ keV in the case of a $50\text{ mm} \cdot \text{atm}$ LVIC filled with xenon).

The effect of additional LVIC parameters on the quality of calibration have been investigated. They are presented in figure 6.7. We can observe that when the LVIC length pressure product is increased, the measured energy range is widened: $50\text{ mm} \cdot \text{atm}$ xenon-filled LVIC have a measured range of $[0, 31]$ keV while $150\text{ mm} \cdot \text{atm}$ xenon-filled LVIC have a measured range of $[0, 49]$ keV. The lower spectral response of argon causes the LVICs to reconstruct the plasma X-ray emission in the $[0, 23]$ keV range only, even with a high chamber depth. The differences observed in the reconstruction are only due to the calibration technique as no electronic noise was considered.

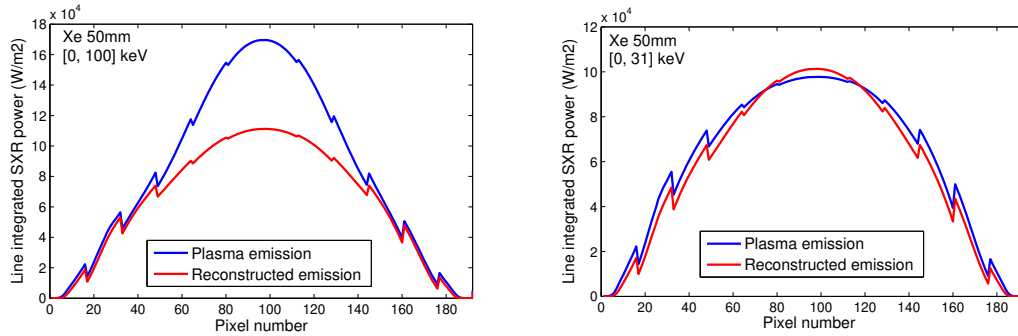


Figure 6.6 – Comparison of the reconstructed and original line-integrated plasma emission. Left: in the full spectral range $[0, 100]$ keV. Right: in the $[0, 31]$ keV range. Calibrated output are obtained from Xe LVICs ($50\text{ mm} \cdot \text{atm}$). The filter was made of $150\mu\text{m}$ of beryllium and $11\mu\text{m}$ of mylar.

The shape of the calibrated line-integrated plasma emissivity does not follow the input faithfully. Indeed, one can notice on figure 6.7 that the line-integrated emissivity in the core is underestimated with 150 mm of argon (right part of the figure). This discrepancy at the core is explained by the spectrum of the emissivity which is reconstructed. For detectors measuring mostly high energy photons, $\langle \eta \rangle$ is lower than the average and therefore overestimated by the calibration method. This leads to an underestimation of the calibration coefficient (see equation 6.9) and of the line-integrated emissivity.

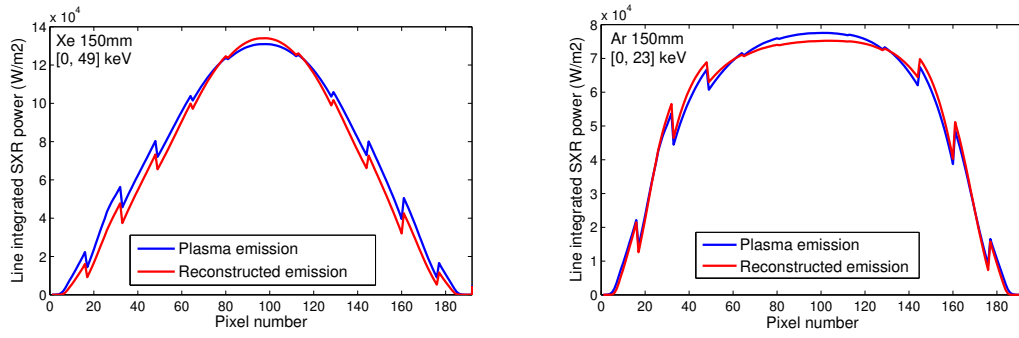


Figure 6.7 – Comparison of the reconstructed and original line-integrated plasma emission. Left: in the [0, 49] keV range. Right: in the [0, 23] keV range. Calibrated output are obtained from Xe (left) and Ar (right) LVICs (150 $mm \cdot atm$). The filter was made of 150 μm of beryllium and 11 μm of mylar.

In the case of xenon, the opposite phenomenon is observed. The xenon chambers looking towards the plasma core measure photons which are located outside of the energy range considered in the average calibration coefficient. Taking these photons into account would lead to an overall degradation of the quality of calibration, as shown in figure 6.6, and they can therefore be considered as a noise added to the measurement. As a result xenon chambers looking at the plasma core slightly overestimate the line-integrated X-ray power. Argon chambers also measure photons outside of their calibration energy range, but due to their low sensitivity it doesn't generate enough charges to overcome the undrestimation of the calibration coefficient.

6.3 Tomography using LVIC

The calibrated synthetic diagnostic tool presented in section 4 was used to reconstruct the SXR emissivity of a ITER high power D-T scenario.[33] A preliminary study was conducted with a restricted energy range from 1 eV to 20 keV before using the full available spectrum up to 100 keV.

6.3.1 Tomographic reconstruction of a SXR-restricted emissivity profile

In order to maximize the detectors spectral response and therefore limit the calibration errors, tomographic reconstruction has first been conducted on the shortened energy range [0, 20] keV. The considered emissivity profile exhibits a hollow shape and is presented in figure 6.8.

Gas length · pressure	Xenon $150mm \cdot atm$	Argon $150mm \cdot atm$	Argon (ideal calibration) $150mm \cdot atm$
RMS_{tomo}^{core}	$3.2 \cdot 10^{-2}$	$8.5 \cdot 10^{-2}$	$5.4 \cdot 10^{-2}$
RMS_{tomo}^{LCMS}	$3.1 \cdot 10^{-1}$	$2.4 \cdot 10^{-1}$	$2.2 \cdot 10^{-1}$
RMS_{line}	3.7	3.7	1.6

Table 6.1 – Figures of merit for tomographic reconstruction over $[0, 20]$ keV.

Soft X-ray emissivity ($W.m^{-3}$)

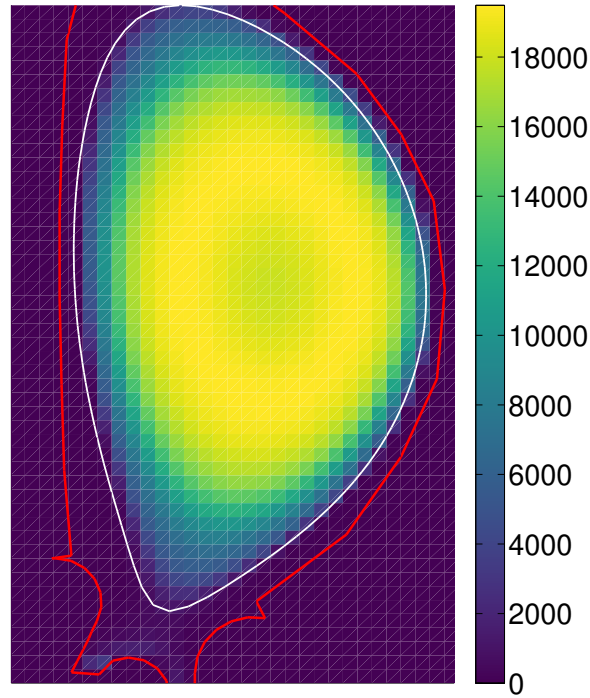


Figure 6.8 – Soft x-ray emissivity profile in the $[0, 20]$ keV range of a high power D-T ITER scenario.

The quality of reconstruction using argon and xenon is compared with $150 mm \cdot atm$ long ionization chambers. The results are displayed on figure 6.9 and table 6.1. Both configurations allow an accurate reconstruction of the emissivity in the plasma core region with low RMS_{tomo}^{core} . Xenon displays a better reconstruction in the core with more than a factor 2 of difference in RMS_{tomo}^{core} with argon. This is explained by its higher detection probability.

Argon exhibits reconstruction artefacts in the shape of two rings of very low reconstruction error. The explanation of the error shape is performed in the case of argon through the study of the radial and vertical cross-sections presented in figure 6.10. The vertical (resp: radial) cross-section of the reconstruction relative error is taken at the radial (resp: vertical) coordinate of the magnetic axis. The tomographic reconstruction

error for each pixel of the cross-section and the calibration error for each line-of-sight are compared. The vertical (resp: radial) coordinate of a line-of-sight is taken as the intersection between the line-of-sight and the radial (resp: vertical) cross-section line. The study of the vertical cross-section (left part of figure 6.10) shows that the calibration error is equal to 0 in four occasions: $Z = -3, -1, 2$ and 4m . The $Z=-3\text{m}$ and $Z=4\text{m}$ points are located out of the plasma and are therefore left out of this study. The two remaining points correspond to the coordinates of the interior ring with very low reconstruction error: $(6.59\text{m}, -0.6\text{m})$ and $(6.59\text{m}, 2\text{m})$.

The radial cross-section is displayed on the right part of figure 6.10. As the vertical lines-of-sight do not cover the whole plasma, the plot representing the calibration error stops at $Z \approx 7\text{m}$. The calibration error is equal to 0 for a single coordinate: $R = 5\text{m}$. This corresponds to the $(5\text{m}, 0.8\text{m})$ point which is located in the external ring with very low reconstruction error.

Due to the anisotropic regularization used in the tomographic reconstruction the three points obtained previously lead to two rings with almost no reconstruction error which follow the magnetic field lines. This confirms the idea that the observed artefacts are coming from the calibration method.

Higher relative errors are observed around the last closed magnetic surface (LCMS) in both cases as it is the region where the calibration coefficients are the furthest from their average value (see figure 6.5) and the SXR emissivity is the lowest. Tomography based on the Tikhonov method with Minimum Fisher Information is also expected to generate errors at the edges of the reconstruction region. [66, 102] The regions where there is a lack of information (i.e. zone with no line-of-sight overlapping) will be exhibiting most of these tomography induced artefacts. The two spikes observed in the bottom left part of figure 6.10 correspond to such artefacts and are therefore not related to calibration or to the low reconstruction error rings exhibited in the upper left plot.

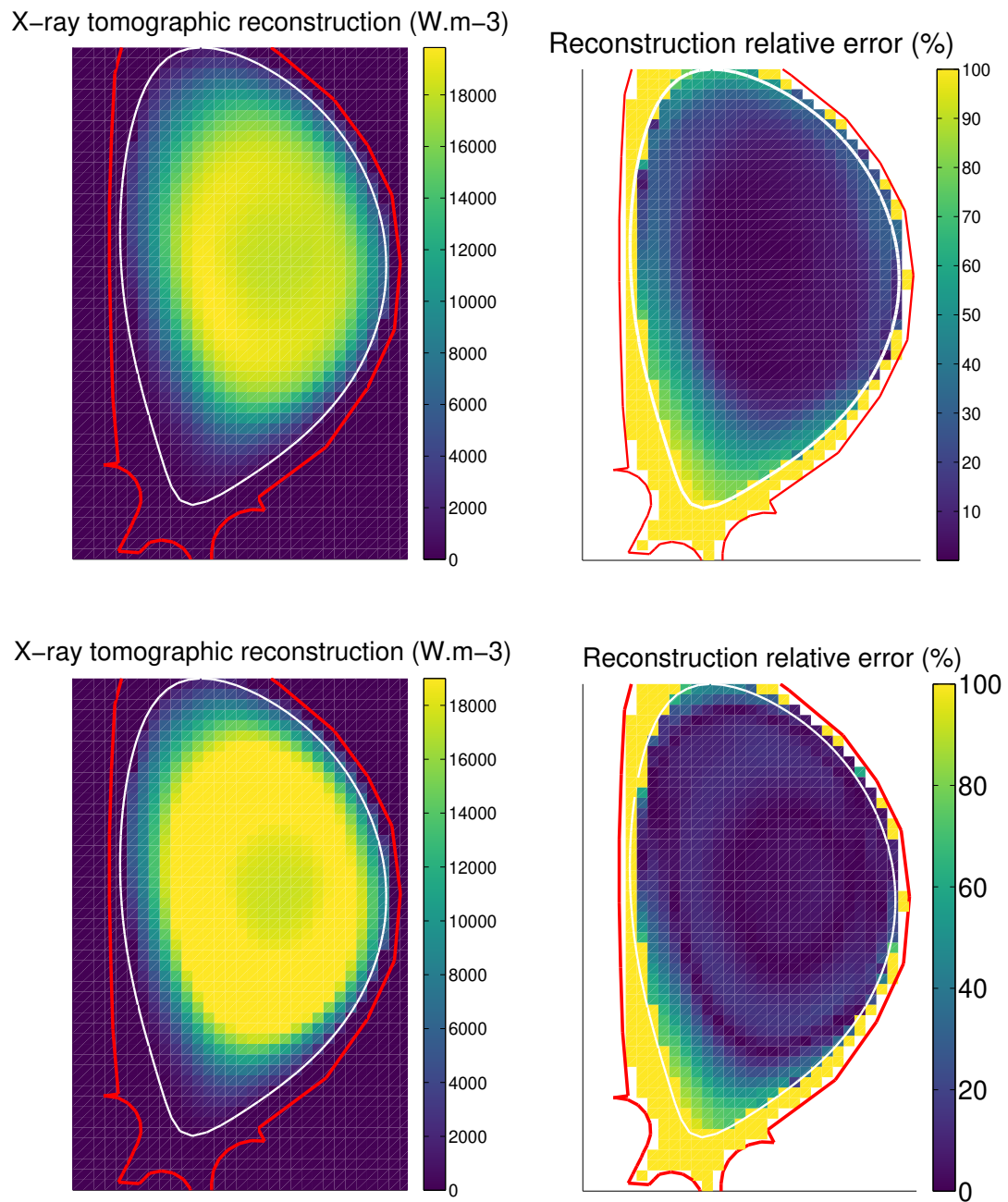


Figure 6.9 – Reconstruction of a soft x-ray only emissivity profile using Ar and Xe. Top line: Tomographic reconstruction using $150 \text{ mm} \cdot \text{atm}$ Xe LVICs (right: reconstructed profile, left: reconstruction error). Bottom line: Tomographic reconstruction using $150 \text{ mm} \cdot \text{atm}$ Ar LVICs (right: reconstructed profile, left: reconstruction error).

When the calibration coefficient is overestimated, so is the power impacting the detector. This explains why the shapes of both errors are similar in the case of the vertical

cross-section. For the both cross-section directions, the tomographic reconstruction errors present a similar shape. This is explained by the facts that tomographic reconstruction follows the magnetic field lines and that the radial detectors are prominent in shaping the error because of the higher amount of lines-of-sight compared to the vertical detectors (192 against 60).

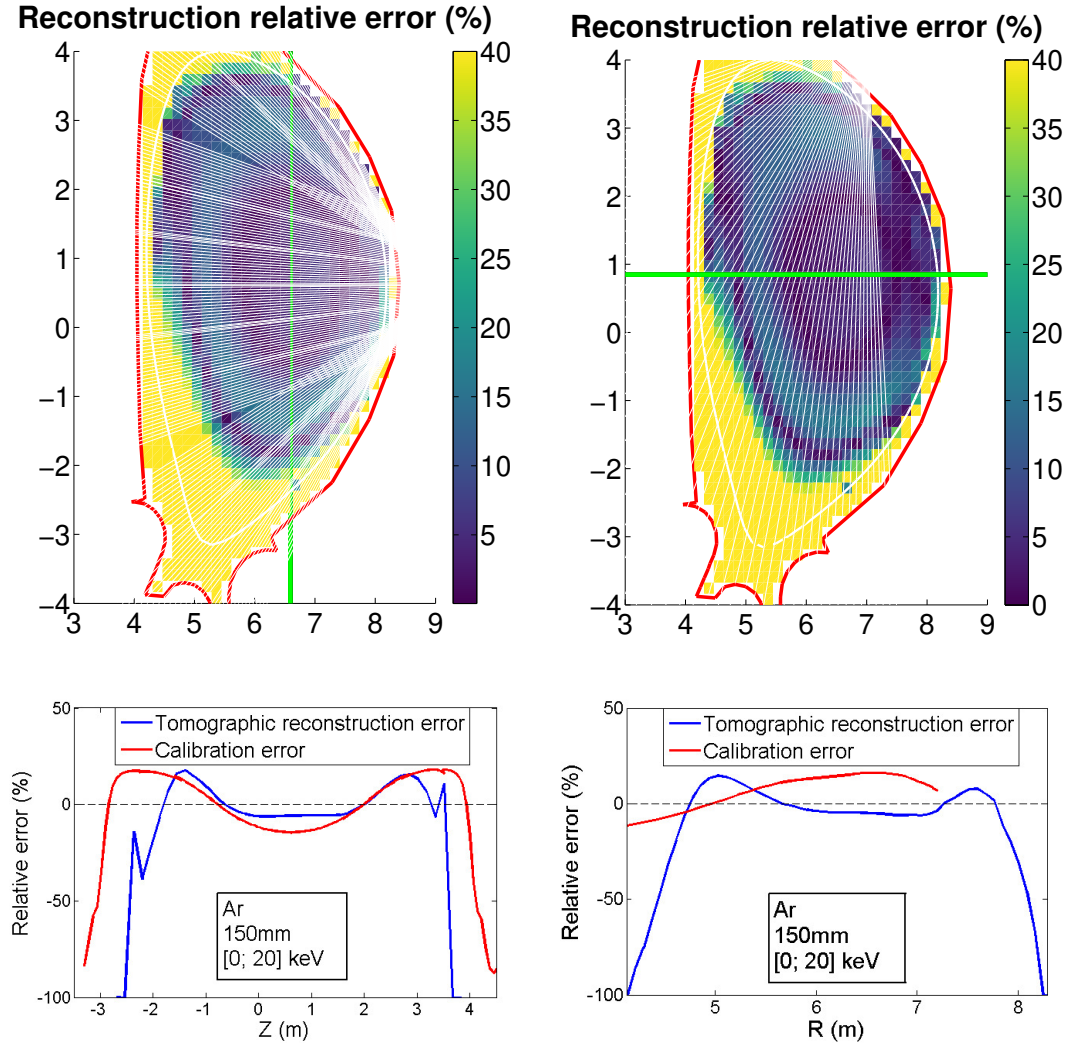


Figure 6.10 – Comparison of the tomographic reconstruction relative error and the relative calibration error through vertical (at R = 6.59m) and radial (at Z = 0.84m) cross-sections. The x-axis coordinate of each line-of-sight corresponds to its Z-coordinate (resp: R-coordinate) at the intersection with the cross-section straight line (green line in the upper figures) in the case of the vertical (resp: radial). The upper figures display the cross-section geometry and the lower ones show the relative errors for both tomographic reconstruction and calibration. The vertical (resp: radial) cross-section plots are located on the left (resp: right) side.

This suggests that the reconstruction artefacts are mainly due to the calibration

method. The tomographic reconstruction is overall satisfactory with low RMS_{tomo}^{core} and RMS_{tomo}^{LCMS} , but its accuracy can be increased through different calibration strategies (through energy discrimination or additional plasma scenarios). A tomographic study using ideal calibration (using a different calibration coefficient for each line-of-sight) can show the extent of the loss of accuracy induced by averaged calibration and is performed in the next section.

6.3.2 Influence of the calibration method on the tomographic reconstruction

Tomographic reconstruction using $150\text{ mm} \cdot \text{atm}$ argon-filled LVICs are performed in this section. The aim is to estimate how much accuracy can be gained by using an ideal calibration method. The incoming photon flux was restricted to the $[0, 20]$ keV range (see figure 6.8). The results are displayed on figure 6.11 and table 6.1.

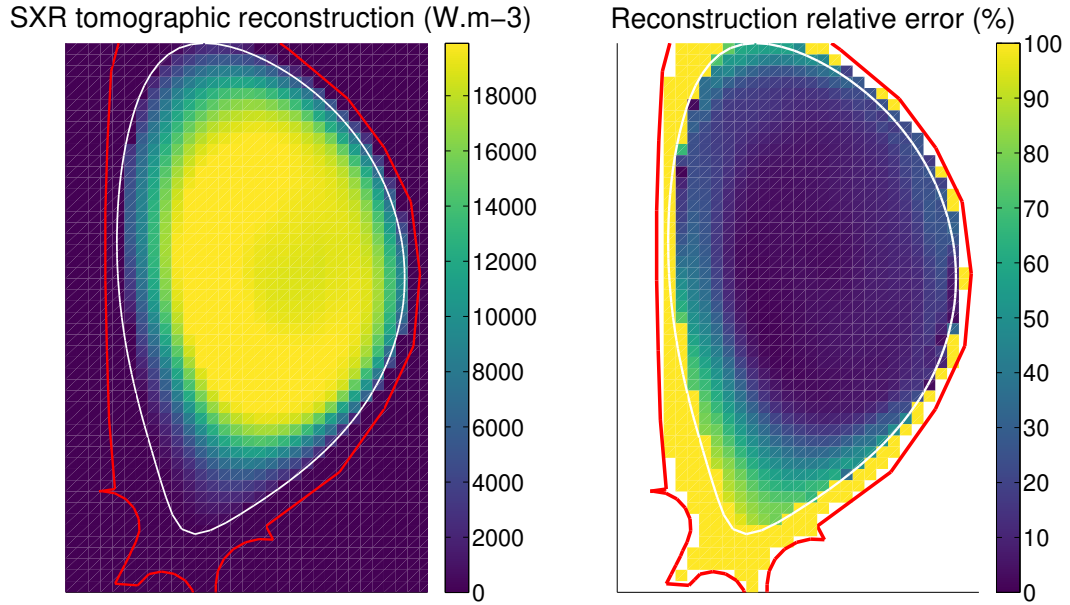


Figure 6.11 – Reconstruction of a soft x-ray only emissivity profile using $150\text{ mm} \cdot \text{atm}$ Ar LVICs with ideal calibration coefficients. Right: reconstructed profile. Left: reconstruction error.

The artefacts observed previously have disappeared and the error seems more constant over the plasma core and has decreased in average, as shown by RMS_{tomo}^{core} . There is however no significant improvement in RMS_{tomo}^{LCMS} . The agreement between the calibrated measurement and its backfitting is much better, as outlined by the low value of RMS_{line} . This confirms the origin of the reconstruction artefacts and shows the improvements which can be obtained with a finely tuned calibration method. This method is not used in the scope of this work as it requires precise knowledge of the

incoming photon flux on each detector, which will not be the case in experimental conditions.

6.3.3 Tomographic reconstruction over a wide energy range

Considering a wide energy spectrum allows to simulate realistic measurement of a full ITER scenario but also increases the difficulty faced for the reconstruction. Indeed, a widening of the energy range leads to an increased variation of the calibration coefficients (figure 6.5). A complete [0, 100] keV emissivity profile, as shown on figure 6.12 has been used in this study.

The tomographic reconstruction for different detectors configurations (gas and length pressure product) is shown on figure 6.13. The energy bandwidths used for reconstruction comparison are those displayed in section 6.2.3 for these detector configurations. The figure of merit of these tomographic reconstructions are shown in table 6.2. The overall accuracy is very encouraging with $RMS_{tomo}^{core} < 10^{-1}$ and $RMS_{tomo}^{LCMS} < 3 \cdot 10^{-1}$. Argon exhibits better figures of merit than xenon, especially RMS_{tomo}^{core} , but its reconstruction range is much shorter. Similar RMS_{line} values are observed, which are very close to those obtained in the restricted SXR range. This shows that the widening of the energy range does not affect the ability of the tomography algorithm to fit the measurement. The previously observed reconstruction artefacts due to calibration seem enhanced. In the case of xenon, the increase in detector length pressure product leads to an increase in the intensity but its shape remains the same. Similarly, argon presents the exact same rings as with a reduced incoming spectrum.

The overall reconstruction accuracy is still satisfactory in the plasma core region where argon features a very precise reconstruction up to 23 keV (see bottom line of figure 6.13) with $RMS_{tomo}^{core} < 6 \cdot 10^{-2}$ and xenon can reconstruct up to almost 50 keV (top line of figure 6.13) with $RMS_{tomo}^{core} < 10^{-1}$. In the right column of figure 6.13, one can notice that there is a discrepancy between the plasma line integrated SXR emissivity and its measurement by the LVIC. This discrepancy is highest in the plasma core (LoS 80-120 and 200-220). It is explained by the fact that the plasma core exhibits the highest difference between the ideal calibration coefficient and the averaged calibration coefficient. This difference in between the line integrated emissivities on tomography is visible at the very core of the plasma, where the reconstruction error is increased. This is especially noticeable in the case of the $50mm \cdot atm$ of xenon tomography (central line of figure 6.13) where the core reconstruction error reaches 30%.

Gas length · pressure	Argon $150\text{mm} \cdot \text{atm}$	Xenon $150\text{mm} \cdot \text{atm}$	Xenon $50\text{mm} \cdot \text{atm}$
RMS_{tomo}^{core}	$5.3 \cdot 10^{-2}$	$9.7 \cdot 10^{-2}$	$8.2 \cdot 10^{-2}$
RMS_{tomo}^{LCMS}	$2.3 \cdot 10^{-1}$	$2.9 \cdot 10^{-1}$	$2.4 \cdot 10^{-1}$
RMS_{line}	3.7	3.5	3.6

Table 6.2 – Figures of merit for tomographic reconstruction over [0, 100] keV.

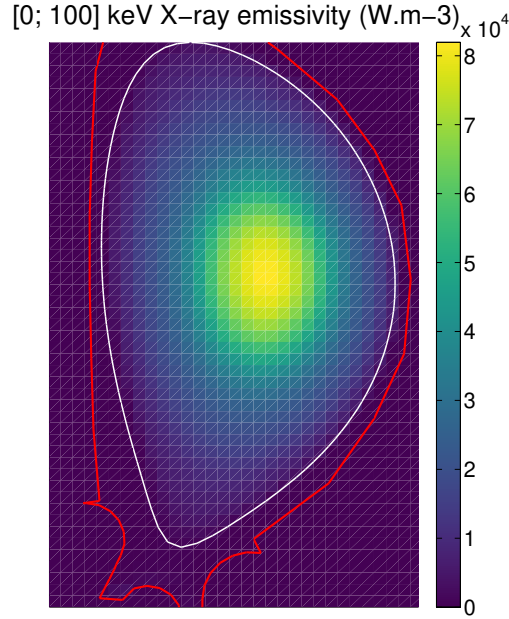


Figure 6.12 – X-ray (in the [0, 100] keV range) emissivity profile of a high power D-T ITER scenario.

6.3.4 Influence of perturbative noise on the tomographic reconstruction

A study has been conducted to estimate how experimental noise can affect the tomographic reconstruction and what levels of noise can be withstood by the system. The full spectrum emissivity measured by $150\text{ mm} \cdot \text{atm}$ Xe LVICs (top line of figure 6.13), reconstructed over [0, 49] keV, can be used as a noise-free reference. A gaussian distribution with different noise amplitudes has been applied to the LVIC currents prior to tomography. The reconstructed profiles and associated errors are presented on figure 6.14 and the associated figures of merit are displayed in table 6.3. It can be noticed that the noise does not significantly affect the quality of reconstruction at the center of the plasma (12% of increase in RMS_{tomo}^{core} for 5% of noise). The performance limitations induced by noise come in the shape of an increased error inside the LCMS (around 50% of increase in RMS_{tomo}^{LCMS} for 5% of noise) and of restriction of the region

of accurate tomographic reconstruction (bottom line of figure 6.14). Results show that for a level of noise lower than 2%, the reconstruction in the core is still very accurate (less than 7% increase for RMS_{tomo}^{core}).

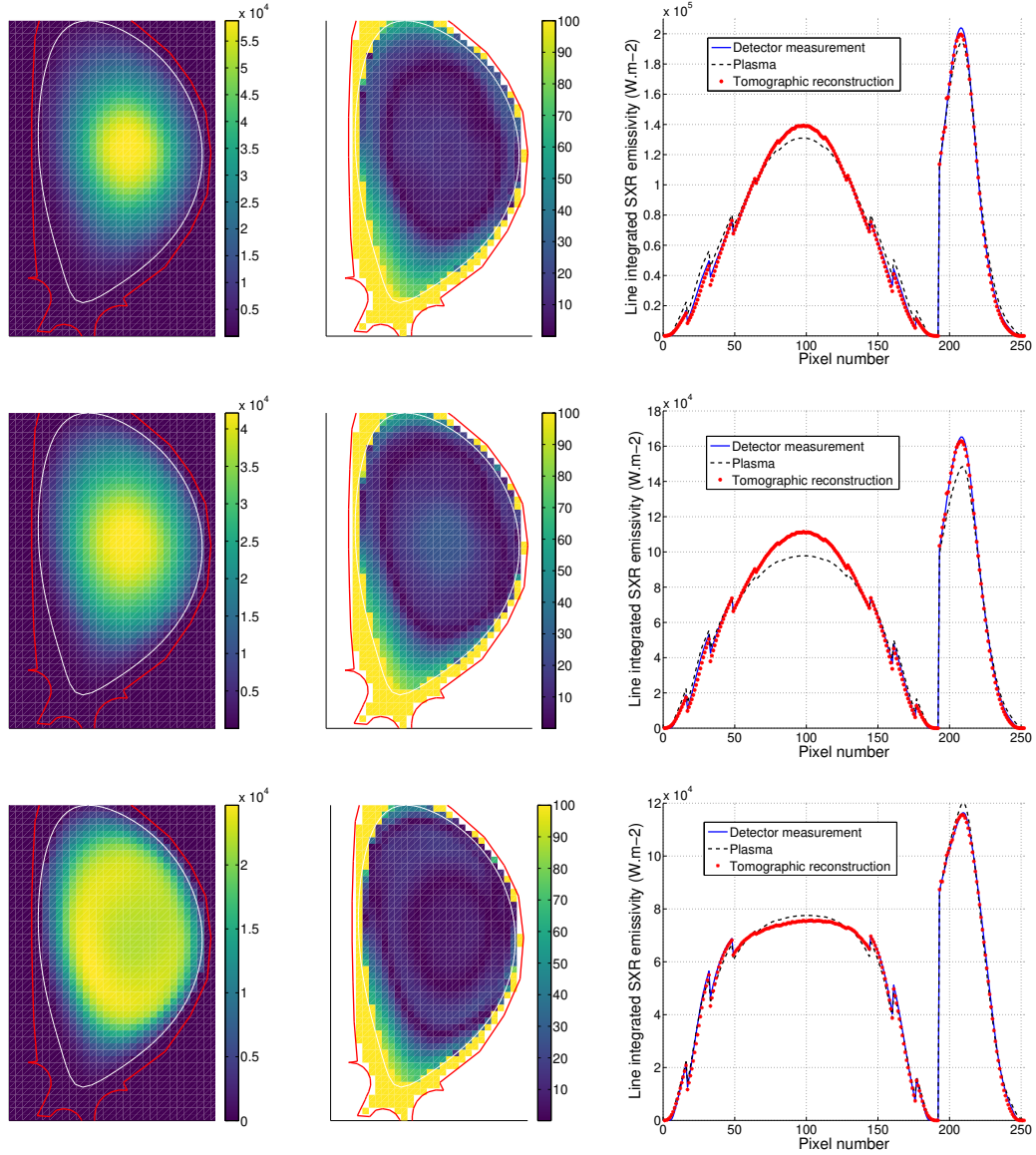


Figure 6.13 – Reconstruction of a wide emissivity profile using different detectors. Left: reconstructed profile ($W \cdot m^{-3}$). Center: reconstruction error (%). Right: line-integrated emissivity and backfitting ($W \cdot m^{-2}$). Top line: 150 $mm \cdot atm$ LVIC filled with Xe, reconstructing the emissivity in the [0, 49] keV range. Middle line: 50 $mm \cdot atm$ LVIC filled with Xe, reconstructing the emissivity in the [0, 31] keV range. Bottom line: 150 $mm \cdot atm$ LVIC filled with Ar, reconstructing the emissivity in the [0, 23] keV range.

Noise level	0%	1%	2%	5%
RMS_{tomo}^{core}	$9.7 \cdot 10^{-2}$	$1.00 \cdot 10^{-1}$	$1.03 \cdot 10^{-1}$	$1.09 \cdot 10^{-1}$
RMS_{tomo}^{LCMS}	$2.9 \cdot 10^{-1}$	$2.8 \cdot 10^{-1}$	$3.3 \cdot 10^{-1}$	$4.4 \cdot 10^{-1}$
RMS_{line}	3.5	3.6	3.1	2.0

Table 6.3 – Figures of merit for the noise study.

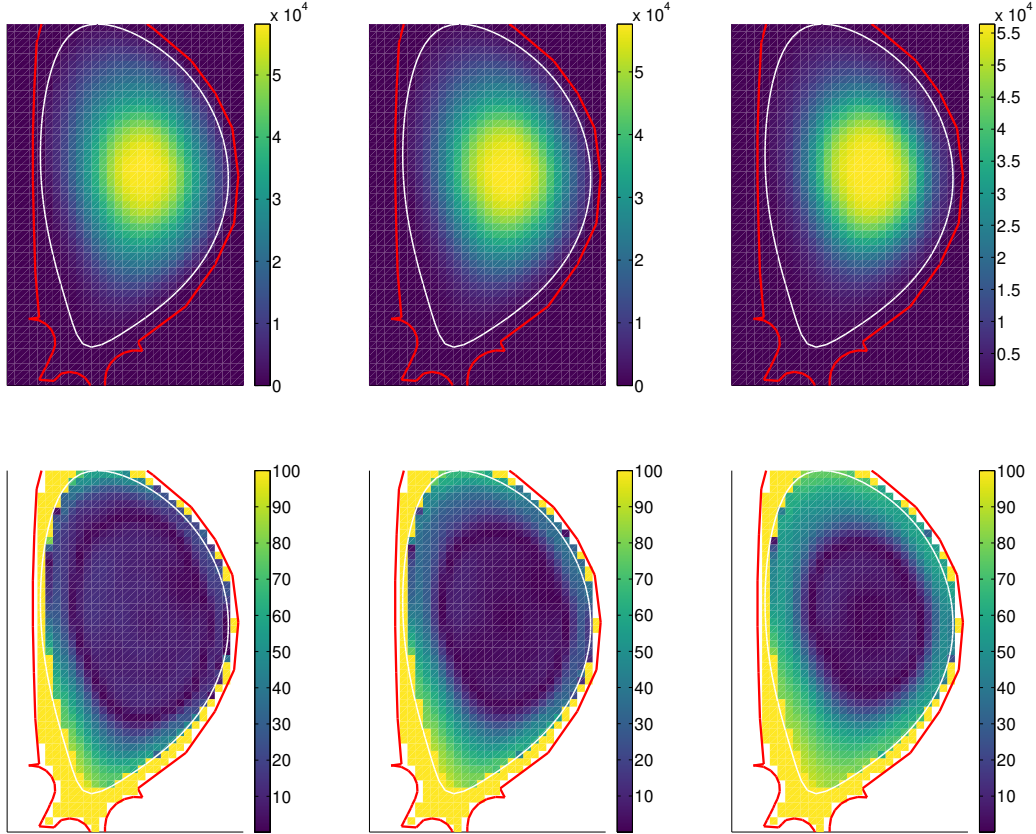


Figure 6.14 – Reconstruction of a wide emissivity profile with different levels of measurement noise. Reconstruction over the $[0, 49]$ keV range using xenon-filled $150 \text{ mm} \cdot \text{atm}$ LVIC. Top line: Tomographic reconstruction ($W \cdot m^{-3}$). Bottom line: Reconstruction error (%). Left column: 1% of noise. Middle column: 2% of noise. Right column: 5% of noise.

6.3.5 Alternative calibration method

The calibration method presented in section 6.2 has the main drawback that it depends on the incoming photon spectrum which varies between lines-of-sight. The use of a constant calibration coefficient therefore leads to inherent reconstruction errors, as shown in section 6.3.2. This line-of-sight dependency can be removed by reconstructing the emissivity convoluted by the spectral response of the detector. It

is a standard approach used for X-ray tomography with semiconductor diodes. [41, 103] It consists of stopping the calibration process to equation 6.6. The input of tomography is therefore:

$$f^\eta = \frac{P_X^\eta}{E} = \frac{e}{E} \int_0^\infty h\nu \eta(h\nu) \varphi(h\nu) d h\nu = W \cdot \frac{I_{LVIC}}{E} \quad (6.10)$$

The main difference between the calibration presented in section 6.2.1 is that this method allows the reconstruction of the emissivity as seen by the detector whereas the previously described method aims at breaking out of the dependence on the detector spectral response and reconstruct all the X-ray emissivity in a given energy band. Tomographic reconstructions using this calibration method are performed using argon-filled and xenon-filled LVIC with a length pressure product of $150\text{mm} \cdot \text{atm}$ and a filter made of $150\mu\text{m}$ of beryllium and $11\mu\text{m}$ of mylar.

Gas length · pressure	Argon $150\text{mm} \cdot \text{atm}$	Xenon $150\text{mm} \cdot \text{atm}$
RMS_{tomo}^{core}	$3.1 \cdot 10^{-2}$	$2.6 \cdot 10^{-2}$
RMS_{tomo}^{LCMS}	$5.8 \cdot 10^{-1}$	$5.9 \cdot 10^{-1}$
RMS_{line}	3.7	3.7

Table 6.4 – Figures of merit for tomographic reconstruction of the emissivity convoluted with the spectral response of the detector.

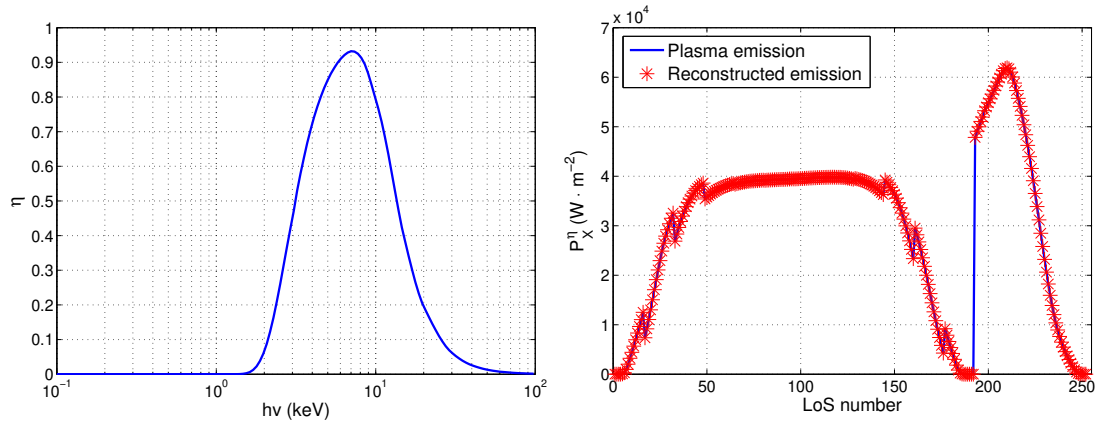


Figure 6.15 – Left: Spectral response as a function of photon energy. Right: Power impacting the detector convoluted by the spectral response and its reconstruction. The detector is an argon-filled LVIC with a length pressure product of $150\text{mm} \cdot \text{atm}$ and a filter made of $150\mu\text{m}$ of beryllium and $11\mu\text{m}$ of mylar.

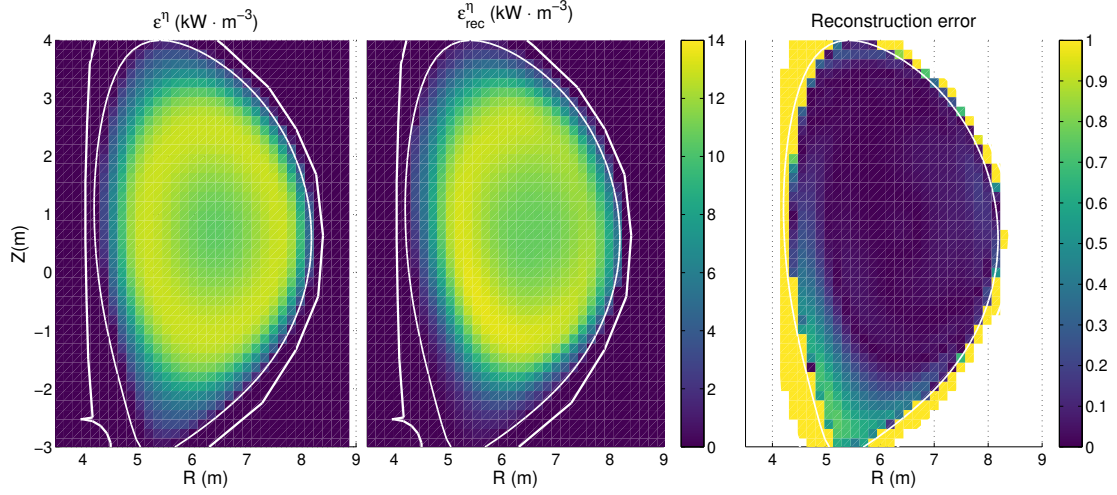


Figure 6.16 – Left: Plasma emissivity convoluted by the spectral response of the detector. Center: Tomographic reconstruction. Right: Reconstruction error. The detector is an argon-filled LVIC with a length pressure product of $150\text{mm} \cdot \text{atm}$ and a filter made of $150\mu\text{m}$ of beryllium and $11\mu\text{m}$ of mylar.

The reconstructions obtained, both with argon (figure 6.16) and xenon (figure 6.18), is quite accurate with low reconstruction error. The fitting of the line-integrals, shown on figure 6.15 for argon and figure 6.17 for xenon, is very good. The figures of merit show that the reconstruction in the core is more accurate with this reconstruction method, with a decrease of RMS_{tomo}^{core} by $\approx 40\%$ for argon and by more than a factor 3 for xenon. The reconstruction over the LCMS-enclosed region suffers from this calibration method: RMS_{tomo}^{LCMS} increases by a factor ≈ 2 for both reconstructions. The calibration method does not affect the fitting of the current as RMS_{line} is essentially the same with both methods.

The main advantage of this method is that it does not require an hypothesis on the incoming photon flux for accurate reconstruction. However, it doesn't allow the reconstruction of the emissivity over a clearly defined energy range. The interest of the calibration method is limited due to the possibility of energy discrimination using LVIC, presented in section 8.

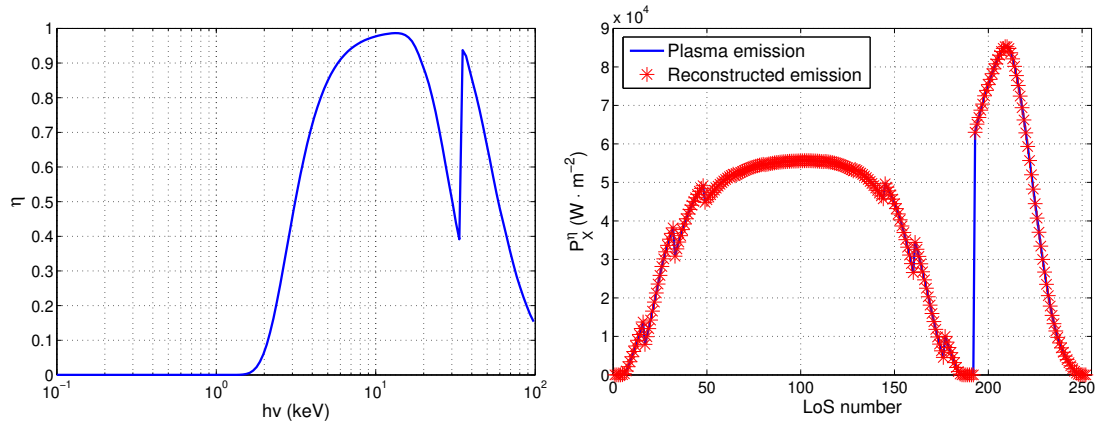


Figure 6.17 – Left: Spectral response as a function of photon energy. Right: Power impacting the detector convoluted by the spectral response and its reconstruction. The detector is a xenon-filled LVIC with a length pressure product of $150\text{mm} \cdot \text{atm}$ and a filter made of $150\mu\text{m}$ of beryllium and $11\mu\text{m}$ of mylar.

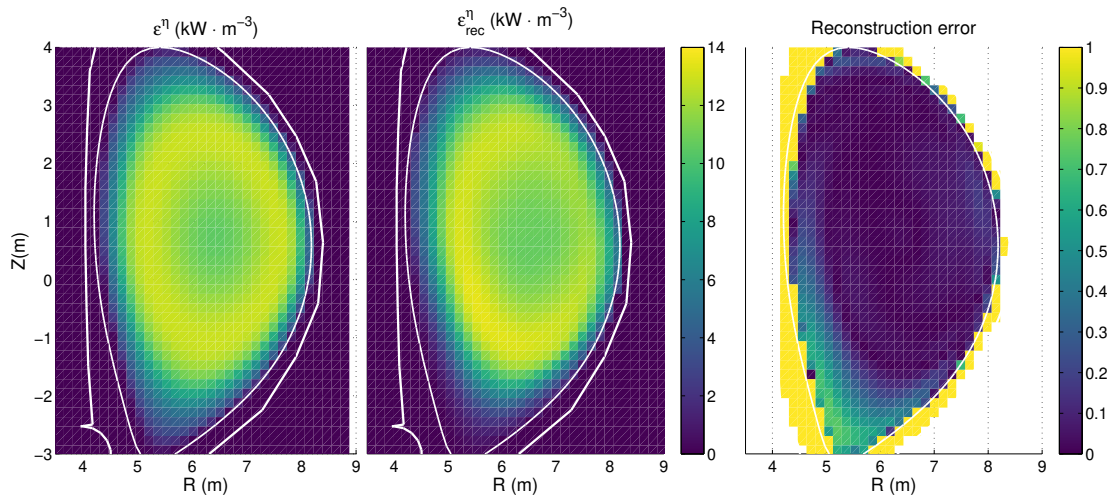


Figure 6.18 – Left: Plasma emissivity convoluted by the spectral response of the detector. Center: Tomographic reconstruction. Right: Reconstruction error. The detector is a xenon-filled LVIC with a length pressure product of $150\text{mm} \cdot \text{atm}$ and a filter made of $150\mu\text{m}$ of beryllium and $11\mu\text{m}$ of mylar.

7 Application to impurity transport study

Sommaire

7.1	Reconstruction of the tungsten transport coefficients on ITER	149
7.1.1	Scenarios	150
7.1.2	LVIC measurement	155
7.1.3	Negative V scenario reconstruction	156
7.1.4	Positive V scenario reconstruction	164
7.2	Poloidal asymmetries	171
7.2.1	Collisional regimes	172
7.2.2	Theory of parallel forces	172
7.2.2.1	Impact of electric field on impurity density	173
7.2.2.2	Impact of inertia on impurity density	173
7.2.2.3	Impurity transport in the presence of poloidal asymmetries	173
7.2.3	Poloidal asymmetries on ITER	174
7.2.3.1	Tomographic setup and simulation process	174
7.2.3.2	Baseline density profile	174
7.2.3.3	Electric field-induced asymmetry	176
7.2.3.4	Centrifugal force-induced asymmetry	178
7.2.3.5	Combined asymmetry	180

7.1 Reconstruction of the tungsten transport coefficients on ITER

The study of impurity transport using LVIC is performed on ITER through the attempt to reconstruct the D and V coefficients in different scenarios. These coefficients are respectively the diffusive and convective radial transport coefficients, leading to the following radial flux of impurities:

$$\vec{\Gamma}_S(r, t) = -D(r)\vec{\nabla}_r n_S(r, t) + n_S(r, t)V(r) \quad (7.1)$$

where $D(r)$ is the diffusive coefficient in $m^2 \cdot s^{-1}$, $V(r)$ is the convection coefficient in $m \cdot s^{-1}$ and $\vec{\nabla}_r$ denotes the radial gradient: $\vec{\nabla}_r f = \partial f / \partial r \cdot \vec{r} / \|r\|$.

The reconstruction of these parameters is achieved through the simulation of a Laser Blow-Off experiments. Laser Blow-Off systems are laser controlled devices which allow the insertion of impurity in the vacuum vessel during plasma shots. A laser with a tunable power and width hits a target made of the element to be injected in the plasma. Different target width can be used in order to control the total amount of impurity released in the plasma. LBO experiments allow the study of particle transport in an environment where the impurity generation is controlled.

7.1.1 Scenarios

A tungsten LBO scenario is generated from the electron temperature and density of the high power D-T scenario, described in section 2.4.1 and shown in figure 7.1.

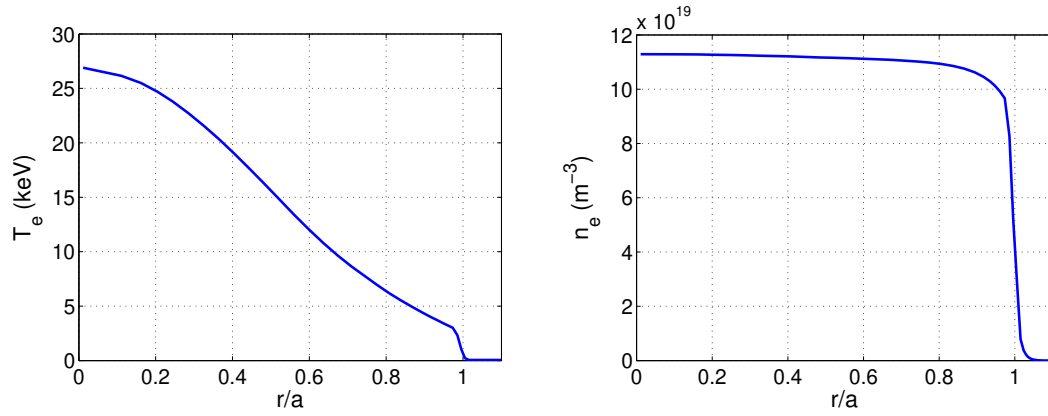


Figure 7.1 – Electron temperature (left) and density (right) profiles of the ITER high power D-T scenario.

The tungsten density and its evolution is set by the diffusive and convective coefficients. Two different scenarios have been generated from two different (D, V) profiles. These profiles are displayed on figure 7.2. The D coefficient is the same for both scenarios: it is low and constant in the plasma core ($r/a < 0.45$), increases linearly up to $r/a \approx 0.85$ and remains constant in the $0.85 < r/a < 1$ region. This means that tungsten diffusion is low in the core and higher in the plasma edge.

Both scenarios exhibit a similar V coefficient for $0.9 < r/a < 1$. In that region V has a high negative value (compared to the rest of the plasma) which increases linearly (in amplitude) with r/a . This means that in the plasma edge there is a strong convection towards descending r/a (i.e. towards the core). In the first profile, the V coefficient outside of the edge is a straight line linking $V(r/a = 0.9)$ and $V(r/a = 0) = 0$. This means that convection is always occurring towards the plasma core, but with a decreasing amplitude as we get closer to the core. The second profile exhibits a positive convection coefficient in the $r/a < 0.4$ region. This means that in the plasma core, tungsten convection transports towards the edge. Due to these differences between

the scenarios, they are respectively labelled the *core negative V* and the *core positive V* scenarios.

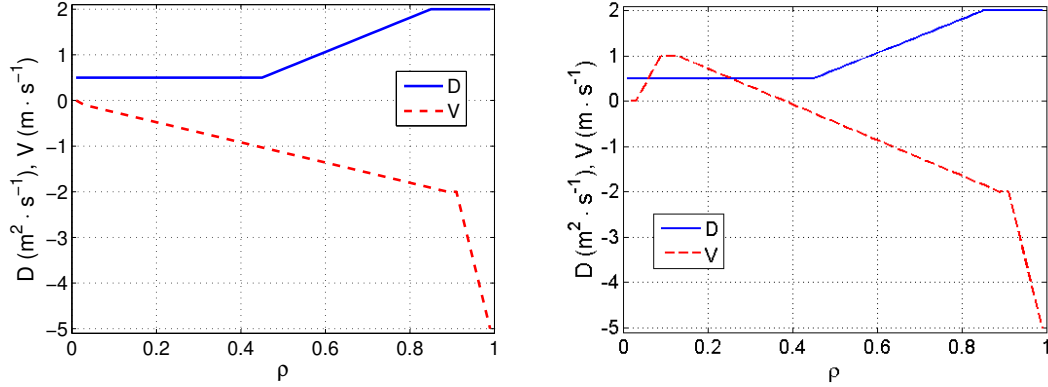


Figure 7.2 – Left: Radial profile of the diffusive and convective coefficients of tungsten in the *core negative V* scenario. Right: Radial profile of the diffusive and convective coefficients of tungsten in the *core positive V* scenario.

Three seconds of the ITER plasma are simulated, with a time step of $dt = 2 \cdot 10^{-3} \text{ s}$. The insertion of tungsten occurs at $t = 1.01 \text{ s}$ and lasts for 14 ms (see figure 7.3). It consists of a tungsten injection of $5 \cdot 10^{18} \text{ m}^{-3} \cdot \text{s}^{-1}$ at $r/a = 0.98$.

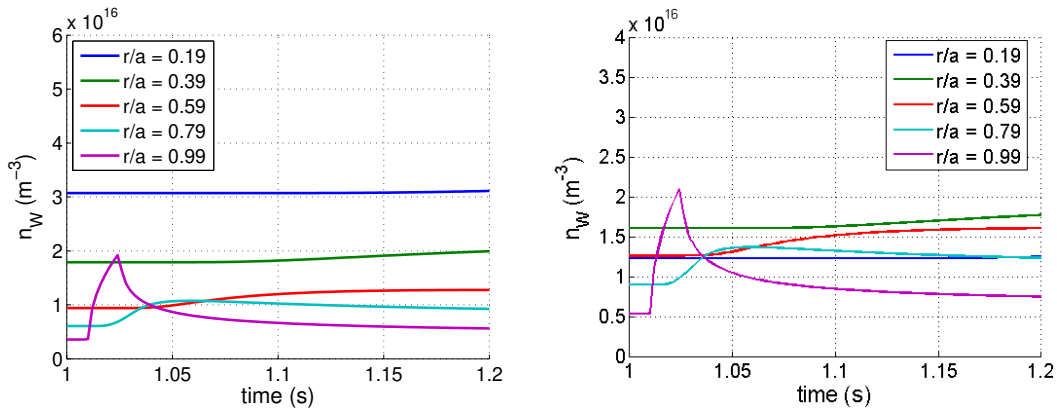


Figure 7.3 – Tungsten density as a function of time for several radial positions for the *core negative V* (left) and the *core positive V* (right) scenarios.

The resulting radial profiles of the tungsten density are displayed on figure 7.4. The *core negative V* scenario exhibits a peaked tungsten density profile, due to convection towards the core. In the *core positive V* scenario the tungsten profile has a hollow shape with a maximal value of n_W at $r/a = 0.4$. This is explained by the fact that convection tends to transport tungsten outwards for $r/a < 0.4$ and inwards for $r/a > 0.4$. Overall, the tungsten density is more spread in this scenario.

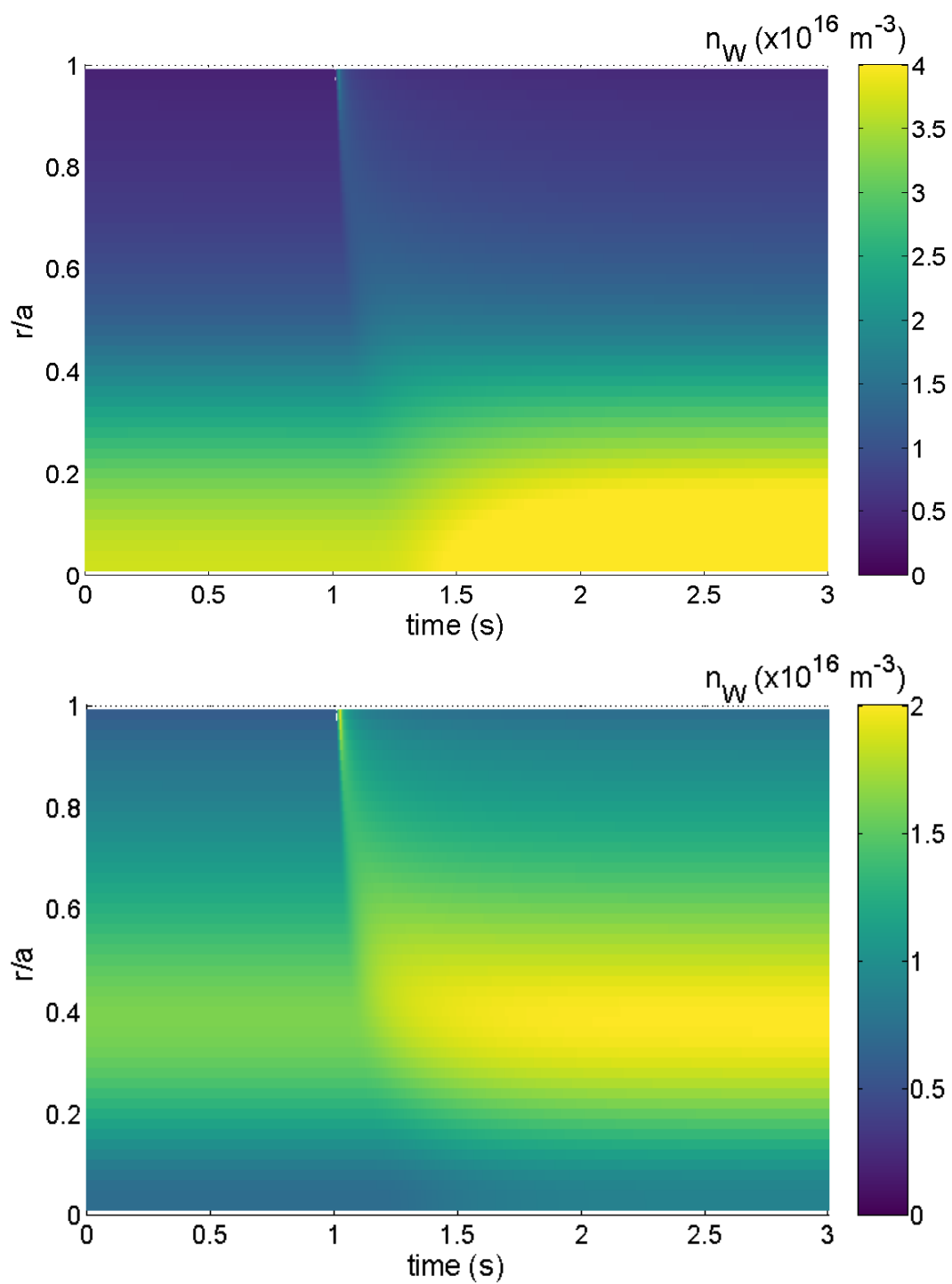


Figure 7.4 – Tungsten density as a function of time and normalised radius for the *core negative V* (top) and the *core positive V* (bottom) scenarios.

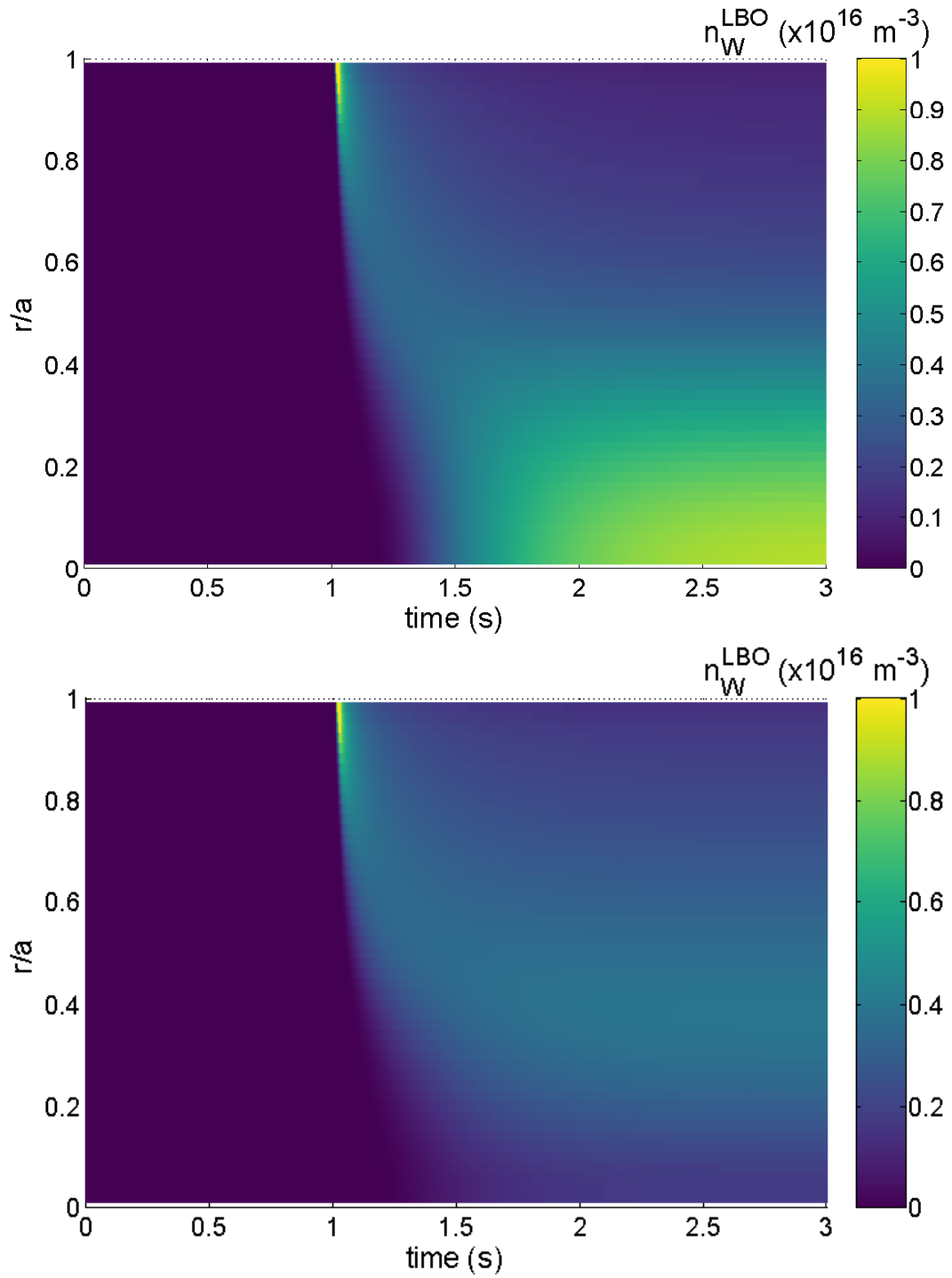


Figure 7.5 – Tungsten density (with initial state subtracted) as a function of time and normalised radius for the *core negative V* (top) and the *core positive V* (bottom) scenarios.

For both scenarios, it can be observed that for $0s < t < 1.01s$ the tungsten density

profile is stable: the plasma is at equilibrium. This period of time can be referred to as the *initial steady state*. At $t = 1.01\text{s}$ the Laser Blow-Off is shot, resulting in the release of a large amount of tungsten at the very edge of the plasma. Tungsten is then transported to the $r/a = 0$ (resp: $r/a = 0.4$) for the core negative (resp: positive) V scenario until an equilibrium is reached: this is the *transient regime*. The transient regime lasts until $t \approx 2.5\text{s}$. For $t > 2.5\text{s}$ the impurity density in the plasma is stable: the *final steady state* is reached.

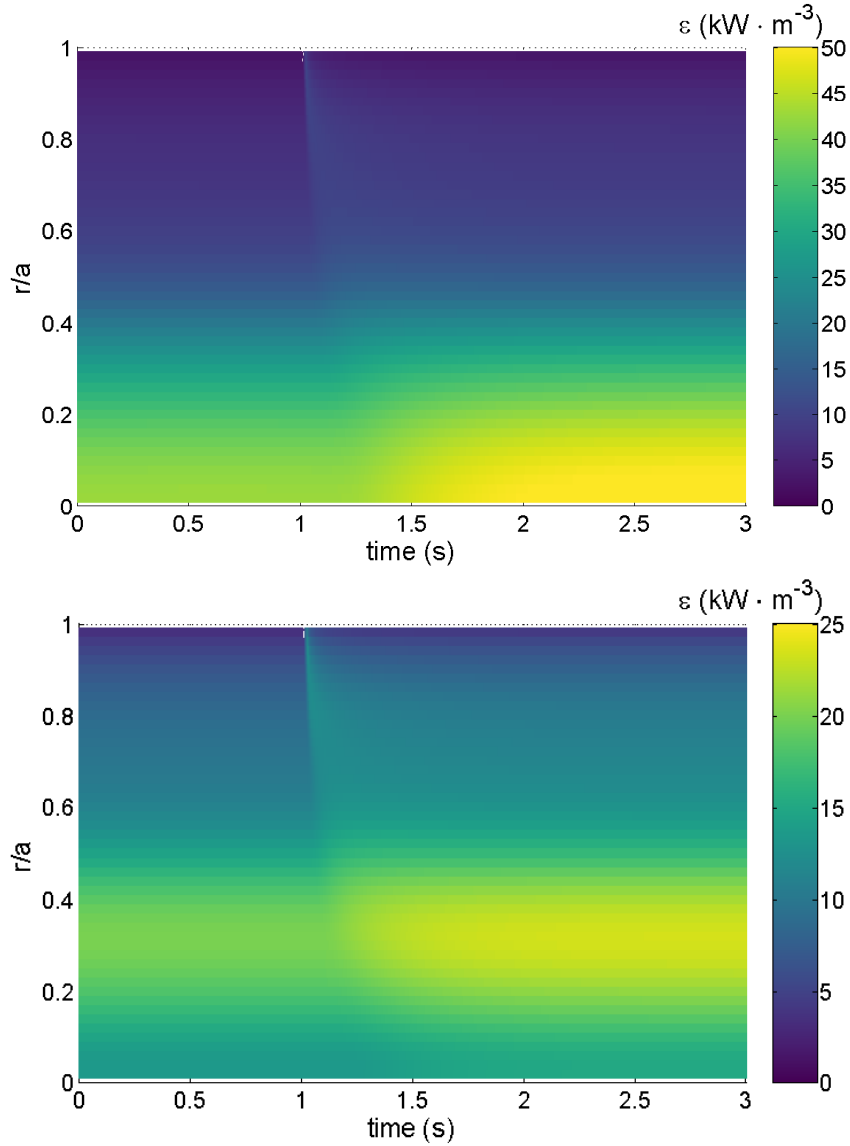


Figure 7.6 – Total X-ray emissivity as a function of time and normalised radius for the *core negative V* (top) and the *core positive V* (bottom) scenarios.

No impurity exhaust is considered in this simulation, and as a result the total tungsten inventory at the end of the LBO experiment is higher than in the initial

steady state. Subtracting the initial steady state density allows the visualisation of the tungsten density resulting from the LBO injection only, as shown on figure 7.5. The transport of tungsten from the edge to $r/a = 0$ (resp: $r/a = 0.4$) for the core negative (resp: positive) V scenario can be identified easily.

The plasma emissivity is computed in the $[1\text{eV}, 31\text{keV}]$ energy range at each time step with the method presented in section 2.4. For each time step, the 2D profile of the emissivity is obtained by interpolation (following the magnetic field lines) from its radial profile: there is no radial asymmetry in the emissivity profile. The time evolution of the radial profile of the total emissivity is displayed for each scenario on figure 7.6. The emissivity profile follows fairly well the tungsten density. At $t = 1.01\text{s}$ the emissivity at the edge rises abruptly as the result of the release of impurity. The transport of tungsten can be seen through the increase of emissivity which propagates towards $r/a = 0$ (resp: $r/a = 0.4$) for the core negative (resp: positive) V scenario.

The emissivity spectrum for various radial positions at $t = 1.5\text{s}$ is shown on figure 7.7. Similarly as in figure 2.7, the region delimited by $0.8 < r/a < 1$ exhibits very strong line radiation around 2 keV (as indicated by the black line of figure 7.7). At $t = 1.01\text{s}$ the emissivity at the edge rises abruptly as the result of the release of impurity. The transport of tungsten can be seen through the increase of emissivity which propagates towards $r/a = 0$ (resp: $r/a = 0.4$) for the core negative (resp: positive) V scenario. Similarly as with the tungsten density, the emissivity is higher over the whole plasma at the end of the experiment.

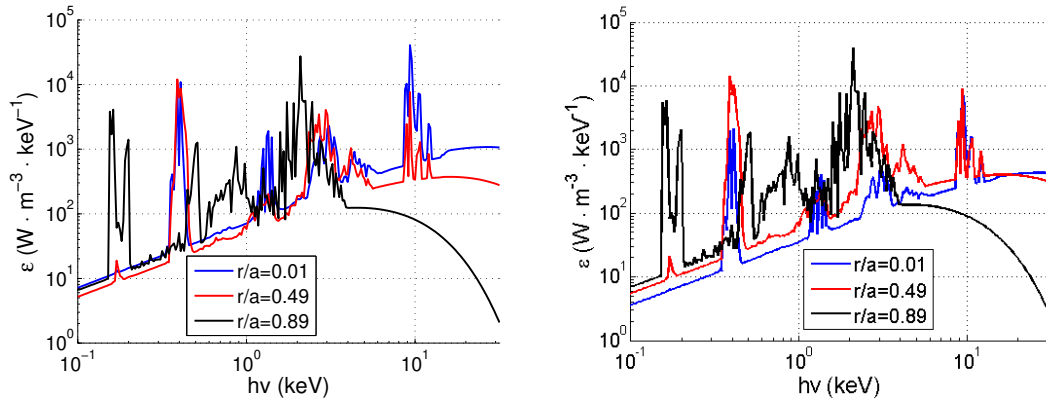


Figure 7.7 – X-ray emissivity spectrum at $t = 1.5\text{s}$ at various radial positions for the *core negative V* (left) and the *core positive V* (right) scenarios.

7.1.2 LVIC measurement

A total of 252 detectors in the 60 vertical lines-of-sight configuration, introduced in section 5.4.1, are simulated. Each LVIC is filled with xenon and has a length pressure product of $100\text{mm} \cdot \text{atm}$. A beryllium window of $200\mu\text{m}$, which is the beryllium window width foreseen on ITER, is considered. The spectral response of the detector is displayed in figure 7.8.

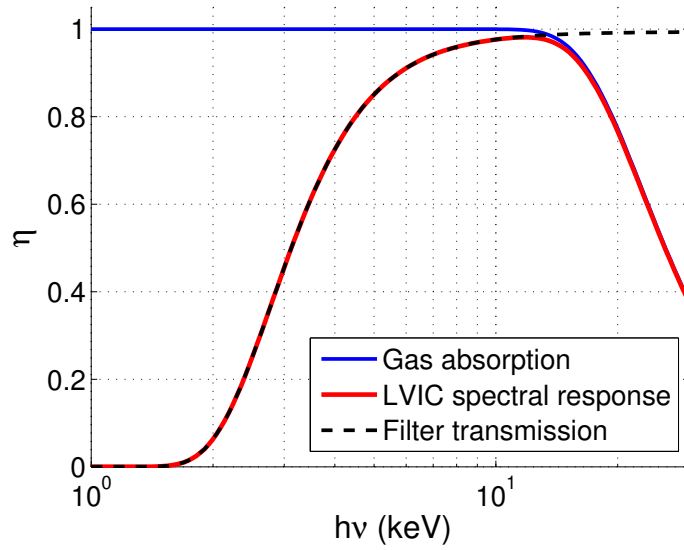


Figure 7.8 – Transmission ratio of a $200\mu m$ Be window, absorption ratio of a $100mm \cdot atm$ Xe-filled LVIC, and spectral response of the combination of the two.

The measurement using LVIC is modelled by convolution of the emissivity by the detector's spectral response. Due to the large amount of time steps included in the simulation, this solution has been chosen instead of the use of the synthetic diagnostic because it is significantly faster. In most of the energy range considered ($[1eV, 31keV]$) xenon X-ray fluorescence does not take place, and in the scope of an ionization chamber, which integrates the collected charges, the influence of the Fano noise is expected to be negligible. As a result, the convolution of the emissivity by the spectral response of the detector should yield the same results than the synthetic diagnostic tools.

7.1.3 Negative V scenario reconstruction

The x-ray emissivities, emitted by the whole plasma and by the injected tungsten only, convoluted by the spectral response of the detector are displayed on figure 7.9. It can be observed that the detector does not measure much of the emissivity at the plasma edge as most of it is located in the $[0.1, 3]keV$ range (see figure 7.7) and is therefore absorbed in the beryllium window. When the background emissivity is subtracted the edge emissivity induced by the LBO injection becomes clearly visible.

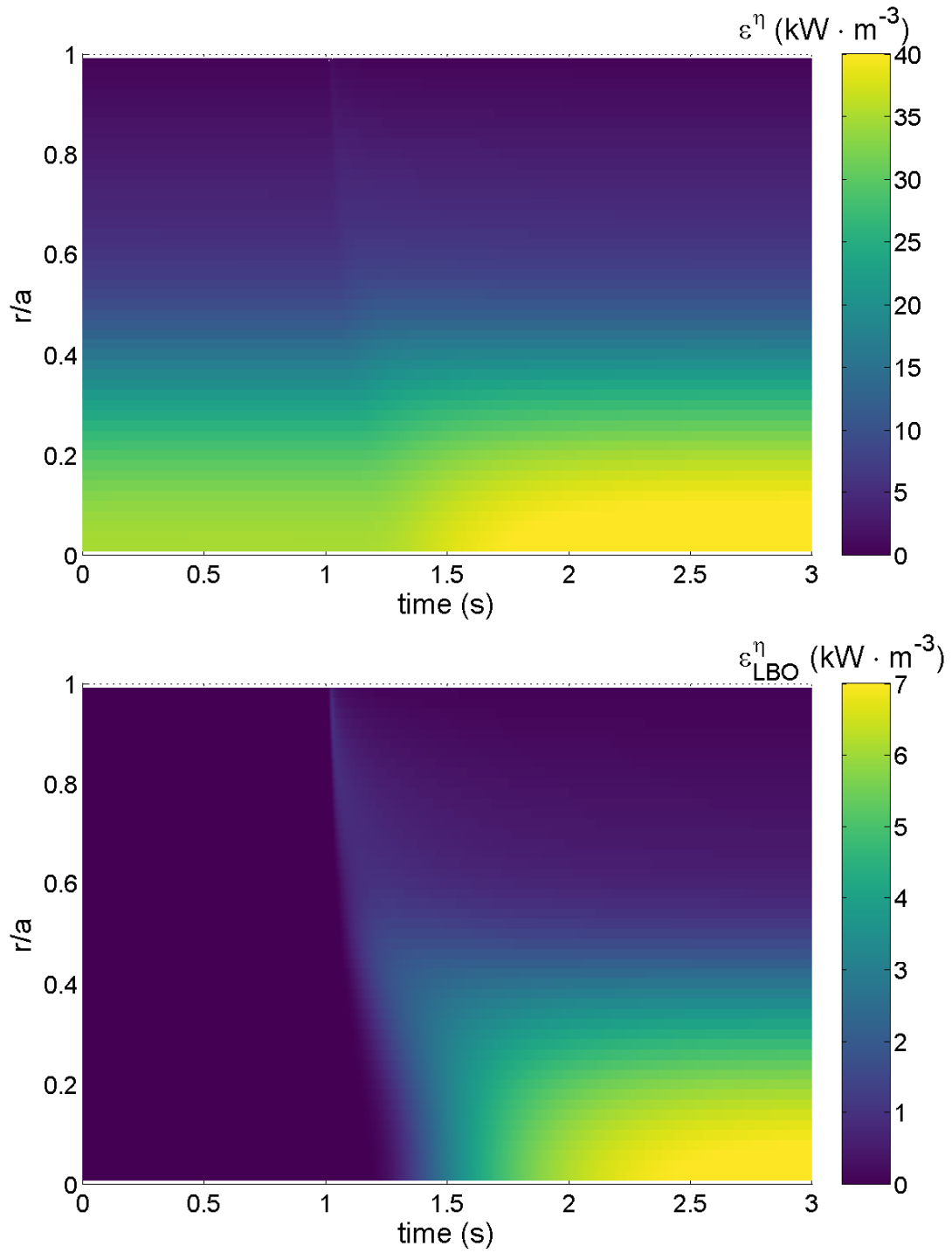


Figure 7.9 – Total (top) and background subtracted (bottom) X-ray emissivities convoluted by the spectral response of the detector as a function of time and normalised radius in the case of the *negative V coefficient* scenario.

The line-integrated emissivities (total and background subtracted) for each line-of-

sight are displayed on figure 7.10. The time evolution of f^η is hard to visualise on the figure, however the background subtracted f_{LBO}^η clearly shows the transport of the emissivity from the plasma edge (lines-of-sight 0-50, 150-192 and 225-252) towards the core (lines-of-sight 50-150 and 193-225).

The total line-integrated emissivity is used as an input for tomography. The tomography setup based on the Minimum Fisher Information method described in section 3.3.2. The reconstructed f^η and f_{LBO}^η are shown on figure 7.11. A good visual agreement between the initial (figure 7.10) and reconstructed profile can be observed. The corresponding X-ray emissivities (total and background subtracted) are displayed on figure 7.12. A good visual agreement between the initial (figure 7.9) and reconstructed profile can be observed as well. In this plasma which only contains tungsten and hydrogen, the tungsten density can be computed from the reconstructed X-ray emissivity (provided that n_e , and the L_H^η and L_W^η cooling factors are known):

$$n_W^{rec} = \frac{\varepsilon^\eta - n_e^2 \cdot L_H^\eta}{n_e \cdot L_W^\eta} \quad (7.2)$$

The reconstructed tungsten densities (total and background subtracted) are shown on figure 7.13. Radial instabilities can be noticed on the reconstruction but overall there is a good agreement with figures 7.4 and 7.5.

From the reconstructed densities, the corresponding D and V transport coefficients can be computed using the method presented in section 2.5.2. Each $n_W(t, r/a)$ point has an associated radial flux $\Gamma_W(t, r/a)$ given by:

$$\Gamma_W(t, r/a) = a \cdot \frac{1}{r/a} \int_0^{r/a} \frac{dn_W(t, \rho)}{dt} \rho d\rho \quad (7.3)$$

A linear fitting of Γ_W/n_W as a function of $dn_W/dt/n_W$ at a given radial position give the reconstructed D and V transport coefficients, D being the slope and V the intercept. In order to limit the impact of the radial instabilities observed on figure 7.13, the reconstructed density is resampled on a wider radial grid.

Figure 7.14 shows Γ_W/n_W as a function of $dn_W/dt/n_W$ for various radial positions. Each blue point corresponds to a time step. It can be seen that a straight line can accurately fit these points, at the exception of the $r/a = 0.73$ radial position. The red dashed line corresponds to the straight line which would be obtained with the D and V coefficients used in the scenario. Ideally the blue points should be very close to the dashed line, as seen for $r/a = 0.07$. It can be observed that, even though the data is not located on the dashed line, a linear fitting would give a slope and intercept fairly close to those of the dashed line for $r/a = 0.19$. In other words, the reconstruction of the D and V coefficients should be fairly accurate for this point. Such observation can be made for the slope (and therefore the D coefficient) at $r/a = 0.49$ as well.

The reconstructed D and V coefficients are displayed on figure 7.15. It can be noticed that the reconstruction is very accurate for $r/a < 0.4$. Outside of this range, however, a

significant discrepancy between the transport coefficients and their reconstruction is observed. This discrepancy is most likely explained by the tomography-induced errors which are stronger at the plasma edge and could have enhanced the instability of this method.

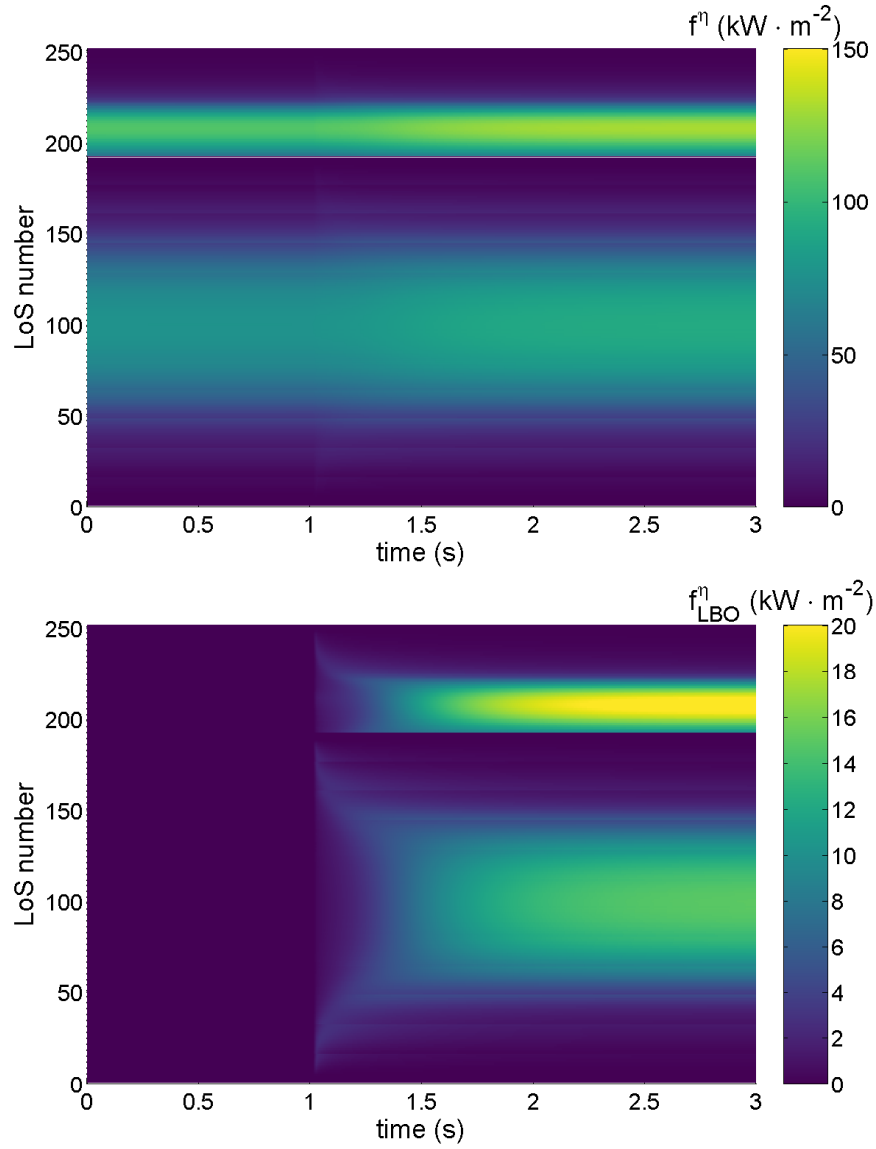


Figure 7.10 – Total (top) and background subtracted (bottom) line-integrated emissivities convoluted by the spectral response of the detector as a function of time and line-of-sight number in the case of the *negative V coefficient* scenario.

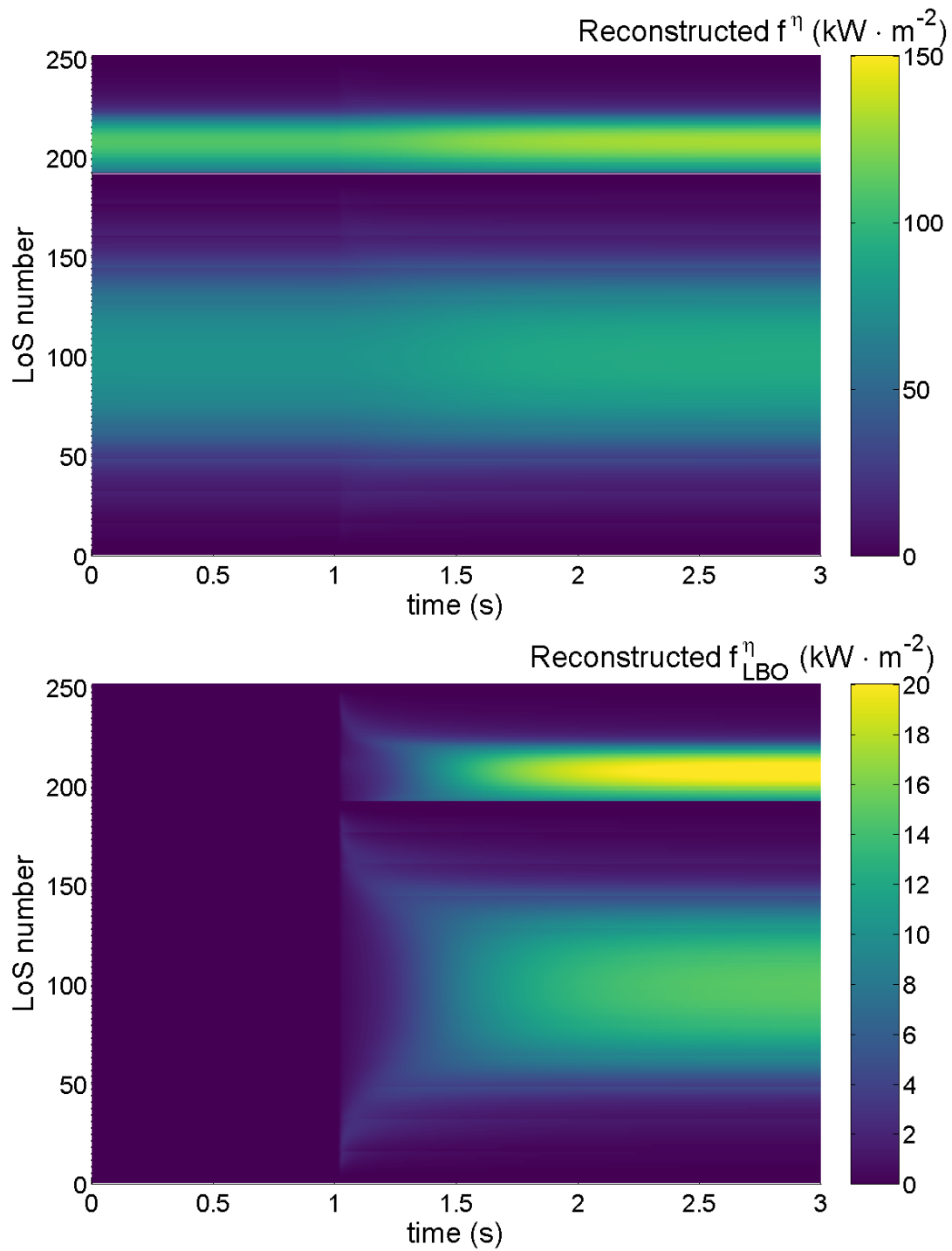


Figure 7.11 – Total (top) and background subtracted (bottom) reconstructed line-integrated emissivities convoluted by the spectral response of the detector as a function of time and line-of-sight number in the case of the *negative V coefficient* scenario.

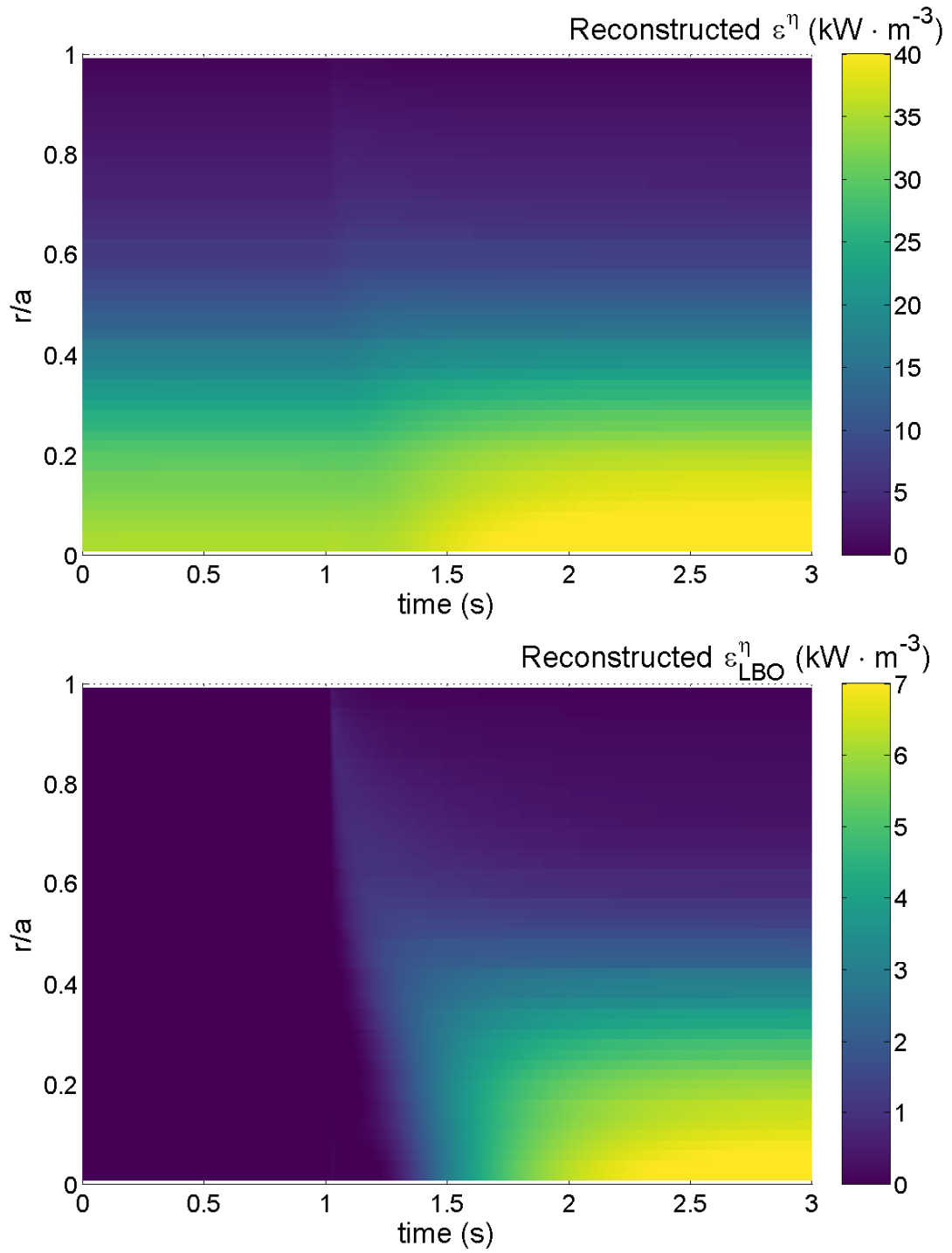


Figure 7.12 – Total (top) and background subtracted (bottom) reconstructed X-ray emissivities convoluted by the spectral response of the detector as a function of time and normalised radius in the case of the *negative V coefficient* scenario.

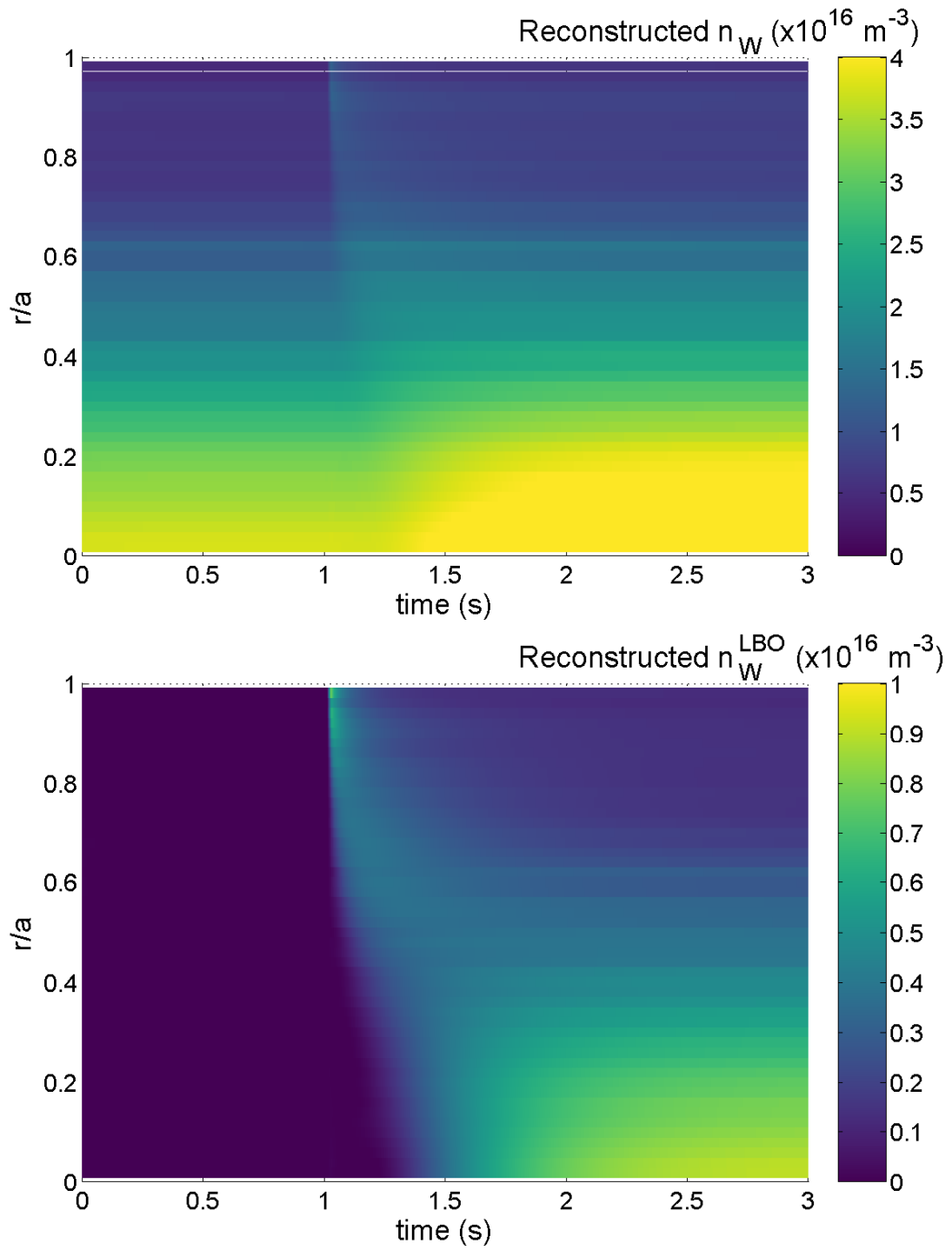


Figure 7.13 – Total (top) and background subtracted (bottom) reconstructed tungsten densities as a function of time and normalised radius in the case of the *negative V coefficient* scenario.

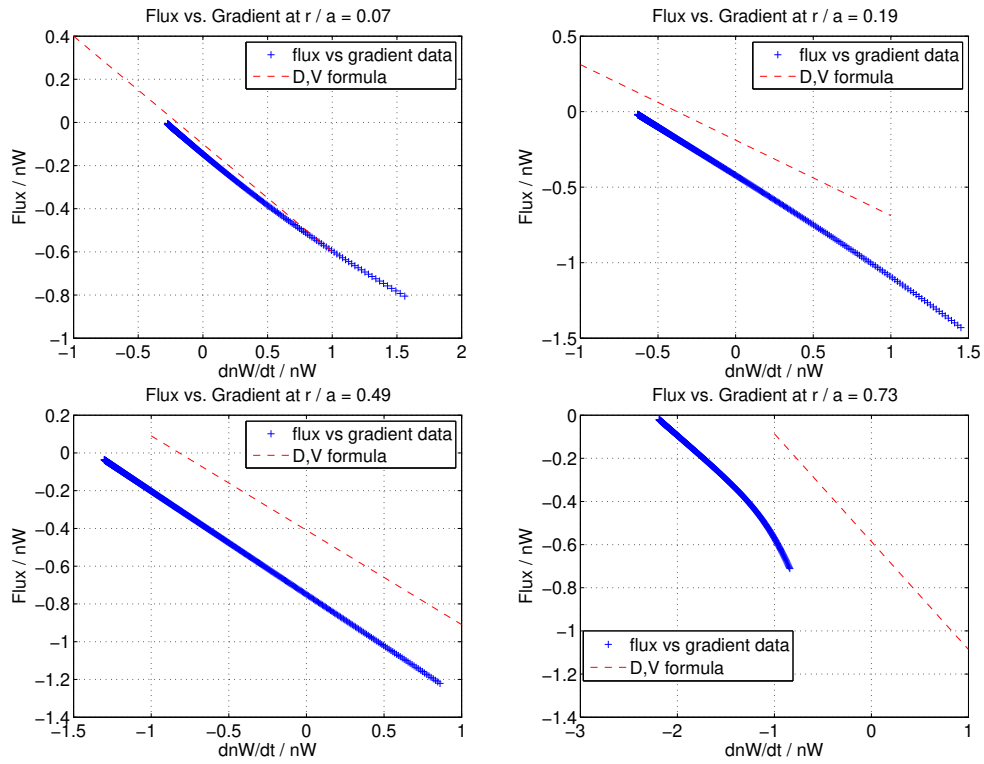


Figure 7.14 – Γ_W/n_W as a function of $dn_W/dt/n_W$ for several radial positions in the case of the *negative V coefficient* scenario. The dash line represents the result which would be obtained with the D and V coefficients of the scenario.

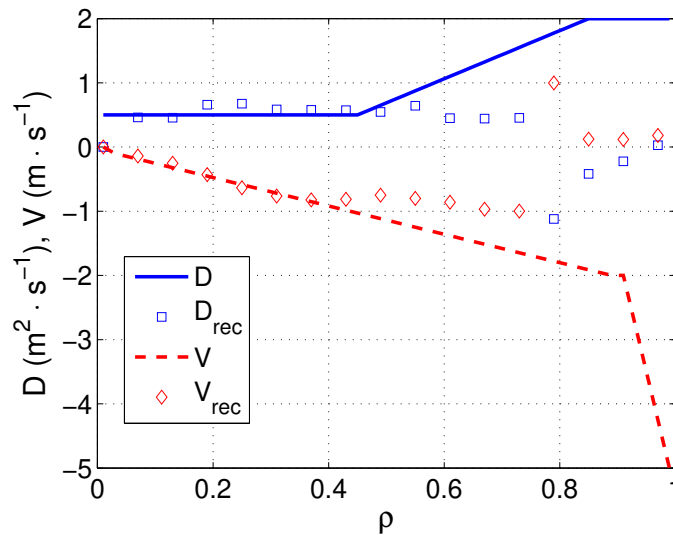


Figure 7.15 – D and V coefficients of the *negative V coefficient* scenario and their reconstruction.

7.1.4 Positive V scenario reconstruction

The x-ray emissivities (total and LBO-injected only), convoluted by the spectral response of the detector, are displayed on figure 7.16. Similarly as for the *negative V coefficient* scenario, most of the edge emissivity is absorbed in the beryllium window of the detector but subtracting background increases its visibility.

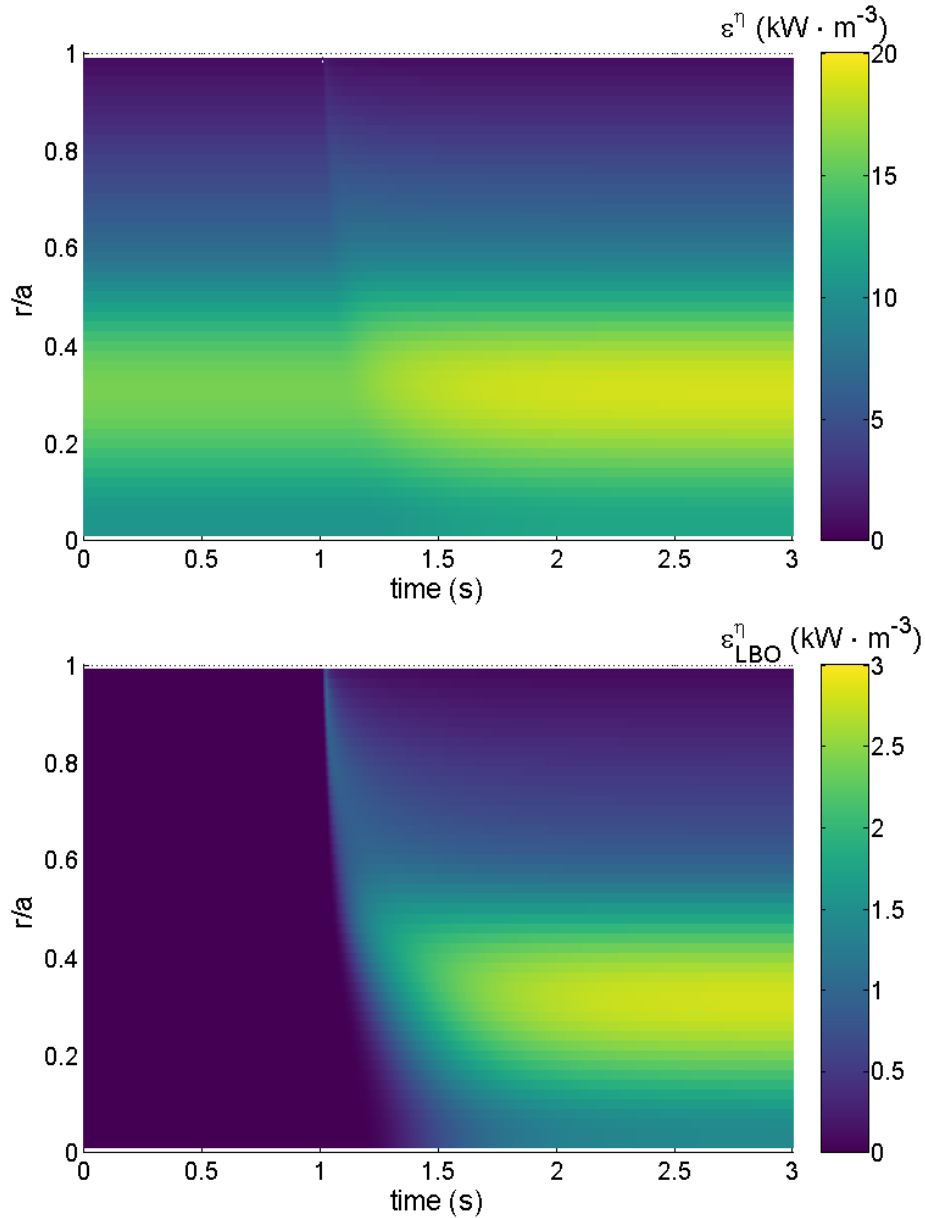


Figure 7.16 – Total (top) and background subtracted (bottom) X-ray emissivities convoluted by the spectral response of the detector as a function of time and normalised radius in the case of the *positive V coefficient* scenario.

The line-integrated emissivities as a function of time and line-of-sight number are shown on figure 7.17. Similar observations can be made as in the *negative V coefficient*: the most of the emissivity comes from the initial composition of the plasma. The reconstructed f^η and f_{LBO}^η are displayed on figure 7.18. Similarly as for the previous scenario, a good visual agreement with figure 7.17 can be observed.

The reconstructed X-ray emissivities (total and background subtracted) are displayed on figure 7.19. A visual comparison with figure 7.16 shows a good agreement between both emissivity profiles. The reconstructions of the total tungsten density and the LBO-injected tungsten density are shown on figure 7.20. Radial instabilities are still present but their intensity is lower than in the previous section. The visual agreement with figures 7.4 and 7.5 is overall satisfying.

Similarly as for the *negative V coefficient* scenario, Γ_W/n_W and $dn_W/dt/n_W$ are computed for each $n_W(t, r/a)$. Γ_W/n_W is displayed as a function of $dn_W/dt/n_W$ for various radial positions in figure 7.21, each blue point corresponding to a time step of the simulation. All these charts (except the $r/a = 0.73$ radial position) can be fitted accurately by a straight line, but the red dashed line is not close to the blue points. However, both the blue points and the red dashed line seem to exhibit fairly similar slopes. There seems to be more error on the intercept though.

The reconstructed D and V coefficients are displayed on figure 7.22. It can be noticed that the reconstruction is quite accurate for $r/a < 0.4$. Outside of this range, however, a significant discrepancy between the transport coefficients and their reconstruction is observed. This discrepancy is most likely explained by the tomography-induced errors which are stronger at the plasma edge and could have enhanced the instability of this method.

A comparison of figures 7.15 and 7.22 shows that the *negative V coefficient scenario* exhibits a slightly more accurate reconstruction of the D and V coefficients for $r/a < 0.4$. For $0.4 < r/a < 0.8$, the *positive V coefficient scenario* is more accurate.

In summary the reconstruction of the D and V coefficients from the X-ray emissivity is possible and its accuracy is very satisfying in the plasma core ($r/a < 0.4$). Outside of this region however, the reconstruction of the D and V coefficients cannot be considered accurate.

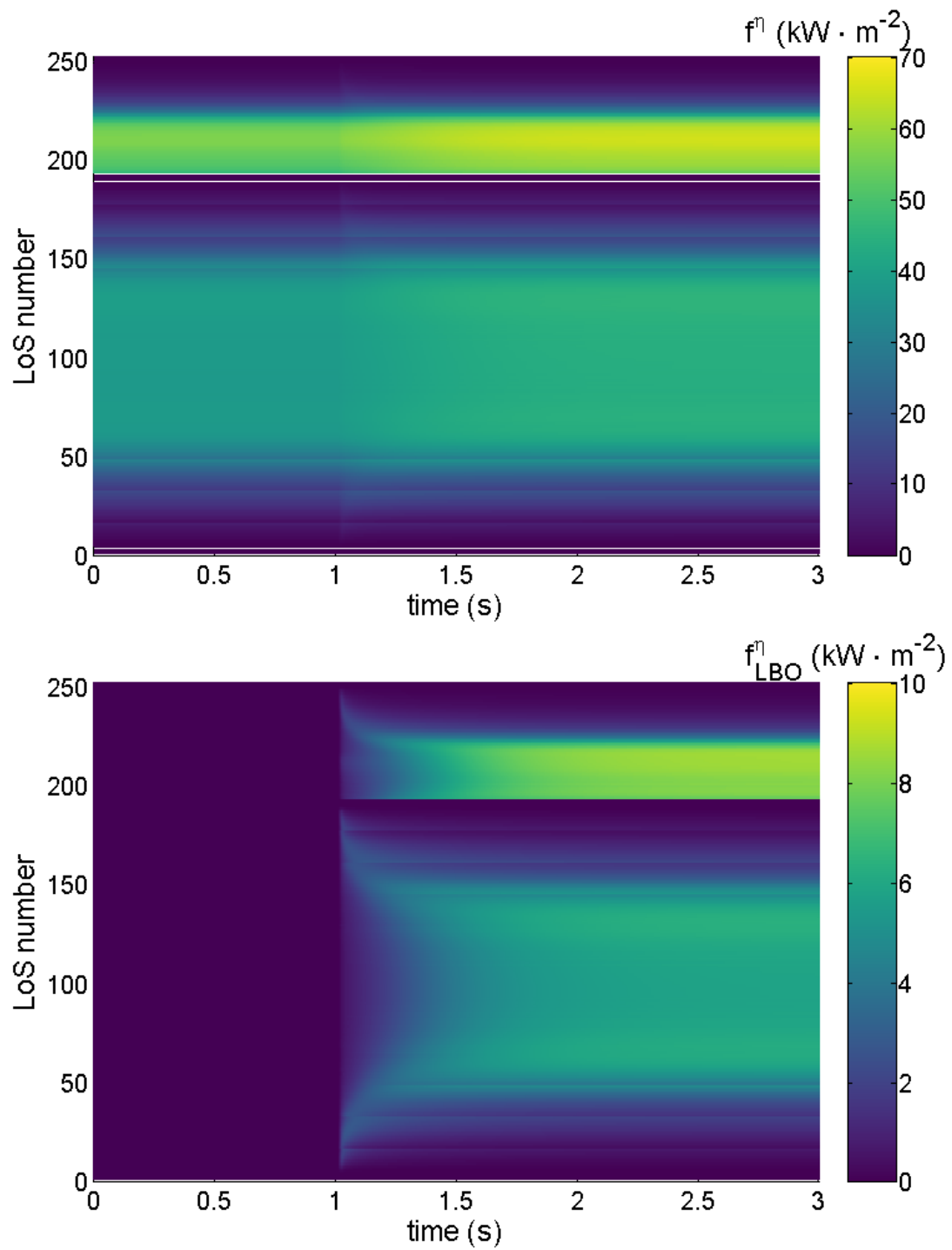


Figure 7.17 – Total (top) and background subtracted (bottom) line-integrated emissivities convoluted by the spectral response of the detector as a function of time and line-of-sight number in the case of the *positive V coefficient* scenario.

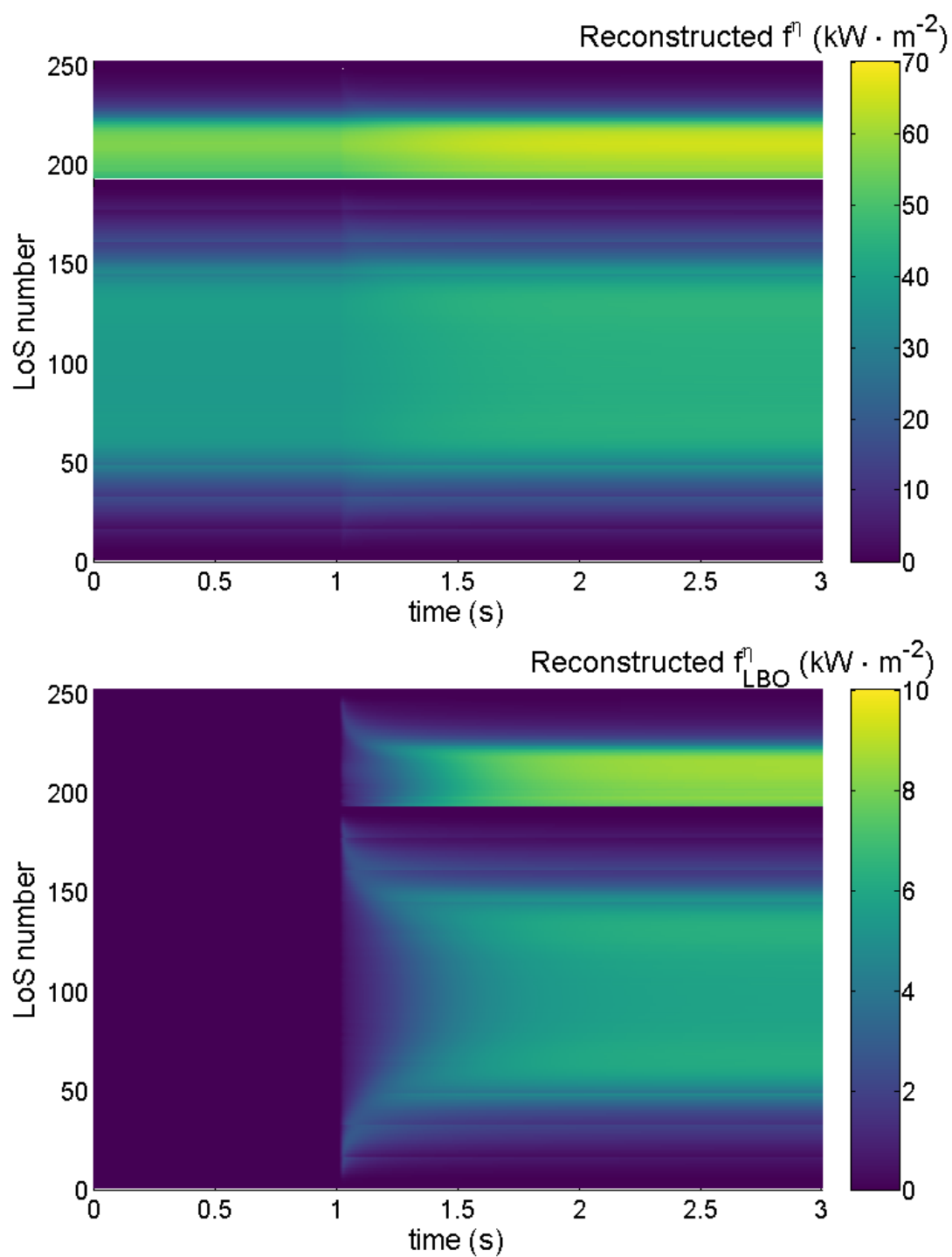


Figure 7.18 – Total (top) and background subtracted (bottom) reconstructed line-integrated emissivities convoluted by the spectral response of the detector as a function of time and line-of-sight number in the case of the *positive V coefficient* scenario.

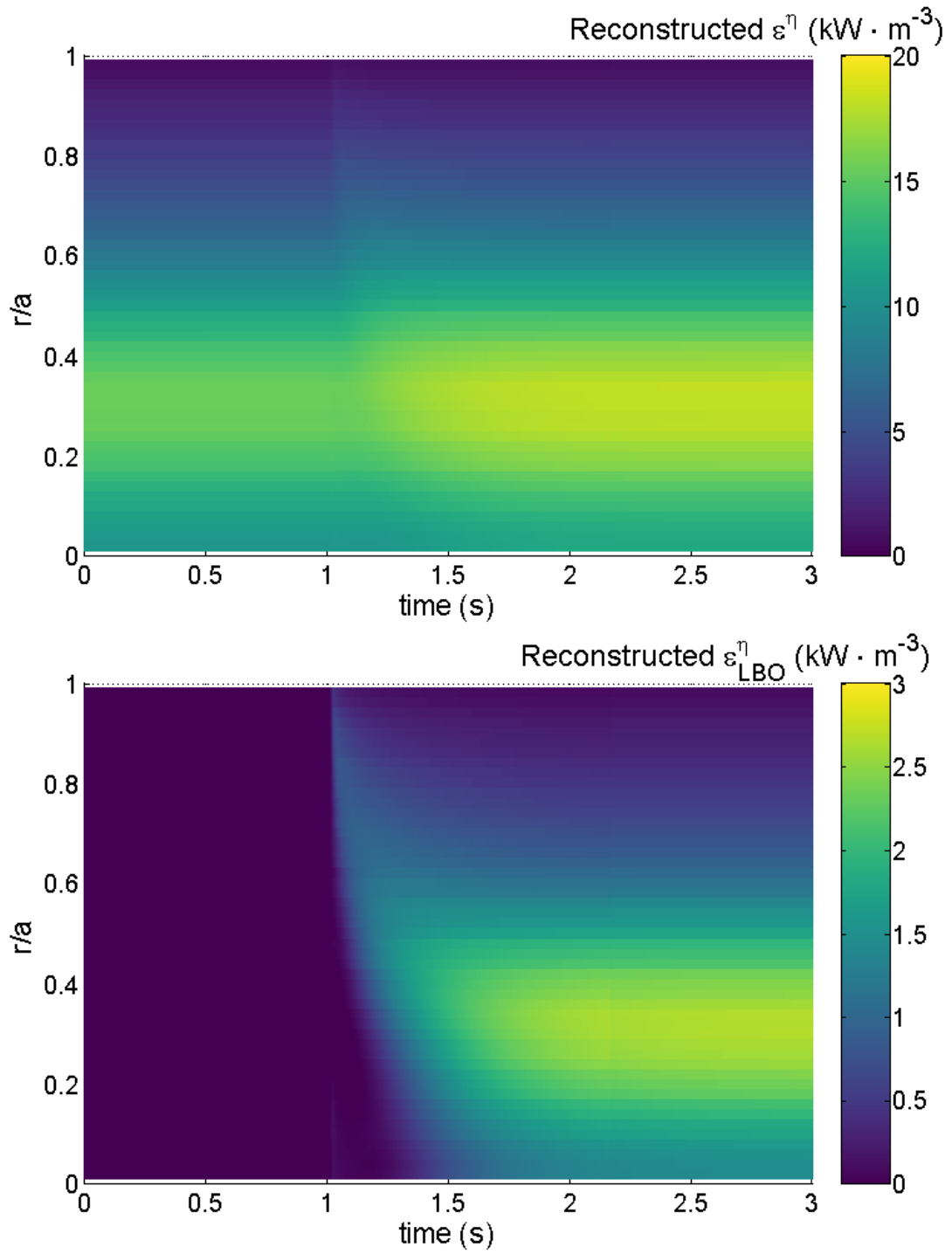


Figure 7.19 – Total (top) and background subtracted (bottom) reconstructed X-ray emissivities convoluted by the spectral response of the detector as a function of time and normalised radius in the case of the *positive V coefficient* scenario.

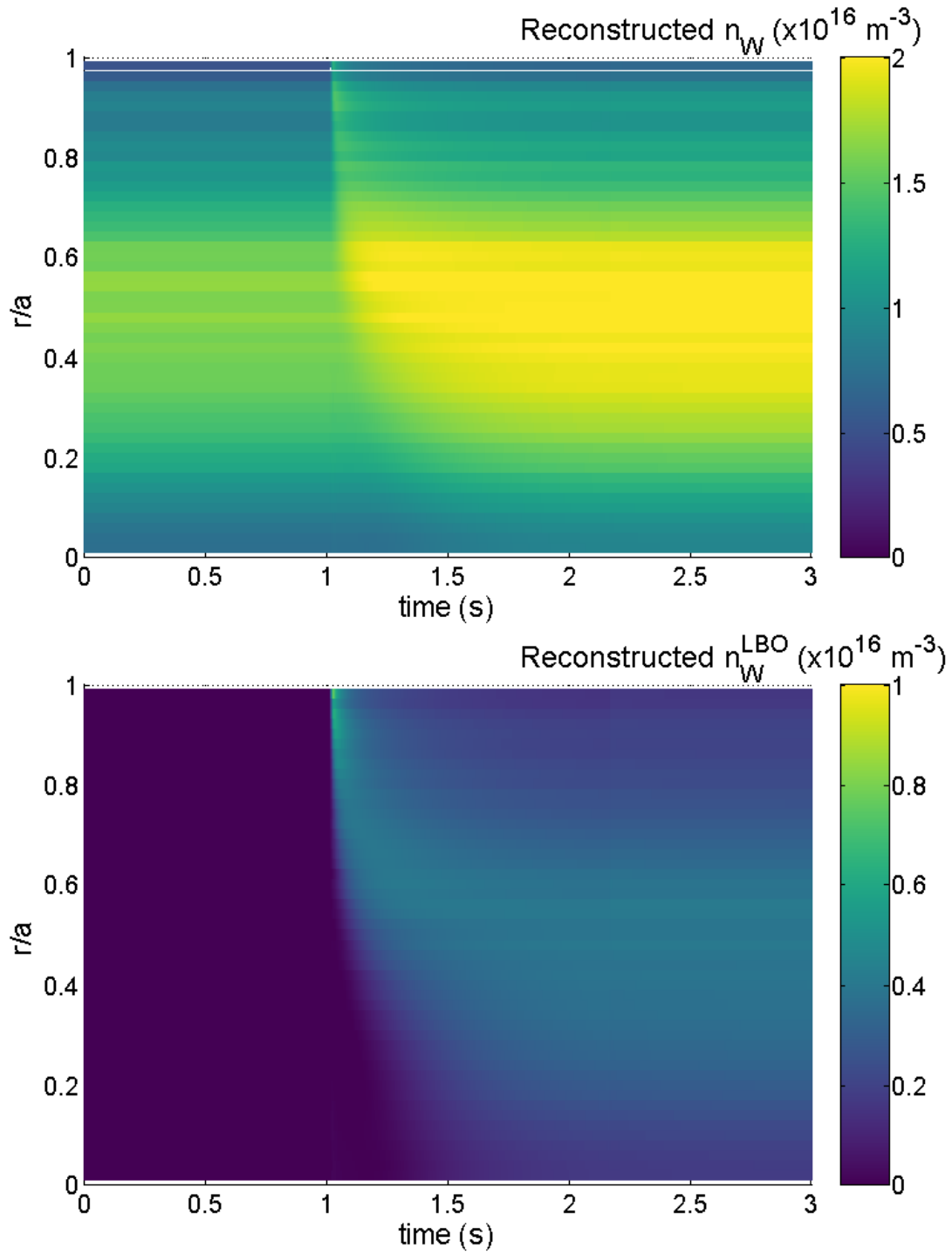


Figure 7.20 – Total (top) and background subtracted (bottom) reconstructed tungsten densities as a function of time and normalised radius in the case of the *positive V coefficient* scenario.

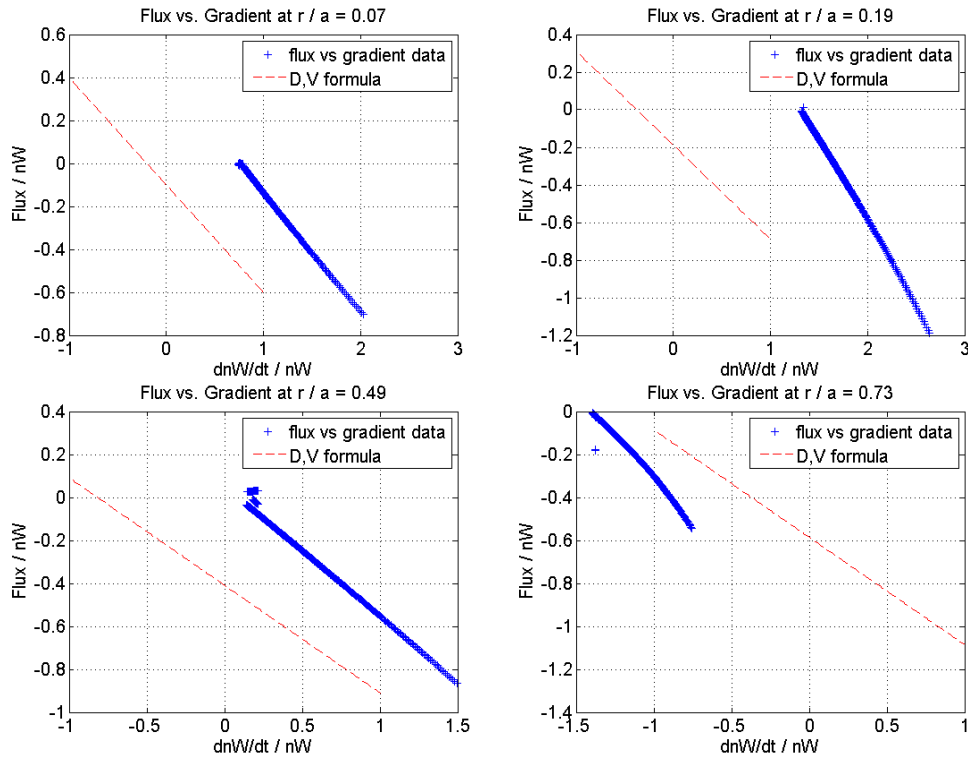


Figure 7.21 – Γ_W/n_W as a function of $dn_W/dt/n_W$ for several radial positions in the case of the *positive V coefficient* scenario. The dash line represents the result which would be obtained with the D and V coefficients of the scenario.

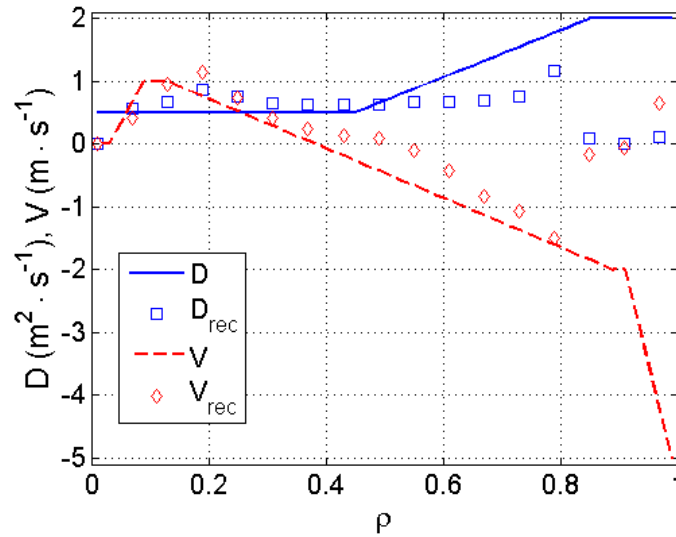


Figure 7.22 – D and V coefficients of the *positive V coefficient* scenario and their reconstruction.

7.2 Poloidal asymmetries

In section 7.1, the impurity density is considered constant over the magnetic surfaces leading to a poloidally symmetrical impurities distribution. This hypothesis is however not always valid, as shown in figure 7.23. Poloidal asymmetries arise from complex transport phenomena which are presented in this section. In order to describe these phenomena accurately, it is necessary to introduce the trapping of particles in the plasma as well as the different collisional regimes in which said particles can be.

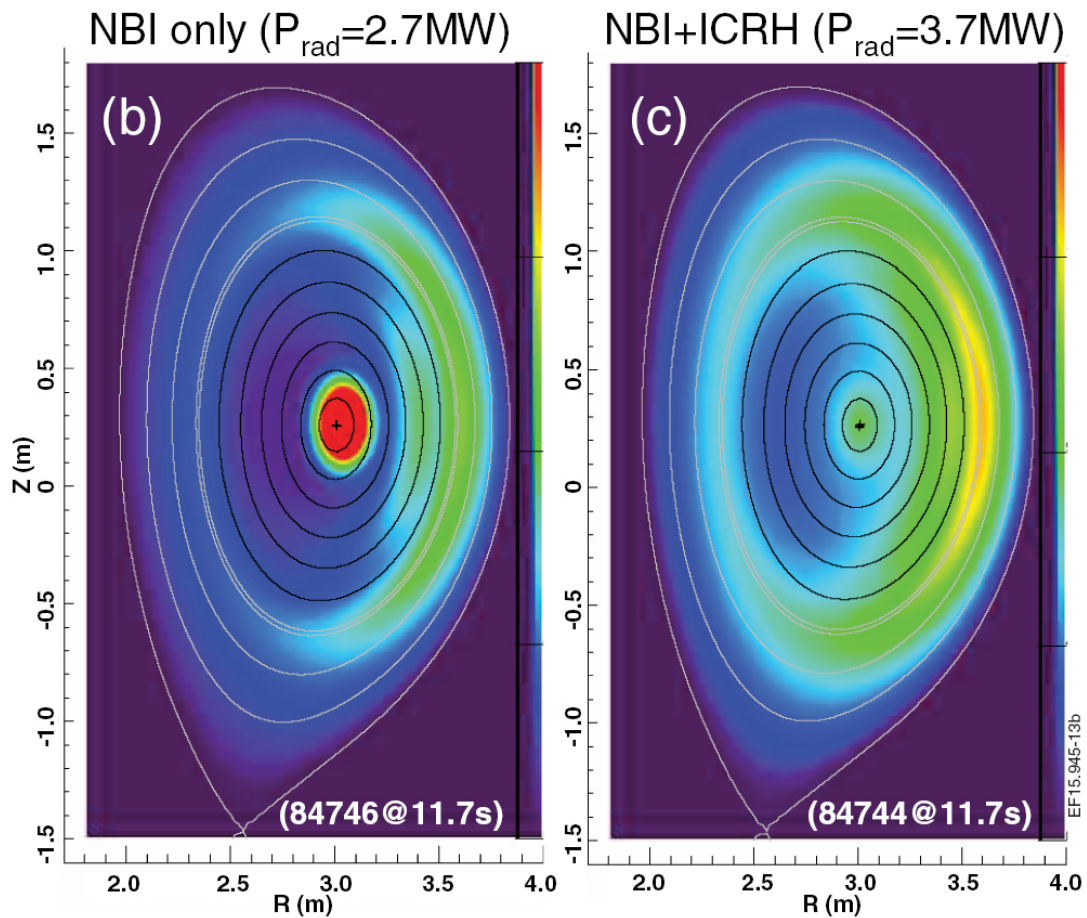


Figure 7.23 – Soft x-ray radiation profiles observed for two different heating strategies in the JET tokamak. Reprinted from [104]

As the magnetic field decreases with $1/R$ between the high and low field sides, particles experience magnetic field fluctuations while following the magnetic field lines. If a particle has a parallel velocity which is too low, it can be trapped along the magnetic field line. The particle bounces then up and down, following the so-called banana orbit shown on figure 7.24. Trapped particles get back to a passing (as opposed to trapped) orbit by collision with another charged particle.

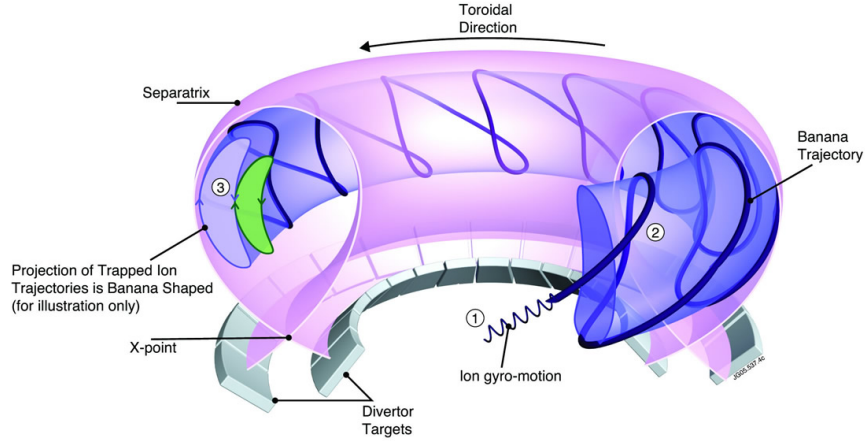


Figure 7.24 – Banana-shaped orbit of a trapped particle. Figure reprinted from [105].

7.2.1 Collisional regimes

The collisionality of a particle is defined the ratio of the detrapping frequency $\nu_{detrapp}$ over the bounce frequency ν_{bounce} :

$$\nu^* = \frac{\nu_{detrapp}}{\nu_{bounce}} \quad (7.4)$$

If $\nu^* < 1$ the trapped particles achieve several banana bounces before being detrapped (in average). This regime is the so-called banana regime. In this regime, transport is ensured exclusively by trapped particles and the diffusion coefficient grow linearly with the collision frequency.

The high collisionality regime, the so-called Pfirsch-Schlüter regime, is defined for $\nu^* > \epsilon^{-3/2}$ where ϵ is the aspect ratio. [106] Trapped particles are detrapped before they bounce and trapped particles do not contribute to transport. The diffusion coefficient also grows linearly with the collision frequency.

If $1 < \nu^* < \epsilon^{-3/2}$, then a fraction of the trapped particles complete several bounces before escaping. In this regime the diffusion coefficient is not affected by the collisionality, hence its name: the plateau regime.

7.2.2 Theory of parallel forces

Impurities are subject to parallel forces (e.g. centrifugal, electrostatic) which lead to parallel transport and potentially to poloidal asymmetries. This forces are described in the so-called *Reinke equation* [107]:

$$\frac{m_Z n_Z \Omega^2}{2} \nabla_{||} R^2 + Z n_Z e \nabla_{||} \phi + T_Z \nabla_{||} n_Z = F_{Z,||} \quad (7.5)$$

where Ω is the rotation frequency, R the major radius, ϕ the electrostatic potential and $F_{Z,\parallel}$ a parallel friction term. The first term of equation 7.5 denotes the inertial force, the second term the electrostatic force and the third one denotes the force resulting from plasma pressure.

7.2.2.1 Impact of electric field on impurity density

Fast trapped ions in the LFS can generate an electric field orthogonal to the magnetic field lines. This electric field tends to push ions away from the LFS. ICRH increases the population of supra-thermal ions in the LFS and therefore can increase this asymmetry. The effect of a radial electric field on impurity density is computed in [108]:

$$n_Z = \langle n_Z \rangle \left(1 + \frac{2r \cos(\theta)}{R_0} \left(\frac{m_Z \omega^2 R_0}{2T_i} \left(1 - \frac{Z m_i}{m_Z} \frac{Z_{eff} T_e}{Z_{eff} T_e + T_i} \right) - \frac{Z f_m}{2} \frac{T_e}{Z_{eff} T_e + T_i} \left(\frac{T_\perp}{T_\parallel} - 1 \right) \right) \right) \quad (7.6)$$

where θ is the poloidal angle, R_0 the major radius, ω the rotation frequency, Z_{eff} the effective charge of the plasma, f_m the minority fraction and $\frac{T_\perp}{T_\parallel}$ the temperature anisotropy.

7.2.2.2 Impact of inertia on impurity density

The plasma rotation leads to a centrifugal force on particles. Heavy impurities such as tungsten are subject to a strong centrifugal force which can lead to asymmetries in density. The effect of inertia on the impurity density is computed in [107]. In the case of a plasma with a single impurity species (W) in trace level ($Z_W n_W^2 \ll n_i$, where n_i is the density of the main ion in the plasma), the impurity density in the presence of a centrifugal force is given by:

$$n_W = n_W(0) \cdot \exp \left(M^2 \left(\frac{A_W}{A_i} - \frac{Z_W T_e}{T_i + Z_i T_e} \right) \left(\frac{R^2}{R_0^2} - 1 \right) \right) \quad (7.7)$$

where M is the mach number of the plasma.

7.2.2.3 Impurity transport in the presence of poloidal asymmetries

Two theories can be used to study transport in tokamaks: the neoclassical and the turbulence theory. The neoclassical theory considers the fluxes arising from particle collisions, while taking into account some specificities of tokamaks (geometry and magnetic configuration). Originally focused on electrons and energy transport, the neoclassical theory has been extended in order to account for impurities such as tungsten. [109, 110]

In the case of a plasma with ions in the banana regime and tungsten in trace level ($Z_W n_W^2 \ll n_i$) and in the Pfirsch-Schlüter regime, the neoclassical flux of impurities is

given by [111]:

$$\Gamma_W^{neo} = \frac{Z_W D_P}{R} \left(\left(\frac{1}{Z_W} \frac{R}{L_{nW}} - \frac{R}{L_{ni}} + \frac{1}{2} \frac{R}{L_{Ti}} \right) \cdot P_A - 0.33 f_P P_B \frac{R}{L_{Ti}} \right) \quad (7.8)$$

where D_P is the diffusion coefficient of the passing (as opposed to trapped) particles, $R/L_X = -(R/X)(dX/dr)$ denotes the normalized logarithmic gradient of X , f_P is the fraction of passing particles, and P_A and P_B are purely geometrical factors (in the absence of asymmetry $P_A = 1$ and $P_B = 0$).

7.2.3 Poloidal asymmetries on ITER

In order to estimate the capabilities of the ITER tomographic system to reconstruct poloidal asymmetries, simple computations of asymmetries based on equations 7.6 and 7.7 have been performed.

7.2.3.1 Tomographic setup and simulation process

For this study, the Minimum Fisher Information algorithm with anisotropy following the magnetic surfaces (presented in section 3.3.2) is used. The detector configuration is the same as in section 7.1.2: 252 lines-of-sight viewing the plasma from radial and vertical angles (see figure 5.4.1 in section 5.4.1). The LVIC is xenon-filled with a pressure length product of $100 \text{ mm} \cdot \text{atm}$ and a $200 \mu\text{m}$ beryllium window. Its spectral response is shown on figure 7.8.

Three poloidally asymmetric tungsten density profiles are computed from equations 7.6 and 7.7, and compared to a symmetrical tungsten density profile. From the density and electron temperature, the X-ray emissivity convoluted by the spectral response of the detector is computed. This is achieved using the method presented in section 2.4.2 which is based on the computation of the cooling factors. Line-integration of the X-ray emissivity over each line-of-sight is then performed. The line-integrals of the emissivity are used as inputs for tomography in order to compute the reconstructed X-ray emissivity ε_{rec}^η . From ε_{rec}^η the reconstructed tungsten density is given by:

$$n_w^{rec} = \frac{\varepsilon_{rec}^\eta - n_e^2 \cdot L_h^\eta}{n_e \cdot L_w^\eta} \quad (7.9)$$

where L_h^η and L_w^η are respectively the cooling factors of H and W, convoluted by the spectral response of the detector.

7.2.3.2 Baseline density profile

In order to assess the impact of the asymmetry on the reconstruction, a symmetrical density profile is firstly used. It is a profile peaked in the plasma core which corresponds to the *negative V coefficient* scenario just before LBO injection which is

introduced in section 7.1.3. The impurity density profile and its reconstruction are shown on figure 7.25. It can be observed that the reconstruction is very accurate for $r/a < 0.4$. Outside of this zone, however, reconstruction errors are visible.

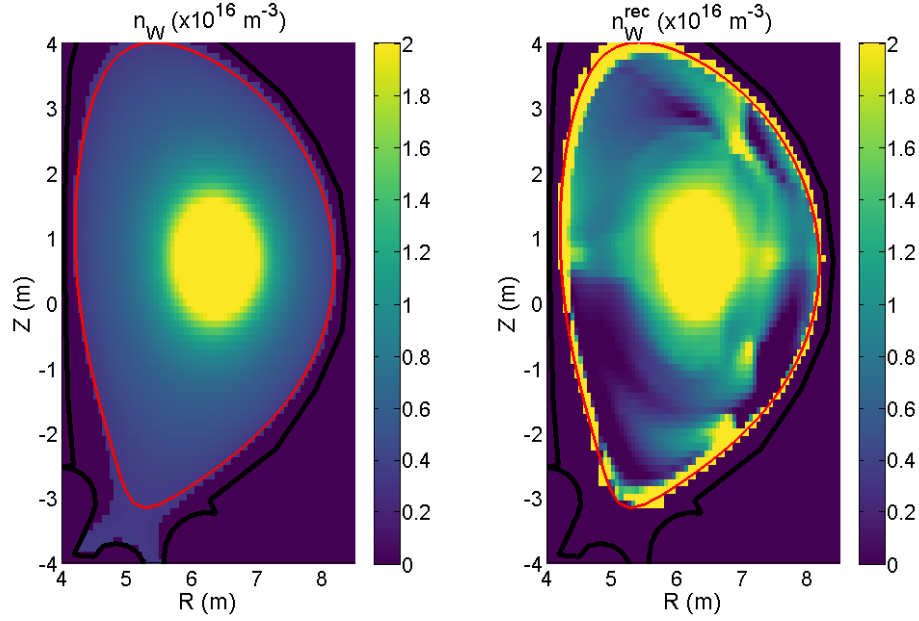


Figure 7.25 – 2D tungsten density profile (left) and its reconstruction (right) in the case of a symmetrical tungsten density profile.

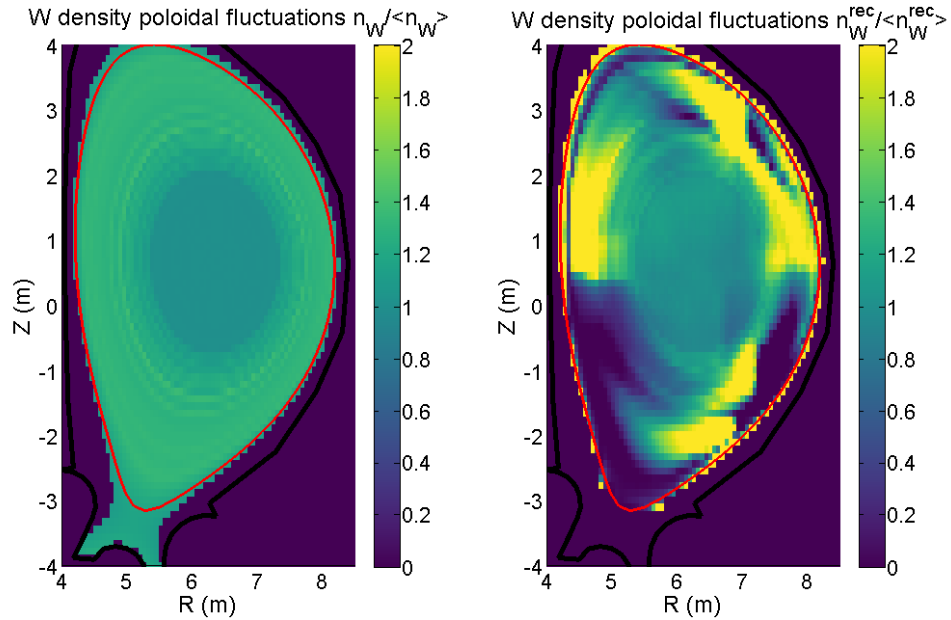


Figure 7.26 – Tungsten density poloidal fluctuation (left) and its reconstruction (right) in the case of a symmetrical tungsten density profile.

The asymmetry of the density can be observed through its poloidal fluctuations. The reconstruction of $n_W / \langle n_W \rangle$ is very accurate for $r/a < 0.4$. Similarly as with the density, significant reconstruction errors are observed outside of this region. Overall this reconstruction is very significant, as most the tungsten inventory (the plasma core) is reproduced well. The presence of inaccuracies for $r/a > 0.4$ in such a simple configuration seems to indicate that they originate from the tomographic inversion. Improving the inversion method or the lines-of-sight configuration should help getting rid of these inaccuracies.

7.2.3.3 Electric field-induced asymmetry

The electric field-induced asymmetry is computed using equation 7.6. $\langle n_W \rangle$ is taken as the baseline tungsten density profile. The toroidal rotation frequency is chosen based on [112] and is shown on figure 7.27. The rotation frequency is linearly decreasing from $1.3 \cdot 10^3$ Hz at $r/a = 0$ to 0 at $r/a = 1$. The temperature anisotropy has been chosen as 5 based on [113] with a gaussian resonance of the electric field arbitrarily centered in $r/a = 0.35$, as shown on figure 7.27. The minority fraction f_m has been chosen arbitrarily as 0.05.

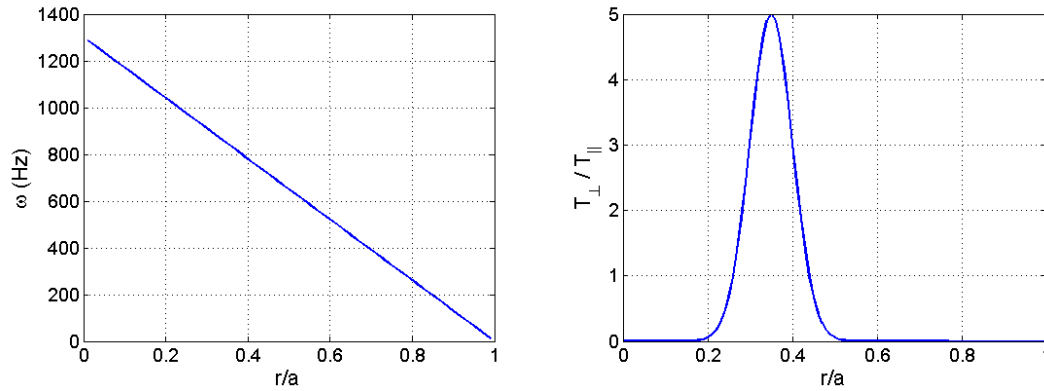


Figure 7.27 – Left: radial profile of the toroidal rotation frequency. Right: Radial profile of the minority temperature anisotropy ratio.

The electron temperature profile introduced in section 2.4.1 and the ion temperature profile from the ITER baseline inductive scenario [114] are used to compute the asymmetry. Both profiles are displayed on figure 7.28.

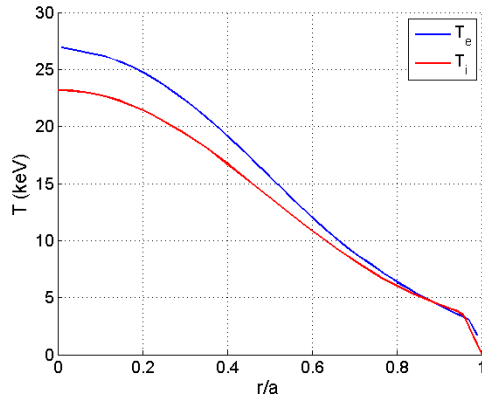


Figure 7.28 – Radial profile of the ion and electron temperatures.

The obtained density profile is shown on the left part of figure 7.29. Similarly as its $\langle n_W \rangle$, the tungsten density is quite peaked in the plasma core. The electric field generated a HFS asymmetry around $r/a = 0.35$ which is pretty localised. The reconstructed density is peaked in the core and the HFS asymmetry can be observed, although it is quite blurry. Less reconstruction errors are present outside of the plasma core.

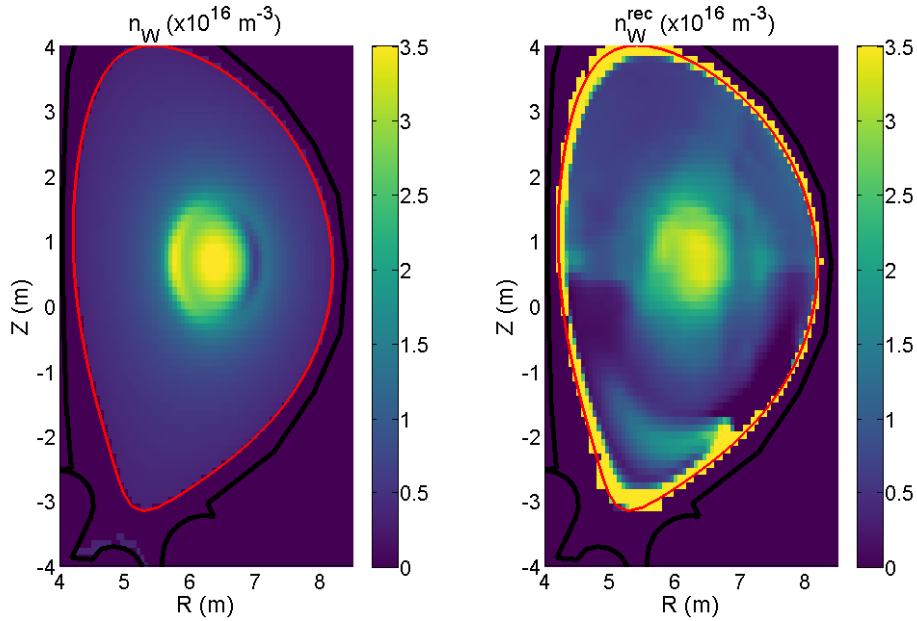


Figure 7.29 – 2D tungsten density profile (left) and its reconstruction (right) in the case of a tungsten density profile exhibiting an electric field-induced asymmetry.

The study of the poloidal fluctuations of the density show that the asymmetry is indeed well reconstructed (still with a slight blurriness). Outside of the ring of asym-

metry the poloidal fluctuations are equal to 1, indicating a symmetrical density profile. Overall the reconstruction of the electric field-induced asymmetry is well reconstructed. The presence of the asymmetry seems to enhance the quality of reconstruction of the symmetrical region ($r/a > 0.45$) as the intensity of the inaccuracies in this region has decreased compared to the baseline profile.

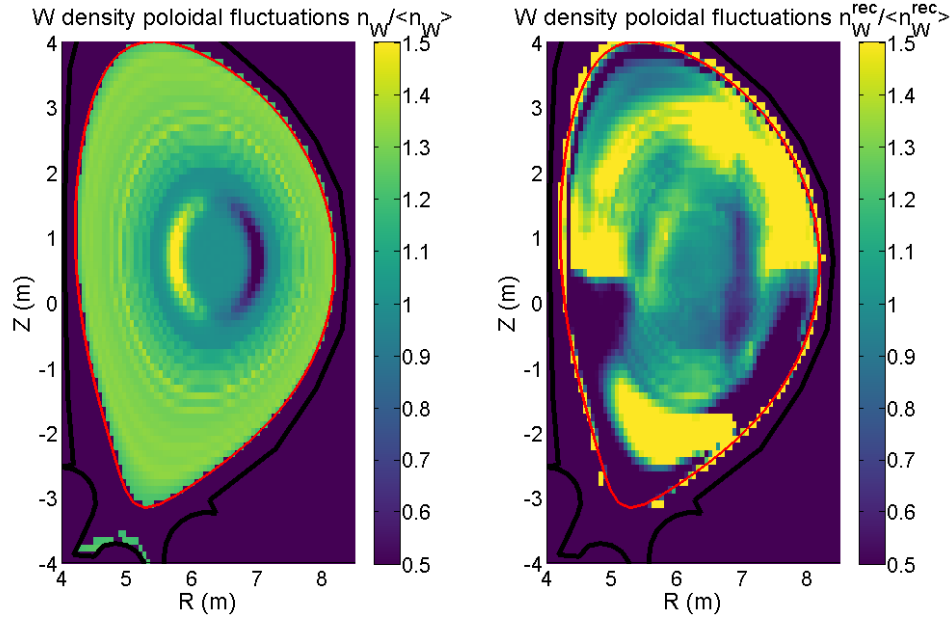


Figure 7.30 – Tungsten density poloidal fluctuation (left) and its reconstruction (right) in the case of a tungsten density profile exhibiting an electric field-induced asymmetry.

7.2.3.4 Centrifugal force-induced asymmetry

The density profile in the presence of an asymmetry induced by a centrifugal force is computed from equation 7.7. Similarly as for the previous density profile, the baseline tungsten profile is used as $n_W(0)$. In order to ensure an intense enough asymmetry, the Mach number of the plasma has been overestimated to $M = 0.35$ (compared to an estimation of 0.05 for ITER [112]).

The obtained tungsten density profile is displayed on the left part of figure 7.31. A clear and intense LFS asymmetry from the plasma core to the LCMS can be observed. The reconstructed tungsten density profile, displayed on the right part of figure 7.31, also exhibits a strong LFS asymmetry although its position is more approximative. The reconstruction of the HFS is fairly accurate, with less reconstruction errors compared to the baseline tungsten density profile.

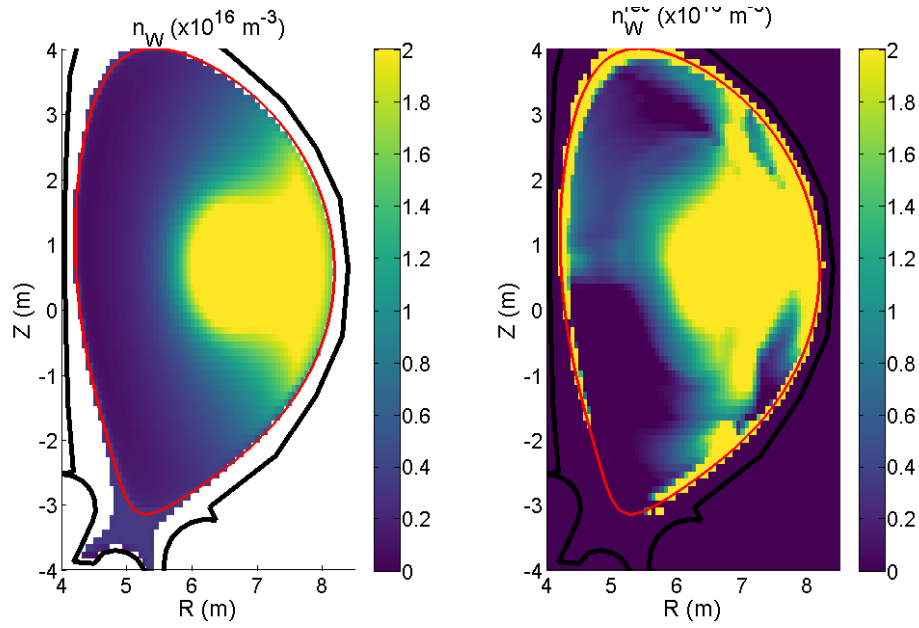


Figure 7.31 – 2D tungsten density profile (left) and its reconstruction (right) in the case of a tungsten density profile exhibiting a centrifugal force-induced asymmetry.

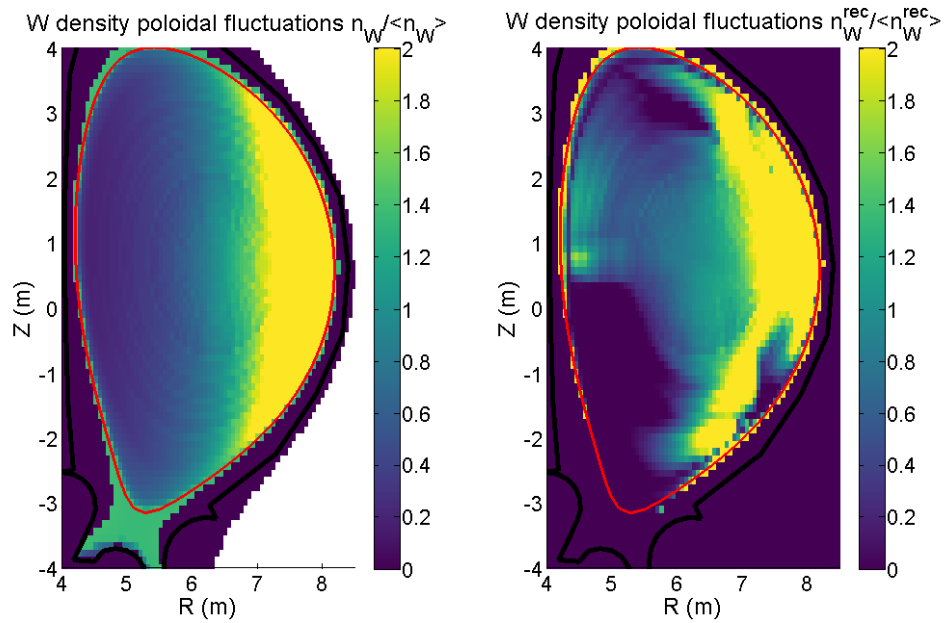


Figure 7.32 – Tungsten density poloidal fluctuation (left) and its reconstruction (right) in the case of a tungsten density profile exhibiting a centrifugal force-induced asymmetry.

The study of $n_W / \langle n_W \rangle$, shown on figure 7.32, confirms the LFS asymmetry as we

can see on the left part of the figure that the poloidal fluctuation increases linearly with R . This feature is not reconstructed precisely (right part of figure 7.32) but the overall behaviour is present. As a result, the reconstruction of a centrifugal force-induced asymmetry can be considered satisfying in this example.

7.2.3.5 Combined asymmetry

The two previous asymmetries have been combined together in a single tungsten density profile which is shown on figure 7.33. Both the HFS asymmetry which is shaped as a ring at $r/a \approx 0.35$ and the LFS asymmetry from core to LCMS can be observed in the density profile. The reconstruction is overall pretty blurry, but one can notice the LFS asymmetry at the plasma edge as well as some structures which can be identified as part of the HFS asymmetry.

The tungsten density poloidal fluctuation (see figure 7.34) is simply the superposition of the fluctuations observed separately with each asymmetric profile. The reconstruction of $n_W / \langle n_W \rangle$ shows a pretty accurate LFS asymmetry. Similarly as in the previous cases, the core reconstruction is pretty blurry but a decrease (resp: increase) of $n_W / \langle n_W \rangle$ can be identified at $r/a \approx 0.35$ towards the LFS (resp: HFS).

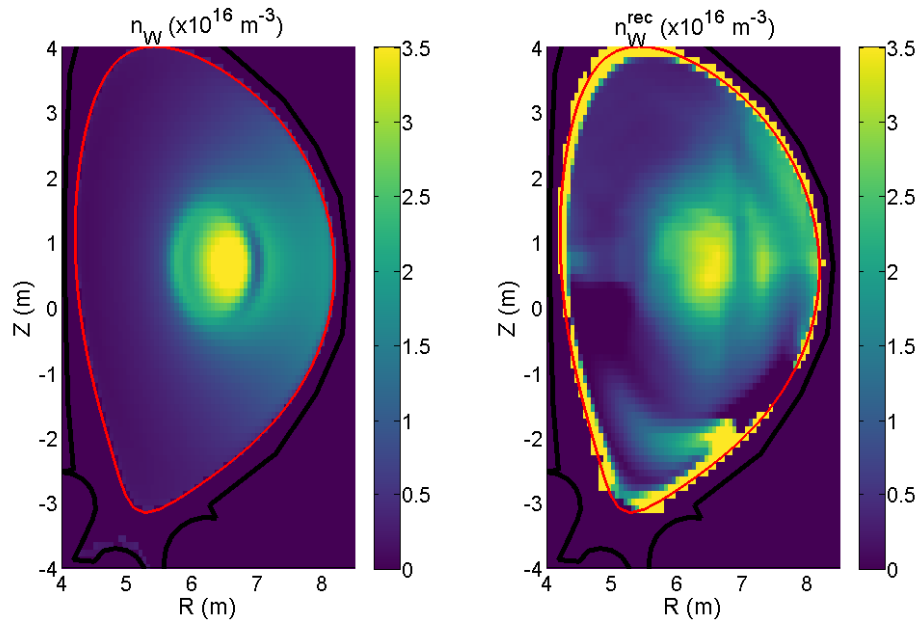


Figure 7.33 – 2D tungsten density profile (left) and its reconstruction (right) in the case of a tungsten density profile exhibiting an asymmetry induced by both an electric field and the centrifugal force.

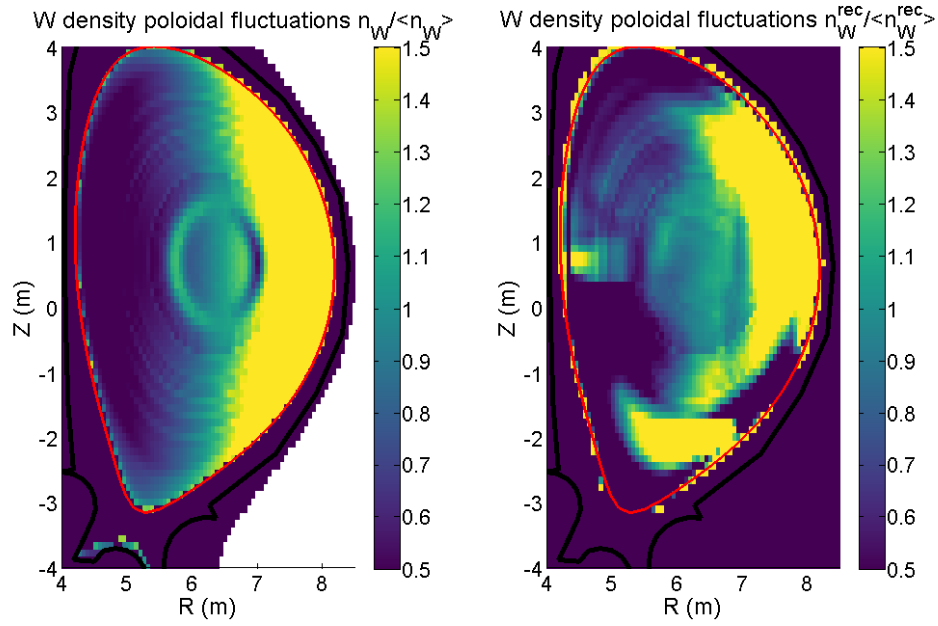


Figure 7.34 – Tungsten density poloidal fluctuation (left) and its reconstruction (right) in the case of a tungsten density profile exhibiting an asymmetry induced by both an electric field and the centrifugal force.

Overall, the LVIC allows a fairly accurate reconstruction of poloidal asymmetries. The main limitation of the system seems to be the tomographic inversion which brings reconstruction errors outside of the plasma core. A slight blurriness is observed in the core but it is low enough to still identify the asymmetries.

8 Energy discrimination using LVIC

Sommaire

8.1	Spectral deconvolution method	183
8.1.1	Hypothesis on the X-ray spectrum	185
8.1.2	Minimization algorithm	187
8.2	Application to ITER	189
8.2.1	Figures of merit	189
8.2.2	Spectral deconvolution using argon-filled MA-LVIC	189
8.2.2.1	Detector setup	189
8.2.2.2	Single lines-of-sight results	190
8.2.2.3	Overall accuracy over all lines-of-sight	192
8.2.3	Spectral deconvolution using xenon-filled MA-LVIC	195
8.2.3.1	Detector setup	195
8.2.3.2	Single lines-of-sight results	195
8.2.3.3	Overall accuracy over all lines-of-sight	197
8.2.4	Comparison between argon and xenon	199
8.2.5	Improving the reconstruction in the [2, 3] keV energy band	199
8.2.6	Sensitivity analysis	201
8.3	Energy-resolved X-ray tomography	202
8.3.1	Figures of merit	203
8.3.2	Results	203
8.3.3	Sensitivity analysis	206
8.4	Reconstruction of the electron temperature	208
8.4.1	Figures of merit	208
8.4.2	Results	209
8.4.3	Sensitivity analysis	210

8.1 Spectral deconvolution method

This chapter covers the deconvolution of the incoming spectrum using Multi-Anodes Low Voltage Ionization Chambers (MA-LVIC), introduced in section 3.2.2. Energy discrimination using ionization chambers is a novel technique which has been developed in the scope of this thesis. It is based on the fact that statistically, low energy photons cover a smaller distance in the gas than high energy photons before interacting with the gas. The idea behind the MA-LVIC is to use the knowledge of where

photoionization occurred in order to infer information on the energy distribution of the incoming photon flux. This is achieved by dividing the detection volume into several sub-chambers. Each sub-chamber is defined by an anode which collects the charge generated in the volume of gas located between the anode and the cathode as shown on figure 8.1.

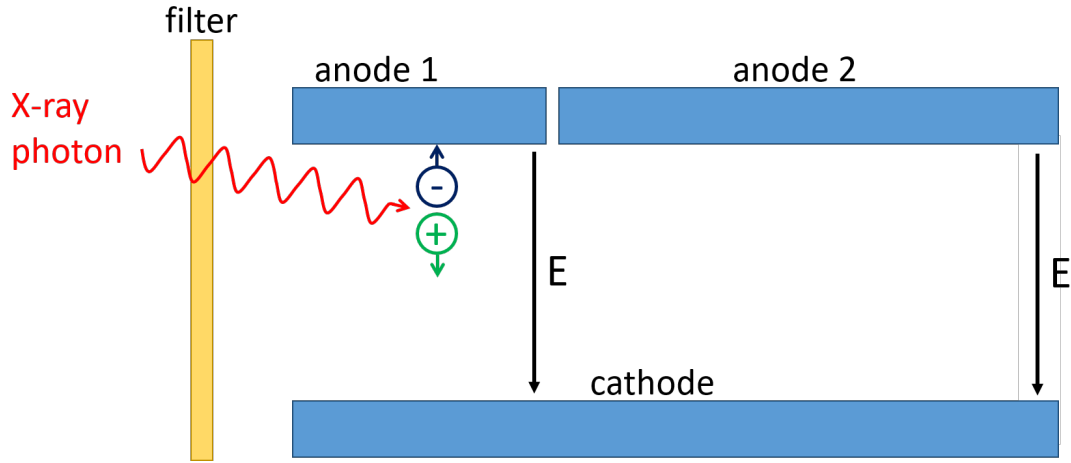


Figure 8.1 – Schematics of a multi-anodes low voltage ionization chamber.

The sub-chambers are numbered in ascending order from the filter: sub-chamber number one is the first volume of gas encountered by the photon flux. From a sub-chamber to the next the photon spectrum is shifted towards higher energies as the lowest energy photons are absorbed. As a result, the current collected by a sub-chamber contains information on a different part of the spectrum, which moves towards higher energy for increasing sub-chamber numbers. The energy discrimination problem consists of finding the spectrum of the incoming photon flux which fits best the measured currents:

$$\phi_0 = \underset{\phi}{\operatorname{arg\,min}}(\|I^{meas} - I(\phi)\|_2^2) \quad (8.1)$$

where ϕ_0 is the solution spectrum, I^{meas} is the vector containing the currents measured by each sub-chamber, I is the function linking a photon spectrum to the currents measured by each sub-chamber - $I(\phi)$ being the vector containing the currents generated by ϕ - and $\|\cdot\|_2$ denotes the Euclidean norm. In the scope of this thesis, no experiment has been made on MA-IVIC and the measured currents refer to currents simulated with the synthetic diagnostic tool presented in chapter 4. Due to the finite amount of measurements, the fact that the spectrum is defined over a continuous space and that the measurements are subject to experimental noise, the spectral deconvolution is a so-called *ill-posed problem*. Its resolution requires the use of regularisation (introduced in section 3.3.2 in the scope of tomographic inversions) or hypothesis on the photon spectrum. The latter approach is chosen in the scope of this thesis and is described in this chapter.

8.1.1 Hypothesis on the X-ray spectrum

The processes leading to the emission of X-ray photons, described in 2.2, are well understood and so is the overall shape of the X-ray spectrum. At low energy ($h\nu < 10\text{keV}$), the spectrum is dominated by line emission. From $h\nu = 10\text{keV}$, X-ray emission mainly comes from radiative recombination and Bremsstrahlung emission which lead to a continuous spectrum decreasing with $\exp(-\frac{h\nu}{k_B T_e})$. The contribution of each impurity considered in the high power D-T scenario to the photon flux impinging line-of-sight number 96 is displayed on figure 8.2.

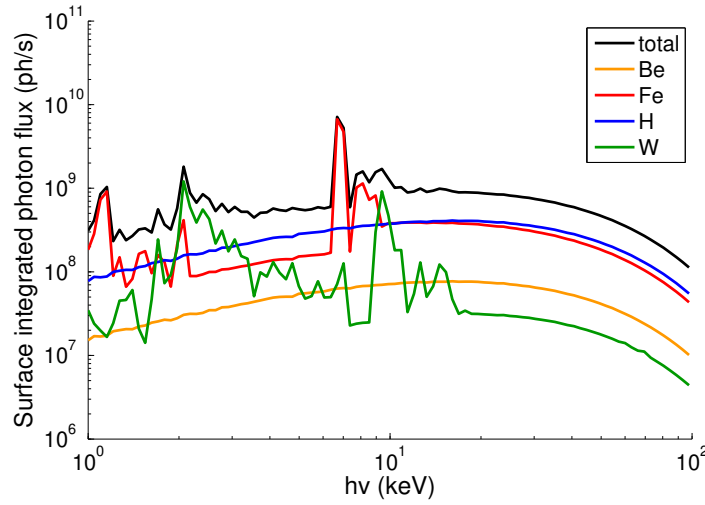


Figure 8.2 – Contribution of each impurity to the incoming photon flux of line-of-sight number 96 which goes through the very core of the plasma.

In the $[2, 100]$ keV range, the incoming photon flux can be modelled with a relatively high accuracy by a simple mathematical function depending on 4 parameters only. Two gaussian peaks are considered in the low energy part of the spectrum, covering the tungsten lines observed at the plasma edge around $h\nu = 2\text{keV}$ (in green in equation 8.2) and the iron line at $h\nu \approx 7\text{keV}$ (in red in equation 8.2). The peak corresponding to the iron line is widened and slightly shifted towards higher energies in order to account for tungsten and iron line radiation located in the $8\text{keV} < h\nu < 10\text{keV}$ range. The width of the tungsten line emission peak is chosen arbitrarily in order to cover the part of tungsten line radiation which is not absorbed by the filter. The continuum is modelled by an exponential decrease coupled to a correction factor C_{cor} . This factor takes into account the fact each line-of-sight integrates the X-ray emissivity over a line where the electron temperature is not constant. Continuity of the mathematical function between the line emission and continuum parts of the spectrum is achieved by adding a straight connecting the $(0\text{keV}, 0)$ and the $(10\text{keV}, f^{exp}(10\text{keV}))$ points (in blue in equation 8.2), where $f^{exp}(10\text{keV})$ corresponds to the value of the exponential

part of the function estimated at $h\nu = 10\text{keV}$. The expression of the function is:

$$f(h\nu, X) = \begin{cases} X_3 \cdot e^{-2 \cdot (h\nu-7)^2} + X_4 \cdot e^{-1.5 \cdot (h\nu-2)^2} + \frac{X_1 \cdot e^{-X_2 \cdot 10}}{10} \cdot h\nu & \text{if } h\nu < 10\text{keV} \\ X_1 \cdot e^{-X_2 \cdot h\nu} \cdot C_{cor}(h\nu) & \text{if } h\nu \geq 10\text{keV} \end{cases} \quad (8.2)$$

where $X = (X_1, X_2, X_3, X_4)$ is the vector containing each coefficient of the function, X_1 and X_2 are respectively the amplitude and the slope of the exponential decrease, X_3 is the amplitude of the peak modelling the iron line emission at $h\nu \approx 7\text{keV}$ and X_4 is the amplitude of the peak modelling the tungsten lines at $h\nu \approx 2\text{keV}$. The photon spectrum derived from the X vector is labelled $\phi = f(X)$.

Due to the lack of additional energy-resolved X-ray emissivity scenarios the actual C_{cor} coefficients have been computed for each line-of-sight and averaged in order to obtain a final coefficient $C_{cor} = \frac{1}{N_{LoS}} \sum_{i=1}^{N_{LoS}} C_{cor}^{LoS}(i)$, which is displayed in black on figure 8.3. Using of a single C_{cor} coefficients for all lines-of-sight aims at demonstrating the geometrical robustness of this method. The application of the function to the fitting of the X-ray spectrum impinging line-of-sight number 96 is displayed on figure 8.3.

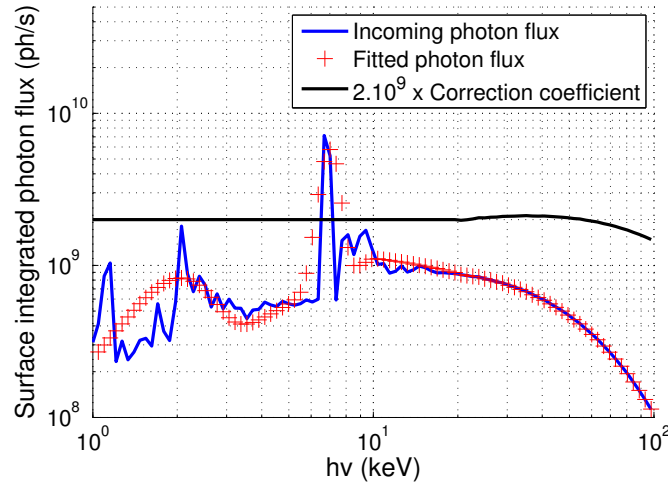


Figure 8.3 – Fitting of the line-of-sight number 96 incoming photon flux. In this figure, the parameters of the function are $X_1 = 1.40 \cdot 10^9$ ph/s, $X_2 = 2.26 \cdot 10^{-2} \text{keV}^{-1}$, $X_3 = 5.0 \cdot 10^9$ ph/s, and $X_4 = 6.0 \cdot 10^8$ ph/s.

The energy deconvolution problem now consists of finding the set of X coefficients which reproduce best the measured currents:

$$X_0 = \arg \min_X (||I^{meas} - I(f(X))||_2^2) \quad (8.3)$$

where X_0 is the solution vector of parameters. The reconstructed flux is therefore $\phi_0 = f(X_0)$.

8.1.2 Minimization algorithm

With the use of the hypothesis on the shape of the photon flux and with enough measurements (i.e. enough sub-chambers), the problem of spectral deconvolution becomes the minimization problem described in equation 8.3. An algorithm minimising the difference between the measured and reconstructed currents has been developed for energy discrimination. It is based on successive gradient descents performed over each X_i parameter. The cost function of this method is defined as:

$$r(X) = \|I^{meas} - I(f(X))\|_2^2 \quad (8.4)$$

The architecture of the algorithm is shown on figure 8.4. The algorithm repeats the same iterations until convergence is achieved.

The initialisation of the parameter vector X_0 depends on the line-of-sight considered. Spectral deconvolution is performed for a line-of-sight at a time and the scanning of all the lines-of-sight is performed from the edge to the core of the plasma: the order of the lines-of-sight is $1 \rightarrow 96$, $192 \rightarrow 97$ and then $193 \rightarrow 252$. For lines-of-sight number 1, 192 and 193, X_0 is chosen arbitrarily as $X_0 = (5 \cdot 10^7, 4 \cdot 10^{-1}, 5 \cdot 10^6, 4 \cdot 10^7)$. The values of this initial vector have been chosen in order to be close to fitting the incoming spectrum of the lines-of-sight looking at the plasma edge while still requiring significant modification from the algorithm. For the rest of the lines-of-sight, X_0 is taken as the solution obtained for the previous line-of-sight. This allows a significant time gain (less iterations are required to reach the solution) by taking into account the space continuity of the X-ray emissivity.

Starting from the initial vector X_0 , gradient descents are performed in each direction \vec{e}_i . For a given direction, the step of the gradient is defined as $\frac{X_0(i)}{10}$. The sense of the gradient descent is computed by comparing the cost function of X_k , $X_k + s\vec{e}_i$ and $X_k - s\vec{e}_i$ where s is the step. If $r(X_k)$ is lower than both $r(X_k + s\vec{e}_i)$ and $r(X_k - s\vec{e}_i)$, then the gradient descent with this step is skipped (arrow number 1 on figure 8.4) as $r(X_k)$ is the lowest value achievable with this step. Otherwise a gradient descent with constant step is then performed (arrow number 2 on figure 8.4) until a minimum of $r(X_k)$ is obtained. From that point, the step is divided by 10 in order to add precision and the process (computation of the sense and gradient descent) is repeated (arrow number 3 on figure 8.4). Consecutive divisions of the step take place a total of 5 times in order to reach a step of $\frac{X_0(i)}{10^6}$.

Once the consecutive gradient descents are performed, the process is repeated for the next direction (arrow number 4 on figure 8.4). When gradient descents have been performed for each direction, the convergence is estimated: if there has not been significant change in between X_k and X_{k+1} , the solution is taken as $X_{solution} = X_{k+1}$. Otherwise, the process is repeated again (arrow number 5 on figure 8.4). The convergence criterion is: $\|X_{k+1} - X_k\| < 10^{-4} \|X_k\|$. The reconstructed photon spectrum is therefore $\phi^{rec} = f(X_{solution})$.

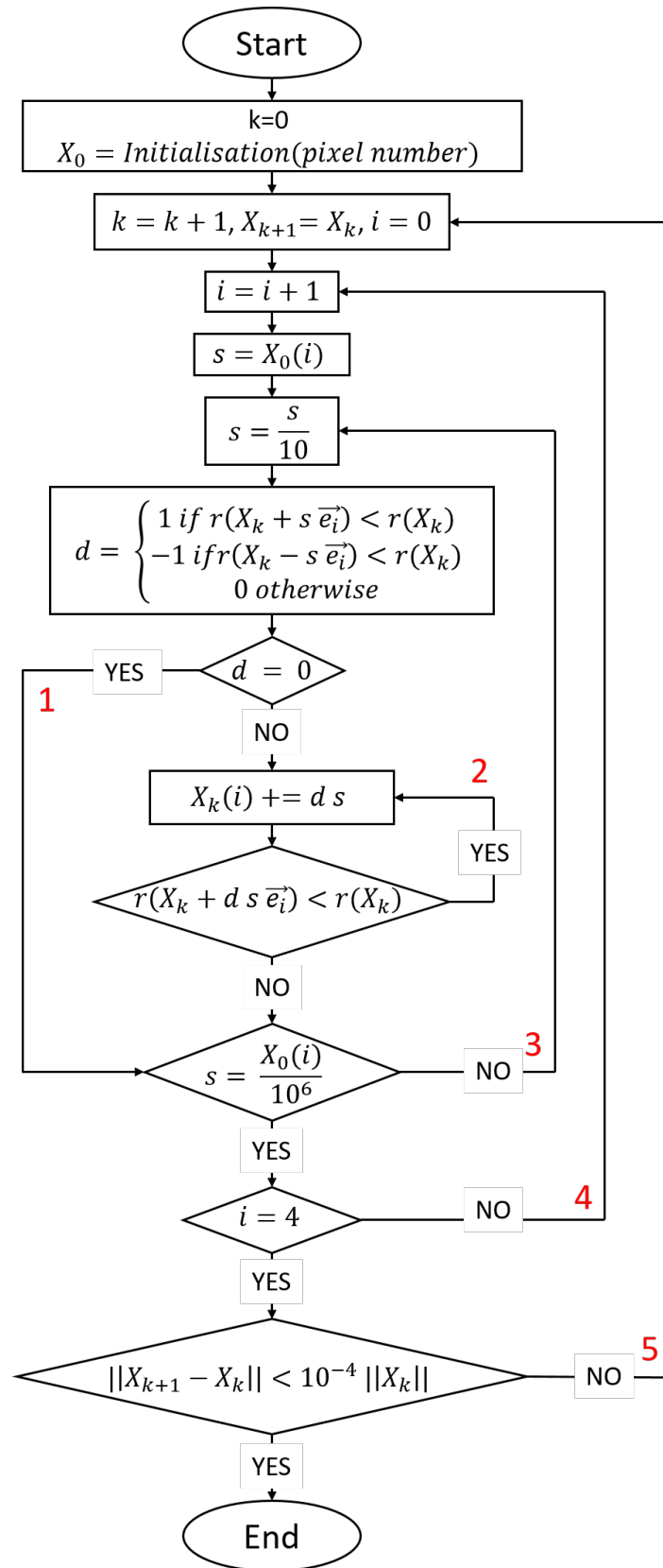


Figure 8.4 – Architecture of the minimization algorithm.

8.2 Application to ITER

The method previously described is applied to the ITER emissivity scenario described in section 2.4.1. The lines-of-sight geometry used is the *60 vertical lines-of-sight configuration* presented in section 5.4.1. Quantification of the accuracy of the deconvolution is introduced. The fitness of argon and xenon for energy discrimination is investigated.

8.2.1 Figures of merit

Similarly as for X-ray tomography, root mean squared estimates of the reconstruction error are used as figures of merit. In order to assess the accuracy of the spectral deconvolution, the following figure of merit is defined:

$$RMS_{dec} = \sqrt{\frac{\sum_{i=1}^{N_{bins}} dh\nu(i)^2 \cdot \left(\frac{\phi(i) - \phi^{rec}(i)}{\phi(i)}\right)^2}{\sum_{i=1}^{N_{bins}} dh\nu(i)^2}} \quad (8.5)$$

where $dh\nu(i)$ is the width of the i -th energy band, N_{bins} is the amount of energy bins, ϕ is the photon flux impacting the detector and ϕ^{rec} is the reconstructed photon flux. It consists of the root mean square of the deconvolution relative error weighted by the width of the energy bands.

Knowing how well the measured currents are fitted allows for identification of malfunctions in the algorithm or the unfitness of the mathematical function to accurately fit the X-ray spectrum. Such information is contained in the following figure of merit:

$$RMS_{cur} = \frac{1}{N_{anodes}} \sqrt{\sum_{i=1}^{N_{anodes}} \left(\frac{I^{meas}(i) - I^{rec}(i)}{I^{meas}(i)} \right)^2} \quad (8.6)$$

where N_{anodes} is the amount of anodes in the MA-LVIC, and $I^{rec} = I(\phi^{rec})$ is the vector of the currents which would be measured by a MA-LVIC irradiated by the photon flux ϕ^{rec} . The fitting of the current is considered satisfactory if $RMS_{cur} < 10^{-2}$.

Because the fitting function is very simple, it will not fit perfectly the incoming spectrum which contains numerous peaks at low energy. Therefore the RMS_{dec} obtained are quite high with regards to RMS_{cur} and will mostly be used to compare different reconstructions (e.g. with different gases).

8.2.2 Spectral deconvolution using argon-filled MA-LVIC

8.2.2.1 Detector setup

Spectral deconvolution has been performed using a MA-LVIC with 5 anodes filled with argon. The pressure length product used for each sub-chamber is 5, 15, 50, 175

and $500 \text{ mm} \cdot \text{atm}$. A MA-LVIC with anodes of 1, 3, 10, 35 and 100 mm under 5 bars of pressure would achieve such pressure length products. A beryllium window of $200 \mu\text{m}$ is considered as a filter. The spectral responses of each sub-chamber are displayed on figure 8.5. The lines-of-sight geometry used in this study is the 60 vertical lines-of-sight configuration presented in section 5.4.1.

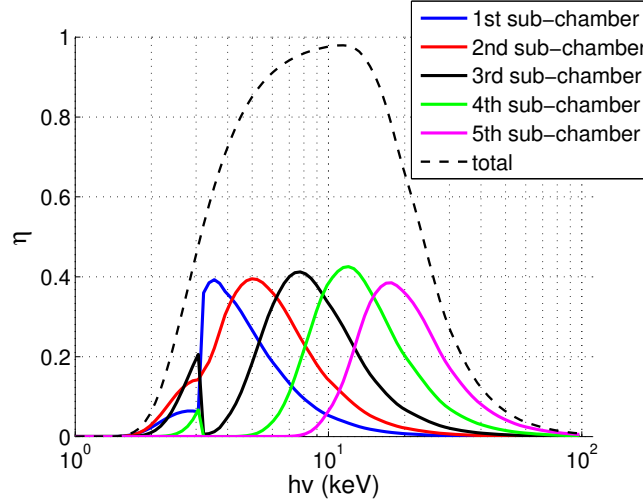


Figure 8.5 – Spectral response of each sub-chamber in a 5 anodes argon-filled MA-LVIC. The length pressure products of the sub-chamber are respectively 5, 15, 50, 175, and $500 \text{ mm} \cdot \text{atm}$, and the filter consists of $200 \mu\text{m}$ of beryllium.

8.2.2.2 Single lines-of-sight results

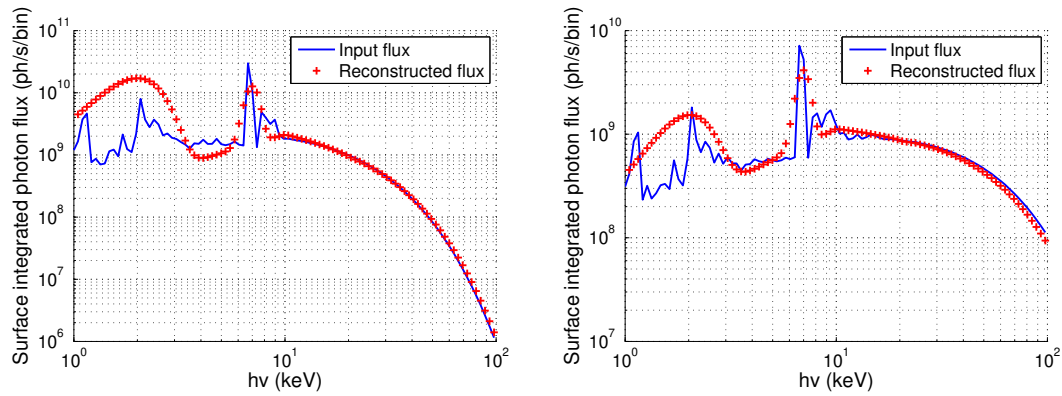


Figure 8.6 – Left: Spectral deconvolution of the photon flux of line-of-sight 45 ($r/a \approx 0.5$). Right: Spectral deconvolution of the photon flux of line-of-sight 96 ($r/a \approx 0$). The MA-LVIC is filled with argon and the sub-chambers have respective length pressure products of 5, 15, 50, 175 and $500 \text{ mm} \cdot \text{atm}$. The beryllium window is $200 \mu\text{m}$ wide.

In this section the accuracy of spectral deconvolution is investigated for different lines-of-sight. The lines-of-sight number 5 (looking at the very edge of the plasma), 45 (looking through the plasma up to $r/a \approx 0.5$) and 96 (looking at the very core of the plasma) are chosen to estimate the quality of reconstruction over different regions and therefore different incoming spectrums.

The spectral reconstruction of the photon flux of the lines-of-sight number 45 and 96 are displayed on figure 8.6. Both reconstructed spectrums look visually good, with a seemingly good reconstruction of the continuum as well as the peaks located around 8 keV. The lower energy peaks, located around 2 keV, are clearly overestimated.

The investigation of the reconstruction of the X-ray spectrum from line-of-sight 5 (see figure 8.7) shows that at the edge the continuum reconstruction is not as good as it is accurately reconstructed up to 20 keV only. The line radiation shows a pretty good agreement between the input and its reconstruction. The energy content of the spectrum after 20 keV is however very low and it can be considered that the overall shape of the spectrum is fairly well reconstructed although the slope of the continuum is not. It is worth noting that the currents measured by the detector in line-of-sight 5 is between 2 and 4 orders of magnitude lower than for lines-of-sight 45 and 96. In addition to that, it is visible that the fitting of the current is not as good for line-of-sight 5.

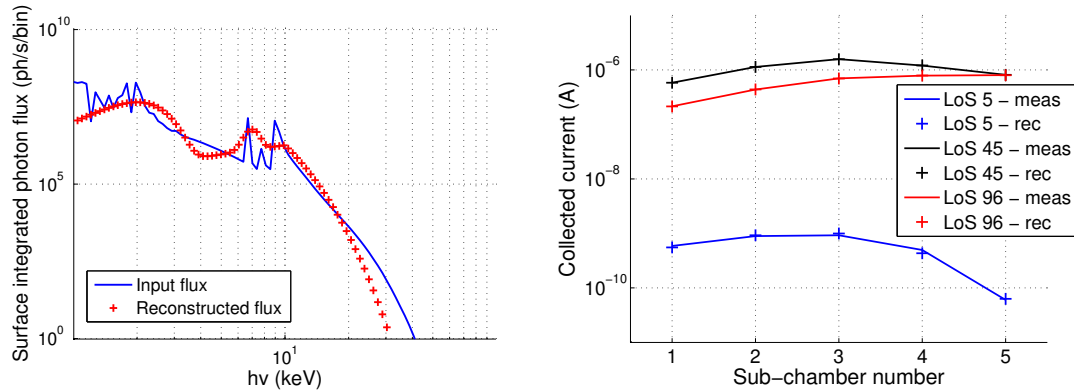


Figure 8.7 – Left: Spectral deconvolution of the photon flux of line-of-sight 5 ($r/a \approx 1$). Right: Measured and reconstructed currents for each sub-chamber for lines-of-sight 5, 45 and 96. The MA-LVIC is filled with argon and the sub-chambers have respective length pressure products of 5, 15, 50, 175 and 500 $mm \cdot atm$. The beryllium window is $200\mu m$ wide.

The study of the figures of merit shows a very good fitting of the currents is obtained for all lines-of-sight except those located at the very edge of the plasma. RMS_{dec} (see figure 8.8) exhibits a fairly flat over most of the plasma and increases by several orders of magnitude towards the edge. Line-of-sight 5 seems to be the limit between the accurate and inaccurate reconstruction regions. This is confirmed by the inspection of the reconstruction of line-of-sight 4: the shape of the incoming photon spectrum is

quite far from the mathematical function used to fit it and therefore the deconvolution is not accurate.

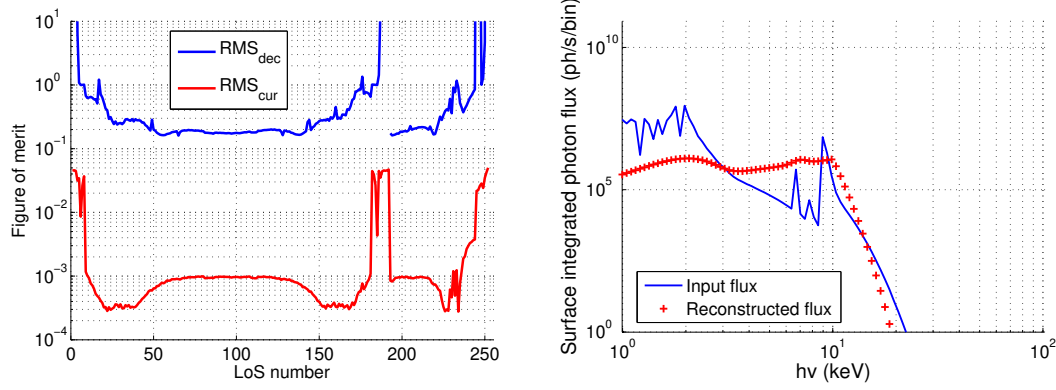


Figure 8.8 – Left: Figures of merit of spectral deconvolution. Right: Spectral deconvolution of the photon flux of line-of-sight 4 ($r/a \approx 1$). The MA-LVIC is filled with argon and the sub-chambers have respective length pressure products of 5, 15, 50, 175 and 500 $mm \cdot atm$. The beryllium window is $200\mu m$ wide.

8.2.2.3 Overall accuracy over all lines-of-sight

The observations made from figures 8.6 and 8.7 are specific to the considered lines-of-sight and do not necessarily reflect the quality of the overall deconvolution. The overall deconvolution can be visualized through the plotting of the surface integrated power as a function of both the energy and the line-of-sight, as shown on figure 8.9. The surface integrated power is given by:

$$P_{LoS}(hv) = \frac{1}{E} \int_{LoS} \varepsilon(r, hv) dr \quad (8.7)$$

where E is the geometrical etendue of the detector in m^2 and $\varepsilon(r, hv)$ is the plasma emissivity in the energy bin corresponding to the energy hv in $W \cdot m^{-3} \cdot bin^{-1}$.

The overall aspect of the surface integrated power is very close between the input and its reconstruction, especially in the continuum ($hv > 10keV$). At low energy, the reconstruction properly identifies that there is more emissivity at the plasma edge than in the core but, as seen previously, this emissivity is highly overestimated (both in width and intensity). The peak corresponding to iron line emission is less intense but wider, so it might be well reconstructed. It is however not possible to conclude on the accuracy of this peak reconstruction from this figure.

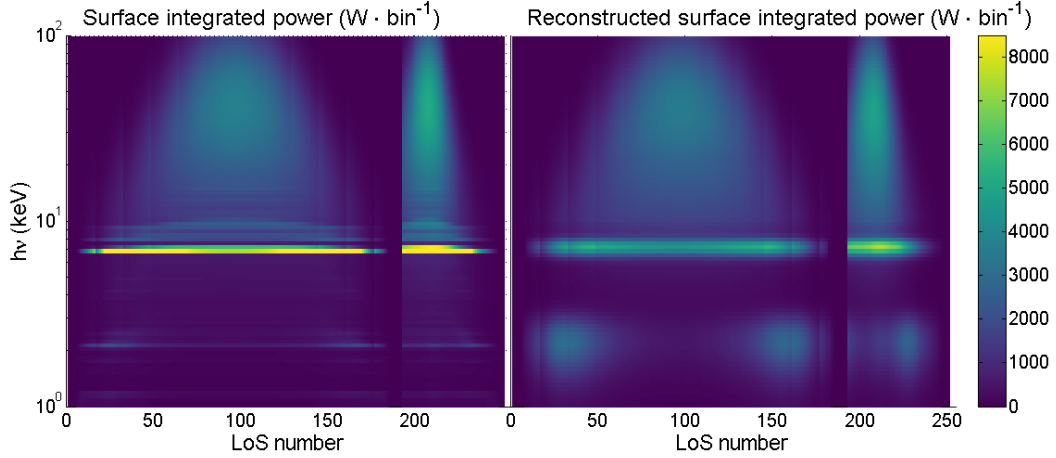


Figure 8.9 – Left: Surface integrated power as a function of the photon energy and the line-of-sight number. Right: Reconstructed surface integrated power as a function of the photon energy and the line-of-sight number. The MA-LVIC is filled with argon and the sub-chambers have respective length pressure products of 5, 15, 50, 175 and 500 $mm \cdot atm$. The beryllium window is 200 μm wide.

By integrating the X-ray power over given energy bands, it is possible to visualize the accuracy of reconstruction in these bands for all lines-of-sight at once and therefore assess whether the accuracy in specific regions of the spectrum, such as the region containing the iron line.

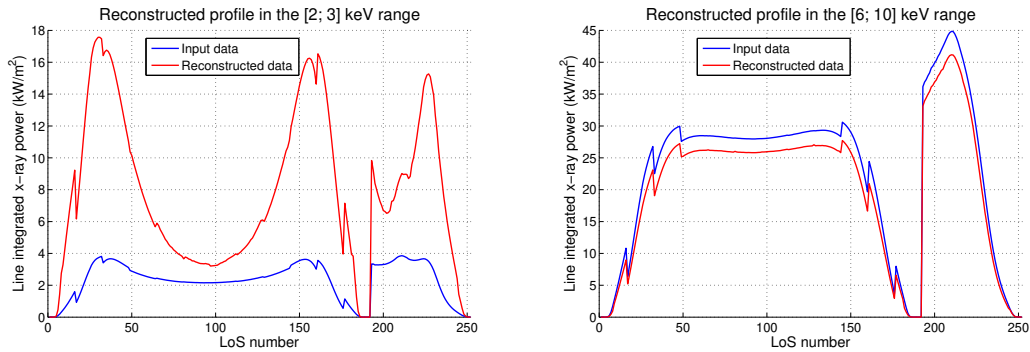


Figure 8.10 – Left: Reconstruction of the line-integrated X-ray emissivity in the [2, 3] keV range for each line-of-sight. Right: Reconstruction of the line-integrated X-ray emissivity in the [6, 10] keV range for each line-of-sight. The MA-LVIC is filled with argon and the sub-chambers have respective length pressure products of 5, 15, 50, 175 and 500 $mm \cdot atm$. The beryllium window is 200 μm wide.

Four energy bands are considered: $[2, 3] keV$, $[6, 10] keV$, $[10, 100] keV$ and $[2, 100] keV$. The first energy band allows the estimation of the accuracy of reconstruction of the

first peak, covering the tungsten lines observed at the plasma edge. The second energy band covers the second peak of the function: the iron line at 7keV and the iron/tungsten lines between 8 and 10 keV. A third energy band is chosen to cover the continuum, and finally the accuracy of reconstruction over the total energy range is estimated with the fourth energy band.

The line-integrated X-ray power in the [2, 3] keV and [6, 10] keV energy bands are displayed on figure 8.10. As suggested by the single lines-of-sight reconstruction, the X-ray power in the [2, 3] keV energy range is highly overestimated (by up to a factor 5). The accuracy of spectral deconvolution in this energy range is discussed with more details in section 8.2.5 In the [6, 10] keV energy range the result is much more accurate, but a significant underestimation of around 10% is observed. This error of reconstruction will be problematic for tomography where it is most likely that this uncertainty will be amplified.

The line-integrated X-ray power in the [10, 100] keV and [2, 100] keV energy bands are displayed on figure 8.11. The deconvolution of the continuum is much more accurate than the line radiation: there is less than 5% of underestimation of the line-integrated X-ray power in the [10, 100] keV energy range. As a result, the overall line-integrated X-ray power is well reconstructed. For the lines-of-sight looking at the plasma core the continuum is dominant and a slight underestimation is observed while for the lines-of-sight directed towards the edge the line radiation is more important and an overestimation of the X-ray power can be observed.

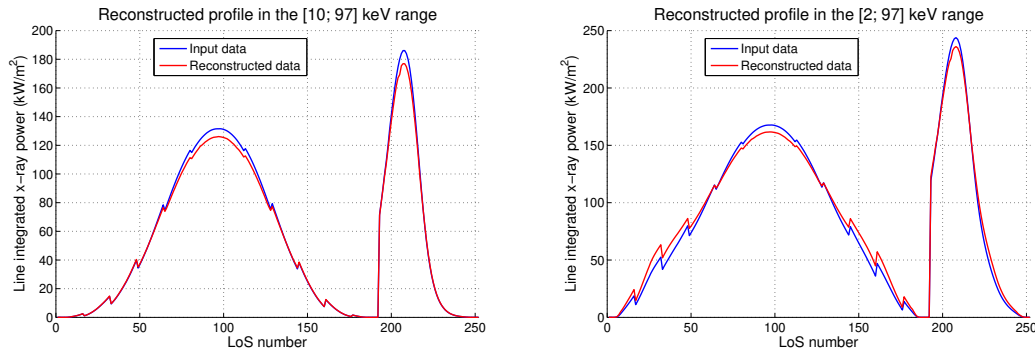


Figure 8.11 – Left: Reconstruction of the line-integrated X-ray emissivity in the [10, 100] keV range for each line-of-sight. Right: Reconstruction of the line-integrated X-ray emissivity in the [2, 100] keV range for each line-of-sight. The MA-LVIC is filled with argon and the sub-chambers have respective length pressure products of 5, 15, 50, 175 and 500 $mm \cdot atm$. The beryllium window is $200\mu m$ wide.

8.2.3 Spectral deconvolution using xenon-filled MA-LVIC

8.2.3.1 Detector setup

Spectral deconvolution has been performed using a MA-LVIC with 5 anodes filled with xenon. The pressure length product used for each sub-chamber is 5, 30, 60, 100 and 150 $\text{mm} \cdot \text{atm}$. A MA-LVIC with anodes of 2.5, 15, 30, 50 and 75 mm under 2 bars of pressure would achieve such pressure length products. A beryllium window of $200\mu\text{m}$ is considered as a filter. The spectral responses of each sub-chamber are displayed on figure 8.12. It can be noticed that the total spectral response of the MA-LVIC is significantly higher than for argon, especially at high energies. The lines-of-sight geometry used in this study is the *60 vertical lines-of-sight configuration* presented in section 5.4.1.

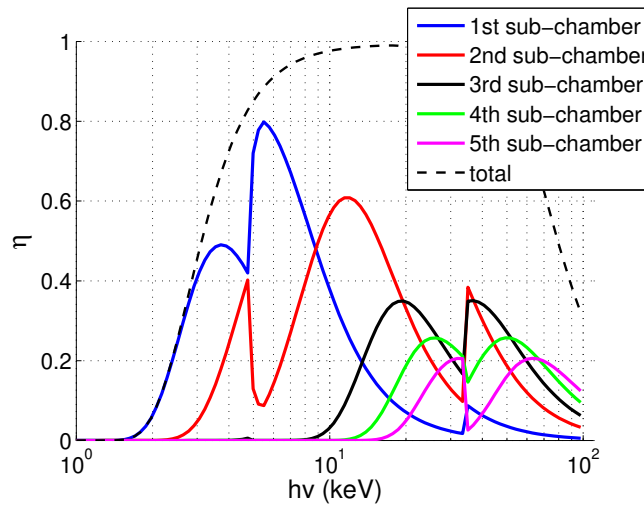


Figure 8.12 – Spectral response of each sub-chamber in a 5 anodes xenon-filled MA-LVIC. The length pressure products of the sub-chamber are respectively 5, 30, 60, 100 and 150 $\text{mm} \cdot \text{atm}$, and the filter consists of $200\mu\text{m}$ of beryllium.

8.2.3.2 Single lines-of-sight results

The results of energy deconvolution using a xenon-filled MA-LVIC are shown on the figures 8.13, 8.14, and 8.15. It can be noticed that for the lines-of-sight 45 and 96 the continuum-dominated region of the spectrum is very well reconstructed: differences between the input and reconstructed fluxes are quite hard to spot. The iron line emission at 7 keV seems also accurately reconstructed: similarly as for argon, the amplitude is slightly lower in the reconstruction but the increased width seems to offset it. The low energy part of the spectrum is not properly reconstructed here as well: no peak is present at 2 keV for line-of-sight 96 while the peak is significantly overestimated for line-of-sight 45.

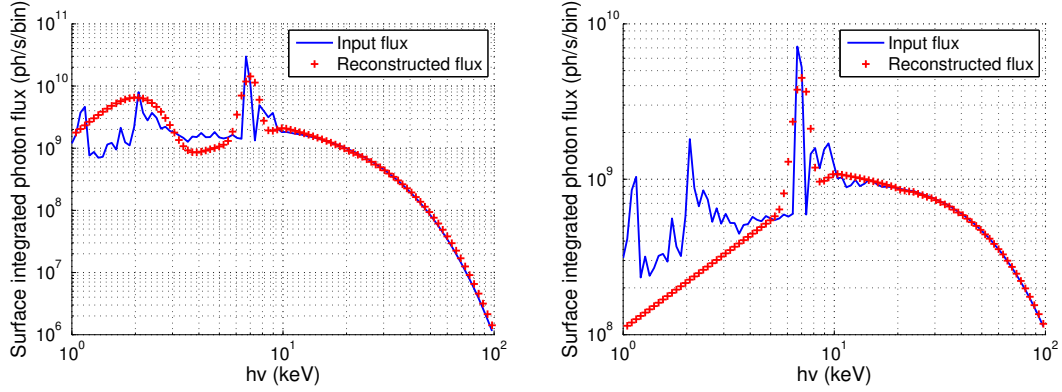


Figure 8.13 – Left: Spectral deconvolution of the photon flux of line-of-sight 45 ($r/a \approx 0.5$). Right: Spectral deconvolution of the photon flux of line-of-sight 96 ($r/a \approx 0$). The MA-LVIC is filled with xenon and the sub-chambers have respective length pressure products of 5, 30, 60, 100 and 150 $mm \cdot atm$. The beryllium window is $200\mu m$ wide.

The study of line-of-sight number 5 shows that the reconstruction of the continuum is inaccurate overall (the slope is not reconstructed) but most of the continuum energy is located in the region which is accurate. However, the line radiation is overestimated at 7 keV and highly underestimated at 2 keV. This might be explained by the fact that the currents collected at line-of-sight number 5 are between 3 and 6 orders of magnitude lower than those collected at lines-of-sight 45 and 96.

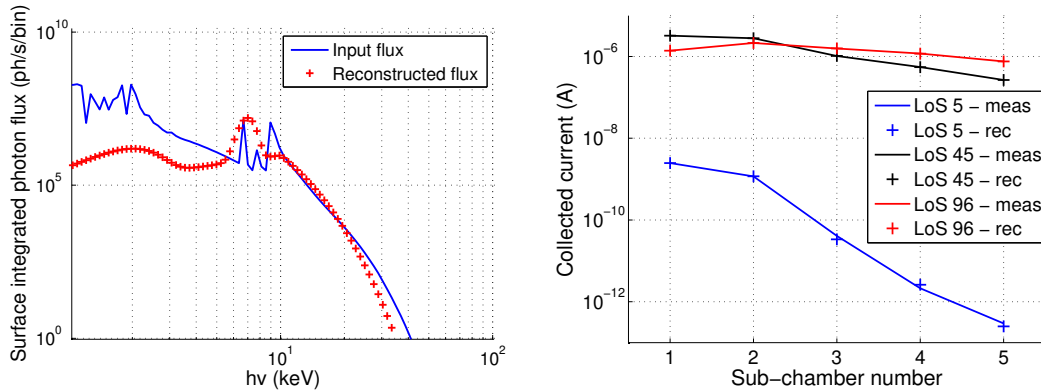


Figure 8.14 – Left: Spectral deconvolution of the photon flux of line-of-sight 5 ($r/a \approx 1$). Right: Measured and reconstructed currents for each sub-chamber for lines-of-sight 5, 45 and 96. The MA-LVIC is filled with xenon and the sub-chambers have respective length pressure products of 5, 30, 60, 100 and 150 $mm \cdot atm$. The beryllium window is $200\mu m$ wide.

The inspection of the figures of merit gives a similar diagnostic than for argon: RMS_{dec} and RMS_{cur} fairly flat over most of the plasma and increases in a very steep

way towards the edges. Line-of-sight 5 also seems to be at the limit between low and high figures of merit. As seen with argon, the shape of the spectrum for line-of-sight number 4 cannot be properly fitted by the mathematical function described in equation 8.2.

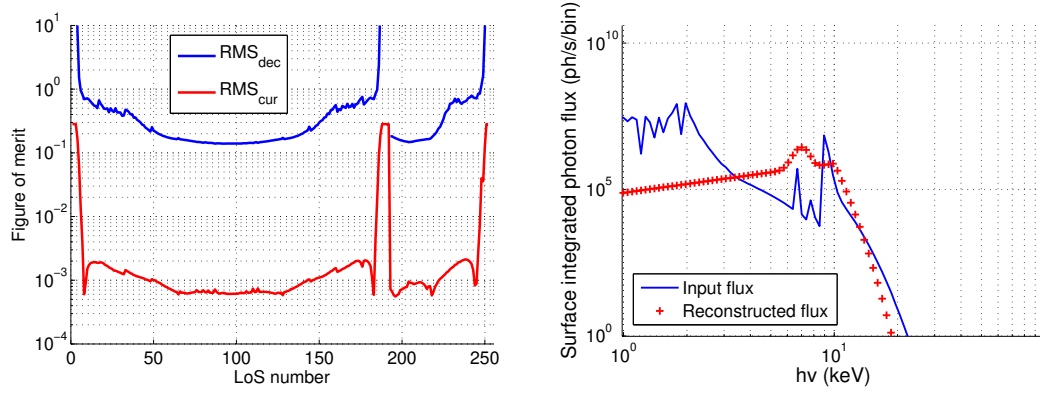


Figure 8.15 – Left: Figures of merit of spectral deconvolution. Right: Spectral deconvolution of the photon flux of line-of-sight 4 ($r/a \approx 1$). The MA-LVIC is filled with xenon and the sub-chambers have respective length pressure products of 5, 30, 60, 100 and 150 $mm \cdot atm$. The beryllium window is $200\mu m$ wide.

8.2.3.3 Overall accuracy over all lines-of-sight

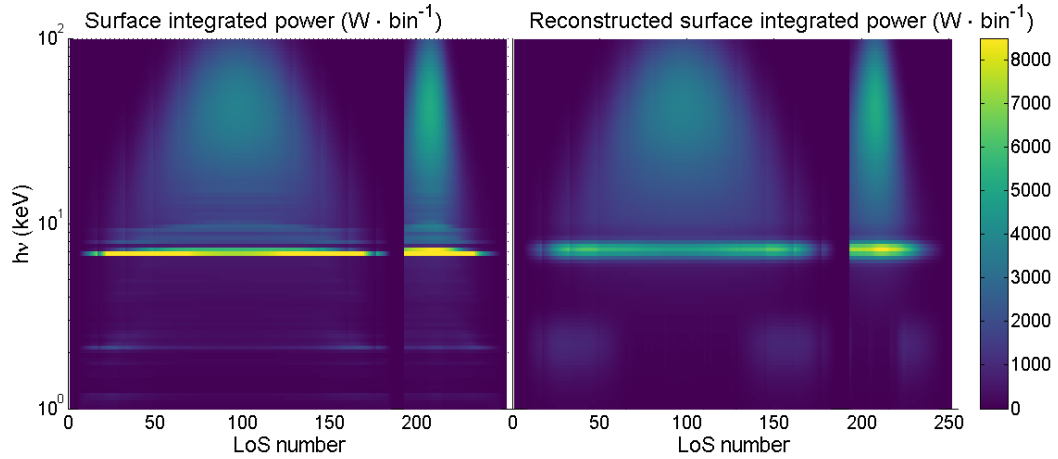


Figure 8.16 – Left: Surface integrated power as a function of the photon energy and the line-of-sight number. Right: Reconstructed surface integrated power as a function of the photon energy and the line-of-sight number. The MA-LVIC is filled with xenon and the sub-chambers have respective length pressure products of 5, 30, 60, 100 and 150 $mm \cdot atm$. The beryllium window is $200\mu m$ wide.

The surface integrated power of each line-of-sight is displayed as a function of energy on figure 8.16. An accurate reconstruction of the overall shape is exhibited, especially in the continuum ($h\nu > 10\text{keV}$). The tungsten line emission around 2 keV in the plasma edge is reconstructed, although the amplitude and width seem overestimated. The iron line emission around 7 keV seems to be more accurate as it is less intense but spread over a wider energy range. In order to verify these observations, the integration over the energy bands defined for the argon analysis (see section 8.2.2.3) is performed as well.

The line-integrated X-ray power in the [2, 3] and [6, 10] keV energy ranges is displayed in figure 8.17. The first energy band exhibits a very inaccurate reconstruction: the power is overestimated by a factor ≈ 1.5 at the edge and underestimated by a factor ≈ 2 in the plasma core. In the region dominated by the iron line emission, the deconvolution yields satisfying results: in the edge the reconstruction is visually equal to the input and in the core there is less than 5% of difference between them.

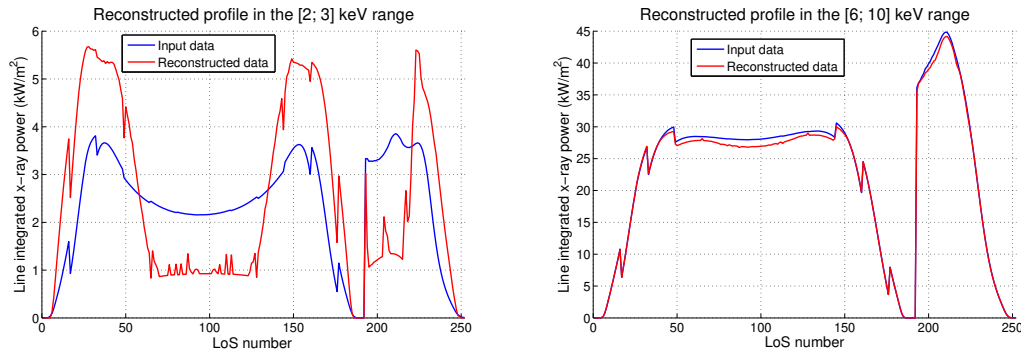


Figure 8.17 – Left: Reconstruction of the line-integrated X-ray emissivity in the [2, 3] keV range for each line-of-sight. Right: Reconstruction of the line-integrated X-ray emissivity in the [6, 10] keV range for each line-of-sight. The MA-LVIC is filled with xenon and the sub-chambers have respective length pressure products of 5, 30, 60, 100 and 150 $\text{mm} \cdot \text{atm}$. The beryllium window is $200\mu\text{m}$ wide.

The line-integrated X-ray power in the [10, 100] and [2, 100] keV energy ranges is displayed in figure 8.18. The energy range dominated by the continuum ([10, 100] keV) is very well reconstructed, the input and its reconstruction are overlapping almost perfectly (with a slight overestimation in the plasma core). Over the whole energy range of the spectrum, the accuracy of reconstruction is also excellent with a slight underestimation in the plasma core which comes from the fact that the [2, 3] energy range is not reconstructed in the core.

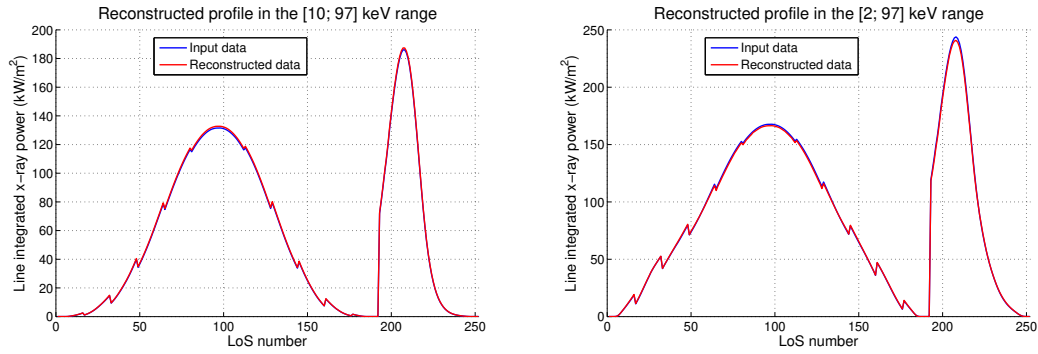


Figure 8.18 – Left: Reconstruction of the line-integrated X-ray emissivity in the [10, 100] keV range for each line-of-sight. Right: Reconstruction of the line-integrated X-ray emissivity in the [2, 100] keV range for each line-of-sight. The MA-LVIC is filled with xenon and the sub-chambers have respective length pressure products of 5, 30, 60, 100 and 150 $mm \cdot atm$. The beryllium window is $200\mu m$ wide.

8.2.4 Comparison between argon and xenon

In the scope of X-ray spectral deconvolution on ITER, both argon and xenon have demonstrated their capabilities as filling gas for a MA-LVIC. The first difference which is observed between them comes from their sensitivity. Indeed, as xenon is much more sensitive to X-ray radiation than argon, it requires a lower length pressure product for a similar spectral response. This is confirmed by the total length pressure product of the MA-LVIC used in sections 8.2.2 and 8.2.3: $745mm \cdot atm$ for argon and $345mm \cdot atm$ for xenon. This means that in terms of integration, for a MA-LVIC filled with argon to fit in a box with a depth of $100mm$ it will need around 7.5 bars of pressure for argon against around 3.5 bars for xenon. In this regard, xenon is a much better candidate than argon. When it comes to the accuracy of reconstruction, xenon exhibits a higher quality of the deconvoluted spectrum in all the different energy bands. As a result, xenon is foreseen as the main candidate for X-ray energy deconvolution on ITER and is used (in the setup presented in section 8.2.3.1) for the rest of the energy deconvolution simulations presented in this thesis.

8.2.5 Improving the reconstruction in the [2, 3] keV energy band

In the energy deconvolution presented in sections 8.2.2 and 8.2.3, significant reconstruction error is observed in the [2, 3] keV energy band. As seen on figure 8.12, the spectral response of the detector is very low at these energy ($< 10\%$ at $h\nu = 2keV$ and 40% at $h\nu = 3keV$). This is explained by the fact that the beryllium window absorbs most of the photon flux at these energies. In this section, several spectral deconvolution simulations are performed in order to assess the influence of the width

of the beryllium window on the reconstruction of the [2, 3] keV range. This range is of specific interest in the scope of impurity transport studies as it is dominated by tungsten line radiation.

The detector setup is the one described in section 8.2.3.1 and the corresponding spectral response for each sub-chamber is displayed on figure 8.12. As the beryllium window mainly absorbs photons of $h\nu < 5\text{keV}$, the spectrum reconstruction in the [5, 100] keV range is not affected by its width. As a result this study will focus solely on the [2, 3] keV energy range.

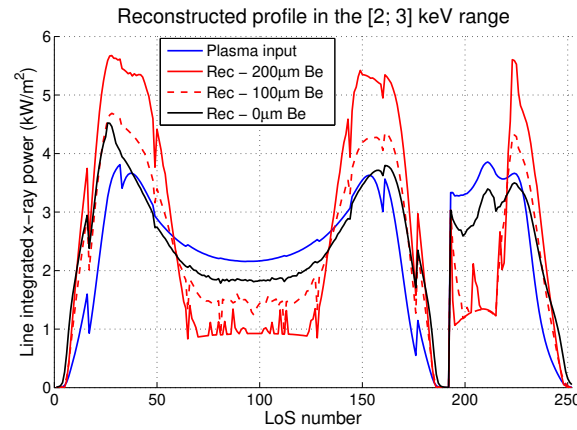


Figure 8.19 – Reconstruction of the line-integrated X-ray emissivity in the [2, 3] keV range as a function of the line-of-sight number for different widths of the beryllium window. The MA-LVIC is filled with xenon and the sub-chambers have respective length pressure products of 5, 30, 60, 100 and 150 $\text{mm} \cdot \text{atm}$.

The reconstruction of the X-ray power impacting the detector in the [2, 3] keV range for three beryllium window depths ($200\mu\text{m}$, $100\mu\text{m}$ and no beryllium window) is displayed on figure 8.19. With a $200\mu\text{m}$ beryllium window, there is a clear overestimation of the power at the plasma edge and an underestimation in the core. Oscillations can be noticed in the core, denoting the lack of stability of the reconstruction in this energy band. When the beryllium window gets thinner, a clear improvement can be noticed: the difference between input and reconstruction is divided by ≈ 2 and the core oscillations have significantly decreased. Without beryllium window, the reconstruction of the shape of the line-integrated power is much better. The overestimation at the edge and underestimation in the core are reduced to $\approx 20\%$ and the oscillations have almost disappeared.

The conclusion of this study is that in order to observe the transport of tungsten at the plasma edge, where the X-ray emission is around 2 keV, it is necessary to have a beryllium as thin as possible.

8.2.6 Sensitivity analysis

During operation on ITER the MA-LVIC measurement will be subject to experimental noise, which is expected to be of the order of magnitude of 1%. In order to estimate the influence of such perturbation, a sensitivity analysis, which consists of 100 reconstructions with a gaussian noise of 1%, is performed. The perturbative noise is added to the measured currents before spectral deconvolution. The detector setup is the one described in section 8.2.3.1. The interest of repeating the process 100 times is to gather enough statistics to estimate the stability of the method with regards to gaussian perturbation. The highest and lowest reconstructions are used to create a so-called envelope inside which a 1% noise reconstruction is most likely to be located.

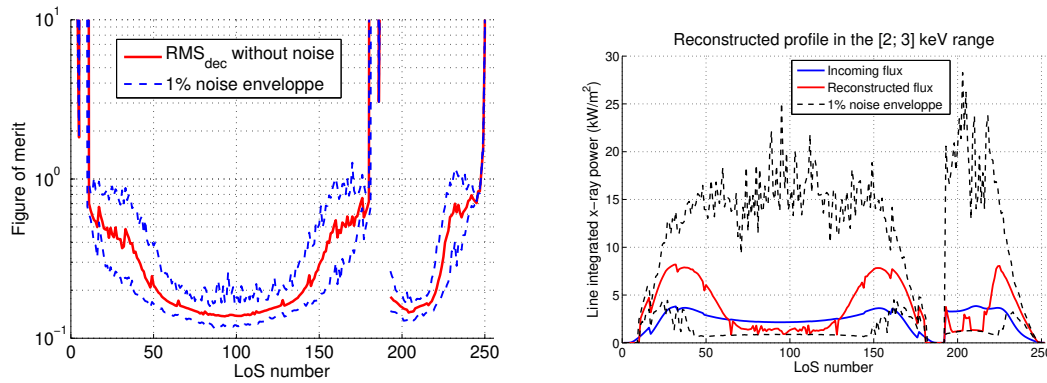


Figure 8.20 – Left: RMS_{dec} and its 1% noise envelope. Right: Reconstruction of the line-integrated X-ray emissivity in the [2, 3] keV energy range and its 1% envelope. The MA-LVIC is filled with xenon and the sub-chambers have respective length pressure products of 5, 30, 60, 100 and 150 $mm \cdot atm$. The beryllium window is $200\mu m$ wide.

RMS_{dec} and its envelope are displayed on the left part of figure 8.20. It can be observed that the noise does not necessarily have a great impact on the figure of merit, and in some cases the noise can prove to be improving it. However, the reconstruction of the line-integrated X-ray emissivity in the [2, 3] keV range (right part of figure 8.20) exhibits a high instability of the reconstruction with up to ten times overestimation of the emissivity. This energy range already displayed instabilities without noise, it is therefore not surprising to observe a very high increase in these instabilities.

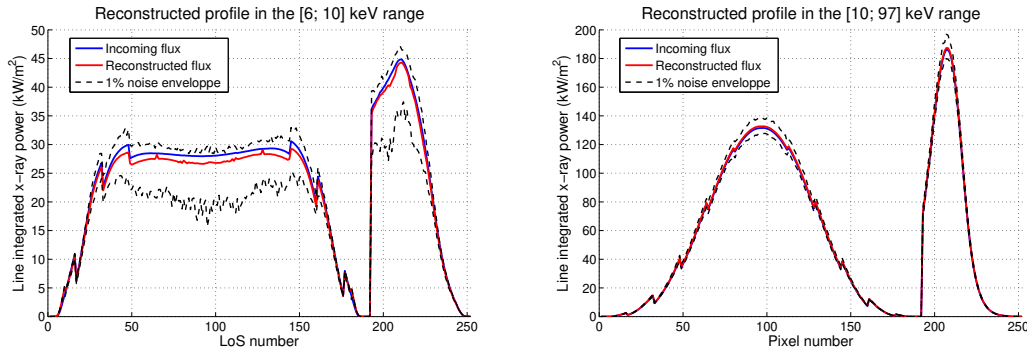


Figure 8.21 – Left: Reconstruction of the line-integrated X-ray emissivity in the [6, 10] keV energy range and its 1% envelope. Right: Reconstruction of the line-integrated X-ray emissivity in the [10, 100] keV energy range and its 1% envelope. The MA-LVIC is filled with xenon and the sub-chambers have respective length pressure products of 5, 30, 60, 100 and 150 $mm \cdot atm$. The beryllium window is $200\mu m$ wide.

The reconstructions of the line-integrated X-ray emissivity in the [6, 10] keV and [10, 100] keV ranges are displayed on figure 8.21. In the range containing the iron line radiation, the system is more stable (in comparison with the [2, 3] keV energy range) but an underestimation of up to 30% can be obtained. The continuum exhibits the highest resilience to perturbation with a maximal error of around 10%. It is the resilience of energy band which explains the low effect of noise on RMS_{dec} : as $d h \nu$ increases exponentially with energy the high energy part of the spectrum has a higher impact on the figure of merit (see equation 8.5).

The impact of noise on spectral deconvolution is therefore quite high in the line emission-dominated part of the spectrum. However, at high energy the reconstruction is much more stable to such perturbations.

8.3 Energy-resolved X-ray tomography

In section 8.2, the X-ray spectrum of individual lines-of-sight generated by the ITER high power D-T scenario is reconstructed. This reconstructed spectrum is applied to tomography in this section in order to compute the local X-ray spectrum over the whole plasma.

As seen in section 2.4.1, the photon flux is divided into a total of 236 energy bins of increasing width. The spectral reconstruction method is only applied to the [2, 100] keV part of the energy range, as no information is collected for lower energies due to absorption in the beryllium window. In this section, energy-resolved tomography is performed through the independent application of tomography to the reconstructed spectrum at each energy bin. Therefore a 2D mapping of the local X-ray emissivity is obtained for each energy bins. The concatenation of these local emissivities gives the local X-ray spectrum emitted at each location of the plasma.

The line-integral of the emissivity at energy $h\nu$, used as input for tomography, is given by:

$$f^{meas}(h\nu) = \frac{\phi(h\nu) \cdot h\nu}{E} \quad (8.8)$$

where E is the geometrical etendue of the aperture-detector system.

The Minimum Fisher Information method, presented in section 3.3.2, is used for the tomographic inversion.

8.3.1 Figures of merit

In order to quantify the accuracy of the energy-resolved tomographic reconstruction, an additional figure of merit is defined.

The RMS_{tomo}^{core} and RMS_{tomo}^{lcms} root mean squares estimates, defined in equation 5.1, are applicable to this process and are estimated for each energy band to assess the accuracy of tomographic reconstruction.

The RMS_{line} parameter (from equation 5.1) is also computed in order to quantify how well the input profile of tomography is fitted by the algorithm. RMS_{line} is also estimated for each energy band.

The accuracy of reconstruction of the local emissivity spectrum is quantified by the RMS_{pix} figure of merit which is estimated for each geometrical pixel of the tokamak. It is defined as:

$$RMS_{pix}(R, Z) = \sqrt{\frac{\sum_{i=1}^{N_{bins}} dh\nu(i)^2 \left(\frac{\varepsilon(R, Z, h\nu(i)) - \varepsilon^{rec}(R, Z, h\nu(i))}{\varepsilon(R, Z, h\nu(i))} \right)^2}{\sum_{i=1}^{N_{bins}} dh\nu(i)^2}} \quad (8.9)$$

8.3.2 Results

Energy-resolved X-ray tomography has been performed using the photon spectrums obtained with xenon-filled MA-LVIC in section 8.2.3. The tomographic reconstructions have been performed independently for each energy bin from $h\nu = 2keV$ to $h\nu = 100keV$. The obtained radial profile of the emissivity spectrum is compared to the input radial profile of the emissivity spectrum on figure 8.22. Visual differences can be observed between the two profiles. However, the overall shape and value are similar for both profiles. The tungsten lines around 2 keV at the plasma edge and the iron line around 7 keV seem qualitatively well reconstructed.

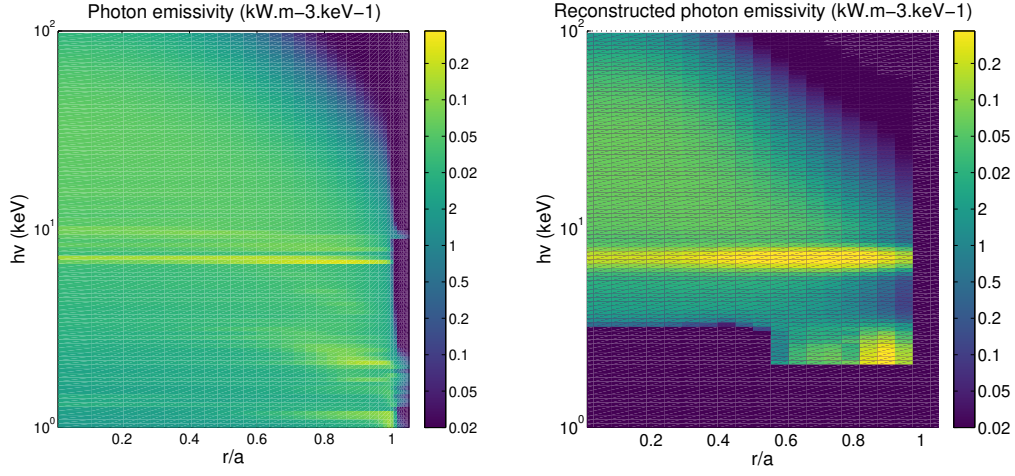


Figure 8.22 – Left: Radiated power profile on ITER as a function of photon energy and normalized radius. Right: Reconstructed radiated power profile as a function of photon energy and normalized radius. The MA-LVIC is filled with xenon and the sub-chambers have respective length pressure products of 5, 30, 60, 100 and 150 $mm \cdot atm$. The beryllium window is 200 μm wide.

A more quantitative estimation of the accuracy of reconstruction is provided by an analysis of the figures of merit, displayed on the figures 8.23 and 8.24. The backfitting of the line-integrated emissivity is fairly stable with energy, with an increase around 7 keV. This means that the tomographic algorithm has not managed to reconstruct this region as well as the rest of the energy spectrum.

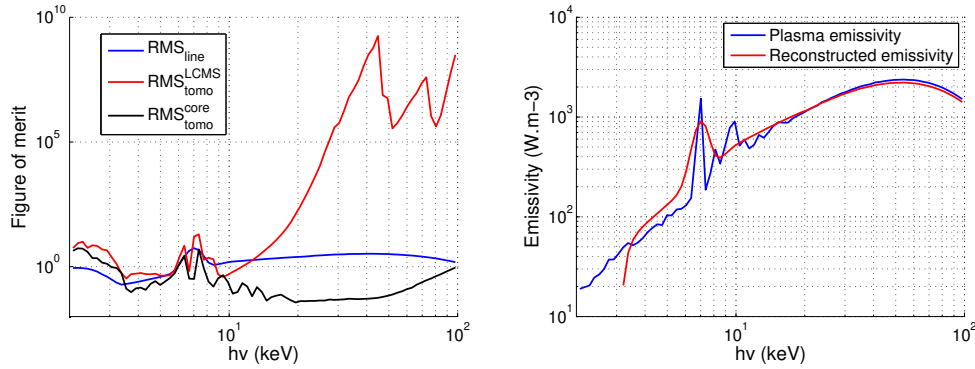


Figure 8.23 – Left: Figures of merit of energy resolved tomography: RMS_{line} , RMS_{LCMS}^{tomo} , and RMS_{core}^{tomo} . Right: Reconstruction of the local plasma emissivity in the plasma core (at $R = 6.27m$ and $Z = 0.57m$). For this pixel, $RMS_{pix} = 3.7 \cdot 10^{-3}$. The MA-LVIC is filled with xenon and the sub-chambers have respective length pressure products of 5, 30, 60, 100 and 150 $mm \cdot atm$. The beryllium window is 200 μm wide.

Overall the discrepancy in the input data has been well spread over the different energy bins. The RMS_{tomo} figures of merit quantify the accuracy of reconstruction of the X-ray emissivity in the core and the LCMS-enclosed region. It can be observed that for the line emission part of the spectrum, the emissivity is fairly well reconstructed in the whole plasma. For $h\nu > 10\text{keV}$, the plasma core exhibits a good reconstruction with RMS_{tomo}^{core} between 10^{-2} and 10^{-1} . However, when considering the LCMS-enclosed region we can observe a very high loss of accuracy with energy: RMS_{tomo}^{LCMS} goes up to almost 10^8 . This is explained by the facts that the plasma edge does not emit high energy photons, due to its low electron temperature, and that the tomographic algorithm tends to be less accurate in the edges.

The reconstruction of the local emissivity for a pixel located at the very core of the plasma ($(R, Z) = (6.27\text{m}, 0.57\text{m})$) is displayed in the right part of figure 8.23. We can observe that the agreement between the shape of the local emissivity and its reconstruction is quite good. This is confirmed by the low RMS_{pix} obtained for this pixel. RMS_{pix} , displayed on figure 8.24, quantifies the difference between the local emissivity spectrum and its reconstruction. Similarly as for the RMS_{tomo} figures of merit, RMS_{pix} is much lower in the core with $RMS_{pix} < 10^{-2}$. This denotes the fact that the reconstruction accuracy is lower at the edge than in the plasma core.

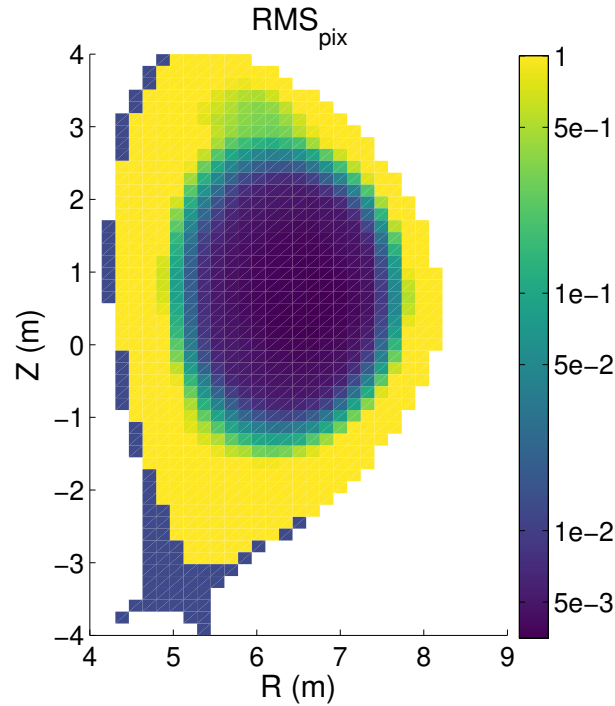


Figure 8.24 – Figure of merit RMS_{pix} of energy resolved tomography. The MA-LVIC is filled with xenon and the sub-chambers have respective length pressure products of 5, 30, 60, 100 and 150 $\text{mm} \cdot \text{atm}$. The beryllium window is $200\mu\text{m}$ wide.

8.3.3 Sensitivity analysis

Energy resolved X-ray tomography has been performed with the outputs of spectral deconvolution in a case where 1% of gaussian perturbative noise was added to the measured currents.

The reconstruction of the local emissivity in the plasma core is displayed on the left part of figure 8.25. The high energy end of the spectrum is quite accurate. However the [2, 10] keV energy range exhibits high inaccuracy, especially below 4 keV. The peak at $h\nu \approx 2\text{keV}$ is highly overestimated and, although the peak at $h\nu \approx 7\text{keV}$ is better, it is overestimated as well. In this range the sensitivity to perturbation is quite high, which corroborates the envelopes obtained in figures 8.20 and 8.21. The use of a different method or the addition of smoothing over the lines-of-sight (using the space continuity of the emissivity) on the inputs for tomography might improve the reconstruction at low energy.

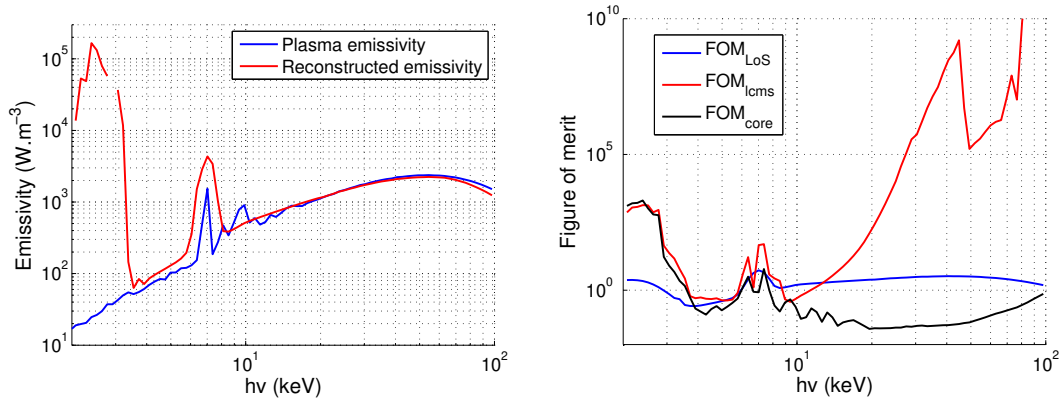


Figure 8.25 – Left: Reconstruction of the local emissivity spectrum in the plasma core (at $R = 6.27\text{m}$ and $Z = 0.57\text{m}$) with 1% of perturbative noise added to the measurement. Right: Figures of merit of energy resolved tomography: RMS_{line} , RMS_{tomo}^{LCMS} and RMS_{tomo}^{core} (respectively labelled as FOM_{LoS} , FOM_{lcms} , and FOM_{core}), with 1% of gaussian perturbative noise on the LVIC measurement. The MA-LVIC is filled with xenon and the sub-chambers have respective length pressure products of 5, 30, 60, 100 and 150 $\text{mm} \cdot \text{atm}$. The beryllium window is $200\mu\text{m}$ wide.

Due to the error levels obtained in the low energy part of figure 8.25 (there is up to a factor 10^4 between the emissivity and its reconstruction), the spectrum has been divided into two energy bands for the calculation of RMS_{pix} : [4, 10] keV and [10, 100] keV. The RMS_{pix} figure of merit is displayed for both of these energy bands in figure 8.26. RMS_{pix} exhibits a high value in the [4, 10] keV range over the whole plasma, but a higher accuracy is observed in the plasma core. This show that, even though the iron line radiation peak is not very well reconstructed by energy resolved tomography, its accuracy is still higher in the plasma core.

In the second energy range, corresponding to the continuum region of the spectrum, RMS_{pix} is low and constant over the whole plasma core. This indicates a satisfactory spectral deconvolution in this region and energy range.

The other figures of merit used to assess the quality of tomography are shown in the right part of figure 8.25. Overall it can be noticed that the figures of merit are of the order of magnitude of those obtained without perturbative noise, shown on figure 8.23. For $2keV < h\nu < 4keV$ the RMS_{tomo} figures of merit have increased by several orders of magnitude with the addition of perturbative noise. However outside of this energy range their shape is not affected much by the perturbation. RMS_{tomo}^{core} exhibits no significant different due to the addition of noise, which means that the reconstruction of the plasma core is very resilient to such perturbation. The value of RMS_{tomo}^{LCMS} is much higher at high energies where it can reach up to 10^{15} compared to 10^{10} without noise. This is explained by the fact that the plasma edge does not emit much high energy photons and therefore a small perturbation can lead to a big relative overestimation of the emissivity.

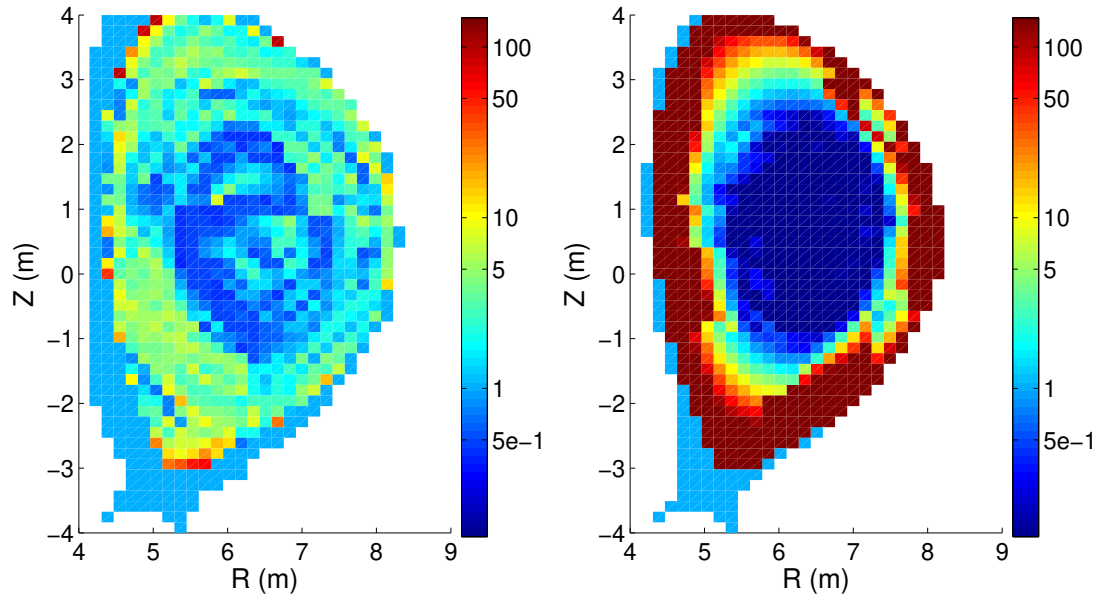


Figure 8.26 – Left: Figure of merit RMS_{pix} of energy resolved tomography with 1% of gaussian perturbative noise on the LVIC measurement computed in the [4, 10] keV range. Right: Figure of merit RMS_{pix} of energy resolved tomography with 1% of gaussian perturbative noise on the LVIC measurement computed in the [10, 100] keV range. The MA-LVIC is filled with xenon and the sub-chambers have respective length pressure products of 5, 30, 60, 100 and 150 $mm \cdot atm$. The beryllium window is $200\mu m$ wide.

The study of RMS_{line} shows that the addition of noise does not affect much the

ability of the tomographic algorithm to fit the input data. It can be concluded that the addition of noise for energy resolved tomography leads to high relative error at high energy on the plasma edge. However, the plasma core exhibits a very good reconstruction in this energy range.

8.4 Reconstruction of the electron temperature

In section 8.3 the local emissivity spectrum has been computed over the whole plasma. The continuous part of the spectrum depends on the electron temperature as shown in section 2.5.3. The knowledge of the local emissivity spectrum therefore allows the computation of the local electron temperature profile.

At high energy, the plasma emissivity is proportional to $\exp(-\frac{\hbar \cdot \nu}{k \cdot T_e}) = \exp(-\frac{h\nu}{2\pi \cdot k \cdot T_e})$. An exponential fitting of the local reconstructed emissivity is performed in order to extract the electron temperature which is inversely proportional to the slope of the exponential curve.

8.4.1 Figures of merit

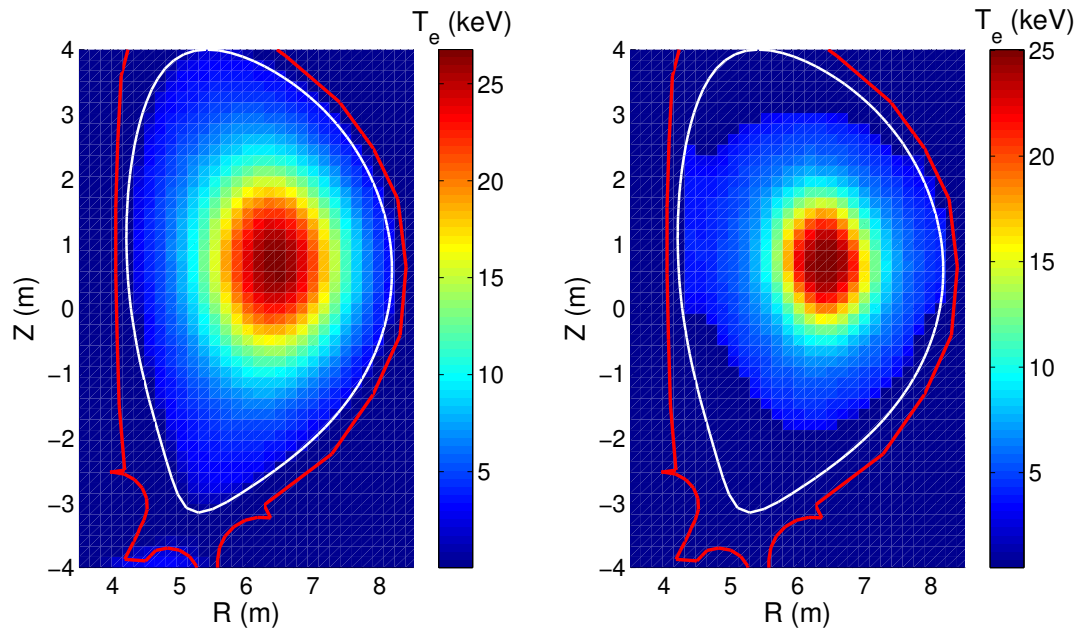


Figure 8.27 – Left: 2D profile of the electron temperature in the ITER high power D-T scenario. Right: Reconstructed 2D profile of the electron temperature. The MA-LVIC is filled with xenon and the sub-chambers have respective length pressure products of 5, 30, 60, 100 and 150 $mm \cdot atm$. The beryllium window is $200\mu m$ wide.

In order to quantify the accuracy of reconstruction of the electron temperature a root mean square estimate of the relative reconstruction error of T_e is defined:

$$RMS_{T_e} = \frac{1}{N_{pixels}} \sqrt{\sum \frac{(T_e^{input} - T_e^{rec})^2}{(T_e^{input})^2}} \quad (8.10)$$

This figure of merit can, similarly as RMS_{tomog} , be estimated over the plasma core or the LCMS-enclosed region.

8.4.2 Results

The initial T_e profile and its reconstruction are displayed on figure 8.27. The corresponding figures of merit are $RMS_{T_e}^{core} = 0.35$ and $RMS_{T_e}^{LCMS} = 0.55$. These values are quite high compared to the RMS_{tomog} obtained in the previous reconstructions but it can be observed that the visual aspect of the electron temperature (shape and amplitude) is well reproduced.

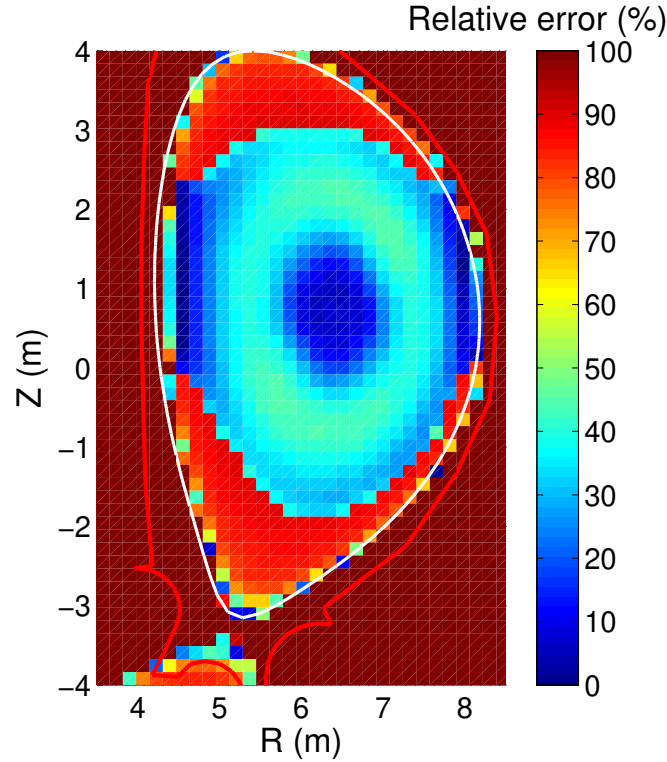


Figure 8.28 – Relative error of the electron temperature reconstruction. The MA-LVIC is filled with xenon and the sub-chambers have respective length pressure products of 5, 30, 60, 100 and 150 $mm \cdot atm$. The beryllium window is $200\mu m$ wide.

The analysis of the relative error, displayed in figure 8.28, confirms the good accuracy of the reconstruction at the very core of the plasma. A ring with an error $\approx 40\%$ surrounds that region, making this result valid only where the temperature is the highest ($T_e \geq 10 \text{ keV}$). In a plasma with a higher temperature, this method should be valid in a wider region.

8.4.3 Sensitivity analysis

The electron temperature has been computed from the local emissivity spectra obtained in section 8.3.3 from MA-LVIC currents with 1% of gaussian noise. The results are shown in figure 8.29. The overall shape and intensity of the profile is satisfactory, although it seems more blurry than in figure 8.27. The relative error, displayed on the right part of figure 8.29, shows that the electron temperature in the core is quite accurate by this accuracy has suffered from the addition noise. There has been an increase in the reconstruction error in the blue ring, which is now 50% instead of 40%. Overall, it can be concluded that the electron temperature reconstruction seems to be quite resilient to this perturbation.

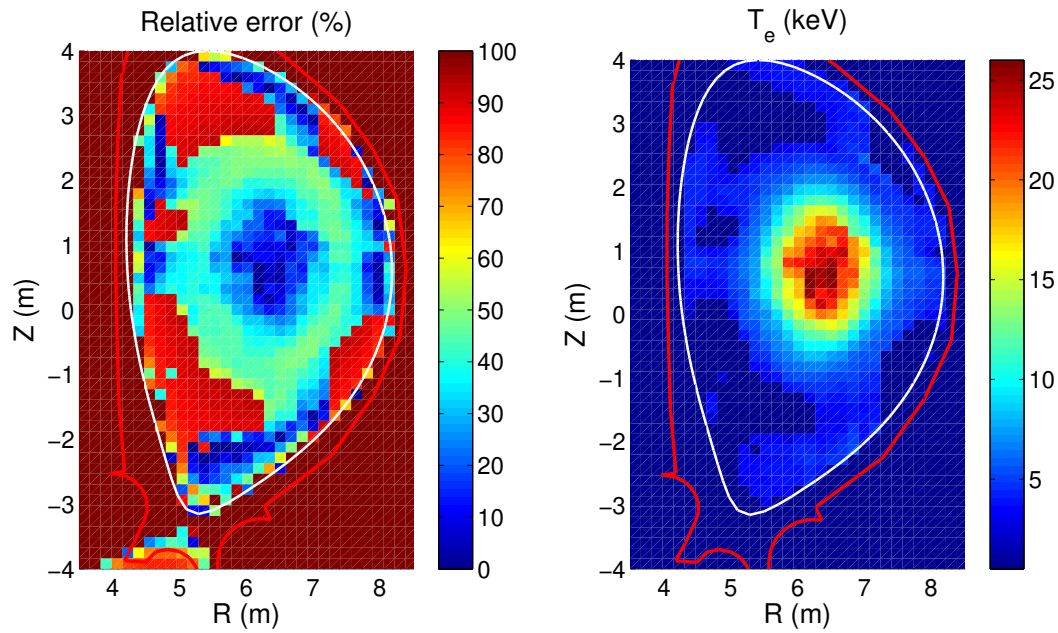


Figure 8.29 – Left: Reconstructed electron temperature profile obtained after energy resolved tomography with 1% of gaussian perturbative noise on the LVIC measurement. Right: Relative error of the electron temperature reconstruction with 1% of gaussian perturbative noise on the LVIC measurement. The MA-LVIC is filled with xenon and the sub-chambers have respective length pressure products of 5, 30, 60, 100 and 150 $\text{mm} \cdot \text{atm}$. The beryllium window is $200 \mu\text{m}$ wide.

9 Conclusion and perspectives

The aim of this thesis was to study the possibility of advanced gas detectors for X-ray measurement on ITER during its nuclear phase. The work presented in this manuscript mainly focuses on the Low Voltage Ionization Chamber. In this framework a synthetic diagnostic tool allowing the modelling of LVIC measurement has been developed and applied to the high power D-T ITER scenario. It demonstrated that argon and xenon-filled LVIC of reasonable size (a couple tens of mm at atmospheric pressure) would collect enough charge for X-ray detection on ITER. Further studies could be performed in this area by investigating the influence of space-charge effects as well as magnetic fields on the measurement.

A geometry study of the ITER X-ray lines-of-sight has been performed in order to estimate the capabilities of the proposed radial X-ray lines-of-sight for tomography. Several phantom emissivity profiles were used and the quality of reconstruction has been assessed. The conclusion of this work is that due to a lack of lines-of-sight overlapping, radially asymmetric profiles cannot be reconstructed accurately. Additional lines-of-sight located in an upper port plug can be used to solve this problem and a geometry taking the ITER integration constraints is proposed in the scope of this thesis.

A complete X-ray tomography (synthetic diagnostic and tomography) has been simulated in order to reconstruct the X-ray emissivity in the case of the high power D-T ITER plasma using the LVIC. This study demonstrated the tomographic capabilities of the LVIC which allowed accurate reconstruction of the plasma emissivity. The parameters of the detector (gas, pressure, dimensions and filters) have been investigated and it turns out that xenon is a better candidate than argon as it allows a reconstruction of the emissivity over a wider energy range. A study of the influence of perturbative noise has been performed and showed that the LVIC can deliver an accurate tomography in the plasma core with up to 2% of gaussian noise added to the measurement. Further investigations can be performed with an accurate estimation of the noise expected on the detector.

The possibility of energy discrimination using the LVIC has been investigated during this PhD thesis. An innovative modification of the LVIC design (addition of anodes) has been proposed for such purpose. A method of spectral deconvolution based on an hypothesis on the incoming photon spectrum has been developed and tested. Accurate reconstruction of the X-ray spectrum in the [3, 100] keV energy range was demonstrated. Energy-resolved tomography using multi-anodes LVIC has been performed and the possibility of reconstruction of the electron temperature from the local emissivity spectrum has been demonstrated accurately in the plasma core. A sen-

sitivity analysis was performed and showed that this method can function accurately with 1% of gaussian perturbative noise. Further improvements of the LVIC-based spectral deconvolution technique could be achieved by a simultaneous spectral and tomographic inversions. By performing these two tasks jointly, an algorithm could efficiently leverage the smoothness of the signal in both the spatial and spectral domain, hence improving the overall reconstruction accuracy.

An experimental validation of the model developed in the scope of this work through prototype testing would be greatly beneficial. The same goes for the spectral deconvolution technique. A prototype could also be used in an irradiation facility in order to estimate the effects of noise on the detection and demonstrate the ability of the LVIC to deliver accurate measurements in a radiative environment.

Bibliography

- [1] Smil V. *Energy Transitions: Global and National Perspectives*. Praeger, 2017. ISBN: 144085324X (cit. on p. 26).
- [2] *BP Statistical Review of World Energy*. 2019. URL: <https://www.bp.com/en/global/corporate/energy-economics/statistical-review-of-world-energy.html> (cit. on p. 26).
- [3] Detlef P Van Vuuren and Brian C O'Neill. "The consistency of IPCC's SRES scenarios to 1990–2000 trends and recent projections". In: *Climatic Change* 75.1-2 (2006), pp. 9–46 (cit. on p. 26).
- [4] F Barbir, TN Veziroğlu, and HJ Plass Jr. "Environmental damage due to fossil fuels use". In: *International journal of hydrogen energy* 15.10 (1990), pp. 739–749 (cit. on p. 27).
- [5] John Wesson and David J Campbell. *Tokamaks*. Vol. 149. Oxford university press, 2011 (cit. on p. 29).
- [6] Ian Cook, G Marbach, L Di Pace, C Girard, and NP Taylor. "Safety and environmental impact of fusion". In: *EUR (01) CCE-FU/FTC* 8.5 (2001) (cit. on p. 29).
- [7] *Wikipedia webpage*. URL: https://en.wikipedia.org/wiki/Nuclear_binding_energy (cit. on p. 30).
- [8] MB Chadwick et al. "ENDF/B-VII. 0: next generation evaluated nuclear data library for nuclear science and technology". In: *Nuclear data sheets* 107.12 (2006), pp. 2931–3060 (cit. on p. 31).
- [9] *Evaluated Nuclear Data File (ENDF)*. URL: <https://www-nds.iaea.org/exfor/endl.htm> (cit. on p. 31).
- [10] John D Lawson. "Some criteria for a power producing thermonuclear reactor". In: *Proceedings of the physical society. Section B* 70.1 (1957), p. 6 (cit. on pp. 31, 32).
- [11] Noel Fleurot, Claude Cavailler, and JL Bourgade. "The Laser Megajoule (LMJ) Project dedicated to inertial confinement fusion: Development and construction status". In: *Fusion Engineering and design* 74.1-4 (2005), pp. 147–154 (cit. on p. 33).
- [12] CA Haynam et al. "National Ignition Facility laser performance status". In: *Applied optics* 46.16 (2007), pp. 3276–3303 (cit. on p. 33).

- [13] T Klinger et al. “Overview of first Wendelstein 7-X high-performance operation”. In: *Nuclear Fusion* 59.11 (2019), p. 112004 (cit. on p. 34).
- [14] *Stellarators*. URL: https://terpconnect.umd.edu/~mattland/projects/1_stellarators/ (cit. on p. 34).
- [15] Shayok Mukhopadhyay. “Fractional order modeling and control: development of analog strategies for plasma position control of the Stor-1M Tokamak”. In: *All Graduate Theses and Dissertations* (2009), p. 460 (cit. on p. 35).
- [16] URL: https://www.centraliens-lille.org/medias/editor/files/Fusion_ITER_286_HD.pdf (cit. on p. 38).
- [17] R Neu et al. “Tungsten as plasma-facing material in ASDEX Upgrade”. In: *Fusion engineering and design* 65.3 (2003), pp. 367–374 (cit. on p. 39).
- [18] Raj Korde, Ajay Ojha, Robert Braasch, and Thomas C English. “The effect of neutron irradiation on silicon photodiodes”. In: *IEEE transactions on nuclear science* 36.6 (1989), pp. 2169–2175 (cit. on p. 40).
- [19] “Dossier de presse WEST”. In: (2017). URL: http://irfm.cea.fr/Images/astImg/693/Dossier-de-presse-WEST_07022017.pdf (cit. on p. 40).
- [20] D Van Houtte et al. “Recent fully non-inductive operation results in Tore Supra with 6 min, 1 GJ plasma discharges”. In: *Nuclear Fusion* 44.5 (2004), p. L11 (cit. on p. 41).
- [21] P Moreau et al. “Measurements and controls implementation for WEST”. In: *Fusion Engineering and Design* 123 (2017), pp. 1029–1032 (cit. on p. 41).
- [22] *ITER Organization website*. URL: <https://www.iter.org> (cit. on p. 44).
- [23] Yu V Gott and MM Stepanenko. “A low-voltage ionization chamber for the ITER”. In: *Instruments and Experimental Techniques* 52.2 (2009), pp. 260–264 (cit. on pp. 46, 76, 81).
- [24] D Colette et al. “Modeling a low voltage ionization chamber based tomography system on ITER”. In: *Review of Scientific Instruments* 91.7 (2020), p. 073504 (cit. on pp. 46, 76, 81).
- [25] Wilhelm Conrad Röntgen. “Über eine neue Art von Strahlen”. In: *Sitzungsber Phys Med Ges Wurtzburg* 9 (1895), pp. 132–141 (cit. on p. 49).
- [26] S Rand. “Inverse bremsstrahlung with high-intensity radiation fields”. In: *Physical Review* 136.1B (1964), B231 (cit. on p. 51).
- [27] John F Seely and Edward G Harris. “Heating of a plasma by multiphoton inverse bremsstrahlung”. In: *Physical Review A* 7.3 (1973), p. 1064 (cit. on p. 51).
- [28] Hans-Joachim Kunze. *Introduction to plasma spectroscopy*. Vol. 56. Springer Science & Business Media, 2009 (cit. on pp. 51, 53).

- [29] Hans R. Griem. *Principles of Plasma Spectroscopy*. Cambridge Monographs on Plasma Physics. Cambridge University Press, 1997. DOI: [10.1017/CB09780511524578](https://doi.org/10.1017/CB09780511524578) (cit. on p. 56).
- [30] Richard H Huddleston and Stanley L Leonard. “Plasma diagnostic techniques”. In: *pdt* 65 (1965) (cit. on p. 58).
- [31] Axel Jardin. “Soft X-ray measurements for impurity transport studies in tokamak plasmas”. PhD thesis. Dec. 2017. DOI: [10.13140/RG.2.2.15801.62562](https://doi.org/10.13140/RG.2.2.15801.62562) (cit. on pp. 59, 83, 84).
- [32] Open-ADAS. *The Open ADAS Project (Atomic Data and Analysis Structure)*. 2017. URL: <http://open.adas.ac.uk> (cit. on pp. 59, 61, 63).
- [33] M. O’Mullane. *Energy resolved radiated power simulations for ITER bolometer study*. Tech. rep. ITER Organization, 2015 (cit. on pp. 62, 136).
- [34] T Casper et al. “Development of the ITER baseline inductive scenario”. In: *Nuclear Fusion* 54.1 (2013), p. 013005 (cit. on p. 62).
- [35] HP Summers and MG O’Mullane. “The atomic data and analysis structure”. In: *Nuclear Fusion Research*. Springer, 2005, pp. 399–413 (cit. on p. 62).
- [36] Sven Wiesen et al. “The new SOLPS-ITER code package”. In: *Journal of nuclear materials* 463 (2015), pp. 480–484 (cit. on p. 62).
- [37] E Rosencher and B Vinter. *Optoélectronique* ■ édition Dunod. 2002 (cit. on p. 71).
- [38] Kevin W Wenzel et al. “Response of X-UV photodiodes to 1.5–17.5 keV x rays and MeV alpha particles”. In: *Review of scientific instruments* 64.7 (1993), pp. 1723–1733 (cit. on p. 71).
- [39] D Mazon et al. “Soft x-ray tomography for real-time applications: present status at Tore Supra and possible future developments”. In: *Review of Scientific Instruments* 83.6 (2012), p. 063505 (cit. on pp. 71, 81).
- [40] Valentin Igochine, Anja Gude, Marc Maraschek, and ASDEX Upgrade Team. “Hotlink based soft x-ray diagnostic on ASDEX Upgrade”. In: (2010) (cit. on p. 71).
- [41] M Anton et al. “X-ray tomography on the TCV tokamak”. In: *Plasma physics and controlled fusion* 38.11 (1996), p. 1849 (cit. on pp. 71, 146).
- [42] B Alper et al. *The JET multi-camera soft X-ray diagnostic*. Tech. rep. 1994 (cit. on p. 71).
- [43] V Weinzettl et al. “Design of multi-range tomographic system for transport studies in tokamak plasmas”. In: *Nuclear Instruments and Methods in Physics Research Section A: Accelerators, Spectrometers, Detectors and Associated Equipment* 623.2 (2010), pp. 806–808 (cit. on p. 71).

- [44] F Lemeilleur, M Glaser, EHM Heijne, P Jarron, and E Occelli. “Neutron-induced radiation damage in silicon detectors”. In: *IEEE transactions on nuclear science* 39.4 (1992), pp. 551–557 (cit. on p. 72).
- [45] M McPherson, BK Jones, and T Sloan. “Effects of radiation damage in silicon p-i-n photodiodes”. In: *Semiconductor science and technology* 12.10 (1997), p. 1187 (cit. on p. 72).
- [46] M. Edwards, G. Hall, and S. Sotthibandhu. “Neutron radiation damage studies of silicon detectors”. In: *Nuclear Instruments and Methods in Physics Research Section A: Accelerators, Spectrometers, Detectors and Associated Equipment* 310.1 (1991), pp. 283–286. ISSN: 0168-9002. DOI: [https://doi.org/10.1016/0168-9002\(91\)91044-V](https://doi.org/10.1016/0168-9002(91)91044-V). URL: <http://www.sciencedirect.com/science/article/pii/016890029191044V> (cit. on p. 72).
- [47] D Vezinet, D Mazon, and P Malard. “Absolute spectral characterization of silicon barrier diode: Application to soft X-ray fusion diagnostics at Tore Supra”. In: *Journal of Applied Physics* 114.2 (2013), p. 023104 (cit. on p. 72).
- [48] K Tritz, DJ Clayton, D Stutman, and M Finkenthal. “Compact “diode-based” multi-energy soft x-ray diagnostic for NSTX”. In: *Review of Scientific Instruments* 83.10 (2012), 10E109 (cit. on p. 72).
- [49] YL Li et al. “Edge multi-energy soft x-ray diagnostic in Experimental Advanced Superconducting Tokamak”. In: *Review of Scientific Instruments* 86.12 (2015), p. 123512 (cit. on p. 72).
- [50] LF Delgado-Aparicio et al. “Simulation, design, and first test of a multi-energy soft x-ray (SXR) pinhole camera in the Madison Symmetric Torus (MST)”. In: *Review of Scientific Instruments* 89.10 (2018), 10G116 (cit. on p. 72).
- [51] Yu V Gott and MM Stepanenko. “The radiation-tolerant x-ray monitor”. In: *Review of Scientific Instruments* 79.10 (2008), 10E930 (cit. on p. 73).
- [52] K.Y. Vukolov, Y.V. Gott, and S.N. Zvonkov. “Effect of neutron irradiation on the electrodes of a vacuum photoemission detector”. In: *Instrum. Exp. Tech.* 50 (2007), pp. 725–729. DOI: [10.1134/S0020441207060024](https://doi.org/10.1134/S0020441207060024) (cit. on p. 73).
- [53] Rutherford Ernest and Geiger Hans. “The charge and nature of the alpha particle”. In: *Proceedings of the Royal Society A: Mathematical, Physical and Engineering Sciences* 81 (1908), pp. 162–173 (cit. on p. 74).
- [54] Hans Geiger and Walther Müller. “Elektronenzählrohr zur messung schwächer aktivitäten”. In: *NW* 16.31 (1928), pp. 617–618 (cit. on p. 74).
- [55] Georges Charpak, R Bouclier, T Bressani, J Favier, and Č Zupančič. “The use of multiwire proportional counters to select and localize charged particles”. In: *Nuclear Instruments and Methods* 62.3 (1968), pp. 262–268 (cit. on p. 74).

- [56] A Oed. "Position-sensitive detector with microstrip anode for electron multiplication with gases". In: *Nuclear Instruments and Methods in Physics Research Section A: Accelerators, Spectrometers, Detectors and Associated Equipment* 263.2-3 (1988), pp. 351–359 (cit. on p. 74).
- [57] Yannis Giomataris, Ph Rebourgeard, Jean Pierre Robert, and Georges Charpak. "MICROMEGAS: a high-granularity position-sensitive gaseous detector for high particle-flux environments". In: *Nuclear Instruments and Methods in Physics Research Section A: Accelerators, Spectrometers, Detectors and Associated Equipment* 376.1 (1996), pp. 29–35 (cit. on p. 74).
- [58] Fabio Sauli. "GEM: A new concept for electron amplification in gas detectors". In: *Nuclear Instruments and Methods in Physics Research Section A: Accelerators, Spectrometers, Detectors and Associated Equipment* 386.2-3 (1997), pp. 531–534 (cit. on pp. 74, 80).
- [59] KARL Buchtela. "Gas ionization detectors". In: *Handbook of Radioactivity Analysis*. Academic Press San Diego, 2003, pp. 123–178 (cit. on p. 75).
- [60] Michael F L'Annunziata. "Radionuclide tracers". In: (1987) (cit. on p. 75).
- [61] Yu V Gott and MM Stepanenko. "Radiation-tolerant X- and γ -ray detectors". In: *Instruments and Experimental Techniques* 53.2 (2010), pp. 180–184 (cit. on p. 76).
- [62] Vezinet et al. "Capteur de rayonnement électromagnétique et/ou de particules" (cit. on p. 77).
- [63] NIST Xcom. "Photon cross sections database". In: *Retrieved April 30* (2013), p. 579 (cit. on p. 77).
- [64] D Mazon et al. "GEM detectors for WEST and potential application for heavy impurity transport studies". In: *Journal of Instrumentation* 11.08 (2016), p. C08006 (cit. on p. 80).
- [65] A Jardin et al. "On a gas electron multiplier based synthetic diagnostic for soft x-ray tomography on WEST with focus on impurity transport studies". In: *Journal of Instrumentation* 12.08 (2017), p. C08013 (cit. on pp. 80, 82).
- [66] A Jardin et al. "Tomographic capabilities of the new GEM based SXR diagnostic of WEST". In: *Journal of Instrumentation* 11.07 (2016), p. C07006 (cit. on pp. 80–82, 138).
- [67] D Mazon et al. "Polycapillary lenses for Soft-X-ray transmission: Model, comparison with experiments and potential application for tomographic measurements in tokamaks". In: *Nuclear Instruments and Methods in Physics Research Section B: Beam Interactions with Materials and Atoms* 355 (2015), pp. 301–306 (cit. on p. 81).
- [68] D Mazon et al. "Polycapillary lenses for soft x-ray transmission in ITER: Model, comparison with experiments, and potential application". In: *Review of Scientific Instruments* 87.11 (2016), 11E302 (cit. on p. 81).

- [69] D Colette et al. “Energy resolved x-ray measurement on ITER with Low Voltage Ionization Chambers”. In: *Review of Scientific Instruments* (2020) (cit. on p. 81).
- [70] Seiji Ogawa, Tso-Ming Lee, Alan R Kay, and David W Tank. “Brain magnetic resonance imaging with contrast dependent on blood oxygenation”. In: *proceedings of the National Academy of Sciences* 87.24 (1990), pp. 9868–9872 (cit. on p. 81).
- [71] Martin Dierolf et al. “Ptychographic X-ray computed tomography at the nanoscale”. In: *Nature* 467.7314 (2010), pp. 436–439 (cit. on p. 81).
- [72] Philip CJ Donoghue et al. “Synchrotron X-ray tomographic microscopy of fossil embryos”. In: *Nature* 442.7103 (2006), pp. 680–683 (cit. on p. 81).
- [73] J Radon. “On the determination of functions from their integrals along certain manifolds”. In: *Ber. Verh, Sachs Akad Wiss.* 69 (1917), pp. 262–277 (cit. on p. 81).
- [74] Johann Radon. “On the determination of functions from their integral values along certain manifolds”. In: *IEEE transactions on medical imaging* 5.4 (1986), pp. 170–176 (cit. on p. 81).
- [75] Jacques Hadamard. *Lectures on Cauchy’s problem in linear partial differential equations*. Yale University Press, 1923 (cit. on p. 82).
- [76] Nils Henrik Abel. “Auflösung einer mechanischen Aufgabe.” In: *Journal für die reine und angewandte Mathematik* 1826.1 (1826), pp. 153–157 (cit. on p. 82).
- [77] Yoshio Nagayama. “Tomography of $m=1$ mode structure in tokamak plasma using least-square-fitting method and Fourier–Bessel expansions”. In: *Journal of applied physics* 62.7 (1987), pp. 2702–2706 (cit. on p. 82).
- [78] Andrey N Tikhonov and Vasiliy Y Arsenin. “Solutions of ill-posed problems”. In: *New York* (1977), pp. 1–30 (cit. on p. 82).
- [79] J Mlynar et al. “Introducing minimum Fisher regularisation tomography to AXUV and soft x-ray diagnostic systems of the COMPASS tokamak”. In: *Review of Scientific Instruments* 83.10 (2012), 10E531 (cit. on p. 82).
- [80] TianBo Wang, D Mazon, J Svensson, D Li, and Geert Verdoolaege. “Bayesian tomography of soft X-ray emissivity on the WEST tokamak”. In: *36th International Workshop on Bayesian Inference and Maximum Entropy Methods in Science and Engineering*. 2017 (cit. on p. 82).
- [81] Tianbo Wang, Didier Mazon, Jakob Svensson, Dong Li, and Geert Verdoolaege. “Bayesian soft X-ray Tomography on Tore Supra and WEST”. In: *on Fusion Data Processing, Validation and Analysis* (2017), p. 27 (cit. on p. 82).
- [82] T Wang et al. “Bayesian data analysis for Gaussian process tomography”. In: *Journal of Fusion Energy* 38.3-4 (2019), pp. 445–457 (cit. on p. 82).
- [83] Matthieu Martin Jean-Andre Simeoni. *Sparse spline approximation on the hypersphere by generalised total variation basis pursuit*. Tech. rep. 2019 (cit. on p. 82).

- [84] Julien Fageot and Matthieu Simeoni. “TV-based reconstruction of periodic functions”. In: *Inverse Problems* (2020) (cit. on p. 82).
- [85] Matthieu Simeoni. “Functional Penalised Basis Pursuit on Spheres”. In: *arXiv preprint arXiv:2006.05761* (2020) (cit. on p. 82).
- [86] Matthieu Martin Jean-Andre Simeoni. *Functional Inverse Problems on Spheres: Theory, Algorithms and Applications*. Tech. rep. EPFL, 2020 (cit. on p. 82).
- [87] Heinz Werner Engl, Martin Hanke, and Andreas Neubauer. *Regularization of inverse problems*. Vol. 375. Springer Science & Business Media, 1996 (cit. on p. 82).
- [88] Peter R Johnston and Ramesh M Gulrajani. “Selecting the corner in the L-curve approach to Tikhonov regularization”. In: *IEEE Transactions on biomedical engineering* 47.9 (2000), pp. 1293–1296 (cit. on p. 83).
- [89] Dorota Krawczyk-StańDo and Marek Rudnicki. “Regularization parameter selection in discrete ill-posed problems—the use of the U-curve”. In: *International Journal of Applied Mathematics and Computer Science* 17.2 (2007), pp. 157–164 (cit. on p. 83).
- [90] Lars Christian Ingesson and DJ Wilson. “Optimization of apertures and collimators for multi-channel plasma diagnostics”. In: *Review of scientific instruments* 73.8 (2002), pp. 2890–2899 (cit. on p. 88).
- [91] LC Ingesson, CF Maggi, and R Reichle. “Characterization of geometrical detection-system properties for two-dimensional tomography”. In: *Review of Scientific Instruments* 71.3 (2000), pp. 1370–1378 (cit. on p. 89).
- [92] LC Ingesson, PJ Böcker, R Reichle, M Romanelli, and P Smeulders. “Projection-space methods to take into account finite beam-width effects in two-dimensional tomography algorithms”. In: *JOSA A* 16.1 (1999), pp. 17–27 (cit. on p. 90).
- [93] Takeshi Watanabe, HW Schnopper, and FN Cirillo. “K X-ray fluorescence yield of argon”. In: *Physical Review* 127.6 (1962), p. 2055 (cit. on p. 93).
- [94] Marjan Hribar, Alojz Kodre, and Jože Pahor. “The determination of the K-shell fluorescence yield of xenon by use of the proportional counter method”. In: *Zeitschrift für Physik A Atoms and Nuclei* 280.3 (1977), pp. 227–229 (cit. on p. 93).
- [95] L G Christophorou, V E Anderson, and J B Birks. “ATOMIC AND MOLECULAR RADIATION PHYSICS.” In: (Jan. 1971) (cit. on p. 99).
- [96] H. Sakurai and B.D. Ramsey. “Dependence of energy resolution on anode diameter in xenon proportional counters”. In: *Nuclear Instruments and Methods in Physics Research Section A: Accelerators, Spectrometers, Detectors and Associated Equipment* 313.1 (1992), pp. 155–160. ISSN: 0168-9002. DOI: [https://doi.org/10.1016/0168-9002\(92\)90092-I](https://doi.org/10.1016/0168-9002(92)90092-I). URL: <http://www.sciencedirect.com/science/article/pii/016890029290092I> (cit. on p. 99).

- [97] U. Fano. “Ionization Yield of Radiations. II. The Fluctuations of the Number of Ions”. In: *Phys. Rev.* 72 (1 1947), pp. 26–29. DOI: [10.1103/PhysRev.72.26](https://doi.org/10.1103/PhysRev.72.26). URL: <https://link.aps.org/doi/10.1103/PhysRev.72.26> (cit. on p. 99).
- [98] Akira Hashiba, Kimiaki Masuda, Tadayoshi Doke, Tan Takahashi, and Yuzo Fujita. “Fano factor in gaseous argon measured by the proportional scintillation method”. In: *Nuclear Instruments and Methods in Physics Research Section A: Accelerators, Spectrometers, Detectors and Associated Equipment* 227.2 (1984), pp. 305–310. ISSN: 0168-9002. DOI: [https://doi.org/10.1016/0168-9002\(84\)90138-4](https://doi.org/10.1016/0168-9002(84)90138-4). URL: <http://www.sciencedirect.com/science/article/pii/0168900284901384> (cit. on p. 99).
- [99] Nobumiti Ishida, Jun Kikuchi, Tadayoshi Doke, and Masayuki Kase. “Fano factor in xenon”. In: *Phys. Rev. A* 46 (3 1992), pp. 1676–1679. DOI: [10.1103/PhysRevA.46.1676](https://doi.org/10.1103/PhysRevA.46.1676). URL: <https://link.aps.org/doi/10.1103/PhysRevA.46.1676> (cit. on p. 99).
- [100] K. Sato, H. Toyokawa, Y. Kohmura, T. Ishikawa, and M. Suzuki. “The Behavior of Ionization Chambers under the Irradiation of High Flux X-Ray Beam”. In: *SPRING-8 Annual Report 1997* (1997). URL: http://www.spring8.or.jp/pdf/en/ann%5C_rep/97/P225-227.pdf (cit. on p. 99).
- [101] John Hammersley. *Monte carlo methods*. Springer Science & Business Media, 2013 (cit. on p. 99).
- [102] T Odstrčil et al. “Optimized tomography methods for plasma emissivity reconstruction at the ASDEX Upgrade tokamak”. In: *Review of Scientific Instruments* 87.12 (2016), p. 123505 (cit. on pp. 113, 138).
- [103] Mathias Anton, MJ Dutch, and Henri Weisen. “Relative calibration of photodiodes in the soft-x-ray spectral range”. In: *Review of scientific instruments* 66.7 (1995), pp. 3762–3769 (cit. on p. 146).
- [104] E Lerche et al. “Optimization of ICRH for core impurity control in JET-ILW”. In: *Nuclear Fusion* 56.3 (2016), p. 036022 (cit. on p. 171).
- [105] *EUROfusion website*. URL: <https://www.euro-fusion.org/news/detail/detail/News/charged-particles-movement/> (cit. on p. 172).
- [106] FL Hinton and Richard D Hazeltine. “Theory of plasma transport in toroidal confinement systems”. In: *Reviews of Modern Physics* 48.2 (1976), p. 239 (cit. on p. 172).
- [107] ML Reinke et al. “Parallel transport studies of high-Z impurities in the core of Alcator C-Mod plasmas”. In: *Physics of Plasmas* 20.5 (2013), p. 056109 (cit. on pp. 172, 173).
- [108] ML Reinke et al. “Poloidal variation of high-Z impurity density due to hydrogen minority ion cyclotron resonance heating on Alcator C-Mod”. In: *Plasma Physics and Controlled Fusion* 54.4 (2012), p. 045004 (cit. on p. 173).

- [109] JA Wesson. “Poloidal distribution of impurities in a rotating tokamak plasma”. In: *Nuclear fusion* 37.5 (1997), p. 577 (cit. on p. [173](#)).
- [110] Emily A Belli, J Candy, and C Angioni. “Pfirsch–Schlüter neoclassical heavy impurity transport in a rotating plasma”. In: *Plasma Physics and Controlled Fusion* 56.12 (2014), p. 124002 (cit. on p. [173](#)).
- [111] C Angioni et al. “The impact of poloidal asymmetries on tungsten transport in the core of JET H-mode plasmas”. In: *Physics of Plasmas* 22.5 (2015), p. 055902 (cit. on p. [174](#)).
- [112] Federico D Halpern et al. “Predictive simulations of ITER including neutral beam driven toroidal rotation”. In: *Physics of Plasmas* 15.6 (2008), p. 062505 (cit. on pp. [176](#), [178](#)).
- [113] Matthew J Hole et al. “The impact of anisotropy on ITER scenarios”. In: *Nuclear Fusion* (2020) (cit. on p. [176](#)).
- [114] T Casper et al. “Development of the ITER baseline inductive scenario”. In: *Nuclear Fusion* 54.1 (2013), p. 013005 (cit. on p. [176](#)).

Résumé

La grande majorité de l'énergie mondiale provient de la combustion de combustibles fossiles. Les réserves de ces combustibles ont atteint un niveau critique ces dernières années et leur combustion émet des gaz à effets de serre, qui sont les principaux responsables du dérèglement climatique. Il est donc impératif de trouver des sources d'énergies propres et durables pour remplacer ces combustibles fossiles. La fusion thermonucléaire contrôlée est un candidat de choix. Le tokamak ITER a pour objectif de démontrer la faisabilité d'un réacteur de fusion générant plus d'énergie qu'il n'en consomme ($Q > 10$). Les composants face au plasma d'ITER seront à l'origine d'une pollution de ce dernier par des impuretés lourdes telles que le tungstène. Ces impuretés sont à l'origine d'importantes pertes radiatives dans la gamme des rayons X dont la mesure est nécessaire pour étudier le transport de ces impuretés et, à terme, pouvoir identifier des actuateurs permettant de limiter leur propagation jusqu'au cœur du plasma. L'environnement radiatif d'ITER limite le choix de détecteurs X aux seuls détecteurs à gaz, dont le LVIC (Low Voltage Ionization Chamber) est le candidat principal. Cette thèse a pour but l'étude des capacités du LVIC pour la mesure de rayons X sur ITER. Un diagnostic synthétique est adapté à partir du GEM (Gas Electron Multiplier) afin de simuler la mesure par ce détecteur. L'inversion tomographique de l'émissivité X à l'aide de LVIC est étudiée et des lignes de visées additionnelles, compatibles avec les contraintes d'intégration sur ITER, sont proposées. La possibilité de discriminer le flux X en énergie est investiguée à travers une modification innovante du détecteur. Une méthode d'inversion basée sur la méthode des moindres carrés est spécifiquement développée pour la déconvolution du spectre X. La température électronique du plasma est extraite du spectre X avec succès. La capacité d'étude du transport d'impuretés du LVIC est démontrée à travers la reconstruction des coefficients de convection et de diffusion du tungstène d'un plasma ITER.

Abstract

The vast majority of the energy consumed in the world is coming from burning fossil fuels. The natural reserves of these fuels have reached a critical level in the last years and their combustion releases greenhouse effect gases, which are the main cause for global warming. It is therefore crucial to develop clean and sustainable energy sources in order to replace fossil fuels. Controlled thermonuclear fusion is one of the main candidates. The ITER tokamak aims at demonstrating the feasibility of a fusion reactor generating more energy than it consumes ($Q > 10$). The ITER plasma facing components will be the source of pollution by heavy impurities such as tungsten in the plasma. Such impurities lead to great radiative losses in the X-ray range. X-ray measurement is mandatory for impurity transport studies in order to, with time, be able to identify actuators preventing impurity accumulation in the plasma core. The ITER radiative environment limits the choice of X-ray detectors to gas detectors, of which the LVIC (Low Voltage Ionization Chamber) is the most promising candidate. This thesis aims at studying the capabilities of the LVIC for X-ray measurement on ITER. A synthetic diagnostic tool has been adapted from the GEM (Gas Electron Multiplier) in order to simulate the measurement with an LVIC. Tomographic inversion of the X-ray emissivity using LVIC is studied and additional lines-of-sight, compliant with the ITER integration constraints, are proposed. The possibility of energy discrimination is investigated through an innovative modification of the detector. An inversion method based on the least squares method is specifically developed to deconvolute the X-ray spectrum. The electron temperature profile is successfully extracted from the X-ray spectrum. The capability of impurity transport study of the LVIC is demonstrated through the reconstruction of the tungsten convection and diffusion coefficients of an ITER plasma.